KUOPION YLIOPISTON JULKAISUJA C. LUONNONTIETEET JA YMPÄRISTÖTIETEET 204
KUOPIO UNIVERSITY PUBLICATIONS C. NATURAL AND ENVIRONMENTAL SCIENCES 204

EEVA BOMAN

Radiotherapy Forward and Inverse Problem Applying Boltzmann Transport Equation

Doctoral dissertation
To be presented by permission of the Faculty of Natural and Environmental Sciences of the University of Kuopio for public examination in Auditorium L22, Snellmania building, University of Kuopio, on Saturday 27$^{\mathrm{th}}$ January 2007, at 12 noon

Department of Physics
University of Kuopio

KUOPION YLIOPISTO

KUOPIO 2007

Distributor: Kuopio University Library
P.O.Box 1627
FI-70210 KUOPIO
FINLAND
Tel. +358 17 163 430
Fax +358 17 163 410
http://www.uku.fi/kirjasto/julkasutoiminta/julkmyyn.html

Series editors: Professor Pertti Pasanen, Ph.D.
Department of Environmental Sciences

Professor Jari Kaipio, Ph.D.
Department of Physics

Author's address: Department of Physics
University of Kuopio
P.O.Box 1627
FI-70210 KUOPIO
FINLAND
Tel. +358 17 162 361
Fax +258 17 162 373
E-mail: Eeva.Boman@uku.fi

Supervisors: Docent Jouko Tervo, Ph.D.
Department of Mathematics and Statistics
University of Kuopio

Docent Marko Vauhkonen, Ph.D.
Department of Physics
University of Kuopio

Reviewers: Professor Simon Arridge, Ph.D.
Department of Computer Science
University College London, UK

Associate Professor Bengt Lind, Ph.D.
Department of Oncology-Pathology, Medical Radiation Physics
Karolinska Institutet and Stockholm University, Sweden

Opponent: Docent Mikko Tenhunen, Ph.D.
Department of Oncology
Helsinki University Central Hospital

ISBN 978-951-27-0682-2
ISBN 978-951-27-0457-6 (PDF)
ISSN 1235-0486
Kopijyvä
Kuopio 2007
Finland

Boman, Eeva. Radiotherapy Forward and Inverse Problem Applying Boltzmann Transport Equation. Kuopio University Publication C. Natural and Environmental Sciences 204. 2006. 138 p.
ISBN 978-951-27-0682-2
ISBN 978-951-27-0457-6 (PDF)
ISSN 1235-0486

ABSTRACT

The aim of radiotherapy is to destroy the unhealthy tumorous tissue with ionizing radiation, while the other parts of the human body are saved. The absorbed dose is used as a measure of the ionizing radiation. In external radiotherapy treatment planning, one tries to select the treatment settings such that the high dose volume conforms the planning target volume, while other sensitive organs and normal tissue receive as low dose as possible. To be able to do this, one needs a physical dose model, which describes the dose distribution within the patient domain, when the treatment settings or radiation flux intensities at the patient boundary are known. This is often referred to a radiation therapy forward problem.

Three coupled time independent linear Boltzmann transport equations can be used to describe the traveling of ionizing radiation, taking rigorously into account tissue inhomogeneities and different scattering phenomena. From the solution of this coupled system the absorbed dose can be computed. In this thesis, the solving of the coupled system of time independent linear Boltzmann equations with assigned boundary conditions is called as the radiotherapy forward problem.

The time independent linear Boltzmann transport equation is a integrodifferential equation, whose solution has spatial, angular and energy variables. In practical geometries, numerical methods are needed to solve the forward problem. In this thesis, finite element method is utilized to solve the radiotherapy forward problem and the existence of the solution is studied. The theories are tested via finite element simulations in two and three spatial dimensions.

Radiotherapy treatment planning is an inverse problem. This means that one knows the desired dose distribution within the patient and the problem is to solve the boundary flux intensities or some treatment settings. In this thesis, the inverse problem of radiotherapy is considered using boundary control optimization method. The novel approach of parametrization is used to make the global optimization possible. With parametrization the number of unknowns is reduced significantly and global optimization is more practical to implement than it would be without the parametrization. These methods are tested with numerical simulations in two spatial dimensions.

AMS (MOS) Classification: 78A35, 78A46, 34B05, 45K05, 49J20, 15A18, 92C50
Universal Decimal Classification: 517.927, 517.95, 517.968.7, 517.977, 519.63
National Library of Medicine Classification: QT 36, QZ 269, WN 250
INSPEC Thesaurus: biomedical engineering; radiation therapy; Boltzmann equation; integrodifferential equations; boundaryvalue problems; inverse problems; finite element analysis; optimal control; singular value decomposition

Acknowledgements

This study was carried out in the Department of Physics, University of Kuopio, during the years 2003-2006, which included also one year maternity leave. The study was supported by Academy of Finland. Here I would like to express my sincere compliments to all who have contributed to this thesis.

First I would like to express my gratitude to my main supervisor Docent Jouko Tervo, Ph.D., for the mathematical perspective of this thesis. Secondly I would like to thank my second supervisor Docent Marko Vauhkonen, Ph.D., for his guidance in the world of mathematical modeling. Without them and their ideas this thesis would never have seen daylight.

I wish to thank the official reviewers Professor Simon Arridge, Ph.D., and Associate Professor Bengt Lind, Ph.D., for their valuable suggestions and comments for the thesis.

I want to thank the members of the former radiotherapy research group in the University of Kuopio. Especially I thank Pekka Kolmonen, Ph.D., and Kai Jaatinen, M.Sc., for valuable scientific discussions during the years. Also I thank Docent Tapani Lahtinen, Ph.D., from the Kuopio University hospital for the support and keeping the hospital needs in mind although this study is strictly academic.

I thank the staff of the Department of Physics at the University of Kuopio. It has been a pleasure to work with them. Especially I want to thank Tanja Tarvainen, Ph.D., for all the help during the years. I also thank Coordinator Antti Vanne, M.Sc., for making the computations in the computer cluster possible.

I warmly thank my mother Milja and Rauno for support and believing in me. I thank my sisters Lea, Asta and Johanna and brother Ari and their families for showing me the importance of relatives. Last but not least I want to express my sincere gratitude to my husband Markus and to my sons Leevi and Samu for making me complete. They remind me every day the priorities of life.

Kuopio, January 24, 2007

Eeva Boman

Abbreviations

1D	One dimensional
2D	Two dimensional
3D	Three dimensional
BTE	Boltzmann transport equation
B-CSDAE	Boltzmann-CSDA equation
CSDA	Continuous slowing down approximation
FEM	Finite element method
IMRT	Intensity modulated radiation therapy
IRTTP	Inverse radiation therapy treatment planning
keV	Kilo electron volts
MC	Monte Carlo
MeV	Mega electron volts
MLC	Multileaf collimator
MV	Mega volts
PTV	Planning target volume
SAAF	Self-adjoint angular flux
SVD	Singular value decomposition
sr	steradian

List of symbols (and units)

$(\cdot)^{\mathrm{Br}}$	Refers to electron bremsstrahlung process
$(\cdot)^{\mathrm{C}}$	Refers to photon Compton effect
$(\cdot)^{\mathrm{h}}$	finite element approximation
$(\cdot)^{\mathrm{Ie}}$	Refers to electron inelastic scattering
$(\cdot)^{\mathrm{R}}$	Refers to electron elastic scattering
$(\cdot)^{\mathrm{sd}}$	Refers to steam-line diffusion method
$(\cdot)^{\mathrm{T}}$	Transpose operator
$(\cdot)^{*}$	Adjoint operator
$(\cdot)'_{\mathrm{e}}, (\cdot)_{\mathrm{e}}$	Refers to electron before and after scattering
$(\cdot)_j$	Refers to particle j
$(\cdot)'_{\mathrm{p}}, (\cdot)_{\mathrm{p}}$	Refers to photon before and after scattering
$(\cdot)_{\mathrm{pr}}$	Refers to scattered primary electron
$(\cdot)_{\mathrm{s}}$	Refers to scattered secondary electron
$(\cdot)_{+}$	Positive part of the function
$(\cdot)_{-}$	Negative part of the function
$\lvert \cdot \rvert$	Absolute value
$\lVert \cdot \rVert$	Euclidean norm
$\bigoplus$	Direct sum

α	Unknown vector in FEM approximation or parameter for the coercivity considerations
γ	Parametrization vector
$\Gamma,\ \Gamma_i$	Patch on the boundary
δ	Stream-line diffusion parameter
$\delta(\cdot)$	Delta function, defined by equation (2.14)
θ	Scattering angle of polar coordinates (rad)
κ	Coercivity parameter
μ	Cosine of the scattering angle θ
ρ	Density ($\mathrm{g/cm^3}$)
σ_{a}	Absorption cross section ($\mathrm{cm^{-1}}$)
σ_{s}	Scattering cross section ($\mathrm{cm^{-1}}$)
$\sigma, \sigma_{\mathrm{t}}$	Total cross section ($\mathrm{cm^{-1}}$)
σ_{d}	Differential cross section ($\mathrm{cm^{-1}MeV^{-1}sr^{-1}}$)
σ_j	Total cross section of particle j ($\mathrm{cm^{-1}}$)
$\sigma_{j'\to j}$	Differential cross section differential in angle and energy to change particle j' to particle j ($\mathrm{cm^{-1}MeV^{-1}sr^{-1}}$)
$\sigma^{\mathrm{r}}_{\mathrm{t}},\ \sigma^{\mathrm{r}}_{\mathrm{d}},$	Restricted total and differential cross sections
σ^{j}_{d}	Total cross section value at point, which is indexed as d
$\sigma^{j'\to j}_{dd}$	Differential cross section (from j' to j) value at point, which is indexed as dd
τ	Total stopping power ($\mathrm{MeVcm^{-1}}$)

τ^{r}	Restricted stopping power (MeVcm^{-1})
τ^{*}	Mean-square stopping power
$\phi_k(\boldsymbol{x}, E, \boldsymbol{\Omega})$	Basis function for particle angular flux
$\phi^{E}_{k_{\mathrm{e}}}$	Separable basis function for E
$\phi^{\boldsymbol{x}}_{k_{\mathrm{s}}}$	Separable basis function for $\boldsymbol{x}$
$\phi^{\theta}_{k_{\mathrm{o}}}$	Separable basis function for θ
$\phi^{\boldsymbol{\Omega}}_{k_{\mathrm{o}}}$	Separable basis function for $\boldsymbol{\Omega}$
φ	Azimuthal angle of polar coordinates (rad)
$\psi(\boldsymbol{x}, E, \boldsymbol{\Omega})$	Particle angular flux ($\mathrm{cm}^{-2}\mathrm{MeV}^{-1}\mathrm{sr}^{-1}$)
ψ^{E}	Angle integrated particle flux i.e. the energy spectrum ($\mathrm{cm}^{-2}\mathrm{MeV}^{-1}$)
ψ^{I}	Angle and energy integrated particle flux (cm^{-2})
ψ_0	Boundary flux
Ψ^0	Boundary flux vector
ω	Scattering angle for isotropic scattering ($\omega = \arccos(\boldsymbol{\Omega}' \cdot \boldsymbol{\Omega})$)
$\boldsymbol{\Omega}', \boldsymbol{\Omega}$	Particle direction before and after scattering ($\boldsymbol{\Omega} = (\cos\varphi \sin\theta, \sin\varphi \sin\theta, \cos\theta)$)
$\boldsymbol{\Omega}_{2\mathrm{D}}$	Particle direction in 2D ($\boldsymbol{\Omega}_{2\mathrm{D}} = (\sin\theta, \cos\theta)$)

$\boldsymbol{A},\ \boldsymbol{A}^{\mathrm{r}}$	Big linear system matrices
$\boldsymbol{b}_j$	Right hand vector of the big linear system, $j = 1, 2$ indicates the boundary condition for photons and electrons
$B,\ B^{\mathrm{r}},\ \widetilde{B}$	Bilinear forms
c_i	Weights at the cost function
$\mathcal{C}(\bar{G})$	Function space of continuous functions on $\bar{G}$
$\mathbf{C}$	Critical organ's region
$D(\boldsymbol{x})$	Absorbed dose ($\mathrm{Gy} \approx 6,24 \cdot 10^{9} \rho \mathrm{MeVcm}^{-3}$)
D_0	Uniform dose in target $\mathbf{T}$
$D_{\mathbf{C}},\ D_{\mathbf{N}}$	Upper bounds of the dose in critical organ and normal tissue
$D_{\mathbf{T}},\ d_{\mathbf{T}}$	Upper and lower bounds of the dose in $\mathbf{T}$
$\mathcal{D}$	Operator for the dose ($\mathcal{D}\psi(\boldsymbol{x}) = D(\boldsymbol{x})$)
$\frac{\mathrm{d}\sigma}{\mathrm{d}E}$	Differential cross section differential in energy ($\mathrm{cm}^{-1}\mathrm{MeV}^{-1}$)
$\frac{\mathrm{d}\sigma}{\mathrm{d}\boldsymbol{\Omega}}$	Differential cross section differential in scattering angle $\boldsymbol{\Omega}$ ($\mathrm{cm}^{-1}\mathrm{sr}^{-1}$)
$\frac{\mathrm{d}\sigma}{\mathrm{d}\theta}$	Differential cross section differential in scattering angle θ
$\frac{\mathrm{d}\sigma}{\mathrm{d}\mu}$	Differential cross section differential in the cosine of the scattering angle
$\frac{\mathrm{d}^2\sigma}{\mathrm{d}E\mathrm{d}\boldsymbol{\Omega}}$	Differential cross section differential in scattering angle and energy ($\mathrm{cm}^{-1}\mathrm{MeV}^{-1}\mathrm{sr}^{-1}$)
$\frac{\mathrm{d}^2\sigma^{\mathrm{a}}}{\mathrm{d}E\mathrm{d}\boldsymbol{\Omega}}$	Differential absorption cross section differential in scattering angle and energy ($\mathrm{cm}^{-1}\mathrm{MeV}^{-1}\mathrm{sr}^{-1}$)

$\frac{\mathrm{d}^2\sigma^{\mathrm{s}}}{\mathrm{d}E\mathrm{d}\boldsymbol{\Omega}}$	Differential scattering cross section differential in scattering angle and energy ($\mathrm{cm}^{-1}\mathrm{MeV}^{-1}\mathrm{sr}^{-1}$)
$\frac{\mathrm{d}^2\sigma}{\mathrm{d}E\mathrm{d}\mu}$	Differential scattering cross section differential in energy and cosine of the scattering angle ($\mathrm{cm}^{-1}\mathrm{MeV}^{-1}$)
E', E	Particle energy before and after scattering (MeV)
E_0	Electron rest energy ($E_0 = 0.511\mathrm{MeV}$)
E_{cut}	Cut-off energy
$E_{\max}$	Maximum energy
$E_{\min}$	Minimum energy
$f(\boldsymbol{x}, E, \boldsymbol{\Omega}, t)$	particle time dependent angular density ($\mathrm{cm}^{-3}\mathrm{MeV}^{-1}\mathrm{sr}^{-1}\mathrm{s}^{-1}$)
G	Domain $V \times I \times S =: G$
$H,\ \widetilde{H}$	Function spaces
I	Energy interval ($I = [E_{\min}, E_{\max}]$)
j	Particle index, $j = 1, 2, 3$ refers to photons, electrons, positrons, respectively, or angular current
J_F	Jacobian matrix of mapping F
K_j	Scattering term for particle j
$L_2(G)$	Lebesgue space of real valued square integrable functions on G
L_{FP}	Fokker-Plank operator
M	Gram-atomic weight of an element (g/atom), gram-molecular weight of a molecule (g/mole) or the total number of node points in all fields
M_i	Total number of node points in field s_i
M_i^{e}	Number of unknowns in the discretization of energy interval in field s_i
M_i^{o}	Number of angle unknowns in the discretization of angular domain in field s_i
M_i^{s}	Number of spatial unknowns in the discretization in field s_i
$\mathcal{M}(m \times n)$	Matrix of size $(m \times n)$
$\boldsymbol{n}$	Normal vector
N	Number of unknowns in the discretization of particle flux ψ_j
N_{e}	Number of unknowns in the discretization of energy interval
N_{o}	Number of angle unknowns in the discretization of angular domain
N_{s}	Number of spatial unknowns in the discretization
N_{A}	Avogadro's constant ($N_{\mathrm{A}} = 6.022 \cdot 10^{23}\mathrm{mole}^{-1}$)
$N_{\partial V}$	Number of subdomains in ∂V with constant normal vector $\boldsymbol{n}$
$\mathbf{N}$	Normal tissue's region
r_0	Classical electron radius ($r_0 = 2.818 \cdot 10^{-13}\mathrm{cm}$)
$\mathbb{R}^n$	n-dimensional real space
s_i	Treatment field ($i = 1, ..., L$)
S	Unit sphere
t	Time variable (s)
$t(\boldsymbol{x}, \boldsymbol{\Omega})$	Distance form point $\boldsymbol{x}$ to the boundary in direction of $\boldsymbol{\Omega}$ (cm)

$\mathbf{T}$	Target volume i.e. PTV
u	Incoming flux distributions for all fields ($u = (u_1, ..., u_L)$)
v	Particle speed (cm/s)
$\boldsymbol{v}$	Particle velocity
v_j	Test function for particle j
V	Spatial domain
$\bar{V}$	Closure of domain V
∂V	The boundary of spatial domain V
$\boldsymbol{x} = (x_1, x_2, x_3)$	Spatial variable
X_h	Linear hull for the discretization of the particle fluxes
Z	Number of electrons per molecule of a compound
Z_i	Number of electrons per atom of an element i (1/atom)
$Q_j(\boldsymbol{x}, E, \boldsymbol{\Omega}, t)$	Time dependent source term for particle j ($\mathrm{cm}^{-3}\mathrm{MeV}^{-1}\mathrm{sr}^{-1}\mathrm{s}^{-1}$)

Chapter I

Introduction

The purpose of radiotherapy treatment is to destroy the tumorous tissue with ionizing radiation by localizing high dose concentrations in the tumor volume while the healthy tissues and organs receive as low dose concentration as possible [188, 106]. In external radiotherapy the ionizing radiation is directed to the patient from the external source. Another possibility is the internal radiotherapy, in which the sources of ionizing radiation are implanted inside the patient [198]. This study considers the external beam radiotherapy, in which the photon and electron beams are the most often used external radiations in clinical applications. The heavy particles such as neutrons and protons are still rarely used because of the enormous cost involved [165, 106].

In external electron or photon radiotherapy, the treatment unit is typically a linear accelerator, in which electrons are accelerated to high energies using high-frequency electromagnetic waves [177, 106]. In electron treatments, electrons are accelerated to desired energy and then directed to the patient. The electrons entering to the patient surface are almost monoenergetic having the maximum energy achieved in the acceleration. In photon treatments, the incoming photons are produced by making the high energy electrons to strike a target such as tungsten, which produces x-rays in bremsstrahlung progress (see 2.4.2). The photon beam is heterogeneous in energy, having the maximum energy to be near the maximum energy of the incident electrons before the strike. Also the lower photon energies are present in the photon beam due to bremsstrahlung progress.

In treatment planning, one seeks the best alternatives for the beam orientations and different field settings to achieve the desired dose distribution in the tumor volume and as low dose as possible in the healthy tissue and organs. Nowadays the use of three dimensional (3D) imaging techniques, such as computer tomography (CT) and magnetic resonance imaging (MRI), enable more accurate patient 3D imaging. This enables the use of conformal radiotherapy, in which the goals of the radiotherapy treatment are met, i.e the high dose volume conforms the planning target volume (PTV) and other healthy tissue and organs receive as low dose as possible. The intensity modulated radiation therapy (IMRT) can be utilized for the conformity purposes [35, 5, 191, 190, 146]. In IMRT, the intensities of the external radiation fluxes are modulated using different field settings such as wedges,

multileaf collimator (MLC). Typically, in IMRT treatments several fields are used with a static [169, 109, 15, 154, 61], dynamic [174, 25, 6, 52, 105] or interrupted dynamic sequences [129]. Other possibility is, for example tomotherapy, in which several small beams are directed to the target [126].

Traditionally, in finding the best treatment plan, the treatment settings (incoming radiation direction and intensity, MLC parameters, wedge angles etc.) are selected by a trial-and-error sequence [48]. However, the use of IMRT greatly increases the degree of freedom in selecting the treatment settings and that is why different optimization techniques are becoming more general [37]. These techniques include direct optimization techniques, in which the intensity modulation apertures, for example the MLC parameters are used directly as free variables in the dose optimization [129, 169, 25], and intensity optimization techniques, in which the beamlet weights of the field intensities are used as free variables in the dose optimization [57, 76, 110]. These optimization problems are often referred to an inverse radiation therapy treatment planning (IRTTP) problems.

From the mathematical point of view, the radiotherapy treatment planning is an inverse problem, i.e. the problem is to find the best source arrangements to receive the desired dose distribution within the patient. In solving the inverse problem, one needs a solution of the forward problem, i.e. a solution for the model of the dose calculation. In the forward problem of the external radiotherapy, one computes the dose distribution in a patient resulted from the external sources of ionizing radiation with some aperture settings. Several models have been developed for the dose calculation [4, 164, 144, 95, 114, 84]. Nowadays, the Monte Carlo (MC) method is assumed to be the most accurate method for the dose calculation for the external photon or electron fluxes [142, 8, 22, 23, 104, 158]. In MC, the paths of the scattering particles are followed by randomly selecting the new directions and energies of the particles. In different scattering interactions, the particles loose their energy, other particles are created and energy is absorbed to matter affecting the dose. With several millions particle histories MC method gives an estimate for the dose distribution. The drawback of the MC method is the long computation time and that is why still so-called pencil-beam models are the most commonly used in treatment planning systems [4, 81, 180]. In pencil-beam models, the dose in a patient is achieved as a superposition of appropriately weighted dose deposition kernels. The kernels can be modeled with Monte Carlo methods, using some approximations or using empirical beam data [167, 42, 31, 151, 110].

Most of the dose calculation models have their roots in Boltzmann transport equation (BTE). The previously presented MC method uses BTE to simulate particle transport in a medium [142, 8, 123, 104, 152]. The Fokker-Plank and Fermi equations can be shown to be approximations of the BTE [149, 150, 33, 28, 111, 138, 24]. In it's original form, the BTE takes rigorously into account the patient inhomogeneity and scattering effects [30]. It is an integro-partial differential equation and it is studied in many fields of physics, for example in nuclear reactor physics [18, 79, 197], astrophysics, optical tomography [103, 89, 43, 10], x-ray spectra and electron microbeam analysis [72, 73, 135]. Excellent books, which consider BTE in detail in variety of fields are for example

[50, 47, 67, 196, 148]. The linear stationary BTE can be used in radiation therapy, because the high energy particles move nearly at the speed of light and the interactions of particles with each other are negligible [147, 30]. In applications, which include pulsed sources, nuclear bursts, reactor kinetics or dynamic movement, the time-dependent form of the BTE is needed [14, 186]. In some applications such as electron gas in semiconductor the nonlinear BTE is used [127, 147].

BTE describes particle traveling in a medium and it is based on the particle equilibrium in a small volume [67]. The unknown function in the BTE based forward problem is the particle angular flux, from which the dose can be calculated [123]. In stationary case, it has six variables, three spatial, two angular and one energy variable. BTE can be solved analytically only in very simplified geometries, in which it does not have very much of practical use. Instead of finding an analytical solution of the BTE, one can seek for a numerical solution, which can be stochastic or deterministic [168]. For example MC and the closely related phase space evolution method [91, 86, 136] are stochastic methods for solving the BTE.

Solving the BTE with deterministic methods is studied by many authors and several production codes are generated in the field of radiation therapy physics [168, 137, 195, 194]. In deterministic methods, the stationary BTE is usually solved using some grid-based numerical method, in which the phase space is discretized in spatial, angular and energy domains [119, 59]. The energy discretization is often done by multi-group approximation, in which the energy range is divided into energy groups and the interaction cross sections are replaced by multi-group cross sections [124, 67, 7]. This leads to the coupled system of monoenergic equations, which only need to be discretized in spatial and angular domains and are often studied without energy variable [11, 12, 55, 118]. The often used methods for angular discretization are for example the discrete ordinates [64, 112, 125, 138, 185], and spherical harmonic approximations [113, 128]. Finite difference and finite element methods (FEM) are usually used in spatial discretization [3, 118, 156] and some times also for angular discretization [41, 130, 131, 54, 141]. Also finite element discretization is used for all variables simultaneously [26, 173]. Often also discontinuous FEM is used [183, 184]. Other methods, which are successfully used to solve the BTE, are the method of characteristics [194, 83], the method of moments [115], the electron multiple scattering theory [93, 98, 97, 94, 99, 96, 100, 151, 77], the collocation method [172] and hybrid collocation-Galerkin-S_n method [139]. Mainly due to computational problems, BTE based deterministic models are not used in dose calculations in clinical applications.

There exist several techniques to overcome the difficulties to solve the BTE. The integral form of the BTE is mostly used in special geometries, in which it is easy to solve [67, 119]. Also some MC applications are based on the integral form of the BTE [142]. It is also used in the studies of gases [77]. The even-parity [1, 65, 66] form is derived in the monoenergetic case to be used for example with multigroup method. The second order form [140, 121, 122] is derived in the case, in which angular discretization is done for example using discrete ordinates. The transport of charged particles is difficult to model using grid based numerical methods because of the large interaction probability in forward directions. To

accomplish this for example a continuous slowing down approximation (CSDA) can be used [17, 116, 117]. Quite accurate models are derived by dividing the scattering coefficients into forward and backward scatterings, and using the CSDA to the forward parts [111, 121, 134, 143, 149, 155, 192, 200, 46]. This approximate form of the BTE is often referred to Boltzmann-CSDA equation (B-CSDAE).

In different interactions, the high energy particles are changed to other types of particles and three coupled BTEs are needed to describe the radiotherapy forward problem, which takes into account photon, electron and positron interactions with medium atoms [124]. Typically positron production is neglected and two coupled BTEs with some boundary conditions are used to model the external radiotherapy forward problem [65, 83, 121, 125]. Also often the bremsstrahlung production is neglected in the electron incident radiotherapy and only one BTE with appropriate approximations is used to describe the electron transport [201, 100, 86, 132, 133, 143].

When deterministic methods are considered, one should guarantee that the solution exists and that it is unique. For time-dependent BTE the existence and uniqueness of the solution can be proven [147, 67]. The existence and uniqueness of variational form of the stationary BTE is studied in [59], in which some additional restrictions are demanded on the scattering parameters. Recently, similar restrictions are shown to hold for the coupled system of BTEs [26]. From the coercivity result the Cea's estimate for FEM convergence can be derived in principle [53, 172]. The FEM convergence for the BTE is also studied, for example in [179, 7]. The existence, uniqueness and FEM convergence analysis of the solution for the approximative forms of the BTE (B-CSDAE, even-parity, second order) are not presented in the literature.

Although MC methods are thought to be one of the future dose calculation models, it is not evident that the MC methods are more efficient than deterministic BTE based models [78, 29, 164]. The deterministic methods have advantages in solving the related inverse problem, which can be directly formulated to the deterministic BTE based model. With MC methods one needs to solve the forward problem several times by changing the incoming source arrangements in solving the related inverse problem [92]. Fast MC methods are generated to accomplish the computational costs [74, 163]. Still deterministic methods are worth studying, because of the advantages in inverse problems and because it is not clear if the MC methods are more efficient than the deterministic methods.

The inverse problem in radiotherapy is usually based on the physical or biological criteria [38]. The physical criteria for the IRTTP problem are defined by the physically measurable quantities such as volume and dose [34]. With biological criteria one tries to quantify the influence of the dose deviation on tumor control and normal tissues reactions, i.e. quantify the probability that the patient will have a desirable treatment outcome [39, 40]. The physical criteria are the most often used quantities in the IRTTP problems. This is probably because the biological criteria are more difficult to implement than the physical criteria and because the biological criteria contain parameters such as normalized dose-response gradient and the dose causing 50% probability of tumor control or severe normal tissue reactions,

from which the normalized dose-response gradient varies from patient to patient and is difficult to determine. In optimization, these criteria are usually connected using cost function, which is then minimized by pre-selecting the weights for different criteria. The unified model [49] handles the physical criteria by proximity function, in which the resulted iterative scheme converges to the feasible solution. The problem of selecting the weights for different criteria in an optimum way can be avoided using method such as the deterministic iterative least-squares method [51] and multi-criteria optimization [36, 160, 159].

Maybe because of the computational problems the IRTTP problems based on BTE and deterministic methods are rarely presented in literature. In the field of image reconstruction and particle transport, the studies based on BTE can be found for example in [16, 145, 70, 71], from which the two latter are based on the computations of the original BTE and it's adjoint form. Related studies are recently done in the field of radiotherapy in the optimization of the dose distribution within the spatial domain [176, 175].

The aims and the contents of the thesis

The purpose of this thesis is to use a BTE based model in radiotherapy purposes. The first aim is to solve the radiotherapy forward problem using the coupled BTEs and/or the coupled B-CSDAEs. The second aim is to used this forward model in solving the radiotherapy inverse problem with the optimal control approach.

The BTE based model consists of three coupled BTEs to describe photons, electrons and positrons with related boundary conditions. The variational form is formulated and the existence and uniqueness of the solution are analyzed. From the existence analysis of the coupled system some restrictions on the scattering coefficients are resulted. Also the coupled system B-CSDAEs is considered and the variational form is presented and the existence and uniqueness of the solution are discussed. The derived forward problem is simulated in three (3D) and two (2D) spatial dimensions using FEM for two coupled B-CSDAEs with photon boundary conditions and for one B-CSDAE with electron boundary condition. The results are compared with the MC simulations using EGSnrc® code system [104].

Some of the results presented in this thesis have been published earlier in the articles [26, 27, 176] and in the University of Kuopio Report series [172, 171]. This thesis summarizes the results of the published works and also gives new theories for the existence of the solution of the coupled B-CSDAEs, uses B-CSDAE for charged particles, presents the stream-line diffusion with FEM discretization and simulates the coupled system and B-CSDAEs in 3D using FEM. Also the BTE based inverse problem in radiotherapy purposes is presented and simulated.

This thesis is divided into six chapters. In Chapter 2, the principles of the external radiotherapy are presented. The chapter also presents detailed the main interactions and the related physical quantities, which are needed to describe the traveling of high energy particles in a medium. This chapter forms the physical basis for the thesis.

In Chapter 3, the coupled system of BTEs is derived from the particle equilibrium in a small element. The chapter also presents the formula for the dose

and external radiotherapy related boundary conditions for photons and electrons. Also, the integral form of the BTE and different approximations such as the B-CSDAE are presented. This chapter gives a solid basis for the BTE in radiotherapy purposes.

The radiotherapy forward problem using FEM and transport equations are discussed in Chapter 4. The chapter derives the variational forms for the coupled BTEs and for the coupled B-CSDAEs. The existence of the solution of these equations are studied. Also the related convergence results based on the coercivity analysis are presented. The finite element discretization is given including the stream-line diffusion method. The radiotherapy forward problem is simulated at the end of the Chapter 4 using two and one B-CSDAEs in 2D and 3D.

A radiotherapy inverse problem based on the BTEs is presented in Chapter 5. The boundary control optimization method is used to solve the related radiotherapy inverse problem. Also a novel approach using the application of parametrization is presented in finding the solution of the control problem. These theories are simulated by one BTE in 2D.

Chapter II

Radiotherapy treatment related physics

The determination of absorbed dose in a patient is one task in radiotherapy treatments [4]. In external radiotherapy, the detectors can be used at the patient surfaces, but there is no information how the dose is distributed inside the patient. That is why one has to use a model to simulate the absorbed dose distribution in patient based on the knowledge of high energy particle fluxes at the patient surface and on the knowledge of the patient inhomogeneity. In the BTE based dose calculation models one has to know the physics behind high energy particles i.e. photons, electrons and positrons [124, 104]. The interactions for photons and electrons (positrons) are significantly different, because photons are uncharged and electrons (positrons) are negative (positive) in charge. The transport of photons, electrons and positrons is coupled due to the fact that incident photons produce electrons, electrons produce photons and sometimes photons produce positron electron pair or this pair produces photons in different interactions with medium atoms.

In this chapter, the main physical features of ionizing radiation are explained for the purposes of the external radiotherapy treatment. The different interactions of high energy particles with medium atoms are presented. In Section 2.1, ionizing radiation and absorbed dose are presented. After that, Section 2.2 describes the scattering probabilities via differential and total cross sections and stopping power, which are needed in the BTE based transport models. In Sections 2.3, 2.4 and 2.5, the differential and total cross sections in different interactions are described for photons, electrons and positrons, respectively. In the last Section 2.6, a method is presented to divide the scattering interaction of charged particles into catastrophic and soft collisions and for these purposes the restricted cross sections and restricted stopping powers are derived.

2.1 Ionizing radiation

Ionizing radiation is used in radiotherapy treatments because of its ability to damage living tissue [13]. The intended high local concentrations of absorbed energy can kill a cell either directly or through the formation of highly reactive chemical species such as free radicals in water, which are always present in a human tis-

sue. A free radical is an atom or a compound with unpaired electron. Ionizing radiation excites and ionizes medium atoms while it is traveling through medium [13]. It is classified into directly ionizing radiation, such as electrons and positrons, which deliver energy to medium directly, and indirectly ionizing radiation, such as photons, which first transfer their energy to charged particles, which then deliver energy to medium.

Photons consist of x-rays and gamma rays named according to their mode of origin although their properties are the same [161, 13]. Electromagnetic radiation emitted by charged particles in changing atomic energy levels is called characteristic or fluorescence x-rays. Continuous or bremsstrahlung x-rays are emitted from inelastic collisions of charged particles in which they slow down in Coulomb force field. Gamma rays are electromagnetic radiation emitted from the nucleus or in annihilation reactions. Annihilation radiation is emitted when positron and electron are combined. β-rays (negative or positive) and δ-rays consist of electrons and positrons [13]. β-rays are emitted from the nucleus and δ-rays are resulted from the charged particle collisions.

Because photons are uncharged they travel quite a long distance in a medium without interacting with medium atoms [193]. On the other hand, charged particles, such as electrons and positrons, travel only a small distance until they undergo interactions with medium atoms. Thus, photons undergo only few interactions until they attenuate and secondary electrons born, while electrons loose their energies in many small interactions with medium atoms along their trajectories [13].

The energy absorbed from the ionizing radiation is usually described by the absorbed dose $D(\boldsymbol{x})$, which is the expectation value of the high energy imparted to medium per unit mass in a point $\boldsymbol{x} \in \mathbb{R}^3$ [13]. Thus,

$$D(\boldsymbol{x}) = \frac{\mathrm{d}\epsilon}{\mathrm{d}m}, \tag{2.1}$$

where $\mathrm{d}\epsilon = \mathrm{d}\epsilon_{\mathrm{in}} - \mathrm{d}\epsilon_{\mathrm{out}} + \mathrm{d}\epsilon_{\mathrm{mass}}$ is the mean energy imparted in an infinitesimal volume $\mathrm{d}V$, $\mathrm{d}\epsilon_{\mathrm{in}}$ is the energy that comes into $\mathrm{d}V$ (including charged and uncharged particles), $\mathrm{d}\epsilon_{\mathrm{out}}$ is the energy that comes out from $\mathrm{d}V$ and $\mathrm{d}\epsilon_{\mathrm{mass}}$ is the net energy derived from rest mass in $\mathrm{d}V$. $\mathrm{d}m$ is the mass of $\mathrm{d}V$. The unit of the absorbed dose is Jkg^{-1} or gray (Gy), having a relation $1\ \mathrm{Gy} = 1\ \mathrm{Jkg}^{-1} \approx 6.24{\cdot}10^9 \rho$ MeVcm^{-3}, in which ρ is the density of the medium.

2.2 Interaction probability and stopping power

High energy particles interact with medium atoms in different ways resulting in their energy to be imparted to matter [13]. In these interactions, the original direction $\boldsymbol{\Omega}'$ and energy E' of the particle are changed to $\boldsymbol{\Omega}$ and E. Sometimes other types of particles result. These interactions are statistical in nature and can be described by probability distributions such as differential cross section and total cross section. Also stopping powers are used to describe the energy absorption to the medium.

2.2.1 Differential cross section

The differential cross section describes the laws for the emission of scattered particles in energy and angle [119]. It is defined by the probability distribution $\frac{\mathrm{d}^2\sigma}{\mathrm{d}E\mathrm{d}\mathbf{\Omega}}(\boldsymbol{x}, E', E, \mathbf{\Omega}' \cdot \mathbf{\Omega})\mathrm{d}E\mathrm{d}\mathbf{\Omega}$, which is the probability per unit path length that a particle in a point $\boldsymbol{x}$, having an energy E' and coming from a direction $\mathbf{\Omega}'$ to scatter into an energy interval $\mathrm{d}E$ about E into a solid angle $\mathrm{d}\mathbf{\Omega}$ about $\mathbf{\Omega}$. The function $\frac{\mathrm{d}^2\sigma}{\mathrm{d}E\mathrm{d}\mathbf{\Omega}}(\boldsymbol{x}, E', E, \mathbf{\Omega}' \cdot \mathbf{\Omega})$ is now the differential cross section and it has unit of per centimeter per MeV per steradians i.e. $\mathrm{cm}^{-1}\mathrm{MeV}^{-1}\mathrm{sr}^{-1}$. The small solid angle $\mathrm{d}\mathbf{\Omega}' = \sin\theta \mathrm{d}\theta\mathrm{d}\varphi$ in standard polar coordinates (φ, θ) on an unit sphere $S \subset \mathbb{R}^3$ (see Figure 3.1). Here the scattering is assumed to be isotropic meaning that the scattering does not depend on the azimuthal angle φ and depends only on the cosine of the scattering angle $\cos\theta = \mathbf{\Omega}' \cdot \mathbf{\Omega}$, not on $\mathbf{\Omega}'$ and $\mathbf{\Omega}$ individually.

2.2.2 Total cross section

Total cross section $\sigma(\boldsymbol{x}, E')$ is a sum of absorption cross section σ_a and integrated scattering cross section σ_s [123], which are obtained by integrating the differential cross sections for absorbed particles $\frac{\mathrm{d}^2\sigma^\mathrm{a}}{\mathrm{d}E\mathrm{d}\mathbf{\Omega}}$ and for scattered particles $\frac{\mathrm{d}^2\sigma^\mathrm{s}}{\mathrm{d}E\mathrm{d}\mathbf{\Omega}}$, respectively, over the energy and angle intervals. Hence,

$$\sigma_\mathrm{a}(\boldsymbol{x}, E') = \int_I \int_S \frac{\mathrm{d}^2\sigma^\mathrm{a}}{\mathrm{d}E\mathrm{d}\mathbf{\Omega}}(\boldsymbol{x}, E', E, \mathbf{\Omega}' \cdot \mathbf{\Omega})\mathrm{d}E\mathrm{d}\mathbf{\Omega}$$

and

$$\sigma_\mathrm{s}(\boldsymbol{x}, E') = \int_I \int_S \frac{\mathrm{d}^2\sigma^\mathrm{s}}{\mathrm{d}E\mathrm{d}\mathbf{\Omega}}(\boldsymbol{x}, E', E, \mathbf{\Omega}' \cdot \mathbf{\Omega})\mathrm{d}E\mathrm{d}\mathbf{\Omega},$$

where I is the energy interval, say $[E_\mathrm{min}, E_\mathrm{max}]$. $\frac{\mathrm{d}^2\sigma^\mathrm{a}}{\mathrm{d}E\mathrm{d}\mathbf{\Omega}}$ is the differential cross section describing an interaction, in which a particle is disappeared (absorbed) and another different type of particle is created. $\frac{\mathrm{d}^2\sigma^\mathrm{s}}{\mathrm{d}E\mathrm{d}\mathbf{\Omega}}$ describes an interaction, in which a particle is scattered to some angle having some new energy. For isotropic scattering the integrated cross sections are totally independent on the scattering angle $\mathbf{\Omega}$. Basically, $\sigma(\boldsymbol{x}, E')$ is the probability per unit path length for particle of energy E' to scatter or to absorb in a point $\boldsymbol{x}$.

The unit of total cross section is cm^{-1} or $\mathrm{cm}^2\mathrm{g}^{-1}$, if the previous is divided by density ($\mathrm{g/cm}^3$). Then it is also called the macroscopic cross section [124]. If the cross section is defined per atom (cm^2/atom) or per molecule (cm^2/molecule), it is called as microscopic cross section. The relation between the macroscopic σ_ma and microscopic σ_mi cross sections is

$$\sigma_\mathrm{ma} = \frac{N_\mathrm{A}}{M}\sigma_\mathrm{mi},$$

where $N_\mathrm{A} = 6.022 \cdot 10^{23}$ mole^{-1} is the Avogadro's constant and M is the gram-atomic weight of an element or the gram-molecular weight of a molecule. Typically the cross sections are defined as microscopic cross sections for an element (unit

cm^2/electron). The macroscopic cross section for a compound σ_{cp} can then be computed from the microscopic cross sections σ_i (i indicates the element) using weighted sum

$$\sigma_{\mathrm{cp}} = \frac{N_{\mathrm{A}}}{M} \sum_i N_i Z_i \sigma_i,$$

where M is a molecular mass in moles for a compound, N_i is the number fraction of the element i in a compound (i.e. the number of atoms in element i in one molecule) and Z_i is the number of electrons per atom of an element. If the microscopic cross section σ_i does not depend on the element i, the macroscopic cross section for a compound becomes

$$\sigma_{\mathrm{cp}} = \frac{N_{\mathrm{A}} Z}{M} \sigma,$$

where Z is the number of electrons per molecule of a compound and $\sigma_i = \sigma \ \forall i$. Similarly, the differential cross section for a compound is

$$\frac{\mathrm{d}^2\sigma_{\mathrm{cp}}}{\mathrm{d}E\mathrm{d}\boldsymbol{\Omega}} = \frac{N_{\mathrm{A}} Z}{M} \frac{\mathrm{d}^2\sigma}{\mathrm{d}E\mathrm{d}\boldsymbol{\Omega}},$$

where $\frac{\mathrm{d}^2\sigma}{\mathrm{d}E\mathrm{d}\boldsymbol{\Omega}}$ is the element independent microscopic differential cross section per electron.

The total cross sections for different photon interactions are very well tabulated in the literature (for example in [13]). One can use also an easy access photon total cross section generating code XCOM [19] developed by National Institute of Standards and Technology (NIST). The differential cross sections are also well formulated in the literature (for example in [124, 104], although those are generated for different purposes than what is needed here and can not be used directly). However, the cited references give the differential cross sections with exact formulas, from which the needed data can be generated. These formulas are given in Sections 2.3 and 2.4.

Instead of total cross section, one often describes ionizing radiation using a variable such as a mean free path, which is the average path length that the particle will travel without interaction [67]. In fact, the mean free path is defined by the total cross section as σ^{-1}.

2.2.3 Stopping power

One important element used to describe the charged particle behavior in a medium is the stopping power. The stopping power $\tau(\boldsymbol{x}, E')$ is the average rate at which the charged particles lose energy at any point along their tracks, i.e. $\tau(\boldsymbol{x}, E') = \left(\frac{\mathrm{d}E'}{\mathrm{d}\boldsymbol{x}}\right)(\boldsymbol{x}, E')$ [87]. Total stopping power is a sum of collision stopping power τ^{Ie} and radiative stopping power τ^{Br}. The collision stopping power is the average energy loss per unit path length due to inelastic collisions (see Section 2.4.1) while the radiative stopping power is the average energy loss per unit path length due to the emission of photon in a bremsstrahlung process (see Section 2.4.2). The

stopping powers are well tabulated in the literature for different materials (see for example [87, 106, 13]). The stopping power is given by the formula

$$\tau(\boldsymbol{x}, E') = \int_0^\infty (E' - E) \frac{\mathrm{d}\sigma}{\mathrm{d}E}(E', E)\mathrm{d}E, \tag{2.2}$$

where $\frac{\mathrm{d}\sigma}{\mathrm{d}E}$ is the differential cross section differential in energy including inelastic scattering and bremsstrahlung. The stopping powers are needed for example in the computation of the dose (see Section 3.3). The unit of the stopping power is typically MeVcm^{-1}.

2.3 Photon interactions

Photons by themselves do not impart energy to matter, but in different interactions the electrons of medium atoms obtain energy from photons and these electrons then impart that energy to matter in many small interactions along their tracks [13]. Photon interactions are dominated by absorption and inelastic scattering collisions, in which photon's energy is reduced. The most important interactions for photons are Compton effect, Photoelectric effect, Pair production and Rayleigh scattering. Figure 2.1 shows the total cross sections for these photon interactions at different energies in water. The values of the total cross sections are comparable to the interaction probabilities. A schematic presentation of different photon interactions are presented in Figure 2.2. To use the same energy units throughout the whole book, the photon energies are described in units (MeV) instead of the standard (MV) unit.

2.3.1 Compton effect

The Compton effect is dominant at energies under about 30 MeV and above about 20 keV in mediums like human tissue or water (number of electrons per molecule $Z = 10$). The dominance region is narrower for high Z mediums. In Compton effect, the incident photon (energy E'_p, direction $\boldsymbol{\Omega}'_\mathrm{p}$) collides with an electron and gives some of its energy to that electron. After the collision the incident photon energy and direction are changed to E_p and $\boldsymbol{\Omega}_\mathrm{p}$, respectively. Also the electron has now kinetic energy E_e and direction $\boldsymbol{\Omega}_\mathrm{e}$. If the electron is assumed to be initially at rest and unbounded, then $E_\mathrm{e} = E'_\mathrm{p} - E_\mathrm{p}$ and the relation between $\boldsymbol{\Omega}'_\mathrm{p}$ and $\boldsymbol{\Omega}_\mathrm{e}$ is obtained by kinematics and is defined later in this section in equation (2.9). Then the macroscopic differential cross section, differential in angle for Compton effect for scattered photon in a compound (in units of $\mathrm{cm}^{-1}\mathrm{sr}^{-1}$), is obtained from the Klein-Nishina equation [13]

$$\frac{\mathrm{d}\sigma^\mathrm{C}}{\mathrm{d}\boldsymbol{\Omega}_\mathrm{p}}(\boldsymbol{x}, E'_\mathrm{p}, E_\mathrm{p}, \boldsymbol{\Omega}'_\mathrm{p} \cdot \boldsymbol{\Omega}_\mathrm{p}) = \frac{N_\mathrm{A} Z \rho r_0^2}{2M} \left(\frac{E_\mathrm{p}}{E'_\mathrm{p}}\right)^2 \left(\frac{E'_\mathrm{p}}{E_\mathrm{p}} + \frac{E_\mathrm{p}}{E'_\mathrm{p}} - \sin^2(\omega_{\mathrm{p}',\mathrm{p}})\right), \tag{2.3}$$

where $\omega_{\mathrm{p}',\mathrm{p}} = \arccos(\boldsymbol{\Omega}'_\mathrm{p} \cdot \boldsymbol{\Omega}_\mathrm{p})$ is the photon scattering angle for isotropic scattering, the classical electron radius $r_0 = 2.818 \cdot 10^{-13}$ cm, M is the molecular weight in

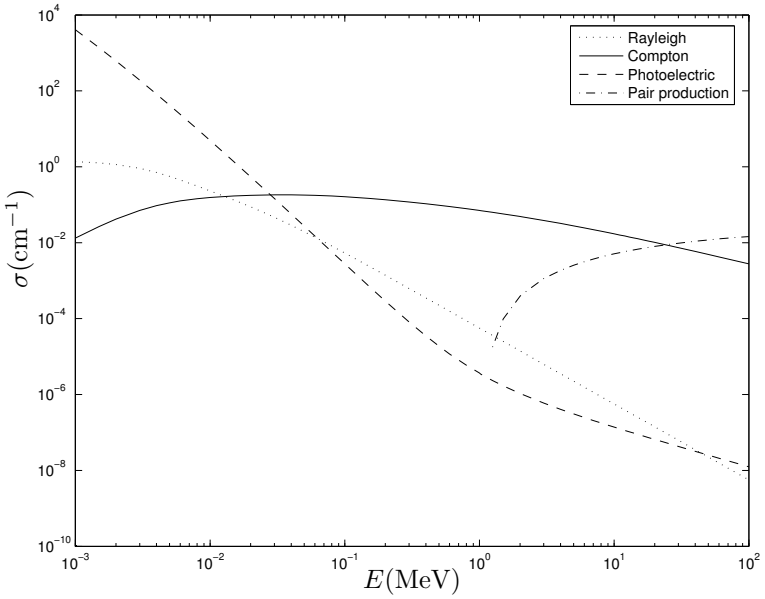

Figure 2.1: The total cross sections $\sigma(\mathrm{cm}^{-1})$ for different photon interactions in water at different energies $E(\mathrm{MeV})$ in logarithmic scale.

units (g/mole) and ρ is the density in units (g/cm^3) . The energy of the scattered photon is

$$E_{\mathrm{p}} = \frac{E'_{\mathrm{p}}}{1 + \frac{E'_{\mathrm{p}}}{E_0}(1 - \mathbf{\Omega}'_{\mathrm{p}} \cdot \mathbf{\Omega}_{\mathrm{p}})}, \tag{2.4}$$

where the electron rest energy $E_0 = 0.511$ MeV.

Because the angle and energy of the scattered photon are kinematically related, the Klein-Nishina cross section differential in angle in equation (2.3) can be expressed as a cross section that is differential in energy [124]. From equation (2.4)

$$\cos(\omega_{\mathrm{p}',\mathrm{p}}) = \mathbf{\Omega}'_{\mathrm{p}} \cdot \mathbf{\Omega}_{\mathrm{p}} = 1 + \frac{E_0}{E'_{\mathrm{p}}} - \frac{E_0}{E_{\mathrm{p}}}, \tag{2.5}$$

where $E_{\mathrm{p}} \in [\frac{E'_{\mathrm{p}}}{E_0 + 2E'_{\mathrm{p}}}, \frac{E'_{\mathrm{p}}}{E_0}]$. From equation (2.5) one receives by differentiation a relation

$$\left| \frac{\mathrm{d}\mathbf{\Omega}_{\mathrm{p}}}{\mathrm{d}E_{\mathrm{p}}} \right| = \frac{2\pi E_0}{E_{\mathrm{p}}^2}, \tag{2.6}$$

where $\mathrm{d}\mathbf{\Omega}_{\mathrm{p}} = 2\pi \sin(\omega_{\mathrm{p}',\mathrm{p}}) \mathrm{d}\omega_{\mathrm{p}',\mathrm{p}}$. Hence, from equations (2.3) and (2.6) one obtains the differential cross section, differential in the energy of the scattered photon

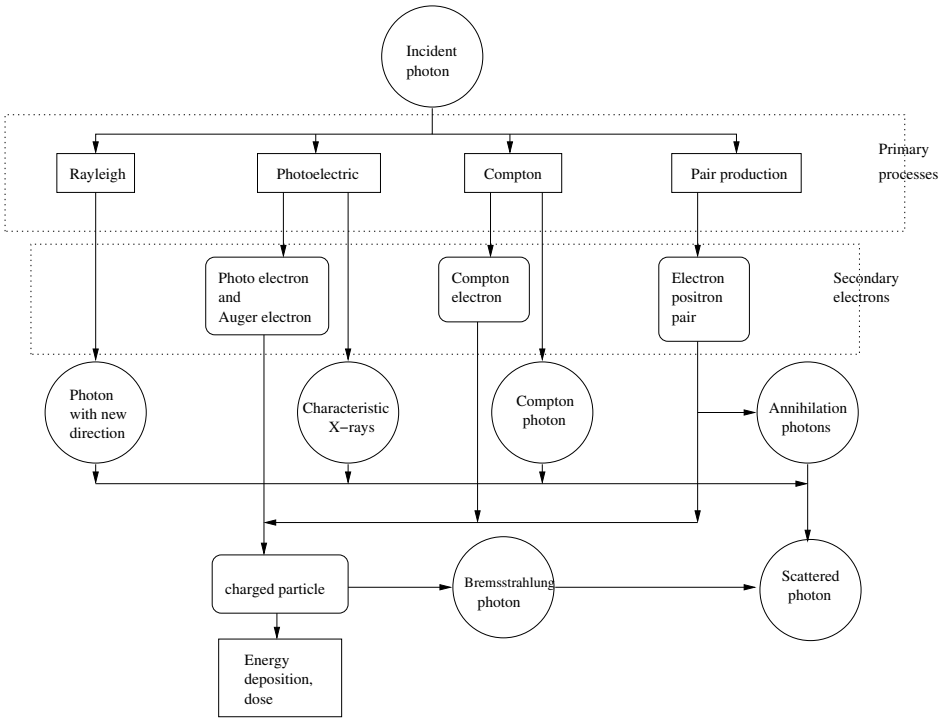

Figure 2.2: The typical interactions that an incident high energy photon can have resulting secondary electron, which imparts energy to the matter.

for Compton effect,

$$\frac{\mathrm{d}\sigma^{\mathrm{C}}}{\mathrm{d}E_{\mathrm{p}}}(\boldsymbol{x}, E'_{\mathrm{p}}, E_{\mathrm{p}}, \boldsymbol{\Omega}'_{\mathrm{p}}\cdot\boldsymbol{\Omega}_{\mathrm{p}}) = \frac{\mathrm{d}\sigma^{\mathrm{C}}}{\mathrm{d}\boldsymbol{\Omega}_{\mathrm{p}}}(\boldsymbol{x}, E'_{\mathrm{p}}, E_{\mathrm{p}}, \boldsymbol{\Omega}'_{\mathrm{p}}\cdot\boldsymbol{\Omega}_{\mathrm{p}})\left|\frac{\mathrm{d}\boldsymbol{\Omega}_{\mathrm{p}}}{\mathrm{d}E_{\mathrm{p}}}\right|$$
$$= \frac{N_{\mathrm{A}}Z\rho\pi r_0^2 E_0}{M(E'_{\mathrm{p}})^2}\left(\frac{E'_{\mathrm{p}}}{E_{\mathrm{p}}} + \frac{E_{\mathrm{p}}}{E'_{\mathrm{p}}} - 1 + \left(1 + \frac{E_0}{E'_{\mathrm{p}}} - \frac{E_0}{E_{\mathrm{p}}}\right)^2\right), \tag{2.7}$$

where also equation (2.5) is used with equation $\sin^2(\omega_{\mathrm{p}',\mathrm{p}}) + \cos^2(\omega_{\mathrm{p}',\mathrm{p}}) = 1$.

The differential cross section, differential in scattered electron direction for Compton effect, is of the form

$$\frac{\mathrm{d}\sigma^{\mathrm{C}}}{\mathrm{d}\boldsymbol{\Omega}_{\mathrm{e}}}(\boldsymbol{x}, E'_{\mathrm{p}}, E_{\mathrm{e}}, \boldsymbol{\Omega}'_{\mathrm{p}}\cdot\boldsymbol{\Omega}_{\mathrm{e}}) = \frac{\mathrm{d}\sigma^{\mathrm{C}}}{\mathrm{d}\boldsymbol{\Omega}_{\mathrm{p}}}(\boldsymbol{x}, E'_{\mathrm{p}}, E_{\mathrm{p}}, \boldsymbol{\Omega}'_{\mathrm{p}}\cdot\boldsymbol{\Omega}_{\mathrm{p}})\frac{(1+\frac{E'_{\mathrm{p}}}{E_0})^2(1-\boldsymbol{\Omega}'_{\mathrm{p}}\cdot\boldsymbol{\Omega}_{\mathrm{p}})^2}{(\boldsymbol{\Omega}'_{\mathrm{p}}\cdot\boldsymbol{\Omega}_{\mathrm{e}})^3}, \tag{2.8}$$

where now the cosine of the electron scattering angle is

$$\mathbf{\Omega}'_{\mathrm{p}} \cdot \mathbf{\Omega}_{\mathrm{e}} = \cos(\omega_{\mathrm{p}',\mathrm{e}}) = \frac{E_0 + E'_{\mathrm{p}}}{E'_{\mathrm{p}}} \left(\frac{2E_0}{E_{\mathrm{e}}} + 1 \right)^{-1/2}, \tag{2.9}$$

where $E_{\mathrm{e}} \in [0, \frac{2(E'_{\mathrm{p}})^2}{E_0^2 + 2E'_{\mathrm{p}}E_0}]$. Again by differentiation one receives from equation (2.9) a relation

$$\left| \frac{\mathrm{d}\mathbf{\Omega}_{\mathrm{e}}}{\mathrm{d}E_{\mathrm{e}}} \right| = \frac{E_0 + E'_{\mathrm{p}}}{E'_{\mathrm{p}}} \frac{2\pi E_0}{E_{\mathrm{e}}^2} \left(\frac{2E_0}{E_{\mathrm{e}}} + 1 \right)^{-3/2}. \tag{2.10}$$

Substituting equations (2.3), (2.5) and (2.9) to equation (2.8) and multiplying it by equation (2.10) one obtains the differential cross section differential in the energy of the scattered electron for Compton effect

$$\frac{\mathrm{d}\sigma^{\mathrm{C}}}{\mathrm{d}E_{\mathrm{e}}}(\boldsymbol{x}, E'_{\mathrm{p}}, E_{\mathrm{e}}, \mathbf{\Omega}'_{\mathrm{p}} \cdot \mathbf{\Omega}_{\mathrm{e}}) = \frac{N_{\mathrm{A}} Z \rho \pi r_0^2 E_0}{M E_{\mathrm{e}}^2} \left(1 - \frac{E_{\mathrm{p}}}{E'_{\mathrm{p}}}\right)^2 \left(\frac{E'_{\mathrm{p}}}{E_{\mathrm{p}}} + \frac{E_{\mathrm{p}}}{E'_{\mathrm{p}}} - \sin^2(\omega_{\mathrm{p}',\mathrm{p}}) \right). \tag{2.11}$$

If one uses the fact $E_{\mathrm{p}} = E'_{\mathrm{p}} - E_{\mathrm{e}}$, then equation (2.11) is the same as equation (2.7) and

$$\frac{\mathrm{d}\sigma^{\mathrm{C}}}{\mathrm{d}E_{\mathrm{e}}}(\boldsymbol{x}, E'_{\mathrm{p}}, E_{\mathrm{e}}, \mathbf{\Omega}'_{\mathrm{p}} \cdot \mathbf{\Omega}_{\mathrm{e}}) = \frac{\mathrm{d}\sigma^{\mathrm{C}}}{\mathrm{d}E_{\mathrm{p}}}(\boldsymbol{x}, E'_{\mathrm{p}}, E'_{\mathrm{p}} - E_{\mathrm{e}}, \mathbf{\Omega}'_{\mathrm{p}} \cdot \mathbf{\Omega}_{\mathrm{p}}). \tag{2.12}$$

In Compton effect, the energy and angle are kinematically related and that is why the differential cross section, differential in angle and energy for scattered photon in Compton effect (in units of $\mathrm{cm}^{-1}\mathrm{sr}^{-1}\mathrm{MeV}^{-1}$), is obtained from

$$\frac{\mathrm{d}^2\sigma^{\mathrm{C}}}{\mathrm{d}E\mathrm{d}\mathbf{\Omega}_{\mathrm{p}}}(\boldsymbol{x}, E', E, \mathbf{\Omega}' \cdot \mathbf{\Omega}) = \frac{\mathrm{d}\sigma^{\mathrm{C}}}{\mathrm{d}E_{\mathrm{p}}}(\boldsymbol{x}, E', E, \mathbf{\Omega}' \cdot \mathbf{\Omega}) \delta(\mathbf{\Omega}' \cdot \mathbf{\Omega} - \mathbf{\Omega}'_{\mathrm{p}} \cdot \mathbf{\Omega}_{\mathrm{p}}), \tag{2.13}$$

where the function $\delta(t)$ is of the form

$$\delta(t) = \begin{cases} 1, & \text{if } t = 0 \\ 0, & \text{elsewhere.} \end{cases} \tag{2.14}$$

Equation (2.13) is written for general variables $E', E, \mathbf{\Omega}'$ and $\mathbf{\Omega}$. The value of $\mathbf{\Omega}'_{\mathrm{p}} \cdot \mathbf{\Omega}_{\mathrm{p}}$ is obtained from equation (2.5). Similarly, the differential cross section, differential in angle and energy for scattered electron in Compton effect, is of the form

$$\frac{\mathrm{d}^2\sigma^{\mathrm{C}}}{\mathrm{d}E\mathrm{d}\mathbf{\Omega}_{\mathrm{e}}}(\boldsymbol{x}, E', E, \mathbf{\Omega}' \cdot \mathbf{\Omega}) = \frac{\mathrm{d}\sigma^{\mathrm{C}}}{\mathrm{d}\mathbf{\Omega}_{\mathrm{e}}}(\boldsymbol{x}, E', E, \mathbf{\Omega}' \cdot \mathbf{\Omega}) \delta(\mathbf{\Omega}' \cdot \mathbf{\Omega} - \mathbf{\Omega}'_{\mathrm{p}} \cdot \mathbf{\Omega}_{\mathrm{e}}), \tag{2.15}$$

where $\mathbf{\Omega}'_{\mathrm{p}} \cdot \mathbf{\Omega}_{\mathrm{e}}$ is obtained from equation (2.9).

The scattering cross section for Compton progress is achieved by integrating the equation (2.7) over the scattered photon energy $E_{\mathrm{p}} \in [\frac{E'_{\mathrm{p}}}{E_0 + 2E'_{\mathrm{p}}}, \frac{E'_{\mathrm{p}}}{E_0}]$. This results in

$$\sigma_{\mathrm{s}}^{\mathrm{C}}(\boldsymbol{x}, E') = \frac{2\pi N_{\mathrm{A}} Z \rho r_0^2}{M} \left(\frac{2}{\epsilon^2} + \frac{1+\epsilon}{(1+2\epsilon)^2} + \left(\frac{\epsilon^2 - 2\epsilon - 2}{2\epsilon^3} \right) \ln(1+2\epsilon) \right),$$

where $\epsilon = \frac{E'_\mathrm{p}}{E_0}$. The absorption cross section is the energyloss probability, in which photons are scattered and attenuated to other particles. Thus, for Compton effect the absorption cross section is obtained by integrating equation (2.11) over the electron scattering energy $E_\mathrm{e} \in [0, \frac{2(E'_\mathrm{p})^2}{E_0^2+2E'_\mathrm{p}E_0}]$. By noting that the differential cross section differential in scattered electron energy can be computed from the equation of the differential cross section differential in scattered photon energy, then one sees that the absorption cross section $\sigma_\mathrm{a}^\mathrm{C}(\boldsymbol{x}, E')$ in Compton effect is the same as the scattering cross section $\sigma_\mathrm{s}^\mathrm{C}(\boldsymbol{x}, E')$. The total cross section $\sigma^\mathrm{C}(\boldsymbol{x}, E')$ is then the sum of absorption and scattering cross sections. Thus, $\sigma^\mathrm{C}(\boldsymbol{x}, E') = 2\sigma_\mathrm{a}^\mathrm{C}(\boldsymbol{x}, E')$.

As it was mentioned, these differential cross section equations for Compton effect assume electrons to be unbounded and initially at rest. In actual case, the electrons in atoms have some binding energy depending on the energy level. Also these electrons are in motion. However, the resulting errors from the use of unbounded and stationary assumptions are only minor in radiotherapy applications at high energies. More accurate differential cross sections for Compton process are obtained by using an impulse approximation, which takes into account the target electron binding effects and the Doppler broadening of the Compton line [44]. The Doppler broadening is caused from the momentum distribution of the target electrons. This leads to the double-differential cross section, differential in energy and angle.

2.3.2 Photoelectric effect

In the photoelectric effect, an incident photon gives all its kinetic energy to a tightly bound electron, such as those in the inner shells of an atom [13]. The photoelectric effect can only occur when the kinetic energy of incident photon is greater than the electron binding energy. However, the photoelectric effect is more probable in lower energies, as long as the energy is more than the binding energy of an electron. The photoelectric effect is dominant at energies below about 20 keV for low Z media. The energy range increases as Z increases.

Photoelectric effect is an event in which an incident photon is disappeared and a so called photo-electron is emerged. The affected cap in the atomic shell is then immediately filled with another electron from the outer less bound atomic shell resulting an emission of the characteristic x-ray, sometimes called fluorescence x-ray or an Auger electron(s) with kinetic energy.

2.3.3 Pair production

In pair production, the incident photon with a minimum energy of $2E_0 = 1.022$ MeV is absorbed and electron and positron are born [13]. Pair production is more dominant at high energies. It can only take place in a Coulomb force field, which is usually near an atomic nucleus. Sometimes pair production can occur in the field of an atomic electron. Then the interaction is called triplet production, because the initial electron achieves also kinetic energy and thus two electrons and one positron has now a significant amount of kinetic energy. An opposite interaction to pair production is an annihilation process, in which electron and

positron disappear and two photons emerge. The differential cross sections for pair or triplet production can be found for example in [124, 104].

2.3.4 Rayleigh scattering

In Rayleigh scattering, the incident photon is scattered by the combined action of the whole atom [13]. That is why it is also called coherent scattering. Rayleigh scattering is elastic, which means that no energy is lost in the interaction, in which the atom moves just enough to conserve momentum and initial photon is redirected in a small angle.

Rayleigh scattering is more significant at low energies, in which the photon scattering angle is bigger. The differential cross sections differential in angle (energy is not changed) can be found for example in [107, 104].

2.4 Electron interactions

Because electrons are charged particles their interaction probabilities are much bigger than those of uncharged particles. For example photons need only few interactions to dissipate all of its kinetic energy rather than electron would typically undergo about 10^5 interaction before losing all of its kinetic energy [13]. Because photons may pass a slab of matter without any interaction or it may lose all of its kinetic energy in a few interaction, it is impossible to predict individual photon traveling distance. On the contrary, because electrons interact almost with every atomic electron or nucleus it passes and loses its kinetic energy gradually in a small friction like processes, it is customary to describe electron traveling by stopping power, range and yield. These are expectation values for a charged particle energy loss per path length, for a path length and for an electromagnetic radiation production, respectively.

Because of the nature of the charged particle, it is not customary to describe charged particle interactions by total cross sections and differential cross sections, which are needed in the Boltzmann transport equation (3.14) and these are found more rarely in the literature than those for photons. These can be found for example in [199, 104, 124].

Electron interactions are elastic scattering, inelastic scattering and radiation processes, which take place in a form of bremsstrahlung and electron positron annihilation [104]. The bremsstrahlung process dominates at high energies where as the inelastic scattering dominates at low electron energies in high Z media. In tissue like materials, the inelastic scattering dominates at all energies and the influence of the bremsstrahlung progress is only few percents [13]. The total cross sections for electron interactions are shown in Figure 2.3. Electron interaction chart illustrates the typical electron interactions in Figure 2.4.

2.4.1 Inelastic electron scattering

Electrons scatter inelastically from the atomic electrons ejecting them from the atom with considerable kinetic energy [13]. The result for the electron inelastic scattering is that incident electron (with energy E'_{e} and direction $\mathbf{\Omega}'_{\mathrm{e}}$) scatters

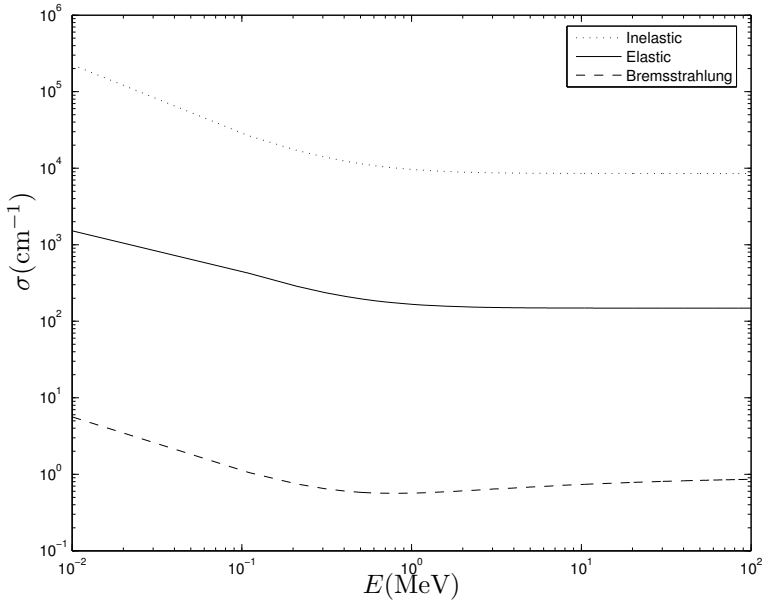

Figure 2.3: The total cross sections σ (cm^{-1}) for different electron interactions in water at different energies E (MeV) in logarithmic scale.

(with new energy E_{pr} and direction $\mathbf{\Omega}_{\mathrm{pr}}$, in which pr indicates now the primary scattered particle) and produces an extra electron (with kinetic energy E_{s} and direction $\mathbf{\Omega}_{\mathrm{s}}$, in which s indicates the secondary particle. This is sometimes called as electron-electron scattering. The higher energy electron after inelastic scattering is considered as the primary electron [124].

If the electron binding effects are ignored, the electron-electron scattering can be described by Møller scattering [87]. The macroscopic differential Møller cross section differential in the energy of the secondary electron for the electron-electron scattering in a compound (in units of $\mathrm{cm}^{-1}\mathrm{MeV}^{-1}$) is of the form

$$\frac{\mathrm{d}\sigma^{\mathrm{Ie}}}{\mathrm{d}E_{\mathrm{s}}}(\boldsymbol{x}, E', E_{\mathrm{s}}) = \frac{C}{\beta^2}\left(\frac{1}{E_{\mathrm{s}}^2} + \frac{1}{(E'-E_{\mathrm{s}})^2} + \frac{\epsilon^2}{(\epsilon+1)^2 E'^2} - \frac{2\epsilon+1}{(\epsilon+1)^2 E_{\mathrm{s}}(E'-E_{\mathrm{s}})}\right), \quad (2.16)$$

where $\epsilon = \frac{E'}{E_0}$, $\beta^2 = 1-(1+\epsilon)^{-2}$ and $C = N_{\mathrm{A}} Z \rho 2\pi r_0^2 E_0 M^{-1}$. The other notations are similar as in Section 2.3. The energy of the scattered particle is related due to the conservation of the energy. If the binding effects are neglected then $E' = E_{\mathrm{pr}} + E_{\mathrm{s}}$.

The scattering angles for inelastic electron scattering are highly forward peaked and are defined by kinematics [124]. The scattering angle for scattered primary

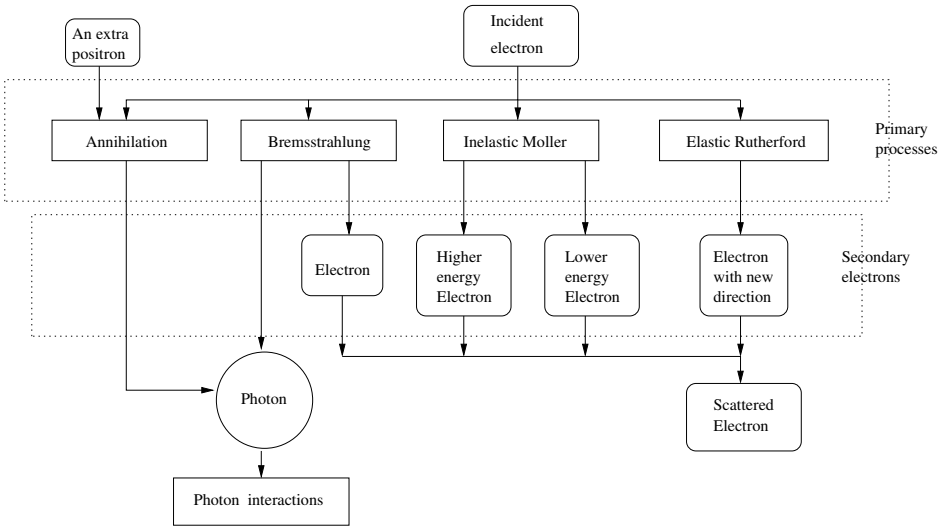

Figure 2.4: The typical interactions for a high energy electron. In bremsstrahlung and annihilation processes secondary photons are emitted.

electron can be obtained from the equation

$$\boldsymbol{\Omega}' \cdot \boldsymbol{\Omega}_{\mathrm{pr}} = \sqrt{\frac{E_{\mathrm{s}}(E' + 2E_0)}{E'(E_{\mathrm{s}} + 2E_0)}} \tag{2.17}$$

and for the scattered secondary electron from the equation

$$\boldsymbol{\Omega}' \cdot \boldsymbol{\Omega}_{\mathrm{s}} = \sqrt{\frac{(E' - E_{\mathrm{s}})(E' + 2E_0)}{E'(E' - E_{\mathrm{s}} + 2E_0)}}. \tag{2.18}$$

The macroscopic differential cross section for the inelastic electron scattering resulting scattered primary electron (in units of $\mathrm{cm}^{-1}\mathrm{sr}^{-1}\mathrm{MeV}^{-1}$) is then of the form

$$\frac{\mathrm{d}^2\sigma^{\mathrm{Ie}}}{\mathrm{d}E_{\mathrm{pr}}\mathrm{d}\boldsymbol{\Omega}_{\mathrm{pr}}}(\boldsymbol{x}, E', E, \boldsymbol{\Omega}' \cdot \boldsymbol{\Omega}) = \frac{\mathrm{d}\sigma^{\mathrm{Ie}}}{\mathrm{d}E_{\mathrm{s}}}(\boldsymbol{x}, E', E' - E)\frac{1}{2\pi}\delta(\boldsymbol{\Omega}' \cdot \boldsymbol{\Omega} - \boldsymbol{\Omega}' \cdot \boldsymbol{\Omega}_{\mathrm{pr}}), \tag{2.19}$$

where $\boldsymbol{\Omega}' \cdot \boldsymbol{\Omega}_{\mathrm{pr}}$ is obtained from the equation (2.17) and where $E \in [E_{\max}/2, E_{\max}]$. $E_{\max}$ is the maximum primary electron energy. Similarly, the macroscopic differential cross section for the inelastic electron scattering resulting secondary electron is of the form

$$\frac{\mathrm{d}^2\sigma^{\mathrm{Ie}}}{\mathrm{d}E_{\mathrm{s}}\mathrm{d}\boldsymbol{\Omega}_{\mathrm{s}}}(\boldsymbol{x}, E', E, \boldsymbol{\Omega}' \cdot \boldsymbol{\Omega}) = \frac{\mathrm{d}\sigma^{\mathrm{Ie}}}{\mathrm{d}E_{\mathrm{s}}}(\boldsymbol{x}, E', E)\frac{1}{2\pi}\delta(\boldsymbol{\Omega}' \cdot \boldsymbol{\Omega} - \boldsymbol{\Omega}' \cdot \boldsymbol{\Omega}_{\mathrm{s}}), \tag{2.20}$$

where $\boldsymbol{\Omega}' \cdot \boldsymbol{\Omega}_{\mathrm{s}}$ is obtained from the equation (2.18) and where $E \in [0, E_{\max}/2[$.

The Møller cross section takes into account relativity, spin effects and two scattered particles indistinguishability [87]. Because the electron with higher energy after scattering is considered to be the primary, the scattering cross section for Møller interactions is obtained via integration of the equation (2.16) from $[E_{\max}/2, E_{\max}]$. The absorption cross section is the same as the scattering cross section σ_{s} and $\sigma = 2\sigma_{\mathrm{s}}$. The Møller cross section increases rapidly to infinity as the energy of the secondary electron tends to zero. That is why the inelastic scattering is usually divided into catastrophic and soft collisions (see Section 2.6).

2.4.2 Bremsstrahlung

The bremsstrahlung process takes place when initial electron passes near atomic nucleus and inelastic radiative interaction occurs [13]. In that process, a photon is emitted and the initial electron gives significant amount of its kinetic energy to this photon and slows down. The name bremsstrahlung is a German word meaning breaking radiation. The bremsstrahlung event is relatively insignificant in tissues at electron energies below 10 MeV.

The formulas of the differential cross section differential in emitted photon energy $\frac{\mathrm{d}\sigma^{\mathrm{Br}}}{\mathrm{d}E_{\mathrm{p}}}(\boldsymbol{x}, E', E_{\mathrm{p}})$ can be obtained for bremsstrahlung event from [104, 124] or one can use the tabulated data from [162]. All these references use the original paper of Koch and Motz [108] as a reference.

When the differential cross section differential in emitted photon energy is known, then the differential cross section differential in both emitted photon energy and scattering angle can be approximated [124]

$$\frac{\mathrm{d}^2\sigma^{\mathrm{Br}}}{\mathrm{d}E_{\mathrm{p}}\mathrm{d}\boldsymbol{\Omega}_{\mathrm{p}}}(\boldsymbol{x}, E', E_{\mathrm{p}}, \boldsymbol{\Omega}'_{\mathrm{e}} \cdot \boldsymbol{\Omega}_{\mathrm{p}}) = \frac{\mathrm{d}\sigma^{\mathrm{Br}}}{\mathrm{d}E_{\mathrm{p}}}(x, E', E_{\mathrm{p}}) \frac{1}{2\pi} \frac{1-\beta^2}{4\pi(1-\beta\boldsymbol{\Omega}'_{\mathrm{e}} \cdot \boldsymbol{\Omega}_{\mathrm{p}})^2},$$

where β is as in Møller scattering in previous section. If $\frac{\mathrm{d}\sigma^{\mathrm{Br}}}{\mathrm{d}E_{\mathrm{p}}}$ is in units of $\mathrm{cm}^{-1}\mathrm{MeV}^{-1}$ then $\frac{\mathrm{d}^2\sigma^{B}}{\mathrm{d}E_{\mathrm{p}}\mathrm{d}\boldsymbol{\Omega}_{\mathrm{p}}}$ is in units of $\mathrm{cm}^{-1}\mathrm{sr}^{-1}\mathrm{MeV}^{-1}$.

It can be approximated that the initial electron does not undergo angular deflection in a bremsstrahlung event. In these circumstances, the differential cross section differential in scattered electron energy and angle is

$$\frac{\mathrm{d}^2\sigma^{\mathrm{Br}}}{\mathrm{d}E_{\mathrm{e}}\mathrm{d}\boldsymbol{\Omega}_{\mathrm{e}}}(\boldsymbol{x}, E', E_{\mathrm{p}}, \boldsymbol{\Omega}'_{\mathrm{e}} \cdot \boldsymbol{\Omega}_{\mathrm{e}}) = \frac{\mathrm{d}\sigma^{\mathrm{Br}}}{\mathrm{d}E_{\mathrm{p}}}(x, E', E_{\mathrm{p}}) \delta(\boldsymbol{\Omega}'_{\mathrm{e}} \cdot \boldsymbol{\Omega}_{\mathrm{e}} - 1.0).$$

As in the case of electron inelastic scattering, bremsstrahlung cross sections tend to infinity as the energy loss becomes small and are often divided into catastrophic and soft collisions as in Section 2.6.

2.4.3 Elastic electron scattering

When electrons scatter elastically, only the direction is changed without a change in electron energy [13]. Thus, electron elastic scattering does not contribute energy

to the medium, but is important mechanism in deflecting electrons. This scattering can be described in a terms of screened Rutherford scattering [104, 124, 199]. The Rutherford macroscopic differential cross section differential in the cosine of the electron scattering angle is then (in units of $\mathrm{cm}^{-1}\mathrm{sr}^{-1}$)

$$\frac{\mathrm{d}\sigma^{\mathrm{R}}}{\mathrm{d}\mu}(\boldsymbol{x}, E', \boldsymbol{\Omega}'\cdot\boldsymbol{\Omega}) = \frac{2\pi N_{\mathrm{A}}\rho Z^2 r_0^2}{M}\frac{E_0^2(E'+E_0)^2}{E'^2(E'+2E_0)^2}\frac{1}{(1-\boldsymbol{\Omega}'\cdot\boldsymbol{\Omega}+2\eta(E'))^2}, \quad (2.21)$$

where η is so-called screening parameter, which have different approximations. One screening parameter, developed by Moliere [199], is of the form

$$\eta(E') = \frac{Z^{2/3}E_0}{4(0.885\cdot 137)^2 E'(E'+2E_0)}\left(1.13 + 3.76\left(\frac{Z}{137\beta}\right)^2\right).$$

Because the energy does not change in elastic scattering, the differential cross section differential in both angle and energy is (in units of $\mathrm{cm}^{-1}\mathrm{sr}^{-1}\mathrm{MeV}^{-1}$)

$$\frac{\mathrm{d}^2\sigma^{\mathrm{R}}}{\mathrm{d}E\mathrm{d}\mu}(\boldsymbol{x}, E', E, \boldsymbol{\Omega}'\cdot\boldsymbol{\Omega}) = \frac{\mathrm{d}\sigma^{\mathrm{R}}}{\mathrm{d}\mu}(\boldsymbol{x}, E', \boldsymbol{\Omega}'\cdot\boldsymbol{\Omega})\delta(E'-E).$$

The total cross section for elastic Rutherford scattering is achieved by integrating the differential cross section in equation (2.21) over the cosine of the scattering angle $\mu \in [-1, 1]$. Thus,

$$\sigma^{\mathrm{R}}(\boldsymbol{x}, E') = \frac{\pi N_{\mathrm{A}}\rho Z^2 r_0^2}{M}\frac{E_0^2(E'+E_0)^2}{E'^2(E'+2E_0)^2}\frac{1}{\eta(E')(1+\eta(E'))}.$$

The screened Rutherford formulas are adequately accurate in tissue-like media at energies above 100 keV [104]. More accurate models for electron elastic scattering at low energies can be achieved by taking into account the spin effects with the help of partial wave analysis [90]. Also one could use the plurar and multiple small-angle scattering theories to approximate the Rutherford cross section [21].

2.5 Positron interactions

Positrons are charged particles and thus behave similarly as electrons. Positron interactions with matter are pretty much the same as those for electrons. Positron inelastic scattering from the atomic electrons can be described by Bhabha scattering [104]. Positron elastic scattering can be expressed in a terms of Rutherford scattering. Usually positrons are annihilated with atomic electron forming two photons. The differential cross section for this can be obtained for example from [104].

2.6 Restricted charged particle cross sections

The charged particle inelastic and bremsstrahlung collisions tend to infinity as the energy loss of the primary particle becomes small [124]. These interactions

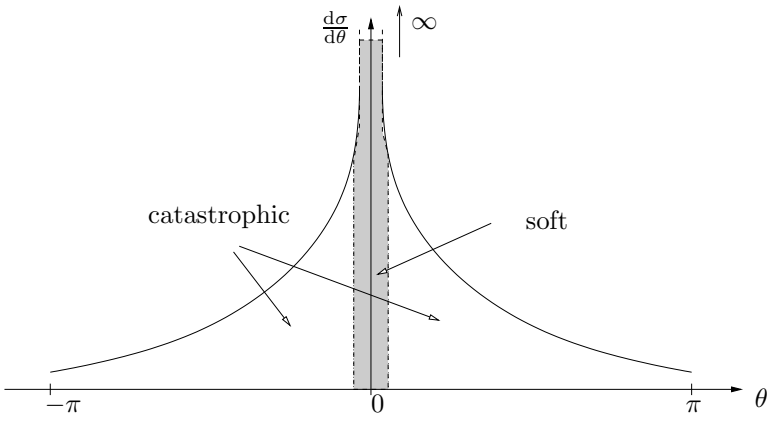

Figure 2.5: An arbitrary differential cross section $\frac{d\sigma}{d\theta}$ with respect to scattering angle $\theta \in [-\pi, \pi[$. The differential cross section tends to infinity as the scattering angle θ becomes zero. The scattering interaction is partitioned into soft and catastrophic events.

are difficult or even impossible to implement accurately by numerical grid based methods and are often divided into catastrophic and soft collisions. The catastrophic interactions result from large energy losses and soft interactions from small energy losses. In catastrophic scattering, the energy loss of the primary particle is more than some threshold, say E_{cut}. The soft collisions are those, in which the energy loss of the primary particle is less than that threshold. In soft collisions the primary particle energy loss is small, which means that the scattering angles of primary and secondary particles are small i.e. the scattering is almost forward peaked. Thus, the soft collisions can be approximated by the continuous energy loss of an electron with no change in direction. The electron transport is then described by restricted CSDA (see Section 3.6.2), in which the soft collisions are handled with a restricted stopping power. The catastrophic scattering is accounted by restricted differential and total cross sections. The relation between the catastrophic and soft collision events with respect to scattering angle is shown in Figure 2.5, in which an arbitrary differential cross section differential in scattering angle is drawn.

In inelastic collisions, the restricted differential cross section for secondary electron scattering is obtained from the equation (2.20), in which now the energy of the scattered secondary electron is $E \in [E_{\mathrm{cut}}, E_{\mathrm{max}}/2[$. Similarly, the restricted differential cross section for primary electron is obtained from the equation (2.19), in which now $E' - E > E_{\mathrm{cut}}$. The restricted total cross section $\sigma^{\mathrm{r,Ie}}$ is achieved by integrating the differential cross section (defined by equation (2.16)) differential in

secondary particle energy E_s over E_s from E_cut to $E_\mathrm{max}/2$. This results in

$$\sigma^{\mathrm{r,Ie}}(\boldsymbol{x}, E') = \frac{C}{\beta^2}\left(C_1 + C_2\frac{\epsilon^2}{(\epsilon+1)^2} + C_3\frac{2\epsilon+1}{(\epsilon+1)^2}\right),$$

where $C_1 = \frac{1}{E_\mathrm{cut}} - \frac{1}{E_\mathrm{max}-E_\mathrm{cut}}$, $C_2 = \frac{E_\mathrm{max}-2E_\mathrm{cut}}{2E_\mathrm{max}^2}$ and $C_3 = \frac{1}{E_\mathrm{max}}\ln\left|\frac{E_\mathrm{cut}}{E_\mathrm{max}-E_\mathrm{cut}}\right|$. The restricted stopping power for inelastic collisions $\tau^{\mathrm{r,Ie}}$ describes the energy loss of primary particle in inelastic soft collision. One can compute the stopping power related to the inelastic catastrophic collisions $\tau^{\mathrm{c,Ie}}(\boldsymbol{x}, E')$ from the equation

$$\begin{aligned}\tau^{\mathrm{c,Ie}}(\boldsymbol{x}, E') &= \int_{E_\mathrm{cut}}^{E_\mathrm{max}/2} E_\mathrm{s}\frac{\mathrm{d}\sigma^{\mathrm{Ie}}}{\mathrm{d}E_\mathrm{s}}(\boldsymbol{x}, E', E_\mathrm{s})\mathrm{d}E_\mathrm{s} \\ &= \frac{C}{\beta^2}\left(C_4 + C_5\frac{\tau^2}{(\tau+1)^2} + C_6\frac{2\tau+1}{(\tau+1)^2}\right), \qquad (2.22)\end{aligned}$$

where $\frac{\mathrm{d}\sigma^{\mathrm{Ie}}}{\mathrm{d}E_\mathrm{s}}(\boldsymbol{x}, E', E_\mathrm{s})$ is obtained from equation (2.16) and where $C_4 = 2 - \frac{E_\mathrm{max}}{E_\mathrm{max}-E_\mathrm{cut}} + \ln\left|\frac{E_\mathrm{max}^2}{4E_\mathrm{cut}(E_\mathrm{max}-E_\mathrm{cut})}\right|$, $C_5 = \frac{1}{8} - \frac{E_\mathrm{cut}^2}{2E_\mathrm{max}^2}$ and $C_6 = \ln\left|\frac{E_\mathrm{max}}{2E_\mathrm{cut}}\right|$. Then the restricted stopping power $\tau^{\mathrm{r,Ie}}$ is obtained from

$$\tau^{\mathrm{r,Ie}}(\boldsymbol{x}, E') = \tau^{\mathrm{Ie}}(\boldsymbol{x}, E') - \tau^{\mathrm{s,Ie}}(\boldsymbol{x}, E'),$$

where $\tau^{\mathrm{Ie}}(\boldsymbol{x}, E')$ is the tabulated electron collision stopping power.

Similarly for the bremsstrahlung progress, the restricted differential cross sections are those, in which the energy loss of the primary electron is more than E_cut. This means that the produced photon has an energy $E_\mathrm{p} > E_\mathrm{cut}$ and that scattered electron has an energy $E_\mathrm{e} < E' - E_\mathrm{cut}$ in bremsstrahlung process. The restricted total cross section $\sigma^{\mathrm{r,Br}}$ is achieved by integrating the differential cross section differential in E_p over E_p from E_cut to E_max. The restricted radiative stopping power $\tau^{\mathrm{r,Br}}(\boldsymbol{x}, E')$ is obtained from

$$\tau^{\mathrm{r,Br}}(\boldsymbol{x}, E') = \tau^{\mathrm{Br}}(\boldsymbol{x}, E') - \tau^{\mathrm{c,Br}}(\boldsymbol{x}, E'),$$

where $\tau^{\mathrm{Br}}(\boldsymbol{x}, E')$ is the tabulated electron radiative stopping power and $\tau^{\mathrm{c,Br}}(\boldsymbol{x}, E')$ is the stopping power related to catastrophic collisions in bremsstrahlung event. $\tau^{\mathrm{c,Br}}(\boldsymbol{x}, E')$ is obtained from equation

$$\tau^{\mathrm{c,Br}}(\boldsymbol{x}, E') = \int_{E_\mathrm{cut}}^{E_\mathrm{max}} E_\mathrm{p}\frac{\mathrm{d}\sigma^{\mathrm{Br}}}{\mathrm{d}E_\mathrm{s}}(\boldsymbol{x}, E', E_\mathrm{p})\mathrm{d}E_\mathrm{p}.$$

Chapter III

Particle transport

As described in the previous chapter, the high energy particles travel in a medium and interact with medium atoms via different interactions. This particle transport in a medium can be described by the coupled time independent linear BTE, which is an integro-partial differential equation and coupled due to the fact that particles change into other types of particles in different interactions. This chapter first makes the definitions needed to present the BTE by particle fluxes. In Section 3.2, the BTE is derived from the particle conservation. After that the dose computation from the charged particle flux is presented in Section 3.3. Section 3.4 outlines the needed boundary conditions for the external radiation therapy. In Sections 3.5 and 3.6, the integral form and the most often used approximations of the BTE are presented.

3.1 Definitions

The high energy particles, photons, electrons and positrons, are assumed to travel in a seven dimensional phase space $(\boldsymbol{x}, E, \boldsymbol{\Omega}, t) \in V \times I \times S \times [0, t_0]$, in which $\boldsymbol{x} = (x_1, x_2, x_3)$ is the spatial coordinate, E is the energy variable, $\boldsymbol{\Omega}$ is the particle direction and t is the time. The domain $V \subset \mathbb{R}^3$ is assumed to be open and bounded and the boundary ∂V is assumed to be piecewise smooth. The energy interval can be for example $I = [E_{\min}, E_{\max}]$. The particle direction $\boldsymbol{\Omega}$ is a point on a unit sphere $S \subset \mathbb{R}^3$ and can be defined in terms of particle velocity $\boldsymbol{v}$ and speed $v = \|\boldsymbol{v}\|$ i.e.

$$\boldsymbol{\Omega} = \frac{\boldsymbol{v}}{v} = (\cos\varphi \sin\theta, \sin\varphi \sin\theta, \cos\theta), \tag{3.1}$$

where (φ, θ) are standard spherical coordinates on S, $\varphi \in [0, 2\pi[$ and $\theta \in [0, \pi[$ (see Figure 3.1).

Particle traveling in a medium can be described by particle distribution $f(\boldsymbol{x}, E, \boldsymbol{\Omega}, t)$, which is sometimes referred to particle angular density [47] or particle phase space density [67]. It is defined that $f(\boldsymbol{x}, E, \boldsymbol{\Omega}, t)\mathrm{d}\boldsymbol{x}\mathrm{d}E\mathrm{d}\boldsymbol{\Omega}$ is the expected number of particles in the volume element $\mathrm{d}\boldsymbol{x}$ about the point $\boldsymbol{x}$ with energies in $\mathrm{d}E$ about E and with directions in $\mathrm{d}\boldsymbol{\Omega}$ about $\boldsymbol{\Omega}$ at time t. The unit of f is typically $\mathrm{cm}^{-3}\mathrm{MeV}^{-1}\mathrm{sr}^{-1}$.

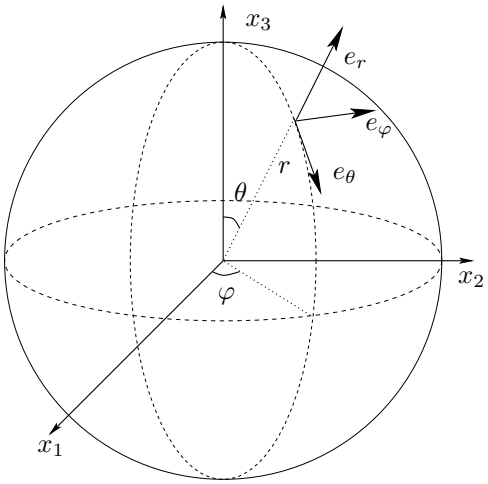

Figure 3.1: Polar coordinates (r,φ,θ) indicating the direction of the particle in a standard coordinate system for $\boldsymbol{x} = (x_1, x_2, x_3)$ with $r = 1$.

Closely related to angular density $f(\boldsymbol{x}, E, \boldsymbol{\Omega}, t)$ is the angular current or phase space current density $\boldsymbol{j}(\boldsymbol{x}, E, \boldsymbol{\Omega}, t) = \boldsymbol{v} f(x, E, \Omega, t)$, in which $\boldsymbol{v}$ is a particle velocity vector. The angular current is defined such that

$$\boldsymbol{j}(\boldsymbol{x}, E, \boldsymbol{\Omega}, t) \cdot \mathrm{d}\boldsymbol{s}\mathrm{d}E\mathrm{d}\boldsymbol{\Omega}\mathrm{d}t = \boldsymbol{v} f(\boldsymbol{x}, E, \boldsymbol{\Omega}, t) \cdot \mathrm{d}\boldsymbol{s}\mathrm{d}E\mathrm{d}\boldsymbol{\Omega}\mathrm{d}t$$

is the number of particles with energies in $\mathrm{d}E$ about E and with directions in $\mathrm{d}\boldsymbol{\Omega}$ about $\boldsymbol{\Omega}$ which cross a small area $\mathrm{d}\boldsymbol{s}$ with unit normal $\boldsymbol{n}$ in a time $\mathrm{d}t$.

The transport of particles is often described in terms of angular flux or phase space flux $\psi(\boldsymbol{x}, E, \boldsymbol{\Omega}, t) = v f(\boldsymbol{x}, E, \boldsymbol{\Omega}, t)$ in units of $\mathrm{cm}^{-2}\mathrm{MeV}^{-1}\mathrm{sr}^{-1}\mathrm{s}^{-1}$. Close to that is the integrated flux $\psi^{\mathrm{I}}(\boldsymbol{x}, t)$ ($\mathrm{cm}^{-2}\mathrm{s}^{-1}$), which is obtained by integrating the angular flux over all angles and energies, thus

$$\psi^{\mathrm{I}}(\boldsymbol{x}, t) = \int_I \int_S \psi(\boldsymbol{x}, E, \boldsymbol{\Omega}, t)\mathrm{d}E\mathrm{d}\boldsymbol{\Omega}. \tag{3.2}$$

In the field of radiotherapy physics, the particle flux term is quite uncommon. However, it is a general term in the particle physics community [196, 67]. The International Commission on Radiation Units and Measurements (ICRU) recommends to use term particle fluence or fluence rates [88], which are in fact the integrated particle fluxes in stationary and time-dependent cases, respectively. An alternative for the particle flux according to ICRU would be a particle fluence differential in energy and angle, which is quite a long term and quite uncommon also in the field of radiotherapy physics. For these reasons it is chosen to use the particle flux term in this thesis.

3.2 Boltzmann transport equation

BTE is a partial-differential-integral equation. It was first derived by Ludvig Boltzmann for dilute gases in a year 1872 from the Liouville equation with appropriate approximations [50]. Although it was generated for ideal gases, it is still used as a basis in nowadays gas theory and adopted from there to the other fields of particle physics. In radiation therapy, the interactions of particles with each other are negligible and the linear BTE can be used to describe the evolution of particles in a medium [147, 30].

3.2.1 Deriving a coupled BTE

BTE is basically a balance equation. In addition to gas theory and Liouville equation, from which the Boltzmann equation was originally derived, the linear BTE can be derived from the particle conservation within a small volume element of a phase space [47]. Here the BTE is derived for the coupled system, including photons, electrons and positrons, assuming particle conservation. The particles are assumed to interact only with medium atoms, not with each other. The particles are also assumed to travel with straight lines between the interactions.

Consider a small volume ΔV with surface ΔS about the point $\boldsymbol{x}$. The number of particles $\mathrm{d}N_j$ of type j in this volume with energies in $\mathrm{d}E$ about E and with directions in $\mathrm{d}\boldsymbol{\Omega}$ about $\boldsymbol{\Omega}$ in time $\mathrm{d}t$ is achieved by integrating the time derivate of the angular density over the volume element i.e.

$$\mathrm{d}N_j = \mathrm{d}E\mathrm{d}\boldsymbol{\Omega}\mathrm{d}t \int_{\Delta V} \frac{\partial f_j(\boldsymbol{x}, E, \boldsymbol{\Omega}, t)}{\partial t} \mathrm{d}\boldsymbol{x}, \tag{3.3}$$

where now the lower index j specifies the particles, $j = 1, 2, 3$ referring to photons, electrons and positrons, respectively. In terms of angular flux $\psi_j(\boldsymbol{x}, E, \boldsymbol{\Omega}, t)$, equation (3.3) can be written in the form

$$\mathrm{d}N_j = \mathrm{d}E\mathrm{d}\boldsymbol{\Omega}\mathrm{d}t \int_{\Delta V} \frac{1}{v_j} \frac{\partial \psi_j(\boldsymbol{x}, E, \boldsymbol{\Omega}, t)}{\partial t} \mathrm{d}\boldsymbol{x}. \tag{3.4}$$

Equation (3.4) should be in balance with the particles with energies in $\mathrm{d}E$ about E and with directions in $\mathrm{d}\boldsymbol{\Omega}$ about $\boldsymbol{\Omega}$ in time $\mathrm{d}t$ that enter and leave the volume ΔV, suffer collisions i.e are attenuated, are born in the different scattering interactions and are produced by sources in ΔV. Thus, one has a balance relation

$$\mathrm{d}N_j = -N_{j,\mathrm{out}} - N_{j,\mathrm{att}} + N_{j,\mathrm{sec}} + N_{j,\mathrm{so}}, \tag{3.5}$$

where $N_{j,\mathrm{out}}$ is the net number of particles j flowing out of the volume ΔV through the surface ΔS in time $\mathrm{d}t$, $N_{j,\mathrm{att}}$ is the number of particles j that are attenuated in ΔV in time $\mathrm{d}t$, $N_{j,\mathrm{sec}}$ is the number of particles j that are born in the scattering interactions with medium atoms in ΔV in time $\mathrm{d}t$ and $N_{j,\mathrm{so}}$ is the number of particles j produced by the sources inside the volume ΔV in time $\mathrm{d}t$.

$N_{j,\mathrm{out}}$ is achieved by integrating the angular current $\boldsymbol{j}_j$ over the surface ΔS. The surface integral can be changed to volume integral using Gauss's theorem [9].

Thus,

$$\begin{aligned} N_{j,\text{out}} &= \mathrm{d}E\mathrm{d}\boldsymbol{\Omega}\mathrm{d}t \int_{\Delta S} (\boldsymbol{j}_j(\boldsymbol{x}, E, \boldsymbol{\Omega}, t) \cdot \boldsymbol{n})\mathrm{d}\boldsymbol{s} \\ &= \mathrm{d}E\mathrm{d}\boldsymbol{\Omega}\mathrm{d}t \int_{\Delta V} \nabla \cdot \boldsymbol{j}_j(\boldsymbol{x}, E, \boldsymbol{\Omega}, t)\mathrm{d}\boldsymbol{x}, \end{aligned} \tag{3.6}$$

where $\boldsymbol{n}$ is the unit outward normal to $\mathrm{d}\boldsymbol{s}$. By the definition $\boldsymbol{j}_j = \boldsymbol{\Omega}\psi_j$ and equation (3.6) is of the form

$$N_{j,\text{out}} = \mathrm{d}E\mathrm{d}\boldsymbol{\Omega}\mathrm{d}t \int_{\Delta V} (\boldsymbol{\Omega} \cdot \nabla\psi_j(\boldsymbol{x}, E, \boldsymbol{\Omega}, t))\mathrm{d}\boldsymbol{x}. \tag{3.7}$$

$N_{j,\text{att}}$ is obtained using the total cross section $\sigma_j(\boldsymbol{x}, E)$, which is defined in Section 2.2.2 to be the probability per unit path length for particle j of energy E to attenuate. The attenuation frequency depends on the particle speed v_j [67]. Thus,

$$v_j\sigma_j(\boldsymbol{x}, E)$$

is the attenuation frequency for a particle j to be absorbed in unit distance that the particle travels. Moreover, the number of particles attenuated $N_{j,\text{att}}$ in a small volume element ΔV is then

$$\begin{aligned} N_{j,\text{att}} &= \mathrm{d}E\mathrm{d}\boldsymbol{\Omega}\mathrm{d}t \int_{\Delta V} v_j\sigma_j(\boldsymbol{x}, E) f_j(\boldsymbol{x}, E, \boldsymbol{\Omega}, t)\mathrm{d}\boldsymbol{x} \\ &= \mathrm{d}E\mathrm{d}\boldsymbol{\Omega}\mathrm{d}t \int_{\Delta V} \sigma_j(\boldsymbol{x}, E)\psi_j(\boldsymbol{x}, E, \boldsymbol{\Omega}, t)\mathrm{d}\boldsymbol{x}. \end{aligned} \tag{3.8}$$

Similarly to attenuation, $N_{j,\text{sec}}$ is obtained using differential cross section $\sigma_{j'\to j} := \sigma_{j'\to j}(\boldsymbol{x}, E', E, \boldsymbol{\Omega}', \boldsymbol{\Omega}) = \frac{\mathrm{d}^2\sigma}{\mathrm{d}E\mathrm{d}\boldsymbol{\Omega}}(\boldsymbol{x}, E', E, \boldsymbol{\Omega}' \cdot \boldsymbol{\Omega})$, which is defined in Section 2.2.1 to be the probability per unit path length that a particle j' with energy E' and direction $\boldsymbol{\Omega}'$ will produce a secondary particle j with energy E and direction $\boldsymbol{\Omega}$. Assume particles $j' = 1, 2, 3$ to have initial energy E' and direction $\boldsymbol{\Omega}'$. Then the rate at which these particles are scattered to secondary particles j, which are of interest now, is [67]

$$\begin{aligned} &(v_1'\sigma_{1\to j}f_1 + v_2'\sigma_{2\to j}f_2 + v_3'\sigma_{3\to j}f_3)\,\mathrm{d}E'\mathrm{d}\boldsymbol{\Omega}' \\ &= \textstyle\sum_{j'=1}^{3} v_{j'}'\sigma_{j'\to j}f_{j'}(\boldsymbol{x}, E', \boldsymbol{\Omega}', t)\mathrm{d}E'\mathrm{d}\boldsymbol{\Omega}', \end{aligned} \tag{3.9}$$

where an abbreviation $f_{j'} := f_{j'}(\boldsymbol{x}, E', \boldsymbol{\Omega}', t)$ is used. Using the previous equation (3.9) $N_{j,\text{sec}}$ can be obtained from equation

$$\begin{aligned} N_{j,\text{sec}} &= \mathrm{d}E\mathrm{d}\boldsymbol{\Omega}\mathrm{d}t \int_{\Delta V}\int_I\int_S \sum_{j'=1}^{3} v_{j'}'\sigma_{j'\to j}f_{j'}(\boldsymbol{x}, E', \boldsymbol{\Omega}', t)\mathrm{d}E'\mathrm{d}\boldsymbol{\Omega}'\mathrm{d}\boldsymbol{x} \\ &= \mathrm{d}E\mathrm{d}\boldsymbol{\Omega}\mathrm{d}t \int_{\Delta V}\int_I\int_S \sum_{j'=1}^{3} \sigma_{j'\to j}\psi_{j'}(\boldsymbol{x}, E', \boldsymbol{\Omega}', t)\mathrm{d}E'\mathrm{d}\boldsymbol{\Omega}'\mathrm{d}\boldsymbol{x}. \end{aligned} \tag{3.10}$$

This is formulated in the general case. In radiotherapy, there are no interactions that change electrons to positrons. Thus, the differential cross section $\sigma_{2\to 3}$ is zero for all energies and angles.

$N_{j,\mathrm{so}}$ is obtained from

$$N_{j,\mathrm{so}} = \mathrm{d}E\mathrm{d}\boldsymbol{\Omega}\mathrm{d}t \int_{\Delta V} Q_j(\boldsymbol{x}, E, \boldsymbol{\Omega}, t)\mathrm{d}\boldsymbol{x}, \tag{3.11}$$

where $Q_j(\boldsymbol{x}, E, \boldsymbol{\Omega}, t)$ is the source term for particle j inside the volume ΔV. $Q_j(\boldsymbol{x}, E, \boldsymbol{\Omega}, t)\mathrm{d}\boldsymbol{x}\mathrm{d}E\mathrm{d}\boldsymbol{\Omega}$ is the number of particles j, which appear per unit time at t in $\mathrm{d}\boldsymbol{x}\mathrm{d}E\mathrm{d}\boldsymbol{\Omega}$ [196].

Finally, using equations (3.7), (3.8), (3.10) and (3.11) the balance equation (3.5) can be written in the form

$$\mathrm{d}E\mathrm{d}\boldsymbol{\Omega}\mathrm{d}t\int_{\Delta V}\left(\frac{1}{v_j}\frac{\partial\psi_j}{\partial t} + \boldsymbol{\Omega}\cdot\nabla\psi_j + \sigma_j\psi_j - \int_I\int_S\sum_{j'=1}^{3}\sigma_{j'\to j}\psi_{j'}\mathrm{d}E'\mathrm{d}\boldsymbol{\Omega}' - Q_j\right)\mathrm{d}\boldsymbol{x} = 0,$$

in which the shortenings σ_j and $\sigma_{j'\to j}$ are used for the total and differential cross sections, respectively. The previous balance equation equals zero if and only if the function inside the parenthesis equals zero. Hence,

$$\frac{1}{v_j}\frac{\partial\psi_j}{\partial t} + \boldsymbol{\Omega}\cdot\nabla\psi_j + \sigma_j\psi_j - \int_I\int_S\sum_{j'=1}^{3}\sigma_{j'\to j}\psi_{j'}\mathrm{d}E'\mathrm{d}\boldsymbol{\Omega}' - Q_j = 0, \tag{3.12}$$

which is the linear time dependent BTE for particle j. When written to all types of particles ($j = 1, 2, 3$), the coupled system of the BTEs is of the form

$$\begin{aligned}
&\tfrac{1}{v_1}\tfrac{\partial\psi_1}{\partial t} + \boldsymbol{\Omega}\cdot\nabla\psi_1 + \sigma_1\psi_1 - \textstyle\int_I\int_S\sum_{j'=1}^{3}\sigma_{j'\to 1}\psi_{j'}\mathrm{d}E'\mathrm{d}\boldsymbol{\Omega}' = Q_1\\
&\tfrac{1}{v_2}\tfrac{\partial\psi_2}{\partial t} + \boldsymbol{\Omega}\cdot\nabla\psi_2 + \sigma_2\psi_2 - \textstyle\int_I\int_S\sum_{j'=1}^{3}\sigma_{j'\to 2}\psi_{j'}\mathrm{d}E'\mathrm{d}\boldsymbol{\Omega}' = Q_2\\
&\tfrac{1}{v_3}\tfrac{\partial\psi_3}{\partial t} + \boldsymbol{\Omega}\cdot\nabla\psi_3 + \sigma_3\psi_3 - \textstyle\int_I\int_S\sum_{j'=1}^{3}\sigma_{j'\to 3}\psi_{j'}\mathrm{d}E'\mathrm{d}\boldsymbol{\Omega}' = Q_3.
\end{aligned} \tag{3.13}$$

3.2.2 Time independent BTE in external radiotherapy

The transport of high energy particles can be described by the stationary BTE, because the high energy particles move at a speed relative to the speed of light and the steady state is achieved in a time which is much smaller than the time the beam is usually on [30]. Thus, the time dependency can be neglected and the time derivative vanishes in equation (3.13). For simplicity the same notations $\psi := \psi(\boldsymbol{x}, E, \boldsymbol{\Omega})$ for particle flux and $Q_j := Q_j(\boldsymbol{x}, E, \boldsymbol{\Omega})$ for the source terms are used in the stationary case as in the time-dependent case. The unit of the stationary particle flux is $\mathrm{cm}^{-2}\mathrm{MeV}^{-1}\mathrm{sr}^{-1}$. The coupled system of the stationary linear BTEs for external radiation therapy is then of the form

$$\begin{aligned}
\boldsymbol{\Omega}\cdot\nabla\psi_1 + K_1\psi &= Q_1\\
\boldsymbol{\Omega}\cdot\nabla\psi_2 + K_2\psi &= Q_2\\
\boldsymbol{\Omega}\cdot\nabla\psi_3 + K_3\psi &= Q_3,
\end{aligned} \tag{3.14}$$

where the notations $\psi := (\psi_1, \psi_2, \psi_3)$ and

$$K_j\psi(\boldsymbol{x}, E, \boldsymbol{\Omega}) = \sigma_j(\boldsymbol{x}, E)\psi_j(\boldsymbol{x}, E, \boldsymbol{\Omega}) - \int_I \int_S \sum_{j'=1}^{3} \sigma_{j'\to j}(\boldsymbol{x}, E', E, \boldsymbol{\Omega}', \boldsymbol{\Omega})\psi_{j'}(\boldsymbol{x}, E', \boldsymbol{\Omega}')\mathrm{d}E'\mathrm{d}\boldsymbol{\Omega}' \tag{3.15}$$

have been made. In the coupled system (3.14), the first term $\boldsymbol{\Omega} \cdot \nabla\psi_j$ describes the transfer of the particles j. The collision term $K_j\psi$ combines attenuation and secondary production. In the equation (3.15), $\sigma_j(\boldsymbol{x}, E)$ is the total cross section for particle j ($j = 1, 2, 3$, referring to photons, electrons and positrons, respectively). $\sigma_{j'\to j}(\boldsymbol{x}, E', E, \boldsymbol{\Omega}', \boldsymbol{\Omega})$ is the differential cross section that changes particle j' ($j' = 1, 2, 3$) to particle j. If the interaction is not possible, zero differential cross section is used.

In external radiation therapy, the incoming beams are usually photon or electron beams, which are controlled by boundary conditions. The source term $Q_j(\boldsymbol{x}, E, t)$ is then usually zero. However, it is still included in the coupled system of BTEs for the sake of generality.

Traditionally the BTE is derived for one species of particles such as neutrons or electrons (neglecting the secondary photon production). Then the BTE is of the form

$$\boldsymbol{\Omega} \cdot \nabla\psi(\boldsymbol{x}, E, \boldsymbol{\Omega}) + K\psi(\boldsymbol{x}, E, \boldsymbol{\Omega}) = Q, \tag{3.16}$$

where ψ is the flux of one type of particles and

$$K\psi = \sigma_{\mathrm{t}}(\boldsymbol{x}, E)\psi(\boldsymbol{x}, E, \boldsymbol{\Omega}) - \int_I \int_S \sigma_{\mathrm{d}}(\boldsymbol{x}, E', E, \boldsymbol{\Omega}', \boldsymbol{\Omega})\psi(\boldsymbol{x}, E', \boldsymbol{\Omega}')\mathrm{d}E'\mathrm{d}\boldsymbol{\Omega}',$$

where $\sigma_{\mathrm{t}}(\boldsymbol{x}, E)$ and $\sigma_{\mathrm{d}}(\boldsymbol{x}, E', E, \boldsymbol{\Omega}', \boldsymbol{\Omega})$ are the total and differential cross sections, respectively.

3.3 Dose calculation

As it was mentioned in Section 2.1, the absorbed dose describes the energy absorption in the matter. Photons, by themselves, do not deposit dose, but photons create high energy charged particles by secondary particle production, which deposit the dose. If the solution of the coupled system (3.2) is known, i.e the angular fluxes $\psi_j(\boldsymbol{x}, E, \boldsymbol{\Omega})$ for all particles are known, then the absorbed dose $D(\boldsymbol{x})$ can be calculated from the formula [123, 153]

$$D(\boldsymbol{x}) = \sum_{j=2}^{3} \int_I \tau_j^{\mathrm{Ie}}(\boldsymbol{x}, E) \int_S \psi_j(\boldsymbol{x}, E, \boldsymbol{\Omega})\mathrm{d}\boldsymbol{\Omega}\mathrm{d}E, \tag{3.17}$$

where $\tau_j^{\mathrm{Ie}}(\boldsymbol{x}, E)$, $(j = 2, 3)$ are the collision stopping power parameters for electrons and positrons to represent the effects of inelastic collisions.

3.4 Boundary conditions for external radiotherapy

In external-beam radiotherapy, the high energy particles are directed to the PTV from outside of the domain V, which is for example a human body or a water tank [188]. The boundary of the V is typically assumed to be a free surface, in which the particles can only escape from the V through the surface ∂V, but they can not reenter it [18, 67]. This assumption is approximatively valid for convex domains, in which a straight line segment connecting any two points in the region lies entirely within the region. In the convex boundary, a particle can not intersect with the surface again once it has left the domain, if the direction of the particle does not change. In practice, the free surface assumption is an idealization, because particles have always some probability to return to the V once they have left it, because of the scattering processes [18]. However, this probability is negligible and it is always possible to choose the boundary to be far enough from the volume of interest so that the free surface assumption is valid.

In the following, the boundary conditions are defined for photon and electron incoming fluxes. Besides of these boundary conditions, one could define a boundary condition for mixed photon and electron incoming fluxes in the situation, in which both photon and electron fluxes are directed to the target.

3.4.1 Photon inflow

In the exterior photon therapy, photon flux enters outside to the domain. This exterior photon flux can be added to the transport problem by setting a boundary condition, which states the photon inflow at the free surface [18, 170]. Let $\boldsymbol{n}(\boldsymbol{x}) = (n_1(\boldsymbol{x}), n_2(\boldsymbol{x}), n_3(\boldsymbol{x}))$ be an outward unit normal vector at a point $\boldsymbol{x}$ on the boundary. The particles, which fulfill the condition $\boldsymbol{n}(\boldsymbol{x}) \cdot \boldsymbol{\Omega} > 0$ at the point $\boldsymbol{x}$ on the boundary, will be crossing the surface in an outward direction, whereas the particles for which $\boldsymbol{n}(\boldsymbol{x}) \cdot \boldsymbol{\Omega} < 0$ will be crossing the surface in an inward direction. The condition $\boldsymbol{n}(\boldsymbol{x}) \cdot \boldsymbol{\Omega} < 0$ for the inward flux means the relation

$$n_1(\boldsymbol{x}) \cos\varphi \sin\theta + n_2(\boldsymbol{x}) \sin\varphi \sin\theta + n_3(\boldsymbol{x}) \cos\theta < 0, \tag{3.18}$$

which is obtained by using equation (3.1).

Once the inward flux is specified, it is possible to set a boundary condition for the inward flux on the boundary. Typical boundary condition for the inward photon angular flux is of the form [170]

$$\begin{aligned} \psi_1 &= \begin{cases} 0, & \text{for } (\boldsymbol{x}, E, \boldsymbol{\Omega}) \in \partial V \setminus \Gamma \times I \times S \text{ such that } \boldsymbol{n}(\boldsymbol{x}) \cdot \boldsymbol{\Omega} < 0 \\ \psi_0, & \text{for } (\boldsymbol{x}, E, \boldsymbol{\Omega}) \in \Gamma \times I \times S \text{ such that } \boldsymbol{n}(\boldsymbol{x}) \cdot \boldsymbol{\Omega} < 0 \end{cases} \\ \psi_2 &= \psi_3 = 0, \text{ for } (\boldsymbol{x}, E, \boldsymbol{\Omega}) \in \partial V \times I \times S \text{ such that } \boldsymbol{n}(\boldsymbol{x}) \cdot \boldsymbol{\Omega} < 0, \end{aligned} \tag{3.19}$$

where Γ is a patch on the surface ∂V of the domain V and ψ_0 is the photon angular flux per unit area incident on Γ. Thus, only the inward photon angular flux on Γ obtain nonzero values. Elsewhere on ∂V the photon inward flux is zero. Also electron and positron fluxes are zero on ∂V. The outward flux of the particles is not constrained.

3.4.2 Electron inflow

Similarly to photon inflow, electron incident boundary condition can be stated for inward electron angular fluxes on a patch Γ on the surface ∂V. The boundary condition is typically of the form

$$\begin{aligned}\psi_2 &= \begin{cases} 0, & \text{for } (\boldsymbol{x}, E, \boldsymbol{\Omega}) \in \partial V \setminus \Gamma \times I \times S \text{ such that } \boldsymbol{n}(\boldsymbol{x}) \cdot \boldsymbol{\Omega} < 0 \\ \psi_0, & \text{for } (\boldsymbol{x}, E, \boldsymbol{\Omega}) \in \Gamma \times I \times S \text{ such that } \boldsymbol{n}(\boldsymbol{x}) \cdot \boldsymbol{\Omega} < 0 \end{cases} \\ \psi_1 &= \psi_3 = 0, \text{ for } (\boldsymbol{x}, E, \boldsymbol{\Omega}) \in \partial V \times I \times S \text{ such that } \boldsymbol{n}(\boldsymbol{x}) \cdot \boldsymbol{\Omega} < 0, \end{aligned} \tag{3.20}$$

where now ψ_0 is the electron angular flux per unit area incident on Γ.

3.5 The integral form of the BTE

The integral form of the BTE can be derived from the time dependent form of the BTE defined by equation (3.12) using the Laplace transform in time [196]. Besides of the Laplace transform, in time independent case the integral form of the BTE can be achieved directly by solving a resulted system of first order differential equations with boundary conditions. This procedure is detailed in the following. Assume V to be convex. Define $t(\boldsymbol{x}, \boldsymbol{\Omega}) > 0$ to be the number for which $\boldsymbol{x} - t(\boldsymbol{x}, E)\boldsymbol{\Omega} \in \partial V$. Thus, $\boldsymbol{x} - \tau\boldsymbol{\Omega}\,(\tau \in [0, t(\boldsymbol{x}, \boldsymbol{\Omega})])$ is the particle trajectory from point $\boldsymbol{x}$ to the boundary in direction $-\boldsymbol{\Omega}$ as shown in Figure 3.2. $t(\boldsymbol{x}, \boldsymbol{\Omega})$ is the length of the trajectory. With these definitions $\boldsymbol{\Omega} \cdot \nabla\psi_j = -\frac{\partial\psi_j}{\partial\tau}$ (when $\psi_j = \psi_j(\boldsymbol{x} - \tau\boldsymbol{\Omega}, E, \boldsymbol{\Omega})$ with fixed E and $\boldsymbol{\Omega}$) and from the coupled system of BTEs (defined by equation (3.14)) one obtains

$$\begin{aligned} -\frac{\partial\psi_1}{\partial\tau}(\boldsymbol{x}-\tau\boldsymbol{\Omega}, E, \boldsymbol{\Omega}) + \sigma_1(\boldsymbol{x}-\tau\boldsymbol{\Omega}, E)\psi_1(\boldsymbol{x}-\tau\boldsymbol{\Omega}, E, \boldsymbol{\Omega}) &= q_1(\boldsymbol{x}-\tau\boldsymbol{\Omega}, E, \boldsymbol{\Omega}) \\ -\frac{\partial\psi_2}{\partial\tau}(\boldsymbol{x}-\tau\boldsymbol{\Omega}, E, \boldsymbol{\Omega}) + \sigma_2(\boldsymbol{x}-\tau\boldsymbol{\Omega}, E)\psi_2(\boldsymbol{x}-\tau\boldsymbol{\Omega}, E, \boldsymbol{\Omega}) &= q_2(\boldsymbol{x}-\tau\boldsymbol{\Omega}, E, \boldsymbol{\Omega}) \\ -\frac{\partial\psi_3}{\partial\tau}(\boldsymbol{x}-\tau\boldsymbol{\Omega}, E, \boldsymbol{\Omega}) + \sigma_3(\boldsymbol{x}-\tau\boldsymbol{\Omega}, E)\psi_3(\boldsymbol{x}-\tau\boldsymbol{\Omega}, E, \boldsymbol{\Omega}) &= q_3(\boldsymbol{x}-\tau\boldsymbol{\Omega}, E, \boldsymbol{\Omega}), \end{aligned} \tag{3.21}$$

where $q_j,\ (j = 1, 2, 3)$ includes the source and scattering terms i.e. $q_j(\boldsymbol{x}, E, \boldsymbol{\Omega}) = Q_j(\boldsymbol{x}, E, \boldsymbol{\Omega}) + \sum_{j'=1}^{3} \int_I \int_S \sigma_{j' \to j}(\boldsymbol{x}, E', E, \boldsymbol{\Omega}', \boldsymbol{\Omega})\psi(\boldsymbol{x}, E', \boldsymbol{\Omega}')\mathrm{d}E'\mathrm{d}\boldsymbol{\Omega}'$.

One finds that $\boldsymbol{n}(\boldsymbol{x}-t(\boldsymbol{x}, \boldsymbol{\Omega})\boldsymbol{\Omega}) \cdot \boldsymbol{\Omega} < 0$, when V is convex. The photon incident boundary condition (3.19) is then

$$\begin{aligned}\psi_1 &= \begin{cases} 0, & \text{for } (\boldsymbol{x}-t(\boldsymbol{x}, \boldsymbol{\Omega})\boldsymbol{\Omega}, E, \boldsymbol{\Omega}) \in \partial V \setminus \Gamma \times I \times S \\ \psi_0, & \text{for } (\boldsymbol{x}-t(\boldsymbol{x}, \boldsymbol{\Omega})\boldsymbol{\Omega}, E, \boldsymbol{\Omega}) \in \Gamma \times I \times S \end{cases} \\ \psi_2 &= \psi_3 = 0, \text{ for } (\boldsymbol{x}-t(\boldsymbol{x}, \boldsymbol{\Omega})\boldsymbol{\Omega}, E, \boldsymbol{\Omega}) \in \partial V \times I \times S. \end{aligned} \tag{3.22}$$

If it is assumed that the right hand side of the equation (3.21) is known, then these first order differential equations with boundary conditions defined by equation (3.22) can be solved and the obtained system of integral equations are

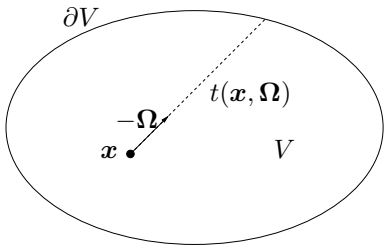

Figure 3.2: The particle traveling trajectory from the point $\boldsymbol{x}$ to the boundary ∂V along a straight line in the direction of $\boldsymbol{\Omega}$. $t(\boldsymbol{x}, \boldsymbol{\Omega})$ is the length of the trajectory.

resulted

$$\begin{aligned}
\psi_1 &= \psi_0(\boldsymbol{x}-t(\boldsymbol{x},\boldsymbol{\Omega})\boldsymbol{\Omega}, E, \boldsymbol{\Omega})\mathrm{e}^{-\int_0^{t(\boldsymbol{x},\boldsymbol{\Omega})}\sigma_1(\boldsymbol{x}-s\boldsymbol{\Omega},E)\mathrm{d}s} \\
&\quad + \int_0^{t(\boldsymbol{x},\boldsymbol{\Omega})} \mathrm{e}^{-\int_0^{\tau}\sigma_1(\boldsymbol{x}-s\boldsymbol{\Omega},E)\mathrm{d}s} q_1(\boldsymbol{x}-\tau\boldsymbol{\Omega}, E, \boldsymbol{\Omega})\mathrm{d}\tau \\
\psi_2 &= \int_0^{t(\boldsymbol{x},\boldsymbol{\Omega})} \mathrm{e}^{-\int_0^{\tau}\sigma_2(\boldsymbol{x}-s\boldsymbol{\Omega},E)\mathrm{d}s} q_2(\boldsymbol{x}-\tau\boldsymbol{\Omega}, E, \boldsymbol{\Omega})\mathrm{d}\tau \\
\psi_3 &= \int_0^{t(\boldsymbol{x},\boldsymbol{\Omega})} \mathrm{e}^{-\int_0^{\tau}\sigma_3(\boldsymbol{x}-s\boldsymbol{\Omega},E)\mathrm{d}s} q_3(\boldsymbol{x}-\tau\boldsymbol{\Omega}, E, \boldsymbol{\Omega})\mathrm{d}\tau.
\end{aligned}$$

The integral form of the BTE can be simplified in some geometries such as plane or spherical geometries. It has been used in many applications and can be used also with numerical methods for solving the BTE [67, 119, 196, 47, 50].

3.6 Different approximations of the BTE

Several different approximative forms of the BTE can be derived from the original BTE equation (3.16), which may ease the numerical solvability of the BTE. Fokker-Plank equation, CSDA equation and restricted CSDA equation are approximative forms of the BTE [121]. Even-parity equation [65] and self-adjoint angular flux (SAAF) equation [140] can be derived from the energy and angle independent forms of the BTE, respectively. These approximative forms are typically used in the radiotherapy applications. The diffusion approximation of the BTE [67] is typically used in the applications of optical tomography and is not presented here.

3.6.1 Boltzmann Fokker-Plank equation

If the particle scattering is assumed to be highly forward peaked, the scattering term $-K_j\psi$ of the linear stationary BTE can be approximated with a partial differential operator using Taylor expansion techniques [138, 121, 133, 155, 46]. This differential operator is often referred to the Fokker-Planck operator L_{FP}. It

is typically used to approximate electron scattering. The Fokker-Plank operator is defined by the spherical coordinates (φ, θ) with $\mu = \cos\theta$ and the particle angular flux is defined as $\widetilde{\psi}(\boldsymbol{x}, E, \mu, \varphi)$. The Fokker-Planck operator L_{FP} is then of the form

$$L_{\mathrm{FP}}\widetilde{\psi}(\boldsymbol{x}, E, \mu, \varphi) = \frac{\partial(\tau(\boldsymbol{x}, E)\widetilde{\psi}(\boldsymbol{x}, E, \mu, \varphi))}{\partial E} + \frac{\partial^2(\tau^*(\boldsymbol{x}, E)\widetilde{\psi}(\boldsymbol{x}, E, \mu, \varphi))}{\partial E^2} + \frac{\chi(\boldsymbol{x}, E)}{2}\left(\frac{\partial}{\partial\mu}(1-\mu^2)\frac{\partial\widetilde{\psi}(\boldsymbol{x}, E, \mu, \varphi)}{\partial\mu} + \frac{1}{1-\mu^2}\frac{\partial^2\widetilde{\psi}(\boldsymbol{x}, E, \mu, \varphi)}{\partial\varphi^2}\right), \quad (3.23)$$

where the first term describes continuous energy loss with the stopping power τ defined by equation (2.2). τ^* is a mean-square stopping power defined as

$$\tau^*(\boldsymbol{x}, E') = \int_0^\infty (E' - E)^2 \frac{\mathrm{d}\sigma}{\mathrm{d}E}(E', E)\mathrm{d}E, \quad (3.24)$$

where $\frac{\mathrm{d}\sigma}{\mathrm{d}E}$ is particle differential cross section differential in energy. The final term includes a momentum transfer

$$\chi(\boldsymbol{x}, E) = 2\pi \int_{-1}^{1} \frac{\mathrm{d}\sigma}{\mathrm{d}\mu}(\boldsymbol{x}, E, \mu)(1-\mu)\mathrm{d}\mu, \quad (3.25)$$

where $\frac{\mathrm{d}\sigma}{\mathrm{d}\mu}$ is the particle differential cross section differential in direction cosine μ.

The Fokker-Planck approximation of the linear stationary BTE is then

$$\boldsymbol{\Omega} \cdot \nabla\widetilde{\psi}(\boldsymbol{x}, E, \mu, \varphi) = L_{\mathrm{FP}}\widetilde{\psi}(\boldsymbol{x}, E, \mu, \varphi) + \widetilde{Q}(\boldsymbol{x}, E, \mu, \varphi). \quad (3.26)$$

This equation is known as the Fokker-Planck equation. It is used to approximate electron traveling. Further assuming monoenergetic case with $\mu = 1$ results in the Fermi equation, which has an analytical form in homogeneous domain [31, 32]. The Fermi-Eyges theory uses Fermi equation and assumes the momentum transfer $\chi(\boldsymbol{x}, E)$ to be a function of approximate electron energy at each depth [85, 114]. Typically empirical correction factors are used to make the results to match the dosimetric data. Different electron dose calculation methods and pencil beam methods have roots on Fermi-Eyges theory [93, 33].

The Fokker-Planck approximation neglects the backward scattering and is thus a quite coarse approximation of the BTE. The backward scattering is taken into account in Boltzmann Fokker-Planck (BFP) equation, in which the scattering is divided into backward scattering, which is described by the integral term, and highly forward peaked scattering, which is approximated by the Fokker-Planck operator. The BFP equation is then

$$\boldsymbol{\Omega} \cdot \nabla\widetilde{\psi}(\boldsymbol{x}, E, \mu, \varphi) + \sigma_{\mathrm{b}}(\boldsymbol{x}, E)\widetilde{\psi}(\boldsymbol{x}, E, \mu, \varphi) = \widetilde{Q}(\boldsymbol{x}, E, \mu, \varphi) \quad (3.27)$$
$$+ \int_0^{2\pi}\int_{-1}^{1}\int_I \widetilde{\sigma}_{\mathrm{b}}(\boldsymbol{x}, E', E, \mu)\widetilde{\psi}(\boldsymbol{x}, E, \mu, \varphi)\mathrm{d}E'\mathrm{d}\mu\mathrm{d}\varphi + L_{\mathrm{FP}}\widetilde{\psi}(\boldsymbol{x}, E, \mu, \varphi),$$

where $\sigma_{\mathrm{b}}(\boldsymbol{x}, E)$ and $\widetilde{\sigma}_{\mathrm{b}}(\boldsymbol{x}, E', E, \mu)$ are the total and differential cross sections describing the backward scattering.

3.6.2 CSDA for BTE

In Section 2.6, the electron inelastic and bremsstrahlung processes were divided into soft and catastrophic collisions to describe small and large energy losses, respectively. The soft collisions can be treated with CSDA, which approximates the soft collisions as a continuous energy loss without angular deflection [121]. In the CSDA, the energy-loss straggling is ignored and thus $\tau^* = 0$ in L_{FP} term in equation (3.27). Also the stopping powers are now restricted stopping powers, which are defined only for soft collision. This means that some small threshold energy is assigned to separate soft and hard collisions. Furthermore, the total and differential cross sections are defined for the catastrophic collisions, neglecting the small energy transfers which are taken into account in the CSDA.

The CSDA equation can be simplified even more for typical electron transport problems, in which the momentum transfer term in the Fokker-Planck operator (3.23) is only important for heavy-charged particle transport and electron beam problems [121]. The equation obtained to describe approximatively electron or positron transport is called as a Boltzmann-CSDA equation (B-CSDAE)

$$\begin{aligned}&\boldsymbol{\Omega}\cdot\nabla\psi(\boldsymbol{x},E,\boldsymbol{\Omega})+\sigma_{\mathrm{t}}^{\mathrm{r}}(\boldsymbol{x},E)\psi(\boldsymbol{x},E,\boldsymbol{\Omega})=Q(\boldsymbol{x},E,\boldsymbol{\Omega})+\\&\int_S\int_I\sigma_{\mathrm{d}}^{\mathrm{r}}(\boldsymbol{x},E',E,\boldsymbol{\Omega}',\boldsymbol{\Omega})\psi(\boldsymbol{x},E',\boldsymbol{\Omega}')\mathrm{d}E'\mathrm{d}\boldsymbol{\Omega}'+\frac{\partial\left(\tau^{\mathrm{r}}(\boldsymbol{x},E)\psi(\boldsymbol{x},E,\boldsymbol{\Omega})\right)}{\partial E},\end{aligned}\tag{3.28}$$

where $\sigma_{\mathrm{t}}^{\mathrm{r}}(\boldsymbol{x},E)$ and $\sigma_{\mathrm{d}}^{\mathrm{r}}(\boldsymbol{x},E',E,\boldsymbol{\Omega}',\boldsymbol{\Omega})$ are the restricted total and differential cross sections, respectively, and $\tau^{\mathrm{r}}(\boldsymbol{x},E)$ is the restricted stopping power.

Because the B-CSDAE (3.28) includes partial derivate respect to energy variable, one should set an adequate initial energy point for the charged particle fluxes. In [115], it is demanded that $\lim_{E\to\infty}\psi_2(\boldsymbol{x},E,\boldsymbol{\Omega})=0$. Now if the energy interval $I=[E_{\min},E_{\max}]$, one could demand that $\psi_2(\boldsymbol{x},E_{\max},\boldsymbol{\Omega})=\psi_3(\boldsymbol{x},E_{\max},\boldsymbol{\Omega})=0\ \forall\boldsymbol{x}\in V,\boldsymbol{\Omega}\in S$, which is physically relevant, if the maximum energy $E_{\max}$ is selected such that it is more than the maximum energy of the incoming particle fluxes and more than the energy of the internal sources.

If the B-CSDAE is used for the charged particle transport, the coupled system is of the form [123]

$$\begin{aligned}\boldsymbol{\Omega}\cdot\nabla\psi_1+K_1\psi&=Q_1\\\boldsymbol{\Omega}\cdot\nabla\psi_2+K_2^{\mathrm{r}}\psi&=Q_2\\\boldsymbol{\Omega}\cdot\nabla\psi_3+K_3^{\mathrm{r}}\psi&=Q_3,\end{aligned}\tag{3.29}$$

where the collision term for photons is of the form

$$\begin{aligned}K_1\psi(\boldsymbol{x},E,\boldsymbol{\Omega})&=\sigma_1(\boldsymbol{x},E)\psi_1(\boldsymbol{x},E,\boldsymbol{\Omega})\\&\quad-\int_I\int_S\sum_{j'=1}^{3}\sigma_{j'\to1}(\boldsymbol{x},E',E,\boldsymbol{\Omega}',\boldsymbol{\Omega})\psi_{j'}(\boldsymbol{x},E',\boldsymbol{\Omega}')\mathrm{d}E'\mathrm{d}\boldsymbol{\Omega}',\end{aligned}\tag{3.30}$$

for electrons

$$\begin{aligned} K_2^{\mathrm{r}}\psi(\boldsymbol{x},E,\boldsymbol{\Omega}) &= \sigma_2^{\mathrm{r}}(\boldsymbol{x},E)\psi_2(\boldsymbol{x},E,\boldsymbol{\Omega}) \\ &\quad -\int_I\int_S \sigma_{1\to 2}(\boldsymbol{x},E',E,\boldsymbol{\Omega}',\boldsymbol{\Omega})\psi_1(\boldsymbol{x},E',\boldsymbol{\Omega}')\mathrm{d}E'\mathrm{d}\boldsymbol{\Omega}' \\ &\quad -\int_I\int_S \sigma_{2\to 2}^{\mathrm{r}}(\boldsymbol{x},E',E,\boldsymbol{\Omega}',\boldsymbol{\Omega})\psi_2(\boldsymbol{x},E',\boldsymbol{\Omega}')\mathrm{d}E'\mathrm{d}\boldsymbol{\Omega}' \\ &\quad -\frac{\partial\left(\tau_2^{\mathrm{r}}(\boldsymbol{x},E)\psi_2(\boldsymbol{x},E,\boldsymbol{\Omega})\right)}{\partial E} \\ &\quad -\int_I\int_S \sigma_{3\to 2}(\boldsymbol{x},E',E,\boldsymbol{\Omega}',\boldsymbol{\Omega})\psi_3(\boldsymbol{x},E',\boldsymbol{\Omega}')\mathrm{d}E'\mathrm{d}\boldsymbol{\Omega}' \end{aligned} \tag{3.31}$$

and for positrons

$$\begin{aligned} K_3^{\mathrm{r}}\psi(\boldsymbol{x},E,\boldsymbol{\Omega}) &= \sigma_3^{\mathrm{r}}(\boldsymbol{x},E)\psi_3(\boldsymbol{x},E,\boldsymbol{\Omega}) \\ &\quad -\int_I\int_S \sigma_{1\to 3}(\boldsymbol{x},E',E,\boldsymbol{\Omega}',\boldsymbol{\Omega})\psi_1(\boldsymbol{x},E',\boldsymbol{\Omega}')\mathrm{d}E'\mathrm{d}\boldsymbol{\Omega}' \\ &\quad -\int_I\int_S \sigma_{3\to 3}^{\mathrm{r}}(\boldsymbol{x},E',E,\boldsymbol{\Omega}',\boldsymbol{\Omega})\psi_3(\boldsymbol{x},E',\boldsymbol{\Omega}')\mathrm{d}E'\mathrm{d}\boldsymbol{\Omega}' \\ &\quad -\frac{\partial\left(\tau_3^{\mathrm{r}}(\boldsymbol{x},E)\psi_3(\boldsymbol{x},E,\boldsymbol{\Omega})\right)}{\partial E}. \end{aligned} \tag{3.32}$$

In the previous collision term equations, $\sigma_2^{\mathrm{r}}(\boldsymbol{x},E)$ and $\sigma_3^{\mathrm{r}}(\boldsymbol{x},E)$ are the restricted total cross sections, $\sigma_{2\to 2}^{\mathrm{r}}(\boldsymbol{x},E',E,\boldsymbol{\Omega}',\boldsymbol{\Omega})$ and $\sigma_{3\to 3}^{\mathrm{r}}(\boldsymbol{x},E',E,\boldsymbol{\Omega}',\boldsymbol{\Omega})$ are the restricted differential cross sections that does not include soft inelastic interactions and τ_2^{r}, τ_3^{r} are the restricted stopping powers.

The boundary conditions are as those stated in Section 3.4. In addition, one demands that

$$\psi_2(\boldsymbol{x},E_{\max},\boldsymbol{\Omega}) = \psi_3(\boldsymbol{x},E_{\max},\boldsymbol{\Omega}) = 0, \text{ when } \boldsymbol{x}\in V,\ \boldsymbol{\Omega}\in S \tag{3.33}$$

$$Q_j(\boldsymbol{x},E_{\max},\boldsymbol{\Omega}) = 0, \text{ when } \boldsymbol{x}\in V,\ \boldsymbol{\Omega}\in S, \tag{3.34}$$

where $E_{\max}$ is selected such that the conditions (3.33) and (3.34) are fulfilled being more than the maximum energy of the incoming fluxes and internal sources. The energy interval $I = [E_{\min}, E_{\max}]$.

3.6.3 Even-parity BTE equation

The standard BTE contains a first order spatial derivate term causing that the Boltzmann transport operator is neither symmetric nor positive definite [65, 119]. In the even-parity approach, the BTE (3.16) is modified by extracting the even- and odd-parity components of the particle flux and then by solving the two components separately. The advantage of the even-parity approach is that the numerical discretization results in a symmetric positive definite linear system. The disadvantages arises for example in full angular flux determination, in reflective boundary conditions, in pure scattering regions and in vacuums [140]. The even-

and odd-parity equations are used for energy-independent situations. The energy dependence is typically handled with multi group method, which gives a group of coupled equations, which are energy independent [124, 67].

3.6.4 SAAF form of the BTE

To accomplish some of the even- and odd-parity equation disadvantages (those arising from splitting the angular flux into two components), the SAAF presentation of the BTE can be used [140]. It is a second order self-adjoint equation that has the whole angular flux as the unknown. It can be derived from the first order form of the BTE. The SAAF formulation is done to discrete ordinates form of the BTE, in which the angular domain is discretized into discrete directions [124, 67]. The SAAF formulation can be done also for the B-CSDAE.

Chapter IV

Forward problem in radiotherapy using FEM

In the forward problem of the external radiotherapy, one solves the particle flux from the coupled system of BTEs (3.14) or from the coupled system of B-CSDAEs (3.29) with the inflow boundary conditions as stated in Section 3.4. The absorbed dose distribution can be computed from the solved particle flux using equation (2.1).

The full FEM discretization of the BTE for all variables is rarely presented in the literature [173, 26, 7], maybe because of the difficulties in handling the resulted big linear system of equations. Increased computer power and parallel computing enables to use FEM discretization for all variables. In this chapter, the FEM discretization is formulated for the coupled system of BTEs and for the coupled system of B-CSDAEs to simulate the radiotherapy forward problem. In Sections 4.1 and 4.2, the FEM is explained in general and some function spaces are introduced to be used in the existence analysis. The variational forms are derived in Sections 4.3 and 4.5. The existence and uniqueness of the solutions of the coupled systems are studied in Sections 4.4 and 4.6. The FEM discretization and convergence are discussed in Section 4.7. At the end of the chapter, the FEM simulations and their discussions are presented.

4.1 Finite element method

In FEM, the domains of the phase space are partitioned into sub-regions which are called elements [2]. In 3D, typical elements are bricks, triangular prisms and tetrahedrons. In 2D, the elements are usually triangular or quadrilateral in shape. A one dimensional (1D) interval is divided into sub-intervals. Typically the boundaries of the spatial elements are located near the surfaces of different materials and one can assume the material properties to be the same within an element.

The FEM discretization is applied to a variational form (weak form) of the original equation [101]. The variational form is achieved by multiplying the original equation by a test function v and integrating over the whole phase space domain. When applying the Green's formula (4.5), the boundary conditions can be appended in the variational form. Typically, the variational form is of the form

$$B(u, v) = F(v),$$

where $B(u, v)$ is a bilinear form and u is an unknown function to be solved.

When using any numerical scheme in finding the solution, one has to ensure that the problem has a solution and it is unique [59]. For these the existence and uniqueness analysis of the variational form should be performed. One can prove that a variational problem has a unique weak solution, if the bilinear form is bounded and coercive in appropriate spaces, using for example generalized Lax-Milgram Lemma [178]. The boundedness and coercivity conditions also result in an estimate for the error of the FEM (the Cea's estimate) [101].

Finally, the finite element approximation u^{h} of an unknown function u is presented by a finite sum [101, 59]

$$u^{\mathrm{h}} = \sum_{k=1}^{N} \alpha_k \phi_k,$$

where ϕ_k is a basis function associated to the node k within elements, α_k is the unknown value and N is the number of nodes. The basis functions are usually some piecewise smooth functions such as piecewise linear, quadratic or cubic polynomials. The nodes are typically at the corners or edges of an element. Applying u^{h} to the variational form N linear equations with unknown vector $\alpha = (\alpha_1, ..., \alpha_N)^{\mathrm{T}}$ are obtained, which can be solved using iterative methods such as conjugate gradient [101, 82]. The superscript T denotes the transpose operation.

4.2 Some function spaces

Here some function spaces are presented to be used in the variational formulations and existence analysis. Let $L_2(G)$ be a Lebesgue space of real valued square integrable functions on $G = V \times I \times S$. The inner product in $L_2(G)$ is defined as

$$\langle f, g \rangle_{L_2(G)} = \int_S \int_I \int_V f(\boldsymbol{x}, E, \boldsymbol{\Omega}) g(\boldsymbol{x}, E, \boldsymbol{\Omega}) \mathrm{d}\boldsymbol{x} \mathrm{d}E \mathrm{d}\boldsymbol{\Omega}.$$

Denote $\bar{G} := \bar{V} \times I \times S$, where $\bar{V}$ is the closure of the domain V. Let $I = [E_{\min}, E_{\max}]$ and $\mathcal{C}(\bar{G})$ to be a function space of continuous functions on $\bar{G}$ and

$$\begin{aligned}
\mathcal{C}^1_V &:= \left\{ f \in \mathcal{C}(\bar{G}) \mid \frac{\partial f}{\partial x_j} \in \mathcal{C}(\bar{G}) \right\} \\
\mathcal{C}^1_{V,E} &:= \left\{ f \in \mathcal{C}(\bar{G}) \mid \frac{\partial f}{\partial x_j}, \frac{\partial f}{\partial E} \in \mathcal{C}(\bar{G}) \right\} \\
\mathcal{C}^1_{V,E,0} &:= \left\{ f \in \mathcal{C}^1_{V,E} \mid f(\cdot, E_{\max}, \cdot) = 0 \right\}.
\end{aligned}$$

Furthermore, let H_1 be the completion of $\mathcal{C}^1_V$ with respect to the inner product

$$\langle f, g \rangle_{H_1} = \langle f, g \rangle_{L_2(G)} + \int_S \int_I \int_{\partial V} |\boldsymbol{\Omega} \cdot \boldsymbol{n}| f g \mathrm{d}\boldsymbol{s} \mathrm{d}E \mathrm{d}\boldsymbol{\Omega},$$

where $\int_{\partial V}(\cdot)\mathrm{d}\boldsymbol{s}$ is a surface integral. Let H_2 be the completion of $\mathcal{C}^1_V$ with respect to the inner product

$$\langle f,g\rangle_{H_2} = \langle f,g\rangle_{L_2(G)} + \langle \boldsymbol{\Omega}\cdot\nabla f, \boldsymbol{\Omega}\cdot\nabla g\rangle_{L_2(G)}.$$

Denote $H := H_1 \cap H_2$. Now H is equipped with the inner product

$$\langle f,g\rangle_H = \langle f,g\rangle_{H_1} + \langle f,g\rangle_{H_2}$$

and of course H is a subspace of H_1.

Moreover, let $\widetilde{H}$ be the completion of $\mathcal{C}^1_{V,E,0}$ with respect to the inner product

$$\langle f,g\rangle_{\widetilde{H}} = \langle f,g\rangle_H + \langle \frac{\partial f}{\partial E}, \frac{\partial g}{\partial E}\rangle_{L_2(G)}.$$

and let $\widetilde{H}_1$ be the completion of $\mathcal{C}^1_{V,E,0}$ with respect to the inner product

$$\langle f,g\rangle_{\widetilde{H}_1} = \langle f,g\rangle_{H_1} + \langle f(\cdot,E_{\min},\cdot), g(\cdot,E_{\min},\cdot)\rangle_{L_2(V\times S)}.$$

One sees that $\widetilde{H} \subset \widetilde{H}_1$, since for $f \in \mathcal{C}^1_{V,E,0}$ one obtains

$$\begin{aligned} |f(\cdot,E_{\min},\cdot)| &= |f(\cdot,E_{\min},\cdot) - f(\cdot,E_{\max},\cdot)| \\ &= \big|-\int_I \frac{\partial f}{\partial E}\mathrm{d}E\big| \le \int_I \big|\frac{\partial f}{\partial E}\big|\mathrm{d}E \\ &\le \sqrt{E_{\max}-E_{\min}}\left(\int_I \big|\frac{\partial f}{\partial E}\big|^2\mathrm{d}E\right)^{1/2}, \end{aligned}$$

where the Cauchy-Schwartz inequality

$$|\langle f,g\rangle_{L_2(I)}| \le \|f\|_{L_2(I)}\|g\|_{L_2(I)}$$

is used. Then one finds that

$$\begin{aligned} \|f\|^2_{\widetilde{H}_1} &\le \|f\|^2_{L_2(G)} + \int_S\int_I\int_{\partial V} |\boldsymbol{\Omega}\cdot\boldsymbol{n}| f^2 \mathrm{d}\boldsymbol{s}\mathrm{d}E\mathrm{d}\boldsymbol{\Omega} + \\ &\quad \int_S\int_V |f(\cdot,E_{\min},\cdot)|^2\mathrm{d}\boldsymbol{s}\mathrm{d}E\mathrm{d}\boldsymbol{\Omega} \\ &\le \|f\|^2_{\widetilde{H}}, \end{aligned}$$

which is an adequate condition for $\widetilde{H}$ to be a subspace of $\widetilde{H}_1$.

The inner product of the product space X^3 is obtained by summing the individual inner products as

$$\langle f,g\rangle_{X^3} = \sum_{j=1}^{3}\langle f_j,g_j\rangle_X.$$

4.3 Variational form of the coupled BTEs

The variational equation is used in a finite element scheme to find the so called weak solution of the related problem. Here the variational formulation is derived for the coupled system of the BTEs (3.14) with the incoming photon (3.19) and electron (3.20) boundary conditions. In the variational formulation of the coupled BTEs (3.14), one can first assume that $\psi,\ v \in (\mathcal{C}_V^1)^3$. To simplify the notations, operators $T : H^3 \to L_2(G)^3$ and $K : L_2(G)^3 \to L_2(G)^3$ are defined as

$$T\psi = \boldsymbol{\Omega}\cdot\nabla\psi := (\boldsymbol{\Omega}\cdot\nabla\psi_1, \boldsymbol{\Omega}\cdot\nabla\psi_2, \boldsymbol{\Omega}\cdot\nabla\psi_3)$$

and

$$K\psi = (K_1\psi, K_2\psi, K_3\psi),$$

where $\psi = (\psi_1, \psi_2, \psi_3)$. T is a linear partial differential operator and K is a linear integral operator. Now the coupled system of the transport equations can be written in a form

$$(T + K)\psi = Q, \tag{4.1}$$

where $Q = (Q_1, Q_2, Q_3)$.

Multiplying equation (4.1) by a test function $v \in (\mathcal{C}_V^1)^3$ ($v = (v_1, v_2, v_3)$) componentwise and integrating over G, one obtains for $\psi \in (\mathcal{C}_V^1)^3$

$$\sum_{j=1}^{3}\langle\boldsymbol{\Omega}\cdot\nabla\psi_j, v_j\rangle_{L_2(G)} + \sum_{j=1}^{3}\langle K_j\psi, v_j\rangle_{L_2(G)} = \sum_{j=1}^{3}\langle Q_j, v_j\rangle_{L_2(G)} \tag{4.2}$$

or

$$\langle T\psi, v\rangle_{L_2(G)^3} + \langle K\psi, v\rangle_{L_2(G)^3} = \langle Q, v\rangle_{L_2(G)^3}. \tag{4.3}$$

The first inner product $\langle\boldsymbol{\Omega}\cdot\nabla\psi_j, v_j\rangle_{L_2(G)}$ in equation (4.2) can be written in the form

$$\langle\boldsymbol{\Omega}\cdot\nabla\psi_j, v_j\rangle_{L_2(G)} = \int_S\int_I\int_V \Omega_1\frac{\partial\psi_j}{\partial x_1}v_j + \Omega_2\frac{\partial\psi_j}{\partial x_2}v_j + \Omega_3\frac{\partial\psi_j}{\partial x_3}v_j \mathrm{d}\boldsymbol{x}\mathrm{d}E\mathrm{d}\boldsymbol{\Omega}, \tag{4.4}$$

where $\mathrm{d}\boldsymbol{x} = \mathrm{d}x_1\mathrm{d}x_2\mathrm{d}x_3$ and Ω_j ($j = 1, 2, 3$) are the components of $\boldsymbol{\Omega}$. The Green's formula [9]

$$\int_V \frac{\partial\psi_j}{\partial x_l}v_j\mathrm{d}\boldsymbol{x} = -\int_V \psi_j\frac{\partial v_j}{\partial x_l}\mathrm{d}\boldsymbol{x} + \int_{\partial V}\psi_j v_j n_l \mathrm{d}\boldsymbol{s} \tag{4.5}$$

is applied to all the $\int_V \frac{\partial\psi_j}{\partial x_l}v_j\mathrm{d}\boldsymbol{x}$ terms in (4.4). In equation (4.5), n_l ($l = 1, 2, 3$) is the l^{th} component of the unit normal $\boldsymbol{n} = (n_1, n_2, n_3)$ in a point $\boldsymbol{x}$ on the surface ∂V. Hence, one can write

$$\begin{aligned}\langle\boldsymbol{\Omega}\cdot\nabla\psi_j, v_j\rangle_{L_2(G)} &= -\int_S\int_I\int_V \Omega_1\psi_j\frac{\partial v_j}{\partial x_1} + \Omega_2\psi_j\frac{\partial v_j}{\partial x_2} + \Omega_3\psi_j\frac{\partial v_j}{\partial x_3}\mathrm{d}\boldsymbol{x}\mathrm{d}E\mathrm{d}\boldsymbol{\Omega}\\ &\quad + \int_S\int_I\int_{\partial V} \Omega_1\psi_j v_j n_1 + \Omega_2\psi_j v_j n_2 + \Omega_3\psi_j v_j n_3 \mathrm{d}\boldsymbol{s}\mathrm{d}E\mathrm{d}\boldsymbol{\Omega}\\ &= -\langle\psi_j, \boldsymbol{\Omega}\cdot\nabla v_j\rangle_{L_2(G)} + \int_S\int_I\int_{\partial V}\psi_j v_j(\boldsymbol{\Omega}\cdot\boldsymbol{n})\mathrm{d}\boldsymbol{s}\mathrm{d}E\mathrm{d}\boldsymbol{\Omega}.\end{aligned} \tag{4.6}$$

Using (4.6) to equation (4.2) results in

$$\sum_{j=1}^{3} -\langle \psi_j, \boldsymbol{\Omega}\cdot\nabla v_j\rangle_{L_2(G)} + \sum_{j=1}^{3}\int_S\int_I\int_{\partial V} \psi_j v_j(\boldsymbol{\Omega}\cdot\boldsymbol{n})\mathrm{d}\boldsymbol{s}\mathrm{d}E\mathrm{d}\boldsymbol{\Omega} + \sum_{j=1}^{3}\langle K_j\psi, v_j\rangle_{L_2(G)} = \sum_{j=1}^{3}\langle Q_j, v_j\rangle_{L_2(G)}. \tag{4.7}$$

By adding the boundary condition (3.19) to the coupled system, the surface integral in equation (4.7) can be written in the form

$$\begin{aligned}
\sum_{j=1}^{3}\int_{\partial V}\psi_j v_j(\boldsymbol{\Omega}\cdot\boldsymbol{n})\mathrm{d}\boldsymbol{s} &= \int_{\partial V}\psi_1 v_1\left[(\boldsymbol{\Omega}\cdot\boldsymbol{n})_+ - (\boldsymbol{\Omega}\cdot\boldsymbol{n})_-\right]\mathrm{d}\boldsymbol{s} \\
&\quad + \int_{\partial V}\psi_2 v_2\left[(\boldsymbol{\Omega}\cdot\boldsymbol{n})_+ - (\boldsymbol{\Omega}\cdot\boldsymbol{n})_-\right]\mathrm{d}\boldsymbol{s} \\
&\quad + \int_{\partial V}\psi_3 v_3\left[(\boldsymbol{\Omega}\cdot\boldsymbol{n})_+ - (\boldsymbol{\Omega}\cdot\boldsymbol{n})_-\right]\mathrm{d}\boldsymbol{s} \\
&= \int_{\partial V}\psi_1 v_1(\boldsymbol{\Omega}\cdot\boldsymbol{n})_+\mathrm{d}\boldsymbol{s} - \int_{\Gamma}\psi_0 v_1(\boldsymbol{\Omega}\cdot\boldsymbol{n})_-\mathrm{d}\boldsymbol{s} \\
&\quad + \int_{\partial V}\psi_2 v_2(\boldsymbol{\Omega}\cdot\boldsymbol{n})_+\mathrm{d}\boldsymbol{s} \\
&\quad + \int_{\partial V}\psi_3 v_3(\boldsymbol{\Omega}\cdot\boldsymbol{n})_+\mathrm{d}\boldsymbol{s} \\
&= \sum_{j=1}^{3}\int_{\partial V}\psi_j v_j(\boldsymbol{\Omega}\cdot\boldsymbol{n})_+\mathrm{d}\boldsymbol{s} - \int_{\Gamma}\psi_0 v_1(\boldsymbol{\Omega}\cdot\boldsymbol{n})_-\mathrm{d}\boldsymbol{s}.
\end{aligned}$$

The terms $(\cdot)_+$ and $(\cdot)_-$ refer to the positive and negative parts of the function. From the boundary condition (3.19) one has that $\psi_2|_{\partial V} = \psi_3|_{\partial V} = 0$, when $\boldsymbol{\Omega}\cdot\boldsymbol{n} < 0$, so the integrals $\int_{\partial V}\psi_2 v_2(\boldsymbol{\Omega}\cdot\boldsymbol{n})_-\mathrm{d}\boldsymbol{s}$ and $\int_{\partial V}\psi_3 v_3(\boldsymbol{\Omega}\cdot\boldsymbol{n})_-\mathrm{d}\boldsymbol{s}$ disappear. Also $\psi_1|_{\Gamma} = \psi_0$, when $\boldsymbol{\Omega}\cdot\boldsymbol{n} < 0$, zero otherwise, which implies that $\int_{\partial V}\psi_1 v_1(\boldsymbol{\Omega}\cdot\boldsymbol{n})_-\mathrm{d}\boldsymbol{s} = \int_{\Gamma}\psi_0 v_1(\boldsymbol{\Omega}\cdot\boldsymbol{n})_-\mathrm{d}\boldsymbol{s}$.

The variational form of the transport problem (3.14) is finally

$$B(\psi, v) = F_j(v) + q(v),\ v \in (\mathcal{C}_V^1)^3, \tag{4.8}$$

where $B(\psi, v) : (\mathcal{C}_V^1)^3 \times (\mathcal{C}_V^1)^3 \to \mathbb{R}$ is the (nonsymmetric) bilinear form

$$B(\psi, v) = \sum_{j=1}^{3} -\langle \psi_j, \boldsymbol{\Omega}\cdot\nabla v_j\rangle_{L_2(G)} + \sum_{j=1}^{3}\int_S\int_I\int_{\partial V} \psi_j v_j(\boldsymbol{\Omega}\cdot\boldsymbol{n})_+\mathrm{d}\boldsymbol{s}\mathrm{d}E\mathrm{d}\boldsymbol{\Omega} + \sum_{j=1}^{3}\langle K_j\psi, v_j\rangle_{L_2(G)}. \tag{4.9}$$

The stated photon (3.19) or electron (3.20) boundary conditions are indicated by a lower index $j = 1, 2$, respectively, and

$$F_j(v) = \int_S \int_I \int_\Gamma \psi_0 v_j (\boldsymbol{\Omega} \cdot \boldsymbol{n})_- \mathrm{d}\boldsymbol{s}\mathrm{d}E\mathrm{d}\boldsymbol{\Omega}. \tag{4.10}$$

The internal source term $q(v)$ is of the form

$$q(v) = \sum_{j=1}^{3} \langle Q_j, v_j \rangle_{L_2(G)}. \tag{4.11}$$

4.4 Existence and uniqueness analysis of the coupled BTEs

As noted in Section 4.1, the use of numerical methods requires one to ensure that the problem has a unique solution. Here the existence of the solution is proven for the variational equation (4.8) of the coupled BTEs. The presentation is based on the generalization of the Lax-Milgram lemma ([178] page 403) and have similarities in the coercivity considerations as described in [59] for the one BTE and in [170, 26] for the coupled system.

The generalized Lax-Milgram lemma states [178]:

Lemma 1 *Let X be a Hilbert space, X' a linear subspace of X, $\widetilde{B}(\cdot,\cdot)$ a bilinear functional on $X \times X'$ having the following properties:*

1. *there is $C > 0$ such that*

$$|\widetilde{B}(u,v)| \leq C\|u\|_X \|v\|_{X'}, \ u \in X, \ v \in X' \text{ (boundedness)}$$

2. *there is $c > 0$ such that*

$$|\widetilde{B}(v,v)| \geq c\|v\|_X^2, \ v \in X' \text{ (coercivity)}.$$

Let $\widetilde{F} : X \to \mathbb{R}$ be a continuous linear functional. Then there exists $\widetilde{u}$ such that

$$\widetilde{B}(\widetilde{u}, v) = \widetilde{F}(v), \text{ for every } v \in X'.$$

For the sake of generality, the differential cross sections are defined on $\mathcal{C}(\bar{V} \times I^2 \times S^2)$ although the angle dependence is often of the form $\boldsymbol{\Omega}' \cdot \boldsymbol{\Omega}$. For the coupled BTEs one can formulate the following.

Theorem 1 *Assume that*

$$\sigma_j(\boldsymbol{x}, E, \boldsymbol{\Omega}) \in \mathcal{C}(\bar{V} \times I \times S)$$
$$\sigma_{j' \to j}(\boldsymbol{x}, E', E, \boldsymbol{\Omega}', \boldsymbol{\Omega}) \in \mathcal{C}(\bar{V} \times I^2 \times S^2).$$

Assume also that there exists $\kappa > 0$ such that for $v \in (\mathcal{C}_V^1)^3$

$$\langle Kv, v \rangle_{L_2(G)^3} \geq \kappa \|v\|_{L_2(G)^3}^2 . \tag{4.12}$$

Then there exists $C > 0$ such that

$$|B(\psi, v)| \leq C\|\psi\|_{H_1^3}\|v\|_{H^3},\ \psi \in (\mathcal{C}_V^1)^3,\ v \in (\mathcal{C}_V^1)^3 \text{ (boundedness)} \tag{4.13}$$

and $c > 0$ such that

$$|B(v, v)| \geq c\|v\|_{H_1^3}^2,\ v \in (\mathcal{C}_V^1)^3 \text{ (coercivity)}. \tag{4.14}$$

Proof. For the boundedness condition (4.13) one finds that the bilinear form (4.9) fulfills for $\psi, v \in (\mathcal{C}_V^1)^3$

$$\begin{aligned}
|B(\psi,v)| &\leq \sum_{j=1}^{3}|\langle\psi_j, \boldsymbol{\Omega}\cdot\nabla v_j\rangle_{L_2(G)}| + \sum_{j=1}^{3}|\langle K_j\psi, v_j\rangle_{L_2(G)}| \\
&\quad + \sum_{j=1}^{3}\Big|\int_S\int_I\int_{\partial V}\psi_j v_j(\boldsymbol{\Omega}\cdot\boldsymbol{n})_+ \mathrm{d}\boldsymbol{s}\mathrm{d}E\mathrm{d}\boldsymbol{\Omega}\Big| \\
&\leq \sum_{j=1}^{3}\|\psi_j\|_{L_2(G)}\|\boldsymbol{\Omega}\cdot\nabla v_j\|_{L_2(G)} + \sum_{j=1}^{3}\|K_j\psi\|_{L_2(G)}\|v_j\|_{L_2(G)} \\
&\quad + \sum_{j=1}^{3}\left(\int_S\int_I\int_{\partial V}\psi_j^2|(\boldsymbol{\Omega}\cdot\boldsymbol{n})_+|\mathrm{d}\boldsymbol{s}\mathrm{d}E\mathrm{d}\boldsymbol{\Omega}\right)^{\frac{1}{2}}\left(\int_S\int_I\int_{\partial V} v_j^2|(\boldsymbol{\Omega}\cdot\boldsymbol{n})_+|\mathrm{d}\boldsymbol{s}\mathrm{d}E\mathrm{d}\boldsymbol{\Omega}\right)^{\frac{1}{2}} \\
&\leq C\|\psi\|_{H_1^3}\|v\|_{H^3},
\end{aligned}$$

where the following inequalities are used:

$$\begin{aligned}
|a+b| &\leq |a| + |b|,\ a, b \in \mathbb{R} \\
|(\boldsymbol{\Omega}\cdot\boldsymbol{n})_+| &\leq |(\boldsymbol{\Omega}\cdot\boldsymbol{n})| \\
|\langle f, g\rangle_{L_2(G)}| &\leq \|f\|_{L_2(G)}\|g\|_{L_2(G)} \quad \text{(Cauchy} - \text{Schwartz)} \\
\|K_j\psi\|_{L_2(G)} &\leq C_1(j)\|\psi_j\|_{L_2(G)} + \sum_{j'=1}^{3} C_2(j', j)\|\psi_{j'}\|_{L_2(G)},
\end{aligned} \tag{4.15}$$

where $C_1(j) = \|\sigma_j\|_{L_\infty(V\times I)}$ and

$$C_2(j', j) = 2\sqrt{4\pi\mu(I)}\sup_{(\boldsymbol{x},E,\boldsymbol{\Omega})\in G}\left(\int_S\int_I \sigma_{j'\to j}(\boldsymbol{x}, E', E, \boldsymbol{\Omega}', \boldsymbol{\Omega})\mathrm{d}E'\mathrm{d}\boldsymbol{\Omega}'\right)^{\frac{1}{2}}.$$

In the previous, $\mu(I)$ is the measure of the energy interval I and $\|f\|_{L_\infty(V\times I)} = \sup_{(\boldsymbol{x},E)\in(V\times I)}|f(\boldsymbol{x}, E)|$.

To prove the coercivity condition (4.14) the bilinear form (4.9) is written in the form

$$\begin{aligned}
B(v,v) &= \sum_{j=1}^{3} -\langle v_j, \boldsymbol{\Omega}\cdot\nabla v_j\rangle_{L_2(G)} + \sum_{j=1}^{3}\int_S\int_I\int_{\partial V} v_j^2(\boldsymbol{\Omega}\cdot\boldsymbol{n})_+\mathrm{d}\boldsymbol{s}\mathrm{d}E\mathrm{d}\boldsymbol{\Omega} \\
&\quad + \langle Kv, v\rangle_{L_2(G)^3}.
\end{aligned} \tag{4.16}$$

When applying the Green's formula (4.5), one obtains for $v_j \in \mathcal{C}_V^1$

$$\langle \boldsymbol{\Omega}\cdot\nabla v_j, v_j\rangle_{L_2(G)} = -\langle v_j, \boldsymbol{\Omega}\cdot\nabla v_j\rangle_{L_2(G)} + \int_S\int_I\int_{\partial V} v_j^2(\boldsymbol{\Omega}\cdot\boldsymbol{n})\mathrm{d}\boldsymbol{s}\mathrm{d}E\mathrm{d}\boldsymbol{\Omega}$$

and further from the previous one obtains

$$\langle v_j, \boldsymbol{\Omega}\cdot\nabla v_j\rangle_{L_2(G)} = \frac{1}{2}\int_S\int_I\int_{\partial V} v_j^2(\boldsymbol{\Omega}\cdot\boldsymbol{n})\mathrm{d}\boldsymbol{s}\mathrm{d}E\mathrm{d}\boldsymbol{\Omega}, \tag{4.17}$$

because $\langle \boldsymbol{\Omega}\cdot\nabla v_j, v_j\rangle_{L_2(G)} = \langle v_j, \boldsymbol{\Omega}\cdot\nabla v_j\rangle_{L_2(G)}$ (for real valued functions). Adding equation (4.17) to equation (4.16) and writing $(\boldsymbol{\Omega}\cdot\boldsymbol{n}) = ((\boldsymbol{\Omega}\cdot\boldsymbol{n})_+ - (\boldsymbol{\Omega}\cdot\boldsymbol{n})_-)$ one obtains

$$\begin{aligned} B(v,v) &= -\frac{1}{2}\sum_{j=1}^{3}\int_S\int_I\int_{\partial V} v_j^2((\boldsymbol{\Omega}\cdot\boldsymbol{n})_+ - (\boldsymbol{\Omega}\cdot\boldsymbol{n})_-)\mathrm{d}\boldsymbol{s}\mathrm{d}E\mathrm{d}\boldsymbol{\Omega} \\ &\quad + \sum_{j=1}^{3}\int_S\int_I\int_{\partial V} v_j^2(\boldsymbol{\Omega}\cdot\boldsymbol{n})_+\mathrm{d}\boldsymbol{s}\mathrm{d}E\mathrm{d}\boldsymbol{\Omega} + \langle Kv, v\rangle_{L_2(G)^3} \\ &= \frac{1}{2}\sum_{j=1}^{3}\int_S\int_I\int_{\partial V} v_j^2|(\boldsymbol{\Omega}\cdot\boldsymbol{n})|\mathrm{d}\boldsymbol{s}\mathrm{d}E\mathrm{d}\boldsymbol{\Omega} + \langle Kv, v\rangle_{L_2(G)^3}, \end{aligned}$$

since $|(\boldsymbol{\Omega}\cdot\boldsymbol{n})| = ((\boldsymbol{\Omega}\cdot\boldsymbol{n})_+ + (\boldsymbol{\Omega}\cdot\boldsymbol{n})_-)$. Thus,

$$|B(v,v)| \geq \frac{1}{2}\sum_{j=1}^{3}\int_S\int_I\int_{\partial V} v_j^2|(\boldsymbol{\Omega}\cdot\boldsymbol{n})|\mathrm{d}\boldsymbol{s}\mathrm{d}E\mathrm{d}\boldsymbol{\Omega} + \kappa\|v\|^2_{L_2(G)^3}$$

and there exists $c \geq 0$ such that coercivity condition (4.14) holds, because of the assumption (4.12). □

By the continuity (4.13) the bilinear form $B(\cdot,\cdot)$ can be uniquely extended on $H_1^3 \times H^3$ and the estimates (4.13) and (4.14) are valid for the extension, which is still denoted by $B(\cdot,\cdot)$. Combining Lemma 1 and Theorem 1 with the extension analysis one can show the following.

Corollary 1 *Assume that*

$$\begin{aligned} &\sigma_j(\boldsymbol{x}, E, \boldsymbol{\Omega}) \in \mathcal{C}(\bar{V}\times I\times S) \\ &\sigma_{j'\to j}(\boldsymbol{x}, E', E, \boldsymbol{\Omega}', \boldsymbol{\Omega}) \in \mathcal{C}(\bar{V}\times I^2\times S^2) \\ &Q_j \in L_2(G),\ \psi_0 \in L_2(\partial V\times I\times S). \end{aligned}$$

Assume also that there exists $\kappa > 0$ such that for $v \in H^3$ inequality (4.12) holds. Then the variational equation (4.8) has one and only one solution $\psi \in H^3$.

Proof. The details of the uniqueness considerations are omitted. The existence of the solution follows straightforwardly from Lemma 1 and Theorem 1. The completion analysis are omitted.□

Because of the coercivity assumption (4.12), additional conditions are required on the cross sections. For one particle system it is known that a sufficient condition for the coercivity is that there exists $\alpha > 0$ such that for $(\boldsymbol{x}, E, \boldsymbol{\Omega}) \in G$

$$\sigma_j(\boldsymbol{x}, E, \boldsymbol{\Omega}) - \int_S \int_I \sigma_{j\to j}(\boldsymbol{x}, E, E', \boldsymbol{\Omega}, \boldsymbol{\Omega}')\mathrm{d}E'\mathrm{d}\boldsymbol{\Omega}' \geq \alpha$$

and

$$\sigma_j(\boldsymbol{x}, E, \boldsymbol{\Omega}) - \int_S \int_I \sigma_{j\to j}(\boldsymbol{x}, E', E, \boldsymbol{\Omega}', \boldsymbol{\Omega})\mathrm{d}E'\mathrm{d}\boldsymbol{\Omega}' \geq \alpha.$$

Here the interactions are only for one particle (from j to j, $(j = 1, 2, 3)$). Theorem 2 is formulated earlier for the coupled system in [26] and here the formulation is repeated. Note that all differential cross sections are included to simplify the notations. In real situations $\sigma_{2\to 3} = 0$.

Theorem 2 *Assume that*

$$\sigma_j(\boldsymbol{x}, E) \in \mathcal{C}(\bar{V} \times I)$$
$$\sigma_{j'\to j}(\boldsymbol{x}, E, E', \boldsymbol{\Omega}, \boldsymbol{\Omega}') \in \mathcal{C}(\bar{V} \times I^2 \times S^2).$$

Suppose that there exists $\alpha > 0$ for all $j = 1, 2, 3$ such that for $(\boldsymbol{x}, E, \boldsymbol{\Omega}) \in G$

$$\sigma_j(\boldsymbol{x}, E) - \int_S \int_I \sum_{j'=1}^{3} \sigma_{j\to j'}(\boldsymbol{x}, E, E', \boldsymbol{\Omega}, \boldsymbol{\Omega}')\mathrm{d}E'\mathrm{d}\boldsymbol{\Omega}' \geq \alpha \tag{4.18}$$

and

$$\sigma_j(\boldsymbol{x}, E) - \int_S \int_I \sum_{j'=1}^{3} \sigma_{j'\to j}(\boldsymbol{x}, E', E, \boldsymbol{\Omega}', \boldsymbol{\Omega})\mathrm{d}E'\mathrm{d}\boldsymbol{\Omega}' \geq \alpha \tag{4.19}$$

Then there exists κ such that inequality (4.12) holds.

Proof. The same idea is used here for the coupled system of BTEs as presented

in [59] for one particle system. By direct calculation one can write

$$\begin{aligned}
\langle Kv, v\rangle_{L_2(G)^3} &= \sum_{j=1}^{3}\langle K_j v, v_j\rangle_{L_2(G)} \\
&= \sum_{j=1}^{3}\int_V\int_S\int_I\Bigg[-\int_S\int_I\Big[\sigma_{1\to j}(\boldsymbol{x},E',E,\boldsymbol{\Omega}',\boldsymbol{\Omega})v_1(\boldsymbol{x},E',\boldsymbol{\Omega}')v_j(\boldsymbol{x},E,\boldsymbol{\Omega}) \\
&\qquad + \sigma_{2\to j}(\boldsymbol{x},E',E,\boldsymbol{\Omega}',\boldsymbol{\Omega})v_2(\boldsymbol{x},E',\boldsymbol{\Omega}')v_j(\boldsymbol{x},E,\boldsymbol{\Omega}) \\
&\qquad + \sigma_{3\to j}(\boldsymbol{x},E',E,\boldsymbol{\Omega}',\boldsymbol{\Omega})v_3(\boldsymbol{x},E',\boldsymbol{\Omega}')v_j(\boldsymbol{x},E,\boldsymbol{\Omega})\Big]\mathrm{d}E'\mathrm{d}\boldsymbol{\Omega}' \\
&\qquad + \sigma_j(\boldsymbol{x},E)v_j^2(\boldsymbol{x},E,\boldsymbol{\Omega})\Bigg]\mathrm{d}E\mathrm{d}\boldsymbol{\Omega}\mathrm{d}\boldsymbol{x} \\
&= \sum_{j=1}^{3}\int_V\Bigg[-\int_{SI}\int_{SI'}\sigma_{1\to j}v_1'v_j - \int_{SI}\int_{SI'}\sigma_{2\to j}v_2'v_j - \int_{SI}\int_{SI'}\sigma_{3\to j}v_3'v_j \\
&\qquad + \int_{SI}\sigma_j v_j^2\Bigg]\mathrm{d}\boldsymbol{x}. \qquad (4.20)
\end{aligned}$$

In equation (4.20), the following simplified notations are used: $v_j := v_j(\boldsymbol{x},E,\boldsymbol{\Omega})$, $v_j' := v_j(\boldsymbol{x},E',\boldsymbol{\Omega}')$, $\sigma_{k\to j} := \sigma_{k\to j}(\boldsymbol{x},E',E,\boldsymbol{\Omega}',\boldsymbol{\Omega})$, $\sigma_j := \sigma_j(\boldsymbol{x},E)$ $(j,k=1,2,3)$, and $\int_{SI} := \int_S\int_I \mathrm{d}E\mathrm{d}\boldsymbol{\Omega}$ and $\int_{SI'} := \int_S\int_I \mathrm{d}E'\mathrm{d}\boldsymbol{\Omega}'$. The double integrals $\int_{SI}\int_{SI'}$ can be approximated by applying the Cauchy-Schwartz inequality (4.15), which results in $\int_{SI}\int_{SI'}fg \le \|f\|_{L_2(S^2\times I^2)}\|g\|_{L_2(S^2\times I^2)}$. Hence, one obtains

$$\begin{aligned}
\int_{SI}\int_{SI'}\sigma_{k\to j}v_k'v_j &\le \left(\int_{SI}\int_{SI'}\sigma_{k\to j}v_k'^2\right)^{\frac{1}{2}}\left(\int_{SI}\int_{SI'}\sigma_{k\to j}v_j^2\right)^{\frac{1}{2}} \\
&= \left(\int_{SI}\int_{SI'}\sigma_{k\to j}'v_k^2\right)^{\frac{1}{2}}\left(\int_{SI}\int_{SI'}\sigma_{k\to j}v_j^2\right)^{\frac{1}{2}}, \qquad (4.21)
\end{aligned}$$

where in the first product term in equation (4.21), the notations $(E',\boldsymbol{\Omega}')$ are changed to $(E,\boldsymbol{\Omega})$ and vise versa. The notation $\sigma_{k\to j}' := \sigma_{k\to j}(\boldsymbol{x},E,E',\boldsymbol{\Omega},\boldsymbol{\Omega}')$ is also made. Therefore, by taking into account the minus sign, one can write

$$\begin{aligned}
\langle Kv, v\rangle_{L_2(G)^3} &\ge \sum_{j=1}^{3}\int_V\Bigg[-\left(\int_{SI}\int_{SI'}\sigma_{1\to j}'v_1^2\right)^{\frac{1}{2}}\left(\int_{SI}\int_{SI'}\sigma_{1\to j}v_j^2\right)^{\frac{1}{2}} \\
&\qquad -\left(\int_{SI}\int_{SI'}\sigma_{2\to j}'v_2^2\right)^{\frac{1}{2}}\left(\int_{SI}\int_{SI'}\sigma_{2\to j}v_j^2\right)^{\frac{1}{2}} \\
&\qquad -\left(\int_{SI}\int_{SI'}\sigma_{3\to j}'v_3^2\right)^{\frac{1}{2}}\left(\int_{SI}\int_{SI'}\sigma_{3\to j}v_j^2\right)^{\frac{1}{2}} \\
&\qquad + \int_{SI}\sigma_j v_j^2\Bigg]\mathrm{d}\boldsymbol{x}. \qquad (4.22)
\end{aligned}$$

By summing the conditions (4.18) and (4.19), one obtains a condition ($j = 1, 2, 3$)

$$\sigma_j \geq \alpha + \frac{1}{2} \int_{SI'} \left(\sigma_{j\to 1} + \sigma_{j\to 2} + \sigma_{j\to 3} + \sigma'_{1\to j} + \sigma'_{2\to j} + \sigma'_{3\to j} \right). \tag{4.23}$$

By adding condition (4.23) to the equation (4.22), writing all sum-terms, reorganizing the terms and using the notation $\int := \int_{SI} \int_{SI'}$, one achieves

$$\begin{aligned}
\langle Kv, v\rangle_{L_2(G)^3} \geq \int_V \Big[& - \left(\int \sigma'_{1\to 1} v_1^2 \right)^{\frac{1}{2}} \left(\int \sigma_{1\to 1} v_1^2 \right)^{\frac{1}{2}} + \frac{1}{2} \left(\int \sigma'_{1\to 1} v_1^2 + \int \sigma_{1\to 1} v_1^2 \right) \\
& - \left(\int \sigma'_{2\to 2} v_2^2 \right)^{\frac{1}{2}} \left(\int \sigma_{2\to 2} v_2^2 \right)^{\frac{1}{2}} + \frac{1}{2} \left(\int \sigma'_{2\to 2} v_2^2 + \int \sigma_{2\to 2} v_2^2 \right) \\
& - \left(\int \sigma'_{3\to 3} v_3^2 \right)^{\frac{1}{2}} \left(\int \sigma_{3\to 3} v_3^2 \right)^{\frac{1}{2}} + \frac{1}{2} \left(\int \sigma'_{3\to 3} v_3^2 + \int \sigma_{3\to 3} v_3^2 \right) \\
& - \left(\int \sigma'_{2\to 1} v_2^2 \right)^{\frac{1}{2}} \left(\int \sigma_{2\to 1} v_1^2 \right)^{\frac{1}{2}} + \frac{1}{2} \left(\int \sigma'_{2\to 1} v_2^2 + \int \sigma_{2\to 1} v_1^2 \right) \\
& - \left(\int \sigma'_{1\to 2} v_1^2 \right)^{\frac{1}{2}} \left(\int \sigma_{1\to 2} v_2^2 \right)^{\frac{1}{2}} + \frac{1}{2} \left(\int \sigma'_{1\to 2} v_1^2 + \int \sigma_{1\to 2} v_2^2 \right) \\
& - \left(\int \sigma'_{3\to 1} v_3^2 \right)^{\frac{1}{2}} \left(\int \sigma_{3\to 1} v_1^2 \right)^{\frac{1}{2}} + \frac{1}{2} \left(\int \sigma'_{3\to 1} v_3^2 + \int \sigma_{3\to 1} v_1^2 \right) \\
& - \left(\int \sigma'_{1\to 3} v_1^2 \right)^{\frac{1}{2}} \left(\int \sigma_{1\to 3} v_3^2 \right)^{\frac{1}{2}} + \frac{1}{2} \left(\int \sigma'_{1\to 3} v_1^2 + \int \sigma_{1\to 3} v_3^2 \right) \\
& - \left(\int \sigma'_{3\to 2} v_3^2 \right)^{\frac{1}{2}} \left(\int \sigma_{3\to 2} v_2^2 \right)^{\frac{1}{2}} + \frac{1}{2} \left(\int \sigma'_{3\to 2} v_3^2 + \int \sigma_{3\to 2} v_2^2 \right) \\
& - \left(\int \sigma'_{2\to 3} v_2^2 \right)^{\frac{1}{2}} \left(\int \sigma_{2\to 3} v_3^2 \right)^{\frac{1}{2}} + \frac{1}{2} \left(\int \sigma'_{2\to 3} v_2^2 + \int \sigma_{2\to 3} v_3^2 \right) \\
& + \alpha \left(\int_{SI} v_1^2 + \int_{SI} v_2^2 + \int_{SI} v_3^2 \right) \Big] \mathrm{d}\boldsymbol{x}.
\end{aligned} \tag{4.24}$$

In the previous equation (4.24), the terms are organized such that each row (except the last row) consists of $-(a)^{\frac{1}{2}}(b)^{\frac{1}{2}} + \frac{1}{2}(a+b) = -\sqrt{ab} + \frac{1}{2}(a+b)$, where a and b are the integrals presented in (4.24). It can easily be shown that $-\sqrt{ab} + \frac{1}{2}(a+b) \geq 0$ for all $a, b \geq 0$. Therefore equation (4.24) comes

$$\langle Kv, v\rangle_{L_2(G)^3} \geq \alpha \int_V \left(\int_{SI} v_1^2 + \int_{SI} v_2^2 + \int_{SI} v_3^2 \right) \mathrm{d}\boldsymbol{x} = \alpha \|v\|^2_{L_2(G)^3}.$$

□

A physical background can be easily found for the condition (4.18), where the integrations over the energy and angular domains basically describe the total absorption and scattering cross sections. The condition (4.18) states that the sum of these cross sections cannot be larger than the total cross section itself. However, by the definition of the total cross section, which is the sum of the absorption and scattering cross section, $\alpha = 0$ in the condition (4.18). This indicates that the system is coercive only weakly and better convergence rate in finding the solution would be obtained if some small value is added to total cross sections σ_j. The physical meaning of the second condition (4.19) is not so clear. It states that those integrated 'inverse' cross sections, which change particles from j' to j cannot be larger than the total cross section of the particle j. Although it is

not so clear, it seems that this second condition also has physical foundations by the assumption that no more particles cannot be created than is disappeared in different interactions. It seems that the condition (4.19) is also near zero.

4.5 Variational form of the coupled B-CSDAEs

In this section, the variational formulation is derived for the coupled system of the B-CSDAEs (3.29) with the boundary conditions (3.19) and (3.20). The variational form of the coupled B-CSDAEs (3.29) has the same form as equation (4.8), but the scattering terms $K_j\psi$ $(j = 1, 2, 3)$ are defined by equations (3.30)-(3.32). Thus, the variational equation of the coupled B-CSDAEs is

$$B^{\mathrm{r}}(\psi, v) = F_j(v) + q(v), \tag{4.25}$$

where F_j is defined by equation (4.10) and $q(v)$ by equation (4.11). The lower index $j = 1, 2$ indicates photon (3.19) or electron (3.20) boundary conditions, respectively. $B^{\mathrm{r}}(\psi, v) : (\mathcal{C}^1_{V,E,0})^3 \times (\mathcal{C}^1_{V,E,0})^3 \to \mathbb{R}$ is the bilinear form

$$\begin{aligned} B^{\mathrm{r}}(\psi, v) &= -\langle \psi, \boldsymbol{\Omega}\cdot\nabla v\rangle_{L_2(G)^3} + \sum_{j=1}^{3}\int_S\int_I\int_{\partial V} \psi_j v_j (\boldsymbol{\Omega}\cdot\boldsymbol{n})_+ \mathrm{d}\boldsymbol{s}\mathrm{d}E\mathrm{d}\boldsymbol{\Omega} \\ &\quad + \langle K^{\mathrm{r}}\psi, v\rangle_{L_2(G)^3}, \end{aligned} \tag{4.26}$$

where $K^{\mathrm{r}}\psi = (K_1\psi, K_2^{\mathrm{r}}\psi, K_3^{\mathrm{r}}\psi)$ is defined by equations (3.30)-(3.32).

4.6 On the existence of the coupled B-CSDAEs

Here the existence of the solution of the coupled system of the B-CSDAEs is studied. The bilinear form (4.26) of the coupled B-CSDAEs can be extended on $\widetilde{H}^3_1 \times \widetilde{H}^3$ and Lemma 1 can be used to prove the existence of the solution. For simplicity the same notations of the functions ψ and v are used in complete spaces $\widetilde{H}^3_1$ and $\widetilde{H}^3$ as in $(\mathcal{C}^1_{V,E,0})^3$. Also the function notations are equal with the functions used for the coupled system of BTEs in the previous Sections 4.3 and 4.4. For the variational form (4.25) of the coupled B-CSDAEs one is able to formulate the following.

Theorem 3 *Assume that*

$$\begin{aligned} &\sigma_1(\boldsymbol{x}, E),\ \sigma_2^{\mathrm{r}}(\boldsymbol{x}, E),\ \sigma_3^{\mathrm{r}}(\boldsymbol{x}, E) \in \mathcal{C}(\bar{V}\times I) \\ &\sigma^{\mathrm{r}}_{j\to j}(\boldsymbol{x}, E', E, \boldsymbol{\Omega}', \boldsymbol{\Omega}),\ \sigma_{j'\to j}(\boldsymbol{x}, E', E, \boldsymbol{\Omega}', \boldsymbol{\Omega}) \in \mathcal{C}(\bar{V}\times I^2\times S^2)\ (j'\neq j) \\ &\frac{\partial\tau_2^{\mathrm{r}}}{\partial E}(\boldsymbol{x}, E),\ \frac{\partial\tau_3^{\mathrm{r}}}{\partial E}(\boldsymbol{x}, E) \in \mathcal{C}(\bar{V}\times I) \\ &\tau_2^{\mathrm{r}}(\boldsymbol{x}, E) \geq 0,\ \tau_3^{\mathrm{r}}(\boldsymbol{x}, E) \geq 0. \end{aligned}$$

Suppose that there exists $\kappa > 0$ such that for $v \in (\mathcal{C}^1_{V,E,0})^3$

$$\langle K^{\mathrm{r}} v, v\rangle_{L_2(G)^3} \geq \kappa \left\|v\right\|^2_{L_2(G)^3}, \tag{4.27}$$

where $K^{\mathrm{r}}v = (K_1 v, K_2^{\mathrm{r}} v, K_3^{\mathrm{r}} v)$ *is defined by equations (3.30)-(3.32) with* $\sigma_j = \sigma_j^{\mathrm{r}}$ *and* $\sigma_{j\to j} = \sigma_{j\to j}^{\mathrm{r}}$ $(j = 2, 3)$. *Also suppose that there exists* $\widetilde{c} > 0$ *such that for* $\psi_j \in \mathcal{C}^1_{V,E,0}$ $(j = 2, 3)$

$$-\langle \frac{\partial(\tau_j^{\mathrm{r}} \psi_j)}{\partial E}, \psi_j \rangle_{L_2(G)} \geq \widetilde{c} \|\psi_j(\boldsymbol{x}, E_{\min}, \boldsymbol{\Omega})\|^2_{L_2(V\times S)}. \tag{4.28}$$

Then there exists $C > 0$ *such that*

$$|B^{\mathrm{r}}(\psi, v)| \leq C\|\psi\|_{\widetilde{H}^3_1} \|v\|_{\widetilde{H}^3},\ \psi \in (\mathcal{C}^1_{V,E,0})^3,\ v \in (\mathcal{C}^1_{V,E,0})^3 \text{ (boundedness)} \tag{4.29}$$

and $c > 0$ *such that*

$$|B^{\mathrm{r}}(v, v)| \geq c\|v\|^2_{\widetilde{H}^3_1},\ v \in (\mathcal{C}^1_{V,E,0})^3 \text{ (coercivity)}. \tag{4.30}$$

Proof. The proof is similar to the proof of Theorem 1. Let $\psi,\ v \in (\mathcal{C}^1_{V,E,0})^3$. To prove the boundedness condition (4.29) $B^{\mathrm{r}}(\psi, v)$ can be written in the form

$$\begin{aligned}
B^{\mathrm{r}}(\psi, v) &= B(\psi, v) - \sum_{j=2}^{3} \langle \frac{\partial(\tau_j^{\mathrm{r}} \psi_j)}{\partial E}, v_j \rangle_{L_2(G)} && (4.31)\\
&= B(\psi, v) + \sum_{j=2}^{3} \int_S \int_I \int_V \tau_j^{\mathrm{r}} \psi_j \frac{\partial v_j}{\partial E} \mathrm{d}\boldsymbol{x}\mathrm{d}E\mathrm{d}\boldsymbol{\Omega}\\
&+ \sum_{j=2}^{3} \int_S \int_V \Big|_{E_{\min}}^{E_{\max}} - \tau_j^{\mathrm{r}} \psi_j v_j \mathrm{d}\boldsymbol{x}\mathrm{d}\boldsymbol{\Omega} && (4.32)\\
&= B(\psi, v) + \sum_{j=2}^{3} \int_S \int_I \int_V \tau_j^{\mathrm{r}} \psi_j \frac{\partial v_j}{\partial E} \mathrm{d}\boldsymbol{x}\mathrm{d}E\mathrm{d}\boldsymbol{\Omega}\\
&+ \sum_{j=2}^{3} \int_S \int_V \tau_j^{\mathrm{r}}(\boldsymbol{x}, E_{\min}) \psi_j(\boldsymbol{x}, E_{\min}, \boldsymbol{\Omega}) v_j(\boldsymbol{x}, E_{\min}, \boldsymbol{\Omega}) \mathrm{d}\boldsymbol{x}\mathrm{d}\boldsymbol{\Omega}, && (4.33)
\end{aligned}$$

where $B(\psi, v)$ is the bilinear form (4.9) of the Boltzmann equation with $\sigma_j = \sigma_j^{\mathrm{r}}$ and $\sigma_{j\to j} = \sigma_{j\to j}^{\mathrm{r}}$, $(j = 2, 3)$. The equation (4.32) is achieved by applying integration by parts to the latter term of the equation (4.31). The substitution of the limits with the assumptions that $\psi_2(\boldsymbol{x}, E_{\max}, \boldsymbol{\Omega}) = 0$ and $\psi_3(\boldsymbol{x}, E_{\max}, \boldsymbol{\Omega}) = 0$ produces the equation (4.33). Now one can use the condition (4.13) and Cauchy-

Schwartz inequality (4.15) and receive for $\psi, v \in (\mathcal{C}^1_{V,E,0})^3$

$$\begin{aligned}
|B^{\mathrm{r}}(\psi,v)| &\leq |B(\psi,v)| + \sum_{j=2}^{3}\left|\int_S\int_I\int_V \tau_j^{\mathrm{r}}\psi_j\frac{\partial v_j}{\partial E}\mathrm{d}\boldsymbol{x}\mathrm{d}E\mathrm{d}\boldsymbol{\Omega}\right| \\
&+ \left|\int_S\int_V \tau_j^{\mathrm{r}}(\boldsymbol{x},E_{\min})\psi_j(\boldsymbol{x},E_{\min},\boldsymbol{\Omega})v_j(\boldsymbol{x},E_{\min},\boldsymbol{\Omega})\mathrm{d}\boldsymbol{x}\mathrm{d}\boldsymbol{\Omega}\right| \\
&\leq C\|\psi\|_{H_1^3}\|v\|_{H^3} + \sum_{j=2}^{3}\widetilde{C}_1(j)\|\psi_j\|_{L_2(G)}\|\frac{\partial v_j}{\partial E}\|_{L_2(G)} \\
&+ \sum_{j=2}^{3}\widetilde{C}_1(j)\|\psi_j(\cdot,E_{\min},\cdot)\|_{L_2(V\times S)}\|v_j(\cdot,E_{\min},\cdot)\|_{L_2(V\times S)} \\
&\leq \widetilde{C}\|\psi\|_{\widetilde{H}_1^3}\|v\|_{\widetilde{H}^3},
\end{aligned}$$

where $\widetilde{C}_1(j) = \|\tau_j^{\mathrm{r}}\|_{L_\infty(V\times I)}$.

Similarly, in the proof of the coercivity condition (4.14) of the coupled BTEs, one obtains for the bilinear form (4.26) of the coupled B-CSDAEs

$$B^{\mathrm{r}}(v,v) = \frac{1}{2}\sum_{j=1}^{3}\int_S\int_I\int_{\partial V} v_j^2|(\boldsymbol{\Omega}\cdot\boldsymbol{n})|\mathrm{d}\boldsymbol{s}\mathrm{d}E\mathrm{d}\boldsymbol{\Omega} + \langle K^{\mathrm{r}}v, v\rangle_{L_2(G)^3}, \tag{4.34}$$

where $K^{\mathrm{r}}v = (K_1v, K_2^{\mathrm{r}}v, K_3^{\mathrm{r}}v)$ is defined by equations (3.30)-(3.32), which differ from the original BTE scattering terms only in the additional restricted stopping power terms τ_j^{r} with the notations $\sigma_j = \sigma_j^{\mathrm{r}}$ and $\sigma_{j\to j} = \sigma_{j\to j}^{\mathrm{r}}$. Hence, one obtains for K^{r}

$$\langle K^{\mathrm{r}}v, v\rangle_{L_2(G)^3} = \langle Kv, v\rangle_{L_2(G)^3} - \sum_{j=2}^{3}\langle\frac{\partial(\tau_j^{\mathrm{r}}v_j)}{\partial E}, v_j\rangle_{L_2(G)^3}, \tag{4.35}$$

where $Kv = (K_1v, K_2v, K_3v)$ is defined by equation (3.15) with $\sigma_j = \sigma_j^{\mathrm{r}}$, $\sigma_{j\to j} = \sigma_{j\to j}^{\mathrm{r}}$ and $\sigma_{2\to 3} = 0$. When applying the conditions (4.27) and (4.28) to equation (4.35), one obtains

$$\langle K^{\mathrm{r}}v, v\rangle_{L_2(G)^3} \geq \kappa\,\|v\|^2_{L_2(G)^3} + \widetilde{c}\|v_j(\cdot,E_{\min},\cdot)\|^2_{L_2(V\times S)}. \tag{4.36}$$

Using equation (4.36) in equation (4.34) one obtains

$$\begin{aligned}
|B^{\mathrm{r}}(v,v)| &\geq \frac{1}{2}\sum_{j=1}^{3}\int_S\int_I\int_{\partial V} v_j^2|(\boldsymbol{\Omega}\cdot\boldsymbol{n})|\mathrm{d}\boldsymbol{s}\mathrm{d}E\mathrm{d}\boldsymbol{\Omega} \\
&\quad +\kappa\,\|v\|^2_{L_2(G)^3} + \widetilde{c}\|v_j(\cdot,E_{\min},\cdot)\|^2_{L_2(V\times S)} \\
&\geq c\|v\|^2_{\widetilde{H}_1^3},
\end{aligned}$$

where $c > 0$. □

Similarly as in Section 4.4, the bilinear form $B^{\mathrm{r}}(\cdot,\cdot)$ (defined by equation (4.26)) can be uniquely extended on $\widetilde{H}_1^3 \times \widetilde{H}^3$ by the continuity (4.29) and the estimates (4.29) and (4.30) are valid for the extension, which is still denoted by $B^{\mathrm{r}}(\cdot,\cdot)$.

From Theorem 2, one obtains that the condition (4.27) holds, if the conditions (4.18)-(4.19) are valid with $\sigma_j = \sigma_j^{\mathrm{r}}$, $\sigma_{j\to j} = \sigma_{j\to j}^{\mathrm{r}}$, $(j = 2,3)$ and $\sigma_{2\to 3} = 0$. Also for the restricted cross sections, the conditions (4.18)-(4.19) have physical foundations, because the restricted scattering cross section σ_s^{r} is achieved by integrating the restricted differential cross section $\sigma_{j'\to j}$, in which the particle j' is scattered to different type of particle j. The restricted absorption cross section σ_a^{r} is achieved by integrating the restricted differential cross section $\sigma_{j\to j}^{\mathrm{r}}$, in which the energy and angle of particle j is changed. In fact, this results $\alpha = 0$, but small constant can be added to the restricted total cross sections such that the conditions (4.18)-(4.19) are fulfilled.

If one makes some assumptions for the shapes of the restricted stopping powers τ_j^{r} $(j = 2,3)$, then it is possible to formulate the following theorem for the coupled B-CSDAEs. Here also a consideration of the condition (4.27) is included.

Theorem 4 *Assume that*

$$\begin{aligned}
&\sigma_1(\boldsymbol{x},E),\ \sigma_2^{\mathrm{r}}(\boldsymbol{x},E),\ \sigma_3^{\mathrm{r}}(\boldsymbol{x},E) \in \mathcal{C}(\bar{V}\times I)\\
&\sigma_{j\to j}^{\mathrm{r}}(\boldsymbol{x},E',E,\boldsymbol{\Omega}',\boldsymbol{\Omega}),\ \sigma_{j'\to j}(\boldsymbol{x},E',E,\boldsymbol{\Omega}',\boldsymbol{\Omega}) \in \mathcal{C}(\bar{V}\times I^2\times S^2)\ (j'\neq j)\\
&\frac{\partial\tau_2^{\mathrm{r}}}{\partial E}(\boldsymbol{x},E),\ \frac{\partial\tau_3^{\mathrm{r}}}{\partial E}(\boldsymbol{x},E) \in \mathcal{C}(\bar{V}\times I)\\
&\tau_2^{\mathrm{r}}(\boldsymbol{x},E) \geq 0,\ \tau_3^{\mathrm{r}}(\boldsymbol{x},E) \geq 0.
\end{aligned}$$

Suppose that there exists $\alpha > 0$ such that the conditions (4.18-4.19) are valid with $\sigma_j = \sigma_j^{\mathrm{r}}$, $\sigma_{j\to j} = \sigma_{j\to j}^{\mathrm{r}}$, $(j = 2,3)$ and $\sigma_{2\to 3} = 0$. Then there exists κ such that the inequality (4.27) holds.

Further, assume that $I = [E_{\min}, E_{\max}]$ and that for the restricted stopping powers τ_j^{r}

$$\frac{\partial\tau_j^{\mathrm{r}}}{\partial E}(\boldsymbol{x},E) \leq 0,\ E\in I,\ \boldsymbol{x}\in V \tag{4.37}$$

holds. Then there exists $\widetilde{c} > 0$ such that the inequality (4.28) holds.

Proof. The condition (4.27) has already been proven to hold in the proof of Theorem 2, if the conditions (4.18)-(4.19) are valid. Now only some of the cross sections have been changed to the restricted cross sections, which does not change the proofing procedure.

To prove the condition (4.28) denote $P := -\langle\frac{\partial(\tau_j^{\mathrm{r}}v_j)}{\partial E}, v_j\rangle_{L_2(G)}$, where $v_j \in \mathcal{C}^1_{V,E,0}$. It can be shown that $P \geq \widetilde{c}\|v_j(\boldsymbol{x},E_{\min},\boldsymbol{\Omega})\|^2_{L_2(V\times S)}$, if the assumption (4.37) is fulfilled. Now P can be cast into the form

$$P = \int_S\int_V\left(\int_I -\tau_j^{\mathrm{r}}v_j\frac{\partial v_j}{\partial E}\mathrm{d}E + \int_I -\frac{\partial\tau_j^{\mathrm{r}}}{\partial E}v_j^2\mathrm{d}E\right)\mathrm{d}\boldsymbol{x}\mathrm{d}\boldsymbol{\Omega}, \tag{4.38}$$

where the differentiation by parts is employed. The first energy integral in equation (4.38) $\int_I -\tau_j^{\mathrm{r}} v_j \frac{\partial v_j}{\partial E} \mathrm{d}E$ can be performed using the generalized Mean Value Theorem, if τ_j^{r} is monotonic in the integration interval. The second energy integral in equation (4.38) can be approximated as $\int_I -\frac{\partial \tau_j^{\mathrm{r}}}{\partial E} v_j^2 \mathrm{d}E \geq 0$, because the integrand $-\frac{\partial \tau_j^{\mathrm{r}}}{\partial E} v_j^2 \geq 0$, when the condition (4.37) holds. Hence, from equation (4.38) one receives ($\xi \in I$)

$$
\begin{aligned}
P &\geq \int_S \int_V -\frac{1}{2}\tau_j^{\mathrm{r}}(\boldsymbol{x},\xi) v_j^2 \Big|_{E_{\min}}^{E_{\max}} \mathrm{d}\boldsymbol{x}\mathrm{d}\boldsymbol{\Omega} \\
&= \int_S \int_V -\frac{1}{2}\tau_j^{\mathrm{r}}(\boldsymbol{x},\xi) \left(v_j^2(\boldsymbol{x}, E_{\max}, \boldsymbol{\Omega}) - v_j^2(\boldsymbol{x}, E_{\min}, \boldsymbol{\Omega}) \right) \mathrm{d}\boldsymbol{x}\mathrm{d}\boldsymbol{\Omega} \\
&= \int_S \int_V \frac{1}{2}\tau_j^{\mathrm{r}}(\boldsymbol{x},\xi) v_j^2(\boldsymbol{x}, E_{\min}, \boldsymbol{\Omega}) \mathrm{d}\boldsymbol{x}\mathrm{d}\boldsymbol{\Omega} \\
&\geq \int_S \int_V \frac{1}{2}\tau_j^{\mathrm{r}}(\boldsymbol{x}, E_{\max}) v_j^2(\boldsymbol{x}, E_{\min}, \boldsymbol{\Omega}) \mathrm{d}\boldsymbol{x}\mathrm{d}\boldsymbol{\Omega} \\
&\geq \widetilde{c}_2 \| v_j(\boldsymbol{x}, E_{\min}, \boldsymbol{\Omega}) \|^2_{L_2(V\times S)},
\end{aligned}
$$

where $\widetilde{c}_2 = \inf_{\boldsymbol{x}\in V} \tau_j^{\mathrm{r}}(\boldsymbol{x}, E_{\max}) \geq 0$. □

Besides of the condition (4.37) for the shape of the restricted stopping power function τ_j^{r}, it is possible to prove similar results for different conditions. Here only this simple case is studied, because τ_j^{r} is based on physical data with the choice of cut-off energy, which can be selected such that the condition (4.37) holds. However, τ_j^{r} may have different shapes depending on the energy and one should ensure that the condition (4.28) is fulfilled. For example, by direct computations it is not possible to fulfill condition (4.28) for τ_j^{r}, which is of the form

$$
\begin{aligned}
&\tfrac{\partial \tau_j^{\mathrm{r}}}{\partial E}(\boldsymbol{x}, E) \leq 0, \ E \in [E_{\min}, E_{\mathrm{f}}], \ \boldsymbol{x} \in V \\
&\tfrac{\partial \tau_j^{\mathrm{r}}}{\partial E}(\boldsymbol{x}, E) > 0, \ E \in]E_{\mathrm{f}}, E_{\max}], \ \boldsymbol{x} \in V \quad ,
\end{aligned}
$$

where $I = [E_{\min}, E_{\mathrm{f}}] \cup [E_{\mathrm{f}}, E_{\max}]$. Thus, one should select the cut-off energy such that τ_j^{r} fulfills the requirement (4.37) or to prove that the condition (4.28) is valid for τ_j^{r}, which has different shape from the presented ones. Also one could try to prove the coercivity and boundedness conditions in different spaces than used in here.

The presented Theorems 3 and 4 give foundations to prove the existence of the solution of the coupled B-CSDAEs when combined with Lemma 1. Theorem 4 gives suggestions what should be demanded on the cross sections and restricted stopping power data.

4.7 Numerical methods

FEM can be used to find a numerical approximation for the weak solution $\psi \in H^3$ or $\widetilde{H}^3$ of the transport problems (4.8) or (4.25) with the stated boundary conditions

(3.19) or (3.20). The systems of linear equations resulted from the variational forms of the coupled BTE and coupled B-CSDAEs can be derived. Before FEM can be used, one should assure the convergence of the FEM. Also one has to choose the basis functions and compute the related integrals. After the linear system is formulated, one has to use some numerical method to solve the system of linear equations. These issues are discussed in the following subsections.

4.7.1 On the FEM convergence

The boundedness (4.13) and coercivity (4.14) conditions imply the Cea's estimate [53] of the variational problem (4.8) of the coupled BTEs. If same basis functions ϕ_k $(k = 1, ..., N)$ are used for all particles, one defines a linear hull $X_\mathrm{h} = [(\phi_1, 0, 0), (\phi_2, 0, 0), ..., (\phi_N, 0, 0), (0, \phi_1, 0), ..., (0, \phi_N, 0), (0, 0, \phi_1), ..., (0, 0, \phi_N)] = [\Phi_1, ..., \Phi_{3N}]$, which is a finite dimensional subspace of H^3. The finite element approximation $\psi^\mathrm{h} = (\psi_1^\mathrm{h}, \psi_2^\mathrm{h}, \psi_3^\mathrm{h})^\mathrm{T}$ of the solution vector $\psi = (\psi_1, \psi_2, \psi_3)^\mathrm{T}$ is defined as a linear combination of the basis functions Φ_k $(k = 1, ..., 3N)$. That is, the finite element approximation is of the form

$$\psi^\mathrm{h}(\boldsymbol{x}, E, \boldsymbol{\Omega}) = \sum_{k=1}^{3N} \alpha_k \Phi_k^\mathrm{T} = \sum_{k=1}^{N} \left(\alpha_{(k)}, \alpha_{(k+N)}, \alpha_{(k+2N)}\right)^\mathrm{T} \phi_k(\boldsymbol{x}, E, \boldsymbol{\Omega}), \qquad (4.39)$$

where α_k are the unknown parameters and are found by demanding

$$B(\psi^\mathrm{h}, v) = F_j(v) + q(v), \ \forall v \in X_\mathrm{h}. \qquad (4.40)$$

If the assumptions of Theorem 1 are valid, the Cea's estimate [53] for the error $\psi - \psi^\mathrm{h}$ of the coupled BTEs is of the form

$$\|\psi - \psi^\mathrm{h}\|_{H_1^3} \leq \frac{C}{c} \inf_{w \in X_\mathrm{h}} \|\psi - w\|_{H^3}, \qquad (4.41)$$

which can be used in principle to prove the convergence of the FEM, if for $\psi \in H^3$ there exists a family of X_h such that $\lim_{h \to 0} \inf_{w \in X_\mathrm{h}} \|\psi - w\|_{H^3} = 0$.

The basis functions of the variational form (4.25) of the coupled B-CSDAEs has to be defined in the space $\widetilde{H}^3$. In fact, X_h can be used for the coupled B-CSDAEs, when the charged particle fluxes ψ_2 and ψ_3 are zeroed at maximum energy node. Basically this means that these rows and columns are removed from the resulted linear matrix equation. The finite element approximation (4.39) of the coupled B-CSDAEs is defined as a solution of the variational equation

$$B^\mathrm{r}(\psi^\mathrm{h}, v) = F_j(v) + q(v), \ \forall v \in X_\mathrm{h}. \qquad (4.42)$$

If the assumptions of Theorem 3 are valid, then the error $\psi - \psi^\mathrm{h}$ satisfies the Cea's estimate

$$\|\psi - \psi^\mathrm{h}\|_{\widetilde{H}_1^3} \leq \frac{C}{c} \inf_{w \in X_\mathrm{h}} \|\psi - w\|_{\widetilde{H}^3},$$

which gives basic estimate for the convergence analysis of the coupled B-CSDAEs. Here the details of the convergence analysis are omitted.

4.7.2 FEM matrix presentation of the coupled system

First the matrix presentation of the variational equation of the coupled BTEs is derived. The finite element approximation and variational problem are defined by equations (4.39) and (4.40), respectively. To test the validity of the variational equation, it is adequate to use the basis functions as test functions $v = \Phi_l$ $(l = 1, ..., 3N)$. The j^{th} component of the vector Φ_k is denoted as $\Phi_{k,j}$ $(j = 1, 2, 3)$. Assume that $Q = \mathbf{0}$. With these definitions, one obtains a system of linear equations from the variational equation (4.40)

$$(\boldsymbol{A}_1 + \boldsymbol{A}_2 + \boldsymbol{A}_3)\alpha = \boldsymbol{b}_j, \tag{4.43}$$

where $\alpha = (\alpha_1, ..., \alpha_{3N})^{\mathrm{T}}$ and $\boldsymbol{A}_i$, $i = 1, 2, 3$ are $3N \times 3N$ matrices such that

$$\boldsymbol{A}_1(l,k) = -\sum_{j=1}^{3} \langle \Phi_{k,j}, \boldsymbol{\Omega} \cdot \nabla \Phi_{l,j} \rangle_{L_2(G)}, \tag{4.44}$$

$$\boldsymbol{A}_2(l,k) = \sum_{j=1}^{3} \int_S \int_I \int_{\partial V} (\boldsymbol{\Omega} \cdot \boldsymbol{n})_+ \Phi_{k,j} \Phi_{l,j} \mathrm{d}\boldsymbol{s} \mathrm{d}E \mathrm{d}\boldsymbol{\Omega}, \tag{4.45}$$

$$\boldsymbol{A}_3(l,k) \quad = \quad \sum_{j=1}^{3} \langle K_j \Phi_k, \Phi_{l,j} \rangle_{L_2(G)}, \tag{4.46}$$

where

$$\begin{aligned} K_j \Phi_k \quad = \quad & -\int_S \int_I \sigma_{1\to j} \Phi_{k,1} \mathrm{d}E \mathrm{d}\boldsymbol{\Omega} \\ & -\int_S \int_I \sigma_{2\to j} \Phi_{k,2} \mathrm{d}E \mathrm{d}\boldsymbol{\Omega} \\ & -\int_S \int_I \sigma_{3\to j} \Phi_{k,3} \mathrm{d}E \mathrm{d}\boldsymbol{\Omega} + \sigma_j \Phi_{k,j}. \end{aligned} \tag{4.47}$$

$\boldsymbol{b}_j$ $(j = 1, 2)$ is a $3N \times 1$ vector such that

$$\boldsymbol{b}_j(l) = \int_S \int_I \int_\Gamma (\boldsymbol{\Omega} \cdot \boldsymbol{n})_- \psi_0 \Phi_{l,j} \mathrm{d}\boldsymbol{s} \mathrm{d}E \mathrm{d}\boldsymbol{\Omega}. \tag{4.48}$$

The matrix presentation of the coupled B-CSDAEs is obtained form the variational form (4.42) and it is of the form

$$(\boldsymbol{A}_1 + \boldsymbol{A}_2 + \boldsymbol{A}_3^{\mathrm{r}})\alpha = \boldsymbol{b}_j, \tag{4.49}$$

where $\boldsymbol{A}_1$, $\boldsymbol{A}_2$ and $\boldsymbol{b}_j$ are defined by equations (4.44), (4.45) and (4.48). Matrix $\boldsymbol{A}_3^{\mathrm{r}}$ is defined as

$$\boldsymbol{A}_3^{\mathrm{r}}(l,k) = \sum_{j=1}^{3} \langle K_j^{\mathrm{r}} \Phi_k, \Phi_{l,j} \rangle_{L_2(G)}, \tag{4.50}$$

where $K_1\Phi_k$ is defined by equation (4.47) and

$$\begin{aligned} K_2^{\mathrm{r}}\Phi_k &= \sigma_2^{\mathrm{r}}\Phi_{k,2} - \int_I\int_S \sigma_{1\to 2}\Phi_{k,1}\mathrm{d}E'\mathrm{d}\boldsymbol{\Omega}' \\ &\quad - \int_I\int_S \sigma_{2\to 2}^{\mathrm{r}}\Phi_{k,2}\mathrm{d}E'\mathrm{d}\boldsymbol{\Omega}' - \frac{\partial\left(\tau_2^{\mathrm{r}}\Phi_{k,2}\right)}{\partial E} \\ &\quad - \int_I\int_S \sigma_{3\to 2}\Phi_{k,3}\mathrm{d}E'\mathrm{d}\boldsymbol{\Omega}', \end{aligned} \tag{4.51}$$

$$\begin{aligned} K_3^{\mathrm{r}}\Phi_k &= \sigma_3^{\mathrm{r}}\Phi_{k,3} - \int_I\int_S \sigma_{1\to 3}\Phi_{k,1}\mathrm{d}E'\mathrm{d}\boldsymbol{\Omega}' \\ &\quad - \int_I\int_S \sigma_{3\to 3}^{\mathrm{r}}\Phi_{k,3}\mathrm{d}E'\mathrm{d}\boldsymbol{\Omega}' - \frac{\partial\left(\tau_3^{\mathrm{r}}\Phi_{k,3}\right)}{\partial E}. \end{aligned} \tag{4.52}$$

The matrices $\boldsymbol{A} := \boldsymbol{A}_1 + \boldsymbol{A}_2 + \boldsymbol{A}_3$ or $\boldsymbol{A}^{\mathrm{r}} := \boldsymbol{A}_1 + \boldsymbol{A}_2 + \boldsymbol{A}_3^{\mathrm{r}}$ are sparse, from which each consist of nine smaller sparse matrices. The matrices $\boldsymbol{A}_3$ or $\boldsymbol{A}_3^{\mathrm{r}}$ couple the system of BTEs. Also it is worth noting that in equations (4.44) and (4.45) only one of the summing terms $j = 1, 2, 3$ is nonzero depending on the values of k and l.

4.7.3 Separable basis functions

To construct the presented linear systems (4.43) or (4.49), one has to select basis functions and compute the integrals. Typically, separable basis functions $\phi_k = \phi_{k_{\mathrm{s}}}^{\boldsymbol{x}}(\boldsymbol{x})\phi_{k_{\mathrm{e}}}^{E}(E)\phi_{k_{\mathrm{o}}}^{\boldsymbol{\Omega}}(\boldsymbol{\Omega})$ $(k = 1, ..., N)$ are used to present the unknown flux $\psi^{\mathrm{h}}(\boldsymbol{x}, E, \boldsymbol{\Omega})$ and the same basis functions are used for all particles. Hence,

$$\psi^{\mathrm{h}}(\boldsymbol{x}, E, \boldsymbol{\Omega}) = \sum_{k_{\mathrm{s}}=1}^{N_{\mathrm{s}}}\sum_{k_{\mathrm{e}}=1}^{N_{\mathrm{e}}}\sum_{k_{\mathrm{o}}=1}^{N_{\mathrm{o}}} (\alpha_k, \alpha_{k+N}, \alpha_{k+2N})^{\mathrm{T}}\phi_{k_{\mathrm{s}}}^{\boldsymbol{x}}(\boldsymbol{x})\phi_{k_{\mathrm{e}}}^{E}(E)\phi_{k_{\mathrm{o}}}^{\boldsymbol{\Omega}}(\boldsymbol{\Omega}),$$

where $\phi_{k_{\mathrm{s}}}^{\boldsymbol{x}}(\boldsymbol{x})$ $(k_{\mathrm{s}} = 1, ...N_{\mathrm{s}})$, $\phi_{k_{\mathrm{e}}}^{E}(E)$ $(k_{\mathrm{e}} = 1, ...N_{\mathrm{e}})$ and $\phi_{k_{\mathrm{o}}}^{\boldsymbol{\Omega}}(\boldsymbol{\Omega})$ $(k_{\mathrm{o}} = 1, ...N_{\mathrm{o}})$ are the basis functions for the spatial, energy and angular grids, respectively. N_{s}, N_{e}, N_{o} denote the number of nodal points in each grid and $N = N_{\mathrm{s}}N_{\mathrm{e}}N_{\mathrm{o}}$. The index k is a function of $(k_{\mathrm{s}}, k_{\mathrm{e}}, k_{\mathrm{o}})$ and depends on the order of Kronecker tensor product. For example, here it is chosen $k = k_{\mathrm{o}} + (k_{\mathrm{e}} - 1)N_{\mathrm{o}} + (k_{\mathrm{s}} - 1)N_{\mathrm{e}}N_{\mathrm{o}}$. The separation of the test function gives $\phi_l = \phi_{l_{\mathrm{s}}}^{\boldsymbol{x}}(\boldsymbol{x})\phi_{l_{\mathrm{e}}}^{E}(E)\phi_{l_{\mathrm{o}}}^{\boldsymbol{\Omega}}(\boldsymbol{\Omega})$. The indexes l and k refer to rows and columns in the matrices, respectively. The index l is a function of $(l_{\mathrm{s}}, l_{\mathrm{e}}, l_{\mathrm{o}})$ similarly as for k.

Also the cross section and stopping power data is presented using the same basis functions. In the case of isotropic scattering, one obtains for the total cross section

$$\sigma_j(\boldsymbol{x}, E) = \sum_{d_{\mathrm{s}}=1}^{N_{\mathrm{s}}}\sum_{d_{\mathrm{e}}=1}^{N_{\mathrm{e}}} \sigma_d^j\phi_{d_{\mathrm{s}}}^{\boldsymbol{x}}\phi_{d_{\mathrm{e}}}^{E},$$

where σ_d^j is the value of $\sigma_j(\boldsymbol{x}, E)$ in a node, which is indexed as d, which is a

function of $(d_\mathrm{s}, d_\mathrm{e})$ as above for k. For the restricted stopping power

$$\tau_j^\mathrm{r}(\boldsymbol{x}, E) = \sum_{d_\mathrm{s}=1}^{N_\mathrm{s}} \sum_{d_\mathrm{e}=1}^{N_\mathrm{e}} \tau_d^{j,r} \phi_{d_\mathrm{s}}^{\boldsymbol{x}} \phi_{d_\mathrm{e}}^{E},$$

where $\tau_d^{j,r}$ is the value of $\tau^\mathrm{r}(\boldsymbol{x}, E)$ in a node, which is indexed similarly as that for the total cross section. For the differential cross section

$$\sigma_{j'\to j}(\boldsymbol{x}, E', E, \boldsymbol{\Omega}', \boldsymbol{\Omega}) = \sum_{d_\mathrm{s}=1}^{N_\mathrm{s}} \sum_{d_\mathrm{e}=1}^{N_\mathrm{e}} \sum_{d'_\mathrm{e}=1}^{N_\mathrm{e}} \sum_{d_\mathrm{o}=1}^{N_\mathrm{o}} \sum_{d'_\mathrm{o}=1}^{N_\mathrm{o}} \sigma_{dd}^{j'\to j} \phi_{d_\mathrm{s}}^{\boldsymbol{x}} \phi_{d_\mathrm{e}}^{E} \phi_{d'_\mathrm{e}}^{E} \phi_{d_\mathrm{o}}^{\boldsymbol{\Omega}} \phi_{d'_\mathrm{o}}^{\boldsymbol{\Omega}},$$

where dd is a function of $(d_\mathrm{s}, d_\mathrm{e}, d'_\mathrm{e}, d_\mathrm{o}, d'_\mathrm{o})$ as above for k and $\sigma_{dd}^{j'\to j}$ is the value of $\sigma_{j'\to j}(\boldsymbol{x}, E', E, \boldsymbol{\Omega}', \boldsymbol{\Omega})$ in a related node. Similar expressions can be derived for the restricted cross sections.

Because the differential cross sections are usually nearly delta-function shaped with respect to energy or angle and because in FEM with linear basis the delta-functions have always some width, depending on the discretization, the differential cross sections are normalized such that the normalization condition

$$\sigma_{dd}^{j'\to j} \int_S \int_I \phi_{d_\mathrm{s}}^{\boldsymbol{x}} \phi_{d_\mathrm{e}}^{E} \phi_{d'_\mathrm{e}}^{E} \phi_{d_\mathrm{o}}^{\boldsymbol{\Omega}} \phi_{d'_\mathrm{o}}^{\boldsymbol{\Omega}} \mathrm{d}E\mathrm{d}\boldsymbol{\Omega} = \int_{S_{dd}} \int_{I_{dd}} \sigma_{j'\to j}(\boldsymbol{x}, E', E, \boldsymbol{\Omega}', \boldsymbol{\Omega}) \mathrm{d}E\mathrm{d}\boldsymbol{\Omega}$$

is fulfilled for every dd. The sub-domains S_{dd} and I_{dd} include the elements, which are connected to the nodes d_o and d_e, respectively. The normalization condition means for example that one divides the differential cross section values σ_{dd} by the value of the integral $\int_{S_{dd}} \phi_{d_\mathrm{o}}^{\boldsymbol{\Omega}} \mathrm{d}\boldsymbol{\Omega}$ if the differential cross section is delta-function shaped with respect to angle. Clearly, this normalization is needed in order the conditions for the cross sections (4.18) and (4.19) to hold.

As mentioned earlier the matrices $\boldsymbol{A}$ or $\boldsymbol{A}^\mathrm{r}$ consist of nine smaller matrices, which means that the linear system $\boldsymbol{A}\alpha = \boldsymbol{b}_j$ defined by (4.43) is of the form

$$\begin{pmatrix} A_{1\to1} & D_{2\to1} & D_{3\to1} \\ D_{1\to2} & A_{2\to2} & D_{3\to2} \\ D_{1\to3} & \mathbf{0} & A_{3\to3} \end{pmatrix} \alpha = \boldsymbol{b}_j, \tag{4.53}$$

where $\boldsymbol{b}_j$ depends on the boundary condition and has a form

$$\boldsymbol{b}_1 = \begin{pmatrix} b \\ \mathbf{0} \\ \mathbf{0} \end{pmatrix}, \quad \boldsymbol{b}_2 = \begin{pmatrix} \mathbf{0} \\ b \\ \mathbf{0} \end{pmatrix}, \tag{4.54}$$

where $j = 1$ indicates photon boundary condition (3.19) and $j = 2$ electron boundary condition (3.20). The matrices $A_{j\to j}$ and $D_{j'\to j}$ $(j = 1, 2, 3,\ j' = 1, 2, 3,\ j' \neq$

j) can be formed for separable basis functions as

$$\begin{aligned} A_{j\to j}(l,k) &= \int_I \phi^E_{k_\mathrm{e}}\phi^E_{l_\mathrm{e}}\mathrm{d}E\Big(-\int_V \phi^{\boldsymbol{x}}_{k_\mathrm{s}}\frac{\partial\phi^{\boldsymbol{x}}_{l_\mathrm{s}}}{\partial x_1}\mathrm{d}\boldsymbol{x}\int_S \cos\varphi\sin\theta\phi^{\boldsymbol{\Omega}}_{k_\mathrm{o}}\phi^{\boldsymbol{\Omega}}_{l_\mathrm{o}}\mathrm{d}\boldsymbol{\Omega} \\ &\quad -\int_V \phi^{\boldsymbol{x}}_{k_\mathrm{s}}\frac{\partial\phi^{\boldsymbol{x}}_{l_\mathrm{s}}}{\partial x_2}\mathrm{d}\boldsymbol{x}\int_S \sin\varphi\sin\theta\phi^{\boldsymbol{\Omega}}_{k_\mathrm{o}}\phi^{\boldsymbol{\Omega}}_{l_\mathrm{o}}\mathrm{d}\boldsymbol{\Omega} \\ &\quad -\int_V \phi^{\boldsymbol{x}}_{k_\mathrm{s}}\frac{\partial\phi^{\boldsymbol{x}}_{l_\mathrm{s}}}{\partial x_3}\mathrm{d}\boldsymbol{x}\int_S \cos\theta\phi^{\boldsymbol{\Omega}}_{k_\mathrm{o}}\phi^{\boldsymbol{\Omega}}_{l_\mathrm{o}}\mathrm{d}\boldsymbol{\Omega} \\ &\quad +\sum_{i=1}^{N_{\partial V}}\int_{\partial V_i}\phi^{\boldsymbol{x}}_{k_\mathrm{s}}\phi^{\boldsymbol{x}}_{l_\mathrm{s}}\mathrm{d}\boldsymbol{s}\int_S(\boldsymbol{\Omega}\cdot\boldsymbol{n}_i)_+\phi^{\boldsymbol{\Omega}}_{k_\mathrm{o}}\phi^{\boldsymbol{\Omega}}_{l_\mathrm{o}}\mathrm{d}\boldsymbol{\Omega}\Big) \\ &\quad +\sum_{d_\mathrm{s}=1}^{N_\mathrm{s}}\sum_{d_\mathrm{e}=1}^{N_\mathrm{e}}\sigma^j_d\int_I\phi^E_{d_\mathrm{e}}\phi^E_{k_\mathrm{e}}\phi^E_{l_\mathrm{e}}\mathrm{d}E\int_V\phi^{\boldsymbol{x}}_{d_\mathrm{s}}\phi^{\boldsymbol{x}}_{k_\mathrm{s}}\phi^{\boldsymbol{x}}_{l_\mathrm{s}}\mathrm{d}\boldsymbol{x}\int_S\phi^{\boldsymbol{\Omega}}_{k_\mathrm{o}}\phi^{\boldsymbol{\Omega}}_{l_\mathrm{o}}\mathrm{d}\boldsymbol{\Omega} \\ &\quad -\sum_{dd}\sigma^{j\to j}_{dd}\int_I\phi^E_{d_\mathrm{e}}\phi^E_{l_\mathrm{e}}\mathrm{d}E\int_I\phi^E_{d'_\mathrm{e}}\phi^E_{k_\mathrm{e}}\mathrm{d}E\int_V\phi^{\boldsymbol{x}}_{d_\mathrm{s}}\phi^{\boldsymbol{x}}_{k_\mathrm{s}}\phi^{\boldsymbol{x}}_{l_\mathrm{s}}\mathrm{d}\boldsymbol{x} \\ &\quad \cdot\int_S\phi^{\boldsymbol{\Omega}}_{d_\mathrm{o}}\phi^{\boldsymbol{\Omega}}_{l_\mathrm{o}}\mathrm{d}\boldsymbol{\Omega}\int_S\phi^{\boldsymbol{\Omega}}_{d'_\mathrm{o}}\phi^{\boldsymbol{\Omega}}_{k_\mathrm{o}}\mathrm{d}\boldsymbol{\Omega} \end{aligned} \tag{4.55}$$

and

$$\begin{aligned} D_{j'\to j}(l,k) &= -\sum_{dd}\sigma^{j'\to j}_{dd}\int_I\phi^E_{d_\mathrm{e}}\phi^E_{l_\mathrm{e}}\mathrm{d}E\int_I\phi^E_{d'_\mathrm{e}}\phi^E_{k_\mathrm{e}}\mathrm{d}E\int_V\phi^{\boldsymbol{x}}_{d_\mathrm{s}}\phi^{\boldsymbol{x}}_{k_\mathrm{s}}\phi^{\boldsymbol{x}}_{l_\mathrm{s}}\mathrm{d}\boldsymbol{x} \\ &\quad \cdot\int_S\phi^{\boldsymbol{\Omega}}_{d_\mathrm{o}}\phi^{\boldsymbol{\Omega}}_{l_\mathrm{o}}\mathrm{d}\boldsymbol{\Omega}\int_S\phi^{\boldsymbol{\Omega}}_{d'_\mathrm{o}}\phi^{\boldsymbol{\Omega}}_{k_\mathrm{o}}\mathrm{d}\boldsymbol{\Omega}. \end{aligned} \tag{4.56}$$

In the previous equations (4.55) and (4.56), $\sigma^{j'\to j}_{dd}$ is the differential cross section value, in which particle j' is changed into particle j, similarly $\sigma^{j\to j}_{dd}$ is the differential cross section value, in which the direction and angle of particle j are changed, and σ^j_d is the total cross section value for particle j. The boundary ∂V is assumed to consist of surfaces ∂V_i $i = 1, ..., N_{\partial V}$, where the outward normal $\boldsymbol{n}_i$ does not depend on $\boldsymbol{x}$ (that is V is polyhedron). For example for cubic domain in 3D $N_{\partial V} = 6$ and the outward unit normals are $\boldsymbol{n}_1 = (1,0,0)$, $\boldsymbol{n}_2 = (-1,0,0)$, $\boldsymbol{n}_3 = (0,1,0)$, $\boldsymbol{n}_4 = (0,-1,0)$, $\boldsymbol{n}_5 = (0,0,1)$ and $\boldsymbol{n}_6 = (0,0,-1)$.

The known flux at the boundary ψ_0 can be written using the same separable basis functions by assuming $\psi_0(\boldsymbol{x}, E, \boldsymbol{\Omega}) = 0$, when $\boldsymbol{x} \in V \setminus \Gamma$. Thus,

$$\psi_0(\boldsymbol{x}, E, \boldsymbol{\Omega}) = \sum_{i_\mathrm{s}=1}^{N_\mathrm{s}}\sum_{i_\mathrm{e}=1}^{N_\mathrm{e}}\sum_{i_\mathrm{o}=1}^{N_\mathrm{o}}\Psi^0_i\phi^{\boldsymbol{x}}_{i_\mathrm{s}}\phi^E_{i_\mathrm{e}}\phi^{\boldsymbol{\Omega}}_{i_\mathrm{o}}, \tag{4.57}$$

where i is a function of $(i_\mathrm{s}, i_\mathrm{e}, i_\mathrm{o})$ similarly as for the index k. The nonzero values of Ψ^0_i are the values of the incoming flux at Γ. Because all the nodes are included in the basis system, there are quite many zeros in the vector $\Psi^0 = (\Psi^0_1, ..., \Psi^0_{3N})$.

The vector b can be easily computed from equation $b = M_{\mathrm{b}}\Psi^0$, where the elements of the matrix M_{b} are

$$M_{\mathrm{b}}(l,i) = \left(\sum_{j=1}^{N_V} \int_{\partial V_j} \phi^{\boldsymbol{x}}_{i_{\mathrm{s}}} \phi^{\boldsymbol{x}}_{l_{\mathrm{s}}} \mathrm{d}\boldsymbol{s} \int_S (\boldsymbol{\Omega}\cdot\boldsymbol{n}_j)_- \phi^{\boldsymbol{\Omega}}_{i_{\mathrm{o}}} \phi^{\boldsymbol{\Omega}}_{l_{\mathrm{o}}} \mathrm{d}\boldsymbol{\Omega} \right) \int_I \phi^E_{i_{\mathrm{e}}} \phi^E_{l_{\mathrm{e}}} \mathrm{d}E. \tag{4.58}$$

Originally in equation (4.48), there is an integration over Γ. In equation (4.58), it is possible to integrate over the whole boundary ∂V, because the integration over Γ is accounted in the coefficient vector Ψ^0. Now it is easy to use the same boundary integrations as needed for $A_{j'\to j}$ matrices.

The previous integral equations are for the linear system (4.43). Similarly one obtains the integral equations for the linear system (4.49) of the coupled B-CSDAEs, which is of the form

$$\begin{pmatrix} A^{\mathrm{r}}_{1\to 1} & D_{2\to 1} & D_{3\to 1} \\ D_{1\to 2} & A^{\mathrm{r}}_{2\to 2} & D_{3\to 2} \\ D_{1\to 3} & \mathbf{0} & A^{\mathrm{r}}_{3\to 3} \end{pmatrix} \alpha = \boldsymbol{b}_j, \tag{4.59}$$

where $\boldsymbol{b}_j$ is defined by equation (4.54) and the matrices $D_{j'\to j}$ are as those in equation (4.56). The matrix $A^{\mathrm{r}}_{j\to j}$ $(j = 1, 2, 3)$ is

$$\begin{aligned} A^{\mathrm{r}}_{j\to j}(l,k) \;=\; & A_{j\to j}(l,k) - \sum_{d_{\mathrm{s}}=1}^{N_{\mathrm{s}}} \sum_{d_{\mathrm{e}}=1}^{N_{\mathrm{e}}} \tau^{\mathrm{r},j}_d \int_I \frac{\partial(\phi^E_{d_{\mathrm{e}}} \phi^E_{k_{\mathrm{e}}})}{\partial E} \phi^E_{l_{\mathrm{e}}} \mathrm{d}E \\ & \cdot \int_V \phi^{\boldsymbol{x}}_{d_{\mathrm{s}}} \phi^{\boldsymbol{x}}_{k_{\mathrm{s}}} \phi^{\boldsymbol{x}}_{l_{\mathrm{s}}} \mathrm{d}\boldsymbol{x} \int_S \phi^{\boldsymbol{\Omega}}_{k_{\mathrm{o}}} \phi^{\boldsymbol{\Omega}}_{l_{\mathrm{o}}} \mathrm{d}\boldsymbol{\Omega}, \end{aligned} \tag{4.60}$$

where $A_{j\to j}(l,k)$ is obtained from equation (4.55) with restricted cross sections $\sigma^{\mathrm{r},j}_d$ and $\sigma^{\mathrm{r},j\to j}_{dd}$.

The previous equations are written for the 3D case. In the simulations also 2D spatial geometry is used. Then it is assumed that the particles travel and scatter in the spatial 2D plane, in which $\boldsymbol{x} = (x_2, x_3)$, and the scattering out of the plane is neglected. Hence, the angular variable is $\theta \in [0, 2\pi[$ and $\boldsymbol{\Omega}_{2\mathrm{D}} = (\sin\theta, \cos\theta)$ meaning that $\theta = 0$ is toward x_3-axis. The angular integrals are now line integrals over $\theta \in [0, 2\pi[$ and the angular basis function is denoted by $\phi^{\theta}_{k_{\mathrm{o}}}$ $(k_{\mathrm{o}} = 1, ..., N_{\mathrm{o}})$. The surface integral is also a line integral. The boundary ∂V is assumed to consists of lines ∂V_i $(i = 1, ..., N_{\partial V})$, in which the normal vector $\boldsymbol{n}_i$ has constant values. For example in rectangular domain $N_{\partial V} = 4$ and $\boldsymbol{n}_1 = (1, 0)$, $\boldsymbol{n}_2 = (0, 1)$, $\boldsymbol{n}_3 = (-1, 0)$, $\boldsymbol{n}_4 = (0, -1)$.

In 2D geometry, the matrices in the linear system (4.53) are of the form

$$\begin{aligned} A_{j\to j}(l,k) &= \int_I \phi^E_{k_\mathrm{e}}\phi^E_{l_\mathrm{e}}\mathrm{d}E\Big(-\int_V \phi^{\boldsymbol{x}}_{k_\mathrm{s}}\frac{\partial\phi^{\boldsymbol{x}}_{l_\mathrm{s}}}{\partial x_2}\mathrm{d}\boldsymbol{x}\int_0^{2\pi}\sin\theta\phi^\theta_{k_\mathrm{o}}\phi^\theta_{l_\mathrm{o}}\mathrm{d}\theta \\ &\quad -\int_V \phi^{\boldsymbol{x}}_{k_\mathrm{s}}\frac{\partial\phi^{\boldsymbol{x}}_{l_\mathrm{s}}}{\partial x_3}\mathrm{d}\boldsymbol{x}\int_0^{2\pi}\cos\theta\phi^\theta_{k_\mathrm{o}}\phi^\theta_{l_\mathrm{o}}\mathrm{d}\theta \\ &\quad +\sum_{i=1}^{N_{\partial V}}\int_{\partial V_i}\phi^{\boldsymbol{x}}_{k_\mathrm{s}}\phi^{\boldsymbol{x}}_{l_\mathrm{s}}\mathrm{d}\boldsymbol{s}\int_0^{2\pi}(\boldsymbol{\Omega}_{\mathrm{2D}}\cdot\boldsymbol{n}_i)_+\phi^\theta_{k_\mathrm{o}}\phi^\theta_{l_\mathrm{o}}\mathrm{d}\theta\Big) \\ &+\sum_{d_\mathrm{s}=1}^{N_\mathrm{s}}\sum_{d_\mathrm{e}=1}^{N_\mathrm{e}}\sigma^j_d\int_I\phi^E_{d_\mathrm{e}}\phi^E_{k_\mathrm{e}}\phi^E_{l_\mathrm{e}}\mathrm{d}E\int_V\phi^{\boldsymbol{x}}_{d_\mathrm{s}}\phi^{\boldsymbol{x}}_{k_\mathrm{s}}\phi^{\boldsymbol{x}}_{l_\mathrm{s}}\mathrm{d}\boldsymbol{x}\int_0^{2\pi}\phi^\theta_{k_\mathrm{o}}\phi^\theta_{l_\mathrm{o}}\mathrm{d}\theta \qquad (4.61) \\ &-\sum_{dd}\sigma^{j\to j}_{dd}\int_I\phi^E_{d_\mathrm{e}}\phi^E_{l_\mathrm{e}}\mathrm{d}E\int_I\phi^E_{d'_\mathrm{e}}\phi^E_{k_\mathrm{e}}\mathrm{d}E\int_V\phi^{\boldsymbol{x}}_{d_\mathrm{s}}\phi^{\boldsymbol{x}}_{k_\mathrm{s}}\phi^{\boldsymbol{x}}_{l_\mathrm{s}}\mathrm{d}\boldsymbol{x}\int_0^{2\pi}\phi^\theta_{d_\mathrm{o}}\phi^\theta_{l_\mathrm{o}}\mathrm{d}\theta\int_0^{2\pi}\phi^\theta_{d'_\mathrm{o}}\phi^\theta_{k_\mathrm{o}}\mathrm{d}\theta \end{aligned}$$

and

$$\begin{aligned} D_{j'\to j}(l,k) &= -\sum_{dd}\sigma^{j'\to j}_{dd}\int_I\phi^E_{d_\mathrm{e}}\phi^E_{l_\mathrm{e}}\mathrm{d}E\int_I\phi^E_{d'_\mathrm{e}}\phi^E_{k_\mathrm{e}}\mathrm{d}E\int_V\phi^{\boldsymbol{x}}_{d_\mathrm{s}}\phi^{\boldsymbol{x}}_{k_\mathrm{s}}\phi^{\boldsymbol{x}}_{l_\mathrm{s}}\mathrm{d}\boldsymbol{x} \\ &\quad\cdot\int_0^{2\pi}\phi^\theta_{d_\mathrm{o}}\phi^\theta_{l_\mathrm{o}}\mathrm{d}\theta\int_0^{2\pi}\phi^\theta_{d'_\mathrm{o}}\phi^\theta_{k_\mathrm{o}}\mathrm{d}\theta. \qquad (4.62) \end{aligned}$$

The vector $\boldsymbol{b}_j$ is achieved similarly as in 3D case. The elements of the matrix M_b are similar to those described in equation (4.58), in which now the angular integral is changed to $\int_0^{2\pi}(\boldsymbol{\Omega}_{\mathrm{2D}}\cdot\boldsymbol{n}_i)_-\phi^\theta_{i_\mathrm{o}}\phi^\theta_{l_\mathrm{o}}\mathrm{d}\theta$ and the surface integral is a line integral. Similar changes can be made to equation (4.60) to obtain the equation for the matrix $A^\mathrm{r}_{j\to j}$ in the coupled B-CSDAEs.

4.7.4 Stream-line diffusion method

The matrices $A_{j\to j}$ or $A^\mathrm{r}_{j\to j}$ $(j=1,2,3)$ contain gradient term, which may produce instability in the solution of the linear systems (4.43) or (4.49) [102, 75]. The system can be stabilized using stream-line diffusion method, in which the test function is chosen to be $v+\delta\boldsymbol{\Omega}\cdot\nabla v$, where $\delta>0$. The parameter δ may depend for example on the spatial discretization and the values of the cross sections. For example,

$$\delta^j_{l,k} = c\min_{d_\mathrm{e}\in\{1,\ldots,N_\mathrm{e}\}}\left\{(\sigma^j_d)^{-1}\right\}, \qquad (4.63)$$

where l,k refer to nodes and c is a small constant [103]. This stabilizes the system of linear equations and fastens the convergence of the solution method.

In the stream-line diffusion method, the variational form is achieved by applying the test function $v+\delta\boldsymbol{\Omega}\cdot\nabla v$ in equation (4.3) resulting (assuming $Q_j=0$ $(j=1,2,3)$)

$$\langle T\psi,v\rangle_{L_2(G)^3}+\langle K\psi,v\rangle_{L_2(G)^3}+\langle T\psi+K\psi,\delta\boldsymbol{\Omega}\cdot\nabla v\rangle_{L_2(G)^3}=0.$$

Then the Green's formula (4.5) is applied to the first term as in Section 4.3 and the variational form of the coupled BTE (3.14) with the stated incoming photon (3.19) or electron (3.20) boundary conditions using the stream-line diffusion method is

$$B(\psi, v) + B_{\mathrm{sd}}(\psi, v) = F_j(v), \ v \in H^3, \tag{4.64}$$

where $B(\psi, v)$ and $F_j(v)$ ($Q_j = 0$) are defined by equations (4.9),(4.10) and where

$$B_{\mathrm{sd}}(\psi, v) \quad = \quad \sum_{j=1}^{3} \langle \boldsymbol{\Omega} \cdot \nabla \psi_j, \delta \boldsymbol{\Omega} \cdot \nabla v_j \rangle_{L_2(G)} + \sum_{j=1}^{3} \langle K_j \psi, \delta \boldsymbol{\Omega} \cdot \nabla v_j \rangle_{L_2(G)}. \tag{4.65}$$

Similarly, the variational form of the coupled B-CSDAEs with the stream-line diffusion method is

$$B^{\mathrm{r}}(\psi, v) + B^{\mathrm{r}}_{\mathrm{sd}}(\psi, v) = F_j(v), \ v \in H^3, \tag{4.66}$$

where $B^{\mathrm{r}}(\psi, v)$ is obtained from equation (4.26) and $B^{\mathrm{r}}_{\mathrm{sd}}(\psi, v)$ is similar to equation (4.65) with $K_j \psi = K^{\mathrm{r}}_j \psi$ defined by the equations (4.47), (4.51) and (4.52).

If separable basis functions are used as test functions the variational form (4.64) results in a linear system $\boldsymbol{A}_{\mathrm{sd}} \alpha = \boldsymbol{b}_j$, which is of the form

$$\begin{pmatrix} A^{\mathrm{sd}}_{1\to 1} & D^{\mathrm{sd}}_{2\to 1} & D^{\mathrm{sd}}_{3\to 1} \\ D^{\mathrm{sd}}_{1\to 2} & A^{\mathrm{sd}}_{2\to 2} & D^{\mathrm{sd}}_{3\to 2} \\ D^{\mathrm{sd}}_{1\to 3} & \mathbf{0} & A^{\mathrm{sd}}_{3\to 3} \end{pmatrix} \alpha = \boldsymbol{b}_j, \tag{4.67}$$

where $\boldsymbol{b}_j$ is defined by equation (4.54). The elements of the matrix $A^{\mathrm{sd}}_{j\to j}$ are

$$A^{\mathrm{sd}}_{j\to j}(l,k) \quad = \quad A_{j\to j}(l,k) + \delta^j_{l,k} \left(A^{\mathrm{sd}}_1(l,k) + A^{\mathrm{sd}}_2(l,k) \right), \tag{4.68}$$

where $A_{j\to j}(l,k)$ is defined by equation (4.55) and where $A_1^{\mathrm{sd}}(l,k)$ is of the form

$$\begin{aligned}
A_1^{\mathrm{sd}}(l,k) &= \int_I \phi^E_{k_\mathrm{e}}\phi^E_{l_\mathrm{e}}\mathrm{d}E\Bigg(\int_V \frac{\partial\phi^{\boldsymbol{x}}_{k_\mathrm{s}}}{\partial x_1}\frac{\partial\phi^{\boldsymbol{x}}_{l_\mathrm{s}}}{\partial x_1}\mathrm{d}\boldsymbol{x}\int_S \cos^2\varphi\sin^2\theta\phi^{\boldsymbol{\Omega}}_{k_\mathrm{o}}\phi^{\boldsymbol{\Omega}}_{l_\mathrm{o}}\mathrm{d}\boldsymbol{\Omega}\\
&+\int_V \frac{\partial\phi^{\boldsymbol{x}}_{k_\mathrm{s}}}{\partial x_1}\frac{\partial\phi^{\boldsymbol{x}}_{l_\mathrm{s}}}{\partial x_2}\mathrm{d}\boldsymbol{x}\int_S \cos\varphi\sin\varphi\sin^2\theta\phi^{\boldsymbol{\Omega}}_{k_\mathrm{o}}\phi^{\boldsymbol{\Omega}}_{l_\mathrm{o}}\mathrm{d}\boldsymbol{\Omega}\\
&+\int_V \frac{\partial\phi^{\boldsymbol{x}}_{k_\mathrm{s}}}{\partial x_1}\frac{\partial\phi^{\boldsymbol{x}}_{l_\mathrm{s}}}{\partial x_3}\mathrm{d}\boldsymbol{x}\int_S \cos\varphi\cos\theta\sin\theta\phi^{\boldsymbol{\Omega}}_{k_\mathrm{o}}\phi^{\boldsymbol{\Omega}}_{l_\mathrm{o}}\mathrm{d}\boldsymbol{\Omega}\\
&+\int_V \frac{\partial\phi^{\boldsymbol{x}}_{k_\mathrm{s}}}{\partial x_2}\frac{\partial\phi^{\boldsymbol{x}}_{l_\mathrm{s}}}{\partial x_1}\mathrm{d}\boldsymbol{x}\int_S \cos\varphi\sin\varphi\sin^2\theta\phi^{\boldsymbol{\Omega}}_{k_\mathrm{o}}\phi^{\boldsymbol{\Omega}}_{l_\mathrm{o}}\mathrm{d}\boldsymbol{\Omega}\\
&+\int_V \frac{\partial\phi^{\boldsymbol{x}}_{k_\mathrm{s}}}{\partial x_2}\frac{\partial\phi^{\boldsymbol{x}}_{l_\mathrm{s}}}{\partial x_2}\mathrm{d}\boldsymbol{x}\int_S \sin^2\varphi\sin^2\theta\phi^{\boldsymbol{\Omega}}_{k_\mathrm{o}}\phi^{\boldsymbol{\Omega}}_{l_\mathrm{o}}\mathrm{d}\boldsymbol{\Omega}\\
&+\int_V \frac{\partial\phi^{\boldsymbol{x}}_{k_\mathrm{s}}}{\partial x_2}\frac{\partial\phi^{\boldsymbol{x}}_{l_\mathrm{s}}}{\partial x_3}\mathrm{d}\boldsymbol{x}\int_S \sin\varphi\cos\theta\sin\theta\phi^{\boldsymbol{\Omega}}_{k_\mathrm{o}}\phi^{\boldsymbol{\Omega}}_{l_\mathrm{o}}\mathrm{d}\boldsymbol{\Omega}\\
&+\int_V \frac{\partial\phi^{\boldsymbol{x}}_{k_\mathrm{s}}}{\partial x_3}\frac{\partial\phi^{\boldsymbol{x}}_{l_\mathrm{s}}}{\partial x_1}\mathrm{d}\boldsymbol{x}\int_S \cos\varphi\cos\theta\sin\theta\phi^{\boldsymbol{\Omega}}_{k_\mathrm{o}}\phi^{\boldsymbol{\Omega}}_{l_\mathrm{o}}\mathrm{d}\boldsymbol{\Omega}\\
&+\int_V \frac{\partial\phi^{\boldsymbol{x}}_{k_\mathrm{s}}}{\partial x_3}\frac{\partial\phi^{\boldsymbol{x}}_{l_\mathrm{s}}}{\partial x_2}\mathrm{d}\boldsymbol{x}\int_S \sin\varphi\cos\theta\sin\theta\phi^{\boldsymbol{\Omega}}_{k_\mathrm{o}}\phi^{\boldsymbol{\Omega}}_{l_\mathrm{o}}\mathrm{d}\boldsymbol{\Omega}\\
&+\int_V \frac{\partial\phi^{\boldsymbol{x}}_{k_\mathrm{s}}}{\partial x_3}\frac{\partial\phi^{\boldsymbol{x}}_{l_\mathrm{s}}}{\partial x_3}\mathrm{d}\boldsymbol{x}\int_S \cos^2\theta\phi^{\boldsymbol{\Omega}}_{k_\mathrm{o}}\phi^{\boldsymbol{\Omega}}_{l_\mathrm{o}}\mathrm{d}\boldsymbol{\Omega}\Bigg)
\end{aligned}\tag{4.69}$$

and $A_2^{\mathrm{sd}}(l,k)$ is of the form

$$\begin{aligned}
A_2^{\mathrm{sd}}(l,k) &= \Bigg(\sum_{d_\mathrm{s}=1}^{N_\mathrm{s}}\sum_{d_\mathrm{e}=1}^{N_\mathrm{e}}\sigma_d^j\int_I \phi^E_{d_\mathrm{e}}\phi^E_{k_\mathrm{e}}\phi^E_{l_\mathrm{e}}\mathrm{d}E\\
&-\sum_{dd}\sigma_{dd}^{j\to j}\int_I \phi^E_{d_\mathrm{e}}\phi^E_{l_\mathrm{e}}\mathrm{d}E\int_I \phi^E_{d'_\mathrm{e}}\phi^E_{k_\mathrm{e}}\mathrm{d}E\int_S \phi^{\boldsymbol{\Omega}}_{d'_\mathrm{o}}\phi^{\boldsymbol{\Omega}}_{k_\mathrm{o}}\mathrm{d}\boldsymbol{\Omega}\Bigg)\\
&\cdot\Bigg(\int_V \phi^{\boldsymbol{x}}_{d_\mathrm{s}}\phi^{\boldsymbol{x}}_{k_\mathrm{s}}\frac{\partial\phi^{\boldsymbol{x}}_{l_\mathrm{s}}}{\partial x_1}\mathrm{d}\boldsymbol{x}\int_S \cos\varphi\sin\theta\phi^{\boldsymbol{\Omega}}_{k_\mathrm{o}}\phi^{\boldsymbol{\Omega}}_{l_\mathrm{o}}\mathrm{d}\boldsymbol{\Omega}\\
&+\int_V \phi^{\boldsymbol{x}}_{d_\mathrm{s}}\phi^{\boldsymbol{x}}_{k_\mathrm{s}}\frac{\partial\phi^{\boldsymbol{x}}_{l_\mathrm{s}}}{\partial x_2}\mathrm{d}\boldsymbol{x}\int_S \sin\varphi\sin\theta\phi^{\boldsymbol{\Omega}}_{k_\mathrm{o}}\phi^{\boldsymbol{\Omega}}_{l_\mathrm{o}}\mathrm{d}\boldsymbol{\Omega}\\
&+\int_V \phi^{\boldsymbol{x}}_{d_\mathrm{s}}\phi^{\boldsymbol{x}}_{k_\mathrm{s}}\frac{\partial\phi^{\boldsymbol{x}}_{l_\mathrm{s}}}{\partial x_3}\mathrm{d}\boldsymbol{x}\int_S \cos\theta\phi^{\boldsymbol{\Omega}}_{k_\mathrm{o}}\phi^{\boldsymbol{\Omega}}_{l_\mathrm{o}}\mathrm{d}\boldsymbol{\Omega}\Bigg).
\end{aligned}\tag{4.70}$$

The elements of the matrix $D^{\mathrm{sd}}_{j'\to j}$ are

$$\begin{aligned}
D^{\mathrm{sd}}_{j'\to j}(l,k) &= D_{j'\to j}(l,k)-\delta^j_{l,k}\sum_{dd}\sigma_{dd}^{j'\to j}\int_I \phi^E_{d_\mathrm{e}}\phi^E_{l_\mathrm{e}}\mathrm{d}E\int_I \phi^E_{d'_\mathrm{e}}\phi^E_{k_\mathrm{e}}\mathrm{d}E\\
&\cdot\int_V \phi^{\boldsymbol{x}}_{d_\mathrm{s}}\phi^{\boldsymbol{x}}_{k_\mathrm{s}}\phi^{\boldsymbol{x}}_{l_\mathrm{s}}\mathrm{d}\boldsymbol{x}\int_S \phi^{\boldsymbol{\Omega}}_{d_\mathrm{o}}\phi^{\boldsymbol{\Omega}}_{l_\mathrm{o}}\mathrm{d}\boldsymbol{\Omega}\int_S \phi^{\boldsymbol{\Omega}}_{d'_\mathrm{o}}\phi^{\boldsymbol{\Omega}}_{k_\mathrm{o}}\mathrm{d}\boldsymbol{\Omega},
\end{aligned}\tag{4.71}$$

where $D_{j'\to j}(l,k)$ is defined by equation (4.56).

Similarly for the variational form (4.66), the linear system $\boldsymbol{A}^{\mathrm{r}}_{\mathrm{sd}}\alpha = \boldsymbol{b}_j$ is obtained and it is of the form

$$\begin{pmatrix} A^{\mathrm{r,sd}}_{1\to 1} & D^{\mathrm{sd}}_{2\to 1} & D^{\mathrm{sd}}_{3\to 1} \\ D^{\mathrm{sd}}_{1\to 2} & A^{\mathrm{r,sd}}_{2\to 2} & D^{\mathrm{sd}}_{3\to 2} \\ D^{\mathrm{sd}}_{1\to 3} & \mathbf{0} & A^{\mathrm{r,sd}}_{3\to 3} \end{pmatrix} \alpha = \boldsymbol{b}_j, \tag{4.72}$$

where $\boldsymbol{b}_j$ is defined by equation (4.54) and $D^{\mathrm{sd}}_{j'\to j}$ by equation (4.56). The elements of the matrix $A^{\mathrm{r,sd}}_{j\to j}$ $(j = 1, 2, 3)$ are

$$\begin{aligned} A^{\mathrm{r,sd}}_{j\to j}(l,k) &= A^{\mathrm{sd}}_{j\to j}(l,k) - \sum_{d_{\mathrm{s}}=1}^{N_{\mathrm{s}}}\sum_{d_{\mathrm{e}}=1}^{N_{\mathrm{e}}} \tau_d^{\mathrm{r},j} \int_I \frac{\partial \phi^E_{d_{\mathrm{e}}}\phi^E_{k_{\mathrm{e}}}}{\partial E}\phi^E_{l_{\mathrm{e}}}\mathrm{d}E \\ &\quad \cdot\Bigg[\int_V \phi^{\boldsymbol{x}}_{d_{\mathrm{s}}}\phi^{\boldsymbol{x}}_{k_{\mathrm{s}}}\phi^{\boldsymbol{x}}_{l_{\mathrm{s}}}\mathrm{d}\boldsymbol{x}\int_S \phi^{\theta}_{k_{\mathrm{o}}}\phi^{\theta}_{l_{\mathrm{o}}}\mathrm{d}\theta \\ &\quad +\delta^j_{l,k}\Bigg(\int_V \phi^{\boldsymbol{x}}_{d_{\mathrm{s}}}\phi^{\boldsymbol{x}}_{k_{\mathrm{s}}}\frac{\partial\phi^{\boldsymbol{x}}_{l_{\mathrm{s}}}}{\partial x_1}\mathrm{d}\boldsymbol{x}\int_S \cos\varphi\sin\theta\phi^{\boldsymbol{\Omega}}_{k_{\mathrm{o}}}\phi^{\boldsymbol{\Omega}}_{l_{\mathrm{o}}}\mathrm{d}\boldsymbol{\Omega} \\ &\quad + \int_V \phi^{\boldsymbol{x}}_{d_{\mathrm{s}}}\phi^{\boldsymbol{x}}_{k_{\mathrm{s}}}\frac{\partial\phi^{\boldsymbol{x}}_{l_{\mathrm{s}}}}{\partial x_2}\mathrm{d}\boldsymbol{x}\int_S \sin\varphi\sin\theta\phi^{\boldsymbol{\Omega}}_{k_{\mathrm{o}}}\phi^{\boldsymbol{\Omega}}_{l_{\mathrm{o}}}\mathrm{d}\boldsymbol{\Omega} \\ &\quad + \int_V \phi^{\boldsymbol{x}}_{d_{\mathrm{s}}}\phi^{\boldsymbol{x}}_{k_{\mathrm{s}}}\frac{\partial\phi^{\boldsymbol{x}}_{l_{\mathrm{s}}}}{\partial x_3}\mathrm{d}\boldsymbol{x}\int_S \cos\theta\phi^{\boldsymbol{\Omega}}_{k_{\mathrm{o}}}\phi^{\boldsymbol{\Omega}}_{l_{\mathrm{o}}}\mathrm{d}\boldsymbol{\Omega}\Bigg)\Bigg], \end{aligned} \tag{4.73}$$

where $A^{\mathrm{sd}}_{j\to j}(l,k)$ is obtained from equation (4.68).

In 2D case, the matrix $A^{\mathrm{sd}}_{j\to j}$ in equation (4.67) is defined by equation (4.68), in which the matrix $A_{j\to j}$ is defined by equation (4.61) and in which

$$\begin{aligned} A^{\mathrm{sd}}_1(l,k) &= \int_I \phi^E_{k_{\mathrm{e}}}\phi^E_{l_{\mathrm{e}}}\mathrm{d}E\Bigg(\int_V \frac{\partial\phi^{\boldsymbol{x}}_{k_{\mathrm{s}}}}{\partial x_2}\frac{\partial\phi^{\boldsymbol{x}}_{l_{\mathrm{s}}}}{\partial x_2}\mathrm{d}\boldsymbol{x}\int_0^{2\pi}\sin^2\theta\phi^{\theta}_{k_{\mathrm{o}}}\phi^{\theta}_{l_{\mathrm{o}}}\mathrm{d}\theta \\ &\quad + \int_V \frac{\partial\phi^{\boldsymbol{x}}_{k_{\mathrm{s}}}}{\partial x_2}\frac{\partial\phi^{\boldsymbol{x}}_{l_{\mathrm{s}}}}{\partial x_3}\mathrm{d}\boldsymbol{x}\int_0^{2\pi}\cos\theta\sin\theta\phi^{\theta}_{k_{\mathrm{o}}}\phi^{\theta}_{l_{\mathrm{o}}}\mathrm{d}\theta \\ &\quad + \int_V \frac{\partial\phi^{\boldsymbol{x}}_{k_{\mathrm{s}}}}{\partial x_3}\frac{\partial\phi^{\boldsymbol{x}}_{l_{\mathrm{s}}}}{\partial x_2}\mathrm{d}\boldsymbol{x}\int_0^{2\pi}\cos\theta\sin\theta\phi^{\theta}_{k_{\mathrm{o}}}\phi^{\theta}_{l_{\mathrm{o}}}\mathrm{d}\theta \\ &\quad + \int_V \frac{\partial\phi^{\boldsymbol{x}}_{k_{\mathrm{s}}}}{\partial x_3}\frac{\partial\phi^{\boldsymbol{x}}_{l_{\mathrm{s}}}}{\partial x_3}\mathrm{d}\boldsymbol{x}\int_0^{2\pi}\cos^2\theta\phi^{\theta}_{k_{\mathrm{o}}}\phi^{\theta}_{l_{\mathrm{o}}}\mathrm{d}\theta\Bigg) \end{aligned} \tag{4.74}$$

and

$$
\begin{aligned}
A_2^{\mathrm{sd}}(l,k) &= \Bigg(\sum_{d_\mathrm{s}=1}^{N_\mathrm{s}} \sum_{d_\mathrm{e}=1}^{N_\mathrm{e}} \sigma_d^j \int_I \phi_{d_\mathrm{e}}^E \phi_{k_\mathrm{e}}^E \phi_{l_\mathrm{e}}^E \mathrm{d}E \\
&\quad - \sum_{dd} \sigma_{dd}^{j\to j} \int_I \phi_{d_\mathrm{e}}^E \phi_{l_\mathrm{e}}^E \mathrm{d}E \int_I \phi_{d'_\mathrm{e}}^E \phi_{k_\mathrm{e}}^E \mathrm{d}E \int_0^{2\pi} \phi_{d'_\mathrm{o}}^\theta \phi_{k_\mathrm{o}}^\theta \mathrm{d}\theta \Bigg) \\
&\quad \cdot \Bigg(\int_V \phi_{d_\mathrm{s}}^{\boldsymbol{x}} \phi_{k_\mathrm{s}}^{\boldsymbol{x}} \frac{\partial \phi_{l_\mathrm{s}}^{\boldsymbol{x}}}{\partial x_1} \mathrm{d}\boldsymbol{x} \int_0^{2\pi} \sin\theta \phi_{k_\mathrm{o}}^\theta \phi_{l_\mathrm{o}}^\theta \mathrm{d}\theta \\
&\quad + \int_V \phi_{d_\mathrm{s}}^{\boldsymbol{x}} \phi_{k_\mathrm{s}}^{\boldsymbol{x}} \frac{\partial \phi_{l_\mathrm{s}}^{\boldsymbol{x}}}{\partial x_2} \mathrm{d}\boldsymbol{x} \int_0^{2\pi} \cos\theta \phi_{k_\mathrm{o}}^\theta \phi_{l_\mathrm{o}}^\theta \mathrm{d}\theta \Bigg). \qquad (4.75)
\end{aligned}
$$

The matrix $D_{j'\to j}^{\mathrm{sd}}$ is defined similarly as in equation (4.71), but in 2D the angular integrals are changed to $\int_0^{2\pi} \phi_{d_\mathrm{o}}^\theta \phi_{l_\mathrm{o}}^\theta \mathrm{d}\theta \int_0^{2\pi} \phi_{d'_\mathrm{o}}^\theta \phi_{k_\mathrm{o}}^\theta \mathrm{d}\theta$ and in which $D_{j'\to j}$ is defined by equation (4.62). Similarly, the matrix $A_{j\to j}^{\mathrm{r,sd}}$ in equation (4.72) is in 2D of the form

$$
\begin{aligned}
A_{j\to j}^{\mathrm{r,sd}}(l,k) &= A_{j\to j}^{\mathrm{sd}}(l,k) - \sum_{d_\mathrm{s}=1}^{N_\mathrm{s}} \sum_{d_\mathrm{e}=1}^{N_\mathrm{e}} \tau_d^{\mathrm{r},j} \int_I \frac{\partial \phi_{d_\mathrm{e}}^E \phi_{k_\mathrm{e}}^E}{\partial E} \phi_{l_\mathrm{e}}^E \mathrm{d}E \\
&\quad \cdot \Bigg[\int_V \phi_{d_\mathrm{s}}^{\boldsymbol{x}} \phi_{k_\mathrm{s}}^{\boldsymbol{x}} \phi_{l_\mathrm{s}}^{\boldsymbol{x}} \mathrm{d}\boldsymbol{x} \int_0^{2\pi} \phi_{k_\mathrm{o}}^\theta \phi_{l_\mathrm{o}}^\theta \mathrm{d}\theta \\
&\quad + \delta_{l,k}^j \Bigg(\int_V \phi_{d_\mathrm{s}}^{\boldsymbol{x}} \phi_{k_\mathrm{s}}^{\boldsymbol{x}} \frac{\partial \phi_{l_\mathrm{s}}^{\boldsymbol{x}}}{\partial x_2} \mathrm{d}\boldsymbol{x} \int_0^{2\pi} \sin\theta \phi_{k_\mathrm{o}}^\theta \phi_{l_\mathrm{o}}^\theta \mathrm{d}\theta \\
&\quad + \int_V \phi_{d_\mathrm{s}}^{\boldsymbol{x}} \phi_{k_\mathrm{s}}^{\boldsymbol{x}} \frac{\partial \phi_{l_\mathrm{s}}^{\boldsymbol{x}}}{\partial x_3} \mathrm{d}\boldsymbol{x} \int_0^{2\pi} \cos\theta \phi_{k_\mathrm{o}}^\theta \phi_{l_\mathrm{o}}^\theta \mathrm{d}\theta \Bigg) \Bigg], \qquad (4.76)
\end{aligned}
$$

where $A_{j\to j}^{\mathrm{sd}}(l,k)$ is obtained from equation (4.68) with 2D matrices defined by equations (4.61), (4.74) and (4.75).

4.7.5 Integration over elements and basis functions

In FEM, the basic idea is that the integration over an element e is done by mapping the actual global elements onto a master element e_0, in which the integration is easier to compute [182]. Figure 4.1 shows a transformation F_e, in which a master element e_0 is mapped onto an element e. Using this mapping the integration over an global element is

$$
\int_\mathrm{e} g(x_1,x_2,x_3)\mathrm{d}\boldsymbol{x} = \int_{e_0} (g\circ F_e)(\xi,\eta,\gamma)|J_{F_e}|\mathrm{d}\xi\mathrm{d}\eta\mathrm{d}\gamma,
$$

where $(g\circ F_e)(\xi,\eta,\gamma) = g(F_e(\xi,\eta,\gamma))$ is the composite function of F_e and g, $|J_{F_e}|$ is the absolute value of the determinant of the Jacobian J_{F_e} and F_e is the transformation depending on the element type. In 3D, F_e is of the form

$$
F_e(\xi,\eta,\gamma) = \sum_{i=1}^{8} \psi_{0,i}(\xi,\eta,\gamma)(x_1^i, x_2^i, x_3^i),
$$

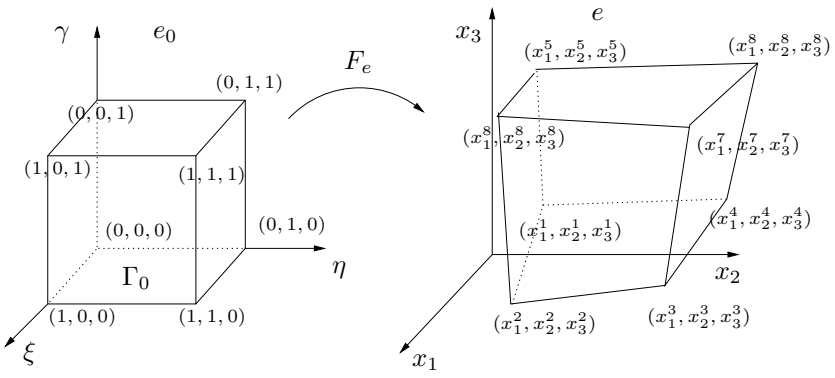

Figure 4.1: Mapping F_e from e_0 onto e for the brick. Γ_0 is the bottom face of an element e_0.

where $(x_1^i, x_2^i, x_3^i) := \boldsymbol{x}_i$ $(i = 1, ..., 8)$ are the nodes of the global element and $\psi_{0,i}$ are the basis functions of the master element e_0.

In FEM, the basis functions are typically such that the basis function ψ_i at nodes $\boldsymbol{x}_j$ fulfill

$$\psi_i(\boldsymbol{x}_j) = \begin{cases} 1, & i = j \\ 0, & \text{otherwise} \end{cases} .$$

This results in a sparse matrices in the linear systems, because most of the integrals become zero. The basis functions for a 3D brick of Figure 4.1 are [58]

$$\begin{aligned}
\psi_{0,1} &= \xi(1-\eta)(1-\gamma) \\
\psi_{0,2} &= \xi\eta(1-\gamma) \\
\psi_{0,3} &= (1-\xi)\eta(1-\gamma) \\
\psi_{0,4} &= (1-\xi)(1-\eta)(1-\gamma) \\
\psi_{0,5} &= \xi(1-\eta)\gamma \\
\psi_{0,6} &= \xi\eta\gamma \\
\psi_{0,7} &= (1-\xi)\eta\gamma \\
\psi_{0,8} &= (1-\xi)(1-\eta)\gamma,
\end{aligned}$$

where the indexes $i = 1, .., 8$ refer to the nodes, in which the basis function $\psi_{0,i}$ is one i.e. to the points $(1,0,0)$, $(1,1,0)$, $(0,1,0)$, $(0,0,0)$, $(1,0,1)$, $(1,1,1)$, $(0,1,1)$, $(0,0,1)$, respectively.

The transpose of the Jacobian matrix $J_{F_e}^{\mathrm{T}}$ can be computed from

$$J_{F_e}^{\mathrm{T}} = L(\xi, \eta, \gamma) X^e,$$

where

$$X^e = \begin{pmatrix} x_1^1 & x_2^1 & x_3^1 \\ \vdots & \vdots & \vdots \\ x_1^8 & x_2^8 & x_3^8 \end{pmatrix}$$

is the node matrix for an element e and

$$L(\xi,\eta,\gamma) = \begin{pmatrix} \frac{\partial\psi_{0,1}}{\partial\xi} & \cdots & \frac{\partial\psi_{0,8}}{\partial\xi} \\ \frac{\partial\psi_{0,1}}{\partial\eta} & \cdots & \frac{\partial\psi_{0,8}}{\partial\eta} \\ \frac{\partial\psi_{0,1}}{\partial\gamma} & \cdots & \frac{\partial\psi_{0,8}}{\partial\gamma} \end{pmatrix}.$$

For the spatial domain one also needs the integrals over the face Γ_e of an element e. This can be computed using the surface integral [182]

$$\int_{\Gamma_e} g(x_1,x_2,x_3)\mathrm{d}\boldsymbol{s} = \int_{\Gamma_0} (g\circ F_e)(\xi,\eta)\left\|\frac{\partial F_e}{\partial\xi}\times\frac{\partial F_e}{\partial\eta}\right\|\mathrm{d}\xi\mathrm{d}\eta,$$

where Γ_0 is the bottom face of the master element e_0 as shown in Figure 4.1.

The basis functions and integrals derived previously are for 3D bricks, which are used as spatial elements in 3D. The angular domain $\boldsymbol{\Omega}$ can be considered as a surface of a unit sphere. This surface can be divided into triangular elements for example by dividing the faces of an octahedron into four smaller triangular elements and in the same time keeping the distance of the new nodes from the origin equal to one. Similar triangular mesh is used in [102], but the refinement is started from an icosahedron. Here the octahedron is chosen as a starting point of the refinements, because it is symmetric in x_1- and x_2-directions. The octahedron based triangular meshes with one and two refinements are shown in Figure 4.2 (a) and (b). One could integrate directly over these triangles. However, this triangular approximation of the unit sphere is quite poor, if coarse mesh is used, because the triangles approximate the sphere only roughly. Instead, one can flatten the refined angles in $(\varphi,\theta)\in[0,2\pi[\times[0,\pi[$ plane and add extra nodes at angles $\theta=0,\pi,\ \varphi\in]0,2\pi]$ and $\varphi=2\pi,\ \theta\in[0,\pi]$ to be used in computations with spherical transformation. This flattening is shown in Figure 4.2 (c).

By triangular refinements one achieves nodes, which are arranged uniformly on a unit sphere. These angles can then be used with spherical transformation to model the surface of the sphere and the integrals over these triangular elements are done by mapping the general element e into a local element e_0. Thus, the angular integrals can be computed using equation

$$\int_e g\mathrm{d}\boldsymbol{\Omega} = \int_{\varphi_e}\int_{\theta_e} g\sin(\theta)\mathrm{d}\theta\mathrm{d}\varphi = \int_{e_0}(g\circ F_{e,\boldsymbol{\Omega}})(\xi,\eta)\sin\circ F_{e,\boldsymbol{\Omega},2}|J_{F_{e,\boldsymbol{\Omega}}}|\mathrm{d}\xi\mathrm{d}\eta,$$

where φ_e and θ_e are the integration intervals of element e and $F_{e,\boldsymbol{\Omega}} = \sum_{i=1}^{3}\psi_{0,i}(\xi,\eta)(\varphi_i,\theta_i)$. The points (φ_i,θ_i) $(i=1,2,3)$ are the coordinates of the triangle nodes of an element e. $F_{e,\boldsymbol{\Omega},2}$ is the second component of mapping $F_{e,\boldsymbol{\Omega}}$.

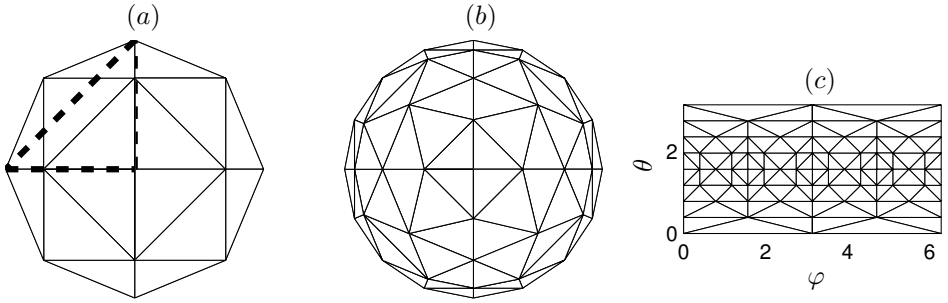

Figure 4.2: Angular mesh over the unit sphere achieved by the refinement of an octahedron. Figure (a) shows angular mesh after one refinement. Also one original face of an octahedron is drawn by dashed line. In (b), there is the angular mesh after two refinements. In (c), there the nodes from (b) are flattened into the plane.

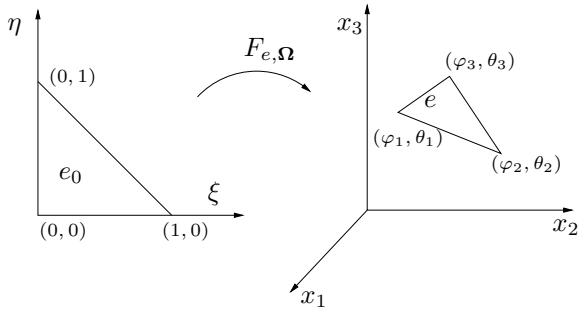

Figure 4.3: Mapping $F_{e,\mathbf{\Omega}}$ from a master element e_0 into general element e

The mapping $F_{e,\mathbf{\Omega}}$ is shown in Figure 4.3. $\psi_{0,i}$ $(i = 1, 2, 3)$ are the basis functions for a master triangular element e_0. The linear basis functions for e_0 are [58]

$$\begin{aligned} \psi_{0,1} &= 1 - \xi - \eta \\ \psi_{0,2} &= \xi \\ \psi_{0,3} &= \eta. \end{aligned}$$

The integration over the energy variable is 1D integral. Thus, the elements are sub-intervals. Again the sub-interval $e = [E_i, E_{i+1}]$ is mapped into a master element $e_0 = [0, 1]$. The mapping is now $F_{e,E} = \sum_{i=1}^{2} \psi_{0,i}(\xi)(E_i)$, where $\psi_{0,i}$ $i = 1, 2$ are the basis functions of the local element e_0. The linear basis functions of

e_0 are [58]

$$\begin{aligned} \psi_{0,1} &= 1-\xi \\ \psi_{0,2} &= \xi. \end{aligned}$$

In 2D spatial geometry, the spatial elements in 2D are chosen to be rectangular in shape. The linear basis functions for these elements are used [58]. The surface integral in 2D is a line integral. Also the angular integrals are line integrals over $\theta \in [0, 2\pi[$.

For simplicity the integrals over the basis functions are often computed using numerical integration techniques such as Gaussian quadrature [58], in which the integral is approximated with a finite sum

$$\int_{e_0} f = \sum_{i=1}^{n} w_i f_i,$$

where w_i are weighting coefficients and f_i is the value of f at a specific integration point. The coefficients and integration points depend on the shape of the master element e_0([58, 166, 20]).

4.7.6 Krylov subspace methods and parallel computing

The linear systems (4.53), (4.59), (4.67) and (4.72) contain matrices, which are large and sparse. The integral term in the BTE causes the matrices contain much more nonzeros than a typical differential equation with the same number of unknowns. Typically, the resulted big matrix is too big for the computer memory or it is at least too expensive to form the whole matrix. Therefor special methods are needed to handle the resulted big matrices. One possibility is to use Krylov subspace methods for solving the linear system $Ax = b$ [181, 82, 102, 157]. $m-$dimensional Krylov subspace is spanned by a given vector x_0, and increasing powers of A applied to x_0, up to the $(m-1)-$th power, that is

$$K_m(x_0, A) = \text{span}\{x_0, Ax_0, ..., A^{m-1}x_0\}.$$

In the Krylov space, the matrix free methods are possible, i.e. one does not need to construct the whole matrix A, instead only the product of the matrix A and the iterate x_i and sometimes the product $A^{\mathrm{T}}x_i$ are needed. In the case of BTE, the matrix A is constructed of smaller matrices including matrices for spatial, angular and energy grids. These matrices can be computed beforehand and the products Ax_i and $A^{\mathrm{T}}x_i$ can be computed using these smaller matrices, for example. These computations can be divided into several parallel computers, which speeds the calculations.

To solve the linear system using Krylov subspace methods, one can use for example a Portable, Extensible Toolkit for Scientific Computation -package (PETSc) [69], which is a library for the numerical solution of partial differential equations and related problems on high performance computers. It is designed for large-scale applications on parallel or serial computers and it uses Message Passing Interface

(MPI) standard for all message-passing communication. In PETSc, the matrix free method has several options for example conjugate gradient, bi-conjugate gradient, generalized minimal residual and least squares method [181, 80].

4.8 Photon incident simulations for the coupled system

Photon traveling in water was simulated using two coupled B-CSDAEs describing photons and electrons. Positron production was neglected. For two coupled B-CSDAEs the linear hull $X_{\mathrm{h}} = [(\phi_1, 0), (\phi_2, 0), ..., (\phi_N, 0), (0, \phi_1), ..., (0, \phi_N)]$ and the finite element approximation

$$\psi^{\mathrm{h}}(\boldsymbol{x}, E, \boldsymbol{\Omega}) = \sum_{k=1}^{N} (\alpha_k, \alpha_{k+N})^{\mathrm{T}} \phi_k(\boldsymbol{x}, E, \boldsymbol{\Omega})$$

in 3D and in 2D

$$\psi^{\mathrm{h}}(\boldsymbol{x}, E, \theta) = \sum_{k=1}^{N} (\alpha_k, \alpha_{k+N})^{\mathrm{T}} \phi_k(\boldsymbol{x}, E, \theta).$$

In the photon incident simulation, the linear system is of the form

$$\begin{pmatrix} A^{\mathrm{r}}_{1\to 1} & D_{2\to 1} \\ D_{1\to 2} & A^{\mathrm{r}}_{2\to 2} \end{pmatrix} \alpha = \begin{pmatrix} b \\ \mathbf{0} \end{pmatrix}, \tag{4.77}$$

where $\alpha = (\alpha_1, ..., \alpha_{2N})^{\mathrm{T}}$. The matrices $A^{\mathrm{r}}_{j\to j}$ and $D_{j'\to j}$ $(j, j' = 1, 2)$ are defined in 3D by equations (4.60) and (4.56), respectively. The vector b is obtained from $b = M_{\mathrm{b}}\Psi_0$, where M_{b} is defined by equation (4.58). In 2D, the matrices $A^{\mathrm{r}}_{j\to j}$, $D_{j'\to j}$ and the vector b are defined at the end of the Section 4.7.3 at page 72.

At the energies around several MeVs the Compton effect (see Section 2.3.1) is the main scattering event, which slows down photons and changes them to electrons. In the coupled system simulations, the maximum energy of the incident photon was around 10 MeV and only Compton effect was taken into account i.e. $\sigma_{1\to 1} = \frac{\mathrm{d}^2\sigma^{\mathrm{C}}}{\mathrm{d}E\mathrm{d}\boldsymbol{\Omega}_{\mathrm{p}}}$, $\sigma_{1\to 2} = \frac{\mathrm{d}^2\sigma^{\mathrm{C}}}{\mathrm{d}E\mathrm{d}\boldsymbol{\Omega}_{\mathrm{e}}}$, which were defined by equations (2.13) and (2.15) to describe the photon interactions. The total cross sections for photons σ_1 at different energies was obtained from the databases [19]. The electron inelastic scattering was included and the bremsstrahlung and elastic scattering were ignored. The bremsstrahlung production neglection means that $\sigma_{2\to 1} = 0$. The electron inelastic interactions were handled by using the restricted cross sections $\sigma^{\mathrm{r}}_{2\to 2} = \frac{\mathrm{d}^2\sigma^{\mathrm{Ie}}}{\mathrm{d}E_{\mathrm{pr}}\mathrm{d}\boldsymbol{\Omega}_{\mathrm{pr}}} + \frac{\mathrm{d}^2\sigma^{\mathrm{Ie}}}{\mathrm{d}E_{\mathrm{s}}\mathrm{d}\boldsymbol{\Omega}_{\mathrm{s}}}$ (defined by equation (2.19) with $E \le E_{\mathrm{cut},k_{\mathrm{e}}}$ and (2.20) with $E \ge E_{\mathrm{cut},k_{\mathrm{e}}}$). The cut-off energy was selected such that for incoming particle with energy $E_{k_{\mathrm{e}}}$ the cut-off energy $E_{\mathrm{cut},k_{\mathrm{e}}} = E_{k_{\mathrm{e}}} - E_{k_{\mathrm{e}}-2}$, where $E_{k_{\mathrm{e}}-2}$ is a lower energy node, when the nodes $E_{k_{\mathrm{e}}}$ are ordered in increasing order for increasing $k_{\mathrm{e}} = 1, .., N_{\mathrm{e}}$. This means that primary particle catastrophic collisions were those, in which the energy after scattering was less or equal to $E_{k_{\mathrm{e}}-2}$ and secondary particle catastrophic collisions were those, in which the energy after scattering was

more than $E_{\mathrm{cut},k_\mathrm{e}}$. The restricted total cross section σ_2^r was computed by integrating the restricted differential cross sections over angle and energy. In 2D, the total and restricted total cross sections were multiplied by π to take into account the scattering out of the plane. The restricted stopping power τ_2^r for electron was obtained as described in Section 2.6. The resulted $\tau_2^\mathrm{r}(\boldsymbol{x}, E)$ was non-monotonic with respect to energy and it was approximated to be constant to fulfill the condition (4.28). Because the equation for electrons in B-CSDAE include the differential term with respect to the energy variable, an initial energy point for the electron flux had to be defined. This additional condition was defined by equation (3.33) and it was accounted by adding one extra energy node at point $E = 11$ MeV and assigning the photon and electron flux values zero at those points by removing the specific rows and columns from the linear system (4.77).

An MC simulation was computed using the EGSnrc® code system in a normal PC (2 GHz Pentium with 2 GB memory) to be compared with the FEM simulation results in 2D and 3D. Because the MC simulation could only be done in 3D, the simulation was ran in a $[-5,5]\times[-5,5]\times[0,20]$ cm^3 water tank and the results were compared to 2D simulation results by considering a $0\times[-5,5]\times[0,20]$ cm^2 slice as a 2D data. The incoming photon beam was directed to $[-2,2]\times[-2,2]\times 0$ cm^2 area. The energy spectrum of the incoming beam was such that the maximum energy was 10 MeV and the energy spectrum decreased linearly from one to zero, when E went from 10 MeV to 8.35 MeV. $5\cdot 10^6$ photon histories were run. The photon and electron flux data were obtained from the scoring planes, which were perpendicular to the incoming beam. The data was scored from the planes of area of $[-1,1]\times[-1,1]$ cm^2 under the incident beam. The computations took approximately six hours. The bremsstrahlung process was excluded to be comparable with FEM simulation results. The results of the MC simulation are presented in Figure 4.4.

All the forward problem FEM simulations presented in this thesis were computed in two steps. First the smaller matrices, in which the linear system could be constructed using Kronecker tensor product, were generated using MATLAB® in a normal PC (2 GHz Pentium with 2 GB memory). These matrices were then written to files in a sparse matrix format. Then the resulted linear system was solved using PETSc and Krylov subspace matrix free methods in a PC cluster, in which 13 2.99 GHz Pentium IV processors were connected in parallel with 48.2 GB of total memory. The least-squares solution algorithm without preconditioning was used from the PETsc package for solving the linear system with Krylov methods [69].

PHOTON1_2D

The first simulation was made in 2D spatial geometry in a $[-5,5]\times[0,20]$cm^2 domain, which consisted of water. The incoming photon flux was located at the center of $[-5,5]$cm interval such that $\Gamma\in[-2,2]$cm, see Figure 4.5. The number of spatial nodes was $N_\mathrm{s} = 357$. The angular domain was divided into 64 evenly distributed elements, $\theta\in[0,2\pi[$ ($N_\mathrm{o} = 64$). In the incoming flux Ψ_0, only the forward node ($\theta = 0$) had nonzero value. Thus, the angular spectrum decreased linearly from 1 to 0, when θ went from 0 to the adjacent nodes $\theta = 2\pi/64$ and

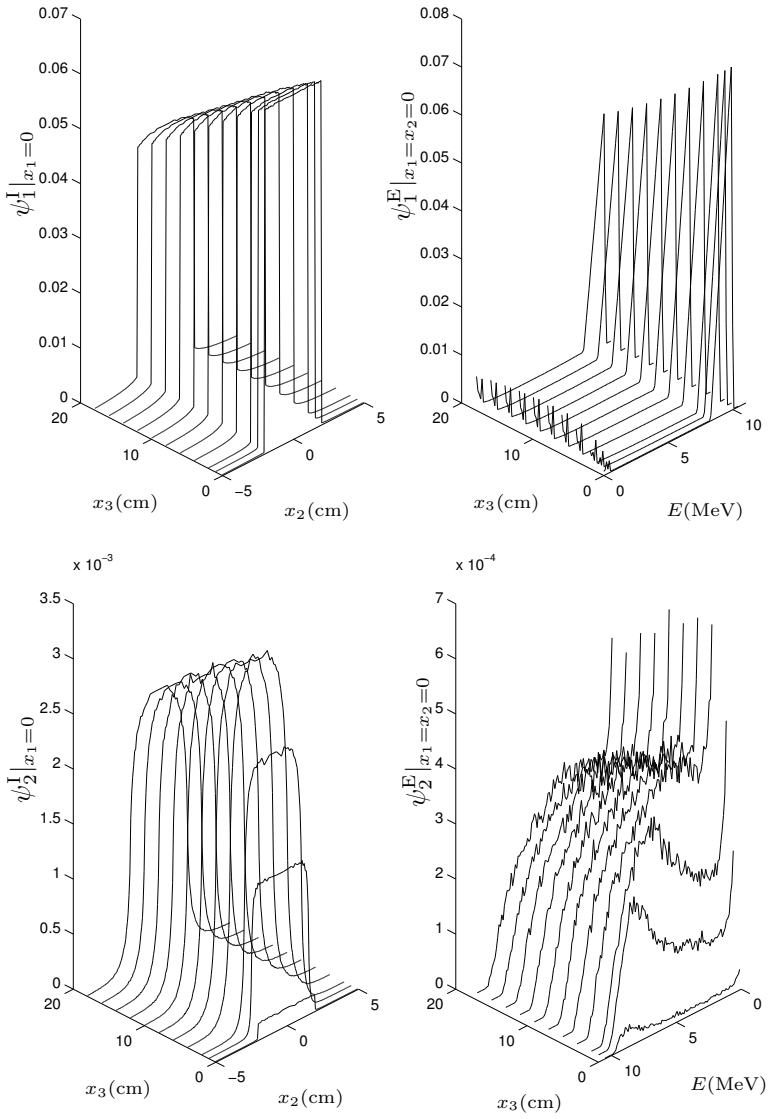

Figure 4.4: The photon incident MC simulation results in 3D. On the upper left corner there is the angle and energy integrated photon flux $\psi_1^{\mathrm{I}}|_{x_1=0}(\boldsymbol{x})(\mathrm{cm}^{-2})$ at the central slice ($x_1 = 0$). On the upper right corner there is the energy spectrum of the photon flux $\psi_1^{\mathrm{E}}|_{x_1=x_2=0}(\boldsymbol{x}, E)(\mathrm{cm}^{-2}\mathrm{MeV}^{-1})$ with respect to the x_3-axis. On the lower left corner there is the angle and energy integrated electron flux $\psi_2^{\mathrm{I}}|_{x_1=0}(\boldsymbol{x})(\mathrm{cm}^{-2})$. On the lower right corner there is the energy spectrum of the electron flux $\psi_2^{\mathrm{E}}|_{x_1=x_2=0}(\boldsymbol{x}, E)(\mathrm{cm}^{-2}\mathrm{MeV}^{-1})$. The MC flux results are presented per incident particle.

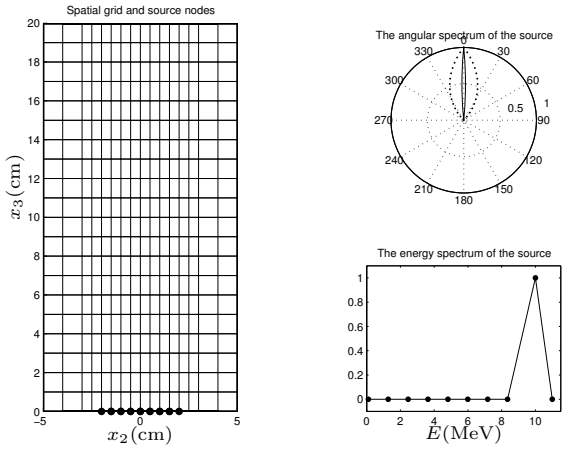

Figure 4.5: On the left there is the spatial grid in a homogeneous domain. The black circles at the bottom of the spatial grid illustrate the source nodes. On the upper right corner there is the angular spectrum of the source for the first FEM simulation (line) and for the second FEM simulation (dots). Below that, the energy spectrum of the source is shown with energy nodes as dots.

$\theta = 2\pi - 2\pi/64$. The energy domain $E = [0.1, 11]$ MeV was divided into nine elements ($N_\mathrm{e} = 10$). The energy spectrum of the incoming flux presented 10 MeV photons, thus the energy spectrum decreased linearly to zero when E went from node $E = 10$ MeV to the adjacent nodes $E = 8.35$ MeV and $E = 11$ MeV. The spatial grid and source information is shown in Figure 4.5. The total number of unknowns was $N = 2N_\mathrm{s}(N_\mathrm{e} - 1)N_\mathrm{o} = 411264$.

In the first photon incident simulation, the MATLAB® computations took approximately 8 minutes and the cluster computations took 3.7 hours. The desired residual (10^{-6}) was received after 6384 iterations. The solved integrated photon $\psi_1^\mathrm{I}(\boldsymbol{x})(\mathrm{cm}^{-2})$ and electron $\psi_2^\mathrm{I}(\boldsymbol{x})(\mathrm{cm}^{-2})$ fluxes (angle and energy integrated fluxes) are shown in Figure 4.6. In the same figure, also the photon $\psi_1^\mathrm{E}|_{x_2=0}(\boldsymbol{x}, E)(\mathrm{cm}^{-2}\mathrm{MeV}^{-1})$ and electron $\psi_2^\mathrm{E}|_{x_2=0}(\boldsymbol{x}, E)(\mathrm{cm}^{-2}\mathrm{MeV}^{-1})$ energy spectra (angle integrated fluxes) with respect to x_3-axis are shown. The FEM simulation results are normalized to match to the MC simulation data near the source. With the same normalization the electron flux FEM results are also multiplied by five to be comparable with the MC results.

PHOTON2_2D

In the second photon incident FEM simulation, the angular domain was divided only in eight evenly distributed elements ($N_\mathrm{o} = 8$). In the incoming flux Ψ_0, only the forward node ($\theta = 0$) had nonzero value and the angular spectrum decreased

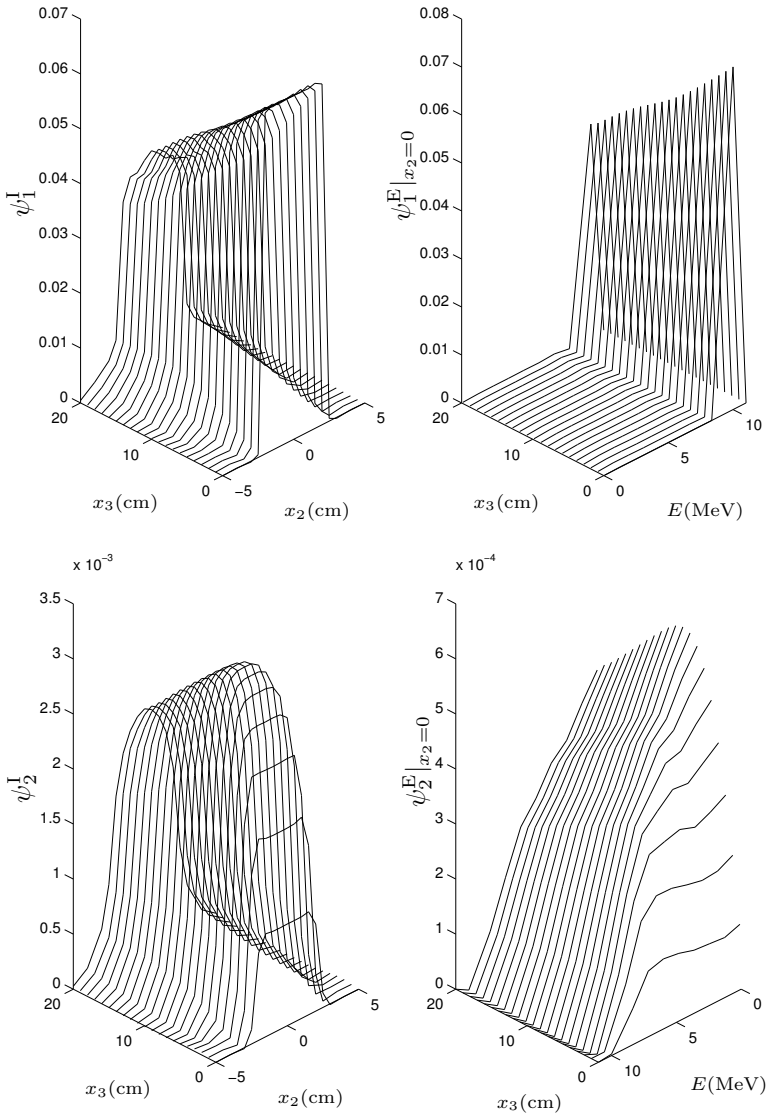

Figure 4.6: Results for PHOTON1_2D simulation. On the upper left corner there is the angle and energy integrated photon flux $\psi_1^{\mathrm{I}}(\boldsymbol{x})(\mathrm{cm}^{-2})$. On the upper right corner there is the energy spectrum of the photon flux $\psi_1^{\mathrm{E}}|_{x_2=0}(\boldsymbol{x}, E)(\mathrm{cm}^{-2}\mathrm{MeV}^{-1})$ with respect to the x_3-axis. On the lower left corner there is the angle and energy integrated electron flux $\psi_2^{\mathrm{I}}(\boldsymbol{x})(\mathrm{cm}^{-2})$. On the lower right corner there is the energy spectrum of the electron flux $\psi_2^{\mathrm{E}}|_{x_2=0}(\boldsymbol{x}, E)(\mathrm{cm}^{-2}\mathrm{MeV}^{-1})$.

linearly from 1 to 0, when θ went from 0 to the adjacent nodes $\theta = 2\pi/8$ and $\theta = 2\pi - 2\pi/8$. The spatial grid ($N_\mathrm{s} = 357$), spatial source nodes, energy spectrum and energy grid ($N_\mathrm{e} = 10$) were the same as in the first photon incident FEM simulation in 2D (Figure 4.5). The total number of unknowns was $N = 51408$. The MATLAB® computations took approximately 1 minute and the cluster computations took 14 minutes with 1500 iterations, reaching the residual of 10^{-6}. The photon and electron flux results are presented in Figure 4.7. The FEM results are normalized to match the MC data near the source. With the same normalization the electron flux FEM results are also multiplied by ten to be comparable with the MC results.

PHOTON1_3D

The third photon incident simulation was made in a 3D water tank, size of $10\times10\times20$ cm^3. The tank was divided into cubic elements. The photon source was directed to $[-2,2]\times[-2,2]\times0$ cm^2 area. The number of spatial nodes was $N_\mathrm{s} = 1029$. The angular domain S was approximated by triangular elements with $N_\mathrm{o} = 66$ being as the angular grid in Figure 4.2 (*b* and *c*). In the incoming flux, only the forward node ($\theta = 0$) had nonzero value 1, and the angular spectrum decreased linearly to the nearest nodes $\theta = \pi/8$ ($\varphi \in [0, 2\pi[$) being symmetric in φ. The spatial grid with source elements and the angular spectrum of the source are shown in Figure 4.8. The energy domain and the energy spectrum of the source was the same as in the previous 2D simulations (Figure 4.5), but now with a finer energy grid $N_\mathrm{e} = 13$. The total number of unknowns was then $N = 1629936$. The MATLAB® computations took approximately 40 minutes and the cluster computations took approximately 59 hours with 5551 iterations in order to reach the desired residual 10^{-6}. The integrated photon and electron fluxes and energy spectra are shown in Figure 4.9. The simulation results are normalized to match the MC data near the source. With the same normalization the FEM electron flux results are also multiplied by four.

PHOTON2_3D

In the fourth photon incident FEM simulation, the computations were made at the same spatial grid as in the previous 3D simulation ($N_\mathrm{s} = 1029$), but now the source was modeled to be more forward peaked ($N_\mathrm{o} = 66$). Thus, only the forward node ($\theta = 0$) had nonzero value at the source value vector Ψ_0. To model better the forward directed source the nearest angular nodes to the forward node were moved to points, in which $\theta = 0.1$, φ remained the same. The spatial grid with source elements, the angular grid and the source angular spectrum are shown in Figure 4.8. The energy domain was as in the previous FEM 3D simulation ($N_\mathrm{e} = 13$). The total number of unknowns was $N = 1629936$. The MATLAB® computations took approximately 40 minutes. The convergence rate in solving the linear system was poor and the cluster computations took approximately 110 hours when the maximum number of iterations (10000) was received with residual 10^{-5}. The integrated photon and electron fluxes and energy spectra are shown in

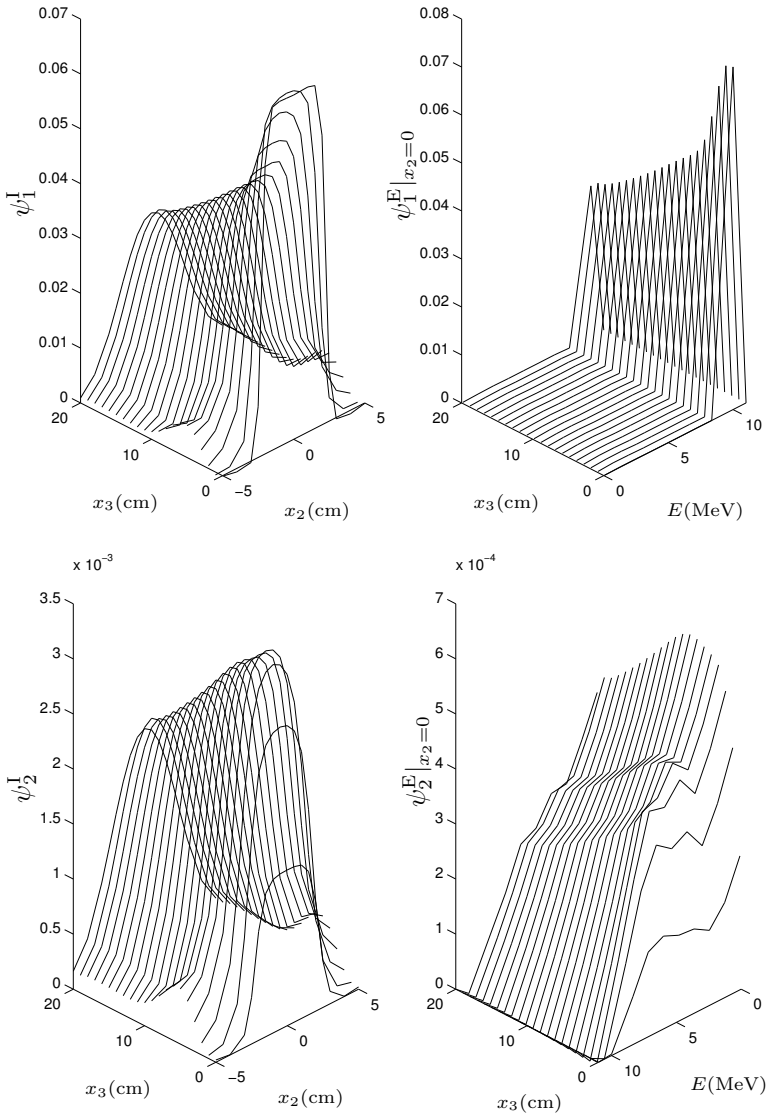

Figure 4.7: Results for PHOTON2_2D simulation. On the upper left corner there is the angle and energy integrated photon flux $\psi_1^{\mathrm{I}}(\boldsymbol{x})(\mathrm{cm}^{-2})$. On the upper right corner there is the energy spectrum of the photon flux $\psi_1^{\mathrm{E}}|_{x_2=0}(\boldsymbol{x}, E)(\mathrm{cm}^{-2}\mathrm{MeV}^{-1})$ with respect to the x_3-axis. On the lower left corner there is the angle and energy integrated electron flux $\psi_2^{\mathrm{I}}(\boldsymbol{x})(\mathrm{cm}^{-2})$. On the lower right corner there is the energy spectrum of the electron flux $\psi_2^{\mathrm{E}}|_{x_2=0}(\boldsymbol{x}, E)(\mathrm{cm}^{-2}\mathrm{MeV}^{-1})$.

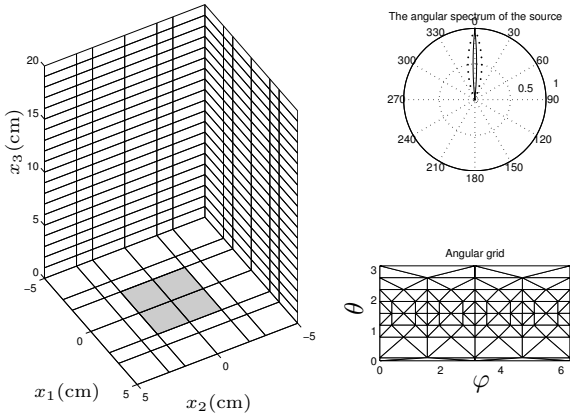

Figure 4.8: On the left there is the spatial 3D grid, in which the boundary source elements are filled with gray color. On the right upper corner there are the angular spectra of the sources for the PHOTON1_3D (dots) and PHOTON2_3D (line) simulations. On the right lower corner there is the angular grid used in PHOTON2_3D simulation.

Figure 4.10. The simulation results are normalized to match the MC data near the source. With the same normalization the FEM electron flux results are also multiplied by three.

For better comparison of the simulations, the integrated photon and electron fluxes are drawn with respect to x_3-variable in Figure 4.11 for all photon incident simulations. In Figure 4.12, the average doses with respect to depth (x_3-axis) are also shown for all photon incident simulations.

4.9 Discussion for the photon incident simulations

The photon incident forward problem was simulated using two coupled B-CSDAEs. The coupled system of BTEs is not used here, because the electron interactions would require very dense spatial grids and make the computations impossible in these geometries with the used methods. With the B-CSDAEs the electron interactions are handled with restricted cross sections and restricted stopping powers, which enables to use sparser spatial grids. The FEM simulations are compared with earlier ran MC results, in which the energy spectrum of the incident beam was slightly different from the one in FEM simulations. However, it is assumed that this has only minor effect on the results of the simulations.

In the PHOTON1_2D simulation, the coupled system was solved in 2D spatial domain with very fine angular mesh. When comparing these results (Figure 4.6) to the MC results (Figure 4.4), it can be seen that the PHOTON1_2D results are in quite good agreement with the MC data. This can also be seen in Figures 4.11

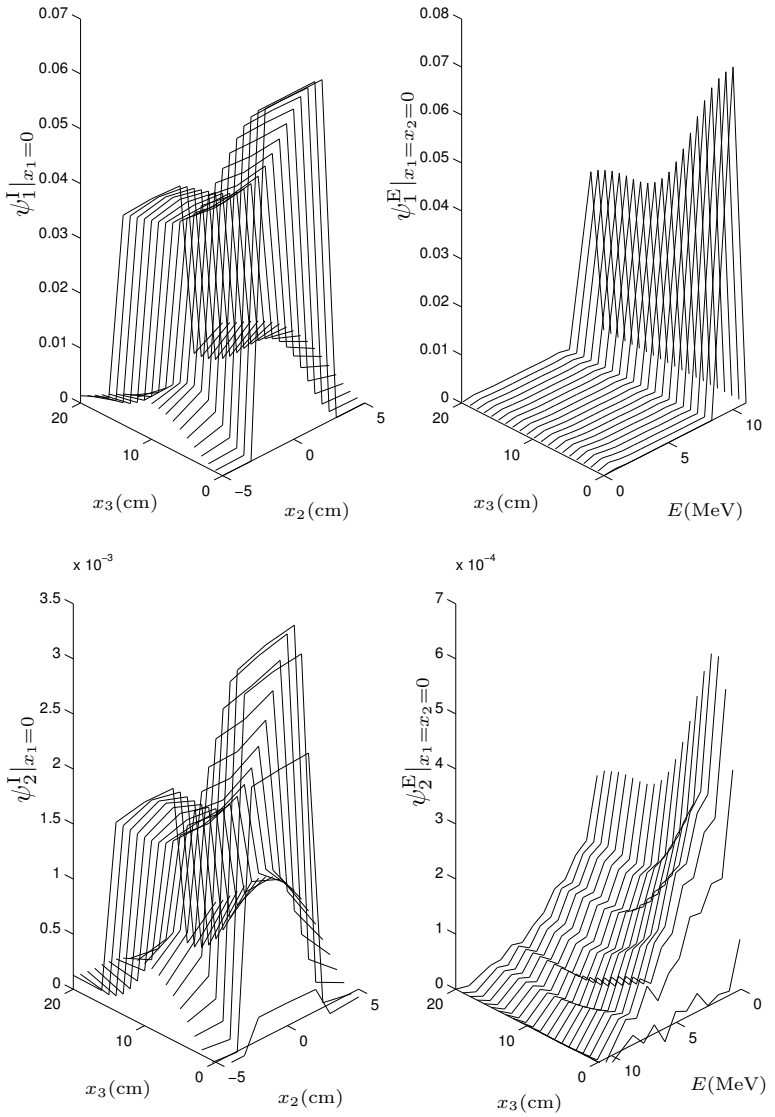

Figure 4.9: Results for PHOTON1_3D simulation. On the upper left corner there is the angle and energy integrated photon flux $\psi_1^{\mathrm{I}}|_{x_1=0}(\boldsymbol{x})(\mathrm{cm}^{-2})$ at the central slide ($x_1 = 0$). On the upper right corner there is the energy spectrum of the photon flux $\psi_1^{\mathrm{E}}|_{x_1=x_2=0}(\boldsymbol{x}, E)(\mathrm{cm}^{-2}\mathrm{MeV}^{-1})$ with respect to the central x_3-axis. On the lower left corner there is the angle and energy integrated electron flux $\psi_2^{\mathrm{I}}|_{x_1=0}(\boldsymbol{x})(\mathrm{cm}^{-2})$. On the lower right corner there is the energy spectrum of the electron flux $\psi_2^{\mathrm{E}}|_{x_1=x_2=0}(\boldsymbol{x}, E)(\mathrm{cm}^{-2}\mathrm{MeV}^{-1})$.

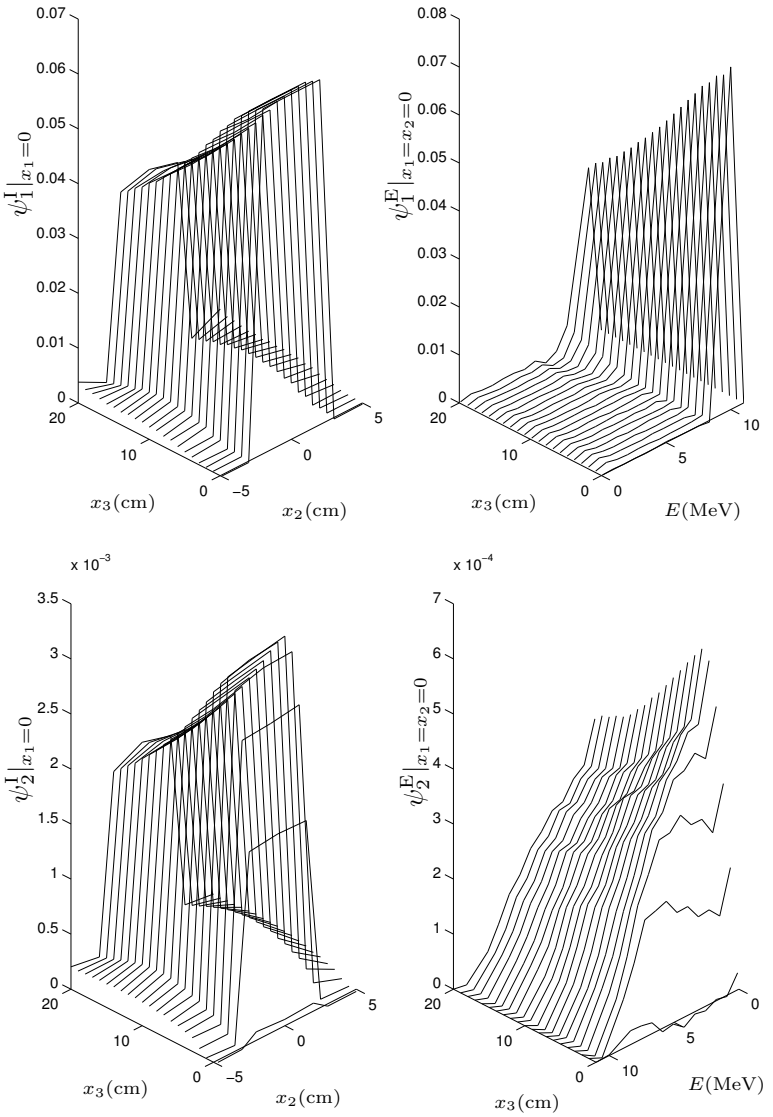

Figure 4.10: Results for PHOTON2_3D simulation. On the upper left corner there is the angle and energy integrated photon flux $\psi_1^{\mathrm{I}}|_{x_1=0}(\boldsymbol{x})(\mathrm{cm}^{-2})$ at the central slide ($x_1 = 0$). On the upper right corner there is the energy spectrum of the photon flux $\psi_1^{\mathrm{E}}|_{x_1=x_2=0}(\boldsymbol{x}, E)(\mathrm{cm}^{-2}\mathrm{MeV}^{-1})$ with respect to the central x_3-axis. On the lower left corner there is the angle and energy integrated electron flux $\psi_2^{\mathrm{I}}|_{x_1=0}(\boldsymbol{x})(\mathrm{cm}^{-2})$. On the lower right corner there is the energy spectrum of the electron flux $\psi_2^{\mathrm{E}}|_{x_1=x_2=0}(\boldsymbol{x}, E)(\mathrm{cm}^{-2}\mathrm{MeV}^{-1})$.

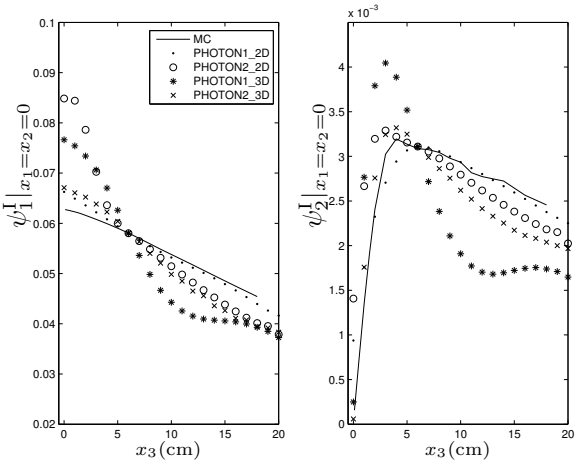

Figure 4.11: All the photon incident FEM and MC simulation results. On the left there are the angle and energy integrated photon fluxes $\psi_1^{\mathrm{I}}|_{x_1=x_2=0}(\boldsymbol{x})(\mathrm{cm}^{-2})$ at the central axis with respect to depth x_3. On the right there are the angle and energy integrated electron fluxes $\psi_2^{\mathrm{I}}|_{x_1=x_2=0}(\boldsymbol{x})(\mathrm{cm}^{-2})$ with respect to depth x_3. The FEM and MC results are normalized to have the same value at the depth $x_3 = 6$ cm.

and 4.12. The integrated photon flux ψ_1^{I} in the FEM results spreads more to the x_2 direction at the depth $x_3 = 20$ cm than the MC photon flux. This error is probably caused by the differences at the incident sources. In the MC simulation, the incident photons were forward directed and the intensity of the incident photon beam was not modulated. Thus, the incident beam has sharp intensity profile at the edge of the incoming boundary. In the FEM simulations, incident photons had small angular deviation, although it was selected to be small, and the source spatial edges were modeled according to the spatial grid and decreased linearly, when x_2 went from the outermost source node to the nearest non-source node. This spreading can also be seen from the integrated electron flux ψ_2^{I} in Figure 4.6. The photon energy spectrum ψ_1^{E} of the PHOTON1_2D results differ also at the small energies, in which the MC data has small integrated flux values. This is probably caused by the coarse energy mesh and by the neglection of the photon elastic scattering and the photoelectric effect and also because the minimum energy was 0.1 MeV in the PHOTON1_2D simulation. The differences in between the PHOTON1_2D and MC results in the electron energy spectrum ψ_2^{E} are probably caused by the coarse energy mesh and by the use of the CSDA for the forward peaked electron scattering. Also the neglection of electron elastic scattering causes some error in the PHOTON1_2D electron flux. Also here the 2D PHOTON1_2D data is compared to the 3D MC data, which alters the results, be-

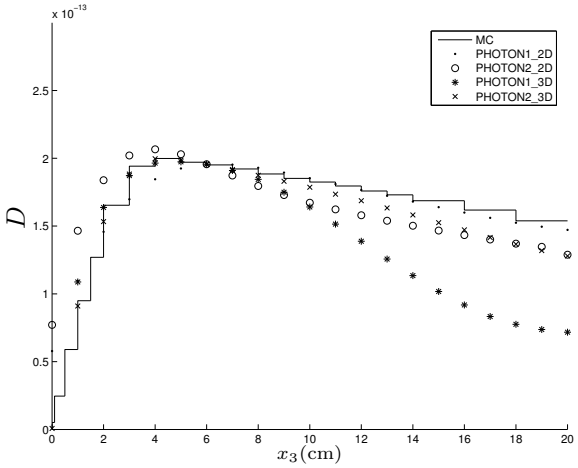

Figure 4.12: The average depth dose profiles for all photon incident simulations. MC dose data D(Gy) per incident particle is the average dose in each scoring plane volume, which include the whole spatial domain in x_1 and x_2 directions. From the FEM simulation electron flux results the average dose is computed at each depth x_3 including x_1 and x_2 directions. The FEM and MC results are normalized to be the same at the depth $x_3 = 6$ cm.

cause the scatterings from the surroundings are neglected in 2D results. However, despite of these errors and comparison difficulties, the PHOTON1_2D simulation results show that the radiotherapy forward problem can be solved quite accurately using FEM in 2D.

In PHOTON2_2D, the angular spectrum of the source nodes was sparser than in PHOTON1_2D simulation. PHOTON2_2D simulation was run to demonstrate the effect of wider angular source distribution. The reason, why in PHOTON1_2D simulation the angular mesh was divided into 64 evenly distributed elements, was to model the forward directed source, which was the case in the MC simulation. When the angular spectrum is wider the MC results are not comparable with the PHOTON2_2D results, because in the MC code it was not possible to change the angular distribution without using some scatterer, which would also create incoming electrons. The effect of wider angular spectrum can be seen from PHOTON2_2D simulation results (Figure 4.7), in which the integrated angular fluxes decrease much faster than the integrated fluxes with more peaked source (Figure 4.6). This is evident because with wider angular spectrum a greater part of the flux is directed out of the central axis and thus the spreading at the deeper depths is greater in both integrated photon and electron fluxes in PHOTON2_2D simulation results than those in PHOTON1_2D simulation results. From Figure 4.11 it can be seen that with wider angular distribution of the source, the integrated photon

flux (with respect to depth) decrease near the source boundary much faster than the MC or the PHOTON1_2D results. The PHOTON2_2D integrated electron flux also increases faster near the source boundary and decreases faster at deeper depths than the MC or the PHOTON1_2D results.

The MC simulation was run in a 3D geometry and some of the FEM simulations were done in a 2D geometry. In 2D geometry, the scattering out of plane is neglected, which may cause some inaccuracy in the results. However, these are thought to be minor due to fact that the scattering from other parts than the plane is only minor or at least the neglection of the scattering out of the plane and to the plane does not change the shape of the particle fluxes at that plane in homogeneous domain. Also these issues are not essential for the purpose of this study, which is to demonstrate the use of transport equation in radiotherapy purposes and not to use it as an accurate dose calculation procedure. These 2D simulations are shown here to demonstrate that FEM is suitable in simulating the transport of ionizing radiation with transport equations. However, the simulation in natural 3D geometry is very important and that is why PHOTON1_3D and PHOTON2_3D simulations were carried out in 3D spatial geometry. In 3D, it was not possible to use as fine angular mesh as in the first simulation and the effect of wider angular spectrum is seen in the PHOTON1_3D simulation results (Figure 4.9). However, these results show that FEM can be used in actual 3D geometry to solve the transport equations for radiotherapy purposes, but so far the computations are too expensive to model forward peaked sources with finer angular mesh. In the depth flux curves in Figure 4.11, one sees oscillations in PHOTON1_3D simulation results. It might indicate that the spatial and angular grids are too sparse. This oscillation is almost disappeared in PHOTON2_3D simulation with more forward directed source.

In PHOTON2_3D simulation, the forward directed source was modeled by reordering the nodes on a sphere. The resulted disordered angular mesh may not be the best option, because it does not consider scatterings from other directions equally. Also the used angular mesh with small element in the forward direction clearly increased the number of iterations in finding the solution, which indicate that the system is numerically unstable. Here the reordering of the angular nodes was just used to demonstrate that with more forward peaked scattering the obtained PHOTON2_3D results in Figure 4.10 are quite close to the MC results, which can be seen better from Figures 4.11 and 4.12. Small oscillation can be seen also from PHOTON2_3D results, which may indicate that the spatial grid is too sparse.

In the coupled system simulations, the FEM results are normalized to agree with the MC results at a specific point. This is done for both photon and electron fluxes. At first it was assumed that only the normalization of photon flux would be enough and that the same normalization factor could be used for the electron flux. However, with the same normalization the FEM simulation electron fluxes had to be multiplied by some value between five to ten depending on the angular grid to make the FEM results comparable with the MC results. This is something that is not clearly understood. The shape of the electron flux from the FEM

results is the same, but its magnitude is less than the electron flux from the MC results. It may be caused by the fact that photon Compton scattering is delta-shaped and this is approximated in a mesh, in which the data has always some width. The cross section data is normalized to fulfill the coercivity condition, which may cause these errors to the computations. This data normalization can be accounted, when computing the dose from the electron flux values, because if the same normalization is used for all scattering data, then the resulted fluxes could be handled according to this normalization. Further, because no exact dose was sought in the simulations, these normalization issues are not the main concerns.

As a conclusion of this discussion, one can say that all the photon incident simulations indicate that FEM can be used in solving the coupled system of B-CSDAEs. Although problems exists in the simulation of the forward directed sources in 3D, these problems are mainly computational and may disappear with more powerful computers. Also it is worth noting that no preconditioning were used in the computations. The use of preconditioning would decrease the computational times significantly.

4.10 Electron incident simulations for one B-CSDAE

The electron traveling in medium was simulated using one B-CSDAE in 3D. The photon production via bremsstrahlung event was neglected. Also positron production was neglected. The linear hull was $X_{\mathrm{h}} = [\phi_1, ..., \phi_N]$ and the finite element approximation of the electron flux was

$$\psi^{\mathrm{h}}(\boldsymbol{x}, E, \boldsymbol{\Omega}) = \sum_{k=1}^{N} \alpha_k \phi_k(\boldsymbol{x}, E, \boldsymbol{\Omega}).$$

The system of linear equations (4.49) reduced to $A^{\mathrm{r}}_{2\to 2}\alpha = b$, where $\alpha = (\alpha_1, ..., \alpha_N)^{\mathrm{T}}$ and $A^{\mathrm{r}}_{2\to 2}$ was obtained from equation (4.60) and $b = M_{\mathrm{b}}\Psi_0$, where M_{b} was achieved from equation (4.58).

The electron incident simulations were done in a 3D geometry having similar spatial domain as in the coupled system 3D simulation in water (Figure 4.8) with $N_{\mathrm{s}} = 1029$. The angular domain consisted of triangular elements with one refinement of the octahedron as shown in Figure 4.2 (a). The source was assumed to have a direction to the positive x_3-axis. Thus, only the forward nodes ($\theta = 0,\ \varphi \in [0, 2\pi[$) received nonzero value at the source value vector Ψ_0 and the source angular spectrum decreased from 1 to 0, when θ went from 0 to adjacent node 0.79. The number of angular nodes was $N_{\mathrm{o}} = 18$. The energy interval $I = [0.1, 11]$ MeV was divided into 12 sub-intervals ($N_{\mathrm{e}} = 13$) and the last node was removed from the linear system to take into account the condition (3.33). The energy spectrum of the source nodes was the same as in the previous photon incident simulations (Figure 4.5). The total number of unknowns was $N = N_{\mathrm{s}}(N_{\mathrm{e}} - 1)N_{\mathrm{o}} = 222264$. The electron elastic scattering was also neglected and only the inelastic scattering was considered. Thus, $\sigma^{\mathrm{r}}_{2\to 2}$ and σ^{r}_{2} were the same as in the photon incident simulation in Section 4.8 with similarly defined

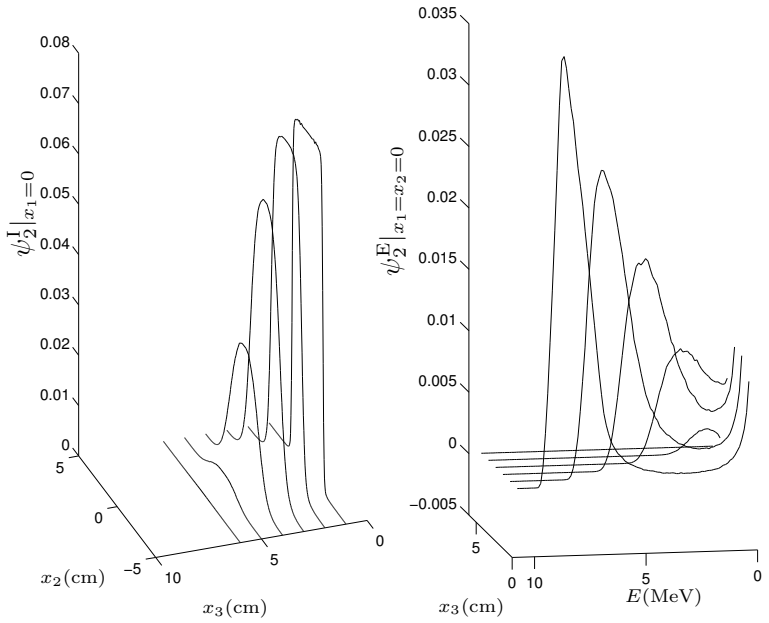

Figure 4.13: The MC electron incident simulation results at the depths of $x_3 = 1, 2, 3, 4, 5, 6$ cm. On the left is the angle and energy integrated electron flux $\psi_2^{\mathrm{I}}|_{x_1=0}(\boldsymbol{x})(\mathrm{cm}^{-2})$ at the central slice. On the right is the angle integrated electron flux $\psi_2^{\mathrm{E}}|_{x_1=x_2=0}(\boldsymbol{x}, E)(\mathrm{cm}^{-2}\mathrm{MeV}^{-1})$. The MC results are presented per incident particle.

cut-off energy $E_{\mathrm{cut},k_{\mathrm{e}}}$. Also the restricted stopping power τ_2^{r} was approximated to be constant with respect to energy to fulfill the condition (4.28).

An MC simulation was run similarly as in Section 4.8, but now for the electron incident flux with electron spectrum as in Figure 4.5. The MC computations took approximately four hours in a normal PC (2 GHz Pentium with 2 GB memory) and the results are shown in Figure 4.13.

ELECTRON1

For the first electron incident FEM simulation, the MATLAB® computations took approximately 9 minutes and the cluster computations took 1.3 hours. The number of iterations needed to solve the linear system was 2377 with the residual of 10^{-6}. The integrated electron flux at the central slice ($x_1 = 0$) and the energy spectrum at the central axis ($x_1 = x_2 = 0$) are shown in Figure 4.14.

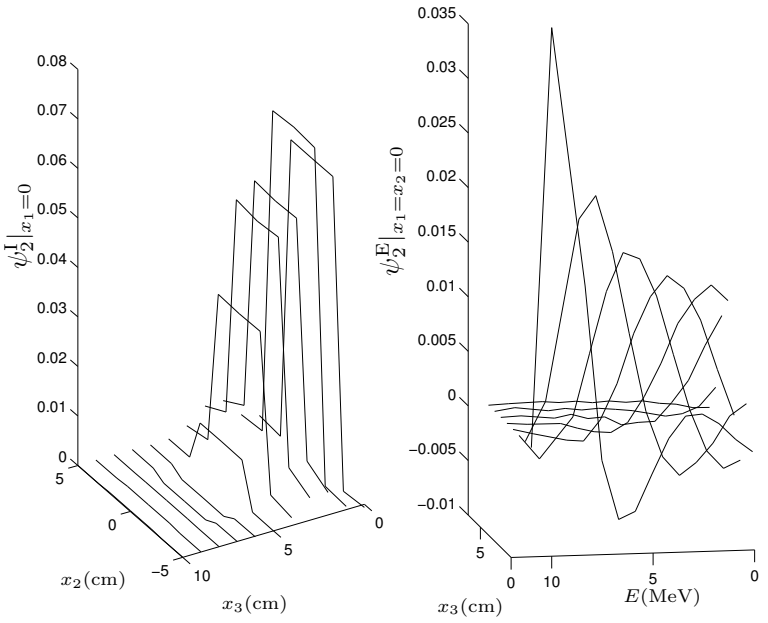

Figure 4.14: ELECTRON1 simulation results. On the left there is the angle and energy integrated electron flux $\psi_2^{\mathrm{I}}|_{x_1=0}(\boldsymbol{x})(\mathrm{cm}^{-2})$ at the central slice. On the right there is the angle integrated electron flux $\psi_2^{\mathrm{E}}|_{x_1=x_2=0}(\boldsymbol{x}, E)(\mathrm{cm}^{-2}\mathrm{MeV}^{-1})$ at the depths of $x_3 = 0, 1, 2, 3, 4, 5, 6, 7$ cm. The results are normalized to be equal with the MC results near the source.

ELECTRON2

In the second electron incident FEM simulation, the stream-line diffusion was used to stabilize the linear system. For one B-CSDAE the linear system with stream-line-diffusion method is of the form $A_{2\to 2}^{\mathrm{r,sd}}\alpha = b$, where now $A_{2\to 2}^{\mathrm{r,sd}}$ is obtained from equation (4.73). The factor $\delta_{l,k}^2$ was selected according to equation (4.63) with $c = 1$, hence $\delta_{l,k}^2 = 0.01$. The MATLAB® computations took approximately 9 minutes and the cluster computations took 1.5 hours with 1166 iterations to obtain the desired residual of 10^{-6}. The integrated electron flux and energy spectrum are shown in Figure 4.15. For better comparisons the integrated electron flux for all electron incident simulations with respect to x_3-variable at the central axis ($x_1 = x_2 = 0$) is shown in Figure 4.16.

4.11 Discussion for the electron incident simulations

The transport of high energy electrons was simulated using one B-CSDAE in 3D geometry. The use of one equation instead of three coupled equations means

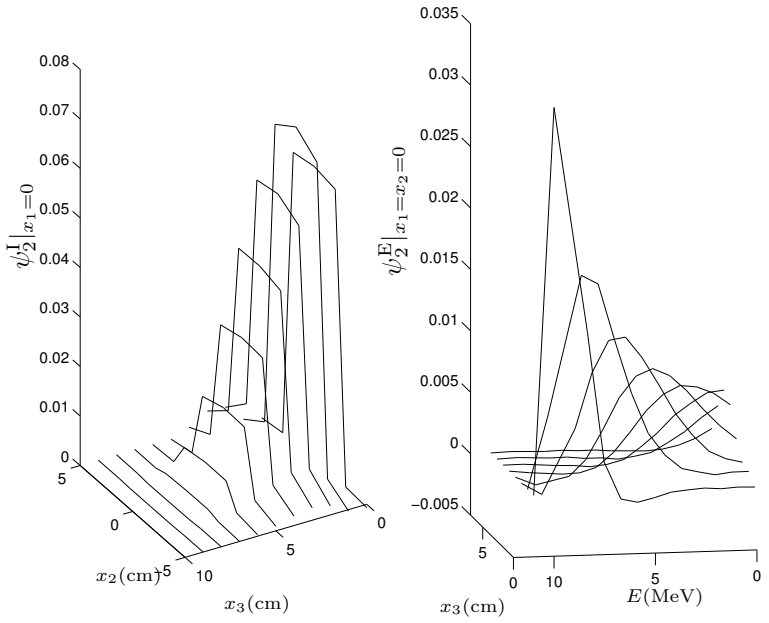

Figure 4.15: ELECTRON2 simulation results, when the stream-line diffusion method was used. On the left there is the angle and energy integrated electron flux $\psi_2^{\mathrm{I}}|_{x_1=0}(\boldsymbol{x})(\mathrm{cm}^{-2})$ at the central slice. On the right there is the angle integrated electron flux $\psi_2^{\mathrm{E}}|_{x_1=x_2=0}(\boldsymbol{x}, E)(\mathrm{cm}^{-2}\mathrm{MeV}^{-1})$ at the depths of $x_3 = 0, 1, 2, 3, 4, 5, 6, 7$ cm. The results are normalized to be equal with the MC results near the source.

that positron and photon productions are neglected. The neglection of photon production causes small error in the results. Also the use of B-CSDAE in electron incident simulation causes errors to results, because the momentum transfer χ (defined by equation (3.25)) is neglected. These errors are thought to be minor to demonstrate that the transport of electrons work in general.

When comparing the angle and energy integrated fluxes ψ_2^{I} and energy spectrum ψ_2^{E} in Figures 4.13-4.15, it can be seen that the FEM results have similarities with the MC results. Most of differences can be found at the energy spectrum at small energies, in which the MC energy spectrum highly increases. In FEM simulations this can not be seen. This error in FEM results is probably because of the CSDA approximation for small energy transfers and the neglection of the electron elastic scattering.

The effect of more wider source angular spectrum can be seen in FEM ψ_2^{I} results, in which at the depth $x_3 = 3$ cm the flux is slightly spread in x_2 direction. This spreading also causes the depth flux in FEM results in Figure 4.16 to decrease

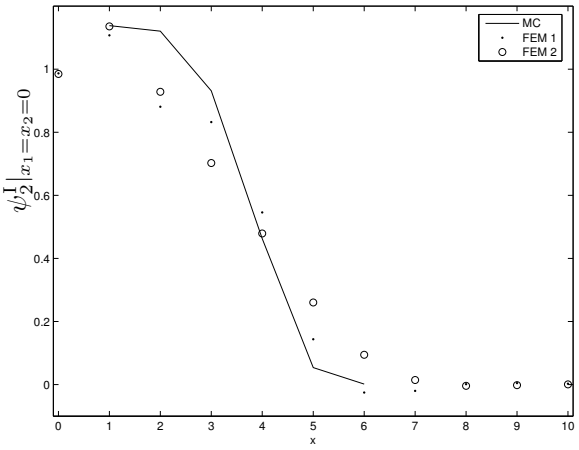

Figure 4.16: The angle and energy integrated electron fluxes $\psi_2^{\mathrm{I}}|_{x_1=x_2=0}(\boldsymbol{x})(\mathrm{cm}^{-2})$ with respect to x_3-variable at the central axis for ELECTRON1 and ELECTRON2 simulations. The MC data is normalized such that it equals the ELECTRON2 simulation results at depth $x_3 = 1$ cm.

much rapidly than the MC results. However, this spreading is much smaller than in the photon incident simulations, which were very sensitive to the source angular spectrum. Probably this is because of the different scattering behavior. The electron scattering is much more forward peaked than the photon scattering. Also because of the CSDA, more sparser spatial grids can be used. Thus, the problems that arose from too sparse spatial grids in photon incident simulations are not seen in these electron incident simulations.

The electron incident simulations demonstrate well the effect of the energy differential term in B-CSDAE. In photon incident simulations in Section 4.8, the photon equation does not have the energy differential term and the photon energy spectrum (Figures 4.6, 4.7 and 4.9) show that the photons travel through the medium almost at the same energy. In electron incident simulations in Section 4.10, the energy differential term decreases the energy of the electrons while they travel through the medium (see the energy spectrum in Figures 4.14 and 4.15). The energy differential term may cause some instability in the solutions, in which oscillating values near zero are obtained in the areas where the energy spectrum should be zero. This can be seen mostly at the boundary of the incoming beam, but smaller oscillations are also present for example the energy spectrum in Figure 4.14 at the depth of $x_3 = 6$ cm and energy over 5 MeV, in which the energy spectrum should be zero. These oscillations produce negative values to the angle and energy integrated flux ψ_2^{I} for example at the depth of $x_3 = 6$ cm. These negative values can also be seen in Figure 4.16, in which the first electron incident integrated flux

is negative at the depth of $x_3 = 6$ cm.

The stream-line diffusion method clearly stabilized the solution of the linear system in ELECTRON2 simulation. The energy spectrum in Figure 4.14 without stream-line diffusion oscillates highly at the boundary $x_3 = 0$ cm. With stream-line diffusion these oscillations are almost disappeared in Figure 4.15. The negative flux values at energy spectrum are still present, but these are small. With the stream-line diffusion method the negative integrated flux values disappear (Figure 4.16). Also the number of iterations needed in finding the solution of the linear system was decreased to half. However, the matrix-free algorithms with Krylov methods increased the computational times, because one matrix-vector calculation took more time than what it took without stream-line diffusion method in the ELECTRON2 simulation. The calculation of the matrix-vector product should be implemented differently to make the stream-line diffusion method more powerful. Here it was used to demonstrate the effect of the method and was added to the earlier made code and that is why the computation time increased although the number of iterations decreased.

From the mathematical point of view the instabilities occur because the coercivity requirements were only weakly fulfilled. For example, increasing the total cross section makes the system more stable and oscillations are removed, but of course then the results do not correspond to electron traveling. Also, it was found that the B-CSDAE is very sensitive to the shape of the restricted stopping power. Although the condition (4.37) for the restricted stopping power suggests that the coercivity condition (4.28) is fulfilled for decreasing or constant function, it seems that not all decreasing functions are valid. For example high negative gradients at the restricted stopping power caused undesired oscillations in the results. For these reasons the restricted stopping power was approximated to be constant with respect to the energy in the simulations. However, this is not a poor approximation, because the restricted stopping power alter only slightly at high energies and the high negative gradient occur only at the lowest energies.

One could assume that the neglection of electron elastic scattering is an important cause for the errors to the results. If electron elastic scattering is considered directly, then one should select the spatial grid such that approximately the length of the grid equals the electron elastic scattering mean free path, which is the inverse of the elastic scattering cross section and is approximately few millimeters [67]. The resulted dense spatial grids are not yet possible because of the memory limits (at least in 3D) and some special methods has to be used when electron elastic scattering is considered. In MC, electron elastic scattering is usually considered with electron multiple scattering theories [104, 22], which could probably be used in deterministic transport codes when formulated properly.

The given simulations suggest that FEM can be used in solving one B-CSDAE to simulate electron traveling in a medium. The used stream-line diffusion method stabilized the linear system, although the stream-line parameter should be selected carefully. Also here the use of preconditioning would shorten the computational times.

Chapter V

Radiotherapy inverse problem with FEM

The aim of the conformal radiotherapy is to achieve a dose distribution, in which the high dosage volume conforms the planning target volume (PTV), while other healthy tissues and organs achieve as low dose as possible [188, 189]. To do this one assigns criteria to the dose at certain locations at the patient domain. Thus, in external radiotherapy inverse problem one knows the desired dose or particle flux distribution in the patient and the problem is to find the optimal dose distribution by defining the field intensity or incoming particle flux at the patient surface or defining the field arrangements and settings i.e. defining the treatment plan.

In this chapter, the radiotherapy inverse problem using the BTEs and FE discretization with a control approach is presented. In Section 5.1, the optimization criteria and related physical objective function are presented. In Section 5.2, the variational forms for the inverse problem are derived. In Section 5.3, the optimal control approach is used by omitting the nondifferentiable terms of a cost function in finding an initial guess for inverse radiotherapy treatment planning (IRTTP) problem and by the approach of parametrization in finding optimal controls for IRTTP problem. In Section 5.4, the finite element discretization is presented for the control systems and in Section 5.5, the parametrization is implemented for the discrete system applying singular value decomposition (SVD). In Section 5.7, the optimal control methods are tested by simulations. The chapter ends with the discussion of the simulations.

5.1 Optimization criteria

Typically physical or biological criteria are used in IRTTP problems [38]. Here the physical criteria are considered. Similar theories can be used for biological criteria. The patient domain $V \subset \mathbb{R}^3$ consists of a target volume $\mathbf{T}$ i.e. PVT, which includes the tumor and some safety margin, critical organs' region $\mathbf{C}$ and normal tissue's region $\mathbf{N}$. Thus, the patient domain is a mutually disjoint union $V = \mathbf{T} \cup \mathbf{C} \cup \mathbf{N}$. The dose $D(\boldsymbol{x})$ can be computed from the particle flux $\psi(\boldsymbol{x}, E, \boldsymbol{\Omega})$ using equation (2.1). One can assign several physical criteria for the dose. One

can simply set [30]

$$D(\boldsymbol{x}) = D_0 \qquad \boldsymbol{x} \in \mathbf{T} \tag{5.1}$$
$$D(\boldsymbol{x}) = 0 \qquad \boldsymbol{x} \in V \setminus \mathbf{T}, \tag{5.2}$$

where D_0 is a prescribed uniform dose in target $\mathbf{T}$. The criterion (5.2) is unrealistic since radiation must pass through healthy tissue to reach the tumor. That is why one usually demands condition (5.1) with conditions

$$D(\boldsymbol{x}) \leq D_{\mathbf{C}} \qquad \boldsymbol{x} \in \mathbf{C} \tag{5.3}$$
$$D(\boldsymbol{x}) \leq D_{\mathbf{N}} \qquad \boldsymbol{x} \in \mathbf{N}, \tag{5.4}$$

where $D_{\mathbf{C}}$ and $D_{\mathbf{N}}$ are the upper bounds of the dose in critical organs $\mathbf{C}$ and in normal tissue $\mathbf{N}$, respectively. Instead of condition (5.1), one can demand a feasibility condition

$$d_{\mathbf{T}} \leq D(\boldsymbol{x}) \leq D_{\mathbf{T}} \qquad \boldsymbol{x} \in \mathbf{T},$$

where $d_{\mathbf{T}}$ and $D_{\mathbf{T}}$ are the lower and upper bounds for the dose in PTV, respectively. The corresponding solution is a feasible solution.

Also so called dose volume constraints can be used [30, 25], which may be necessary for certain structures, for example for critical organs $\mathbf{C}$. Dose volume constraint states that the dose $D(\boldsymbol{x})$ can not be greater than some prescribed dose $d_{\mathbf{C}}$ in a volume fraction $v(D)$ which is smaller than some volume v_0. Thus, the dose volume constraint for critical organ $\mathbf{C}$ is

$$v(D) \leq v_0, \text{ when } D \geq d_{\mathbf{C}}, \tag{5.5}$$

where v_0 is a given volume fraction and $d_{\mathbf{C}}$ is a given dose. This volume fraction function $v(D)$ is the same as is the dose-volume histogram often used in radiotherapy physics [106]. It is a decreasing function of dose having $v(0) = 1$ and $v(D) = 0$ for sufficiently large D values, say $D \geq D_{\max}$. The dose volume constraint (5.5) is equivalent to

$$v(d_{\mathbf{C}}) \leq v_0,$$

which means that

$$\frac{\mu(\{\boldsymbol{x} \in \mathbf{C} \mid D(\boldsymbol{x}) \geq d_{\mathbf{C}}\})}{\mu(\mathbf{C})} \leq v_0, \tag{5.6}$$

where μ is the Lebesgue measure. Let $H : \mathbb{R} \to \mathbb{R}$ be a Heaviside function

$$H(x) = \begin{cases} 1, & x \geq 0 \\ 0, & x < 0 \end{cases}.$$

Then the dose volume constraint (5.6) can be expressed as

$$\frac{1}{\mu(\mathbf{C})} \int_{\mathbf{C}} H(D(\boldsymbol{x}) - d_{\mathbf{C}}) \mathrm{d}\boldsymbol{x} \leq v_0. \tag{5.7}$$

To make dose volume constraints more practical to handle in numerical calculations, condition (5.7) can be replaced by an approximation

$$\frac{1}{N_{\mathbf{C}}}\sum_{p=1}^{N_{\mathbf{C}}} H(D(\boldsymbol{x}_p) - d_{\mathbf{C}}) \leq v_0,$$

where $p = 1, ..., N_{\mathbf{C}}$ are the indexes of the discretization points in critical organ $\mathbf{C}$. In computations, it is useful to replace the exact Heaviside function H by the modified smooth function like

$$H_{\mathrm{a}}(x) = \mathrm{erf}_{\varepsilon}(x) := \frac{1}{\sqrt{\pi}\varepsilon}\int_{-\infty}^{x} e^{-s^2/\varepsilon^2}\mathrm{d}s,$$

where ε is a small number or by the functions like

$$H_{\mathrm{a}}(x) = C_1 + C_2\overline{\mathrm{arc}}\tan(C_3 x)$$

$$H_{\mathrm{a}}(x) = C_1 + C_2\tanh(C_3 x),$$

where the constants C_j $(j = 1, 2, 3)$ are selected such that the function $H_{\mathrm{a}}(x)$ approximates the Heaviside function.

5.2 Variational form

Now assume that one has L fields $s_i,\ i = 1, ..., L$. This could mean that the gantry, couch and collimator angles are predetermined and the whole treatment has L different angle settings. Instead of the traditional predetermination of the beam directions, one could only preset L fields such that a field only defines a boundary of the incoming beam and use the angle and energy as free variables in optimization. Then the intensities of the directions and energies at different locations in the field boundary could be used as a free variable in dose optimization. Basically this means that a field consists of several subfields which could be treated for example using tomotherapy as indicated in Figure 5.1.

Let the incoming flux distribution of the i^{th} field s_i be u_i. Denote the corresponding disjoint patches of ∂V by Γ_i. The union $\Gamma := \cup_{i=1}^{L}\Gamma_i$ is mutually disjoint. Further define $u_i \in L_2(\Gamma_i \times I \times S)$ and denote $u = (u_1, ..., u_L) \in L_2(\Gamma \times I \times S) := L_2(\Gamma_1 \times I \times S) \times \cdots \times L_2(\Gamma_L \times I \times S)$. The space $L_2(\Gamma \times I \times S)$ is equipped with an inner product

$$\langle u, \tilde{u}\rangle_{L_2(\Gamma\times I\times S)} = \sum_{i=1}^{L}\langle u, \tilde{u}\rangle_{L_2(\Gamma_i\times I\times S)}.$$

The effect of incoming fluxes (consisting of particles of type j ($j = 1$ or 2)) is given by the functional

$$F_j(v) = \sum_{i=1}^{L}\int_S\int_I\int_{\Gamma_i} (\boldsymbol{\Omega}\cdot\boldsymbol{n})_- u_i v_j \mathrm{d}\boldsymbol{s}\mathrm{d}E\mathrm{d}\boldsymbol{\Omega}, \tag{5.8}$$

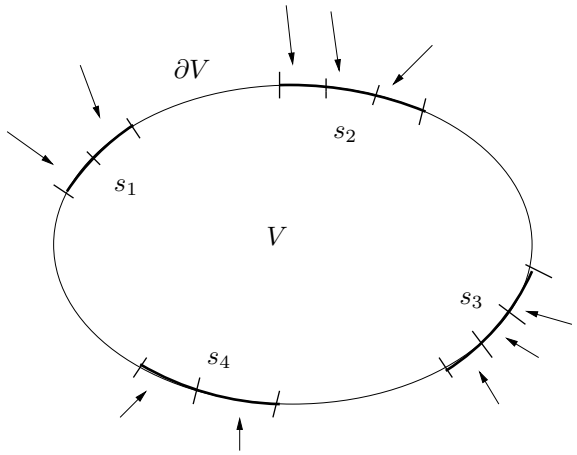

Figure 5.1: Schematic patient domain V with four fields $s_i,\ (i = 1, ..., 4)$ on the patient surface ∂V to demonstrate a tomotherapy approach, in which the field s_i consists of several subfields whose directions and energies can be used in dose optimization.

which is the same as in equation (4.10), but now for L different fields. The bilinear forms $B(\psi, v)$ or $B^{\mathrm{r}}(\psi, v)$ are defined by equations (4.9) or (4.26), respectively. The variational forms are then

$$B(\psi, v) = F_j(v),\ v \in H^3 \tag{5.9}$$

and

$$B^{\mathrm{r}}(\psi, v) = F_j(v),\ v \in \widetilde{H}^3. \tag{5.10}$$

The total dose $D = D(\boldsymbol{x})$ is obtained from the functional, which is defined by equation (3.17). Now denote $\mathcal{D}\psi(\boldsymbol{x}) := D(\boldsymbol{x})$. One finds that $\mathcal{D}$ is a linear operator $L_2(G)^3 \to L_2(V)$.

In the following sections, the derivations are made for the coupled system of BTEs. The derivations for the coupled B-CSDAEs can be done similarly by the variational form (5.10) and using appropriate function spaces.

5.3 Optimal control problem

In this section, the radiotherapy inverse problem is considered with the optimal control approach. Let $\tilde{F}_j : L_2(\Gamma \times I \times S) \to (H^3)^*$ be an operator defined by

$$(\tilde{F}_j u)(v) = \sum_{i=1}^{L} \int_S \int_I \int_{\Gamma_i} (\boldsymbol{\Omega} \cdot \boldsymbol{n})_- u_i v_j \mathrm{d}\boldsymbol{s}\mathrm{d}E\mathrm{d}\boldsymbol{\Omega}, \tag{5.11}$$

where $j = 1, 2$ indicate the incoming particle. From equation (5.8) one finds $(\tilde{F}_j u)(v) = F_j(v)$. Now the solution $\psi = \psi(u)$ satisfies the variational equation of the coupled BTEs, which is of the form

$$B(\psi(u), v) = (\tilde{F}_j u)(v), \ v \in H^3. \tag{5.12}$$

Since $\tilde{F}_j$ is a linear function of u, one can show by the uniqueness of solutions that the solution ψ is a linear function of u as well. Furthermore, the dose functional $\mathcal{D}$ is a linear function of ψ. One can show that $\psi : L_2(\Gamma \times I \times S) \to L_2(G)^3$ and $\mathcal{D} : L_2(G)^3 \to L_\infty(V)$ are bounded operators. Hence, $\mathcal{D}$ is Fréchet differentiable and $\mathcal{D}'\psi = \mathcal{D}$.

Now assume that in the treatment planning, the dose $\mathcal{D}\psi(u)(\boldsymbol{x})$ should be as near as possible the described dose D_0 in tumor and the upper bounds of the dose in critical organs and normal tissue should not be violated. Hence, one tries to optimize the dose distribution by selecting the incoming fluxes u_i such that these hold. The concrete implementation of this leads to the following optimization problem.

Define a cost functional by

$$\begin{aligned} J(u) &= c_1 ||D_0 - \mathcal{D}\psi(u)||^2_{L_2(\mathbf{T})} \\ &+ c_2 ||(D_{\mathbf{C}} - \mathcal{D}\psi(u))_-||^2_{L_2(\mathbf{C})} \\ &+ c_3 ||(D_{\mathbf{N}} - \mathcal{D}\psi(u))_-||^2_{L_2(\mathbf{N})} \\ &+ c_4 \left(\left(v_0 - \frac{1}{N_{\mathbf{C}}} \sum_{p=1}^{N_{\mathbf{C}}} H_{\mathrm{a}}(\mathcal{D}\psi(u)(\boldsymbol{x}_p) - d_{\mathbf{C}}) \right)_- \right)^2 \\ &+ c_5 ||(u)_-||^2_{L_2(\Gamma \times I \times S)} + c_6 ||u||^2_{L_2(\Gamma \times I \times S)}, \end{aligned} \tag{5.13}$$

where c_i, $(i = 1, ..., 6)$ are positive weights. The minimization of the second and third terms tries to take care of the requirements (5.3) and (5.4), respectively. Also the dose volume constraint is added. The notation $()_-$ is the negative part of the function. To keep the admissible control set as the whole space $L_2(\Gamma \times I \times S)$ or its suitable linear subspace U a penalty term $c_5 ||(u)_-||^2_{L_2(\Gamma \times I \times S)}$ is added to hinder the violation of the constraint $u_i \geq 0$. The last (convex) term regularizes the schemes and helps the optimization process in theory and in numerical considerations. The minimization of $||u||^2_{L_2(\Gamma \times I \times S)}$ may also be of practical importance, since it minimizes the incoming flux.

One can state the corresponding optimization problem to the coupled BTEs. *Find the minimum*

$$\min_{u \in U} J(u) \tag{5.14}$$

such that (5.12) is valid.

The optimal control u_0 minimizes the cost functional J among the set, say U_{ad}, of admissible controls u [120, 59]. The well known necessary condition for the optimal control u_0 is that u_0 satisfies equation (5.12) and that

$$J'(u_0)(u - u_0) \geq 0 \text{ for all } u \in U_{\mathrm{ad}}. \tag{5.15}$$

In the case, where U_{ad} is the linear space U (as in the case here), the condition (5.15) reduces to

$$J'(u_0) = 0. \tag{5.16}$$

In the case, where J is a convex function, the condition (5.16) is also sufficient for the optimal control. The functional J given by (5.13), however contains also non-convex terms.

5.3.1 Initial solution for the optimal control approach

This optimal control approach is presented in [176], which is based on the (Fréchet) differentiable approximation of a cost functional J (defined by equation (5.13), for example). Then J is differentiable and a system of nonlinear equations is resulted. Because of the nonlinearities the resulted discretized system has to be solved with iterative techniques such as Newton iteration schemes [82] and a good initial guess is a necessity in finding the solution of the nonlinear system. Here the initial solution is considered using a convex quadratic cost functional

$$J_0(u) = c_1||D_0 - \mathcal{D}\psi(u)||^2_{L_2(\mathbf{T})} + c_6||u||^2_{L_2(\Gamma\times I\times S)}. \tag{5.17}$$

Before the theory of the initial solution can be presented, the following operators are defined. Let A be a Lebesgue measurable subset of V. Furthermore, let e_A be the "extension by zero operator" from a set A on V i.e $e_A f = f(x),\ x \in A$ and $e_A f = 0,\ x \in V \setminus A$. An adjoint $\mathcal{D}^*$ of the operator $\mathcal{D}$ is defined to satisfy the following equation

$$\langle f, \mathcal{D}g\rangle_{L_2(V)} = \langle \mathcal{D}^* f, g\rangle_{L_2(G)^3},\ g \in L_2(G)^3.$$

Now the adjoint $\mathcal{D}^* : L_2(V) \to L_2(G)^3$ of $\mathcal{D}$ (with the definition for the dose given in equation (3.17)) can be computed and

$$\mathcal{D}^* w = (0, \tau_2^{\text{Ie}} w, \tau_3^{\text{Ie}} w), \quad w \in L_2(V).$$

In addition, the adjoint $\tilde{F}_j^* : (H^3)^* \to L_2(\Gamma \times I \times S)(\approx \bigoplus_{i=1}^{L} L_2(\Gamma_i \times I \times S))$ of $\tilde{F}_j$ (defined by equation (5.11)) is

$$\tilde{F}_j^* v = \big(r_{\Gamma_1}((\boldsymbol{\Omega}\cdot\boldsymbol{n})_- v_j), ..., r_{\Gamma_L}((\boldsymbol{\Omega}\cdot\boldsymbol{n})_- v_j)\big), \tag{5.18}$$

where r_{Γ_i} is the restriction operator on Γ_i.

The existences of the solutions of the variational problem (4.8) is discussed in Section 4.4. The assumptions of Theorem 1 imply sufficient conditions for the existence of the variational solutions $\psi \in H^3$. Moreover, it can be proven that the solution is unique. Similar considerations can be made for the variational problem defined by equation (4.8) and one can prove that the adjoint problem $B(v, \psi^*) = \hat{F}_j v$ has a unique solution $\psi^* \in H^3$. $\hat{F}_j v$ is defined later in the definition of the adjoint problem in equation (5.21) by an inner product.

Now one possibility for the initial guess in radiotherapy optimization is to use the solution of the following control problem.

Theorem 5 *Let the assumptions in the Theorem 1 be valid. Define the cost functional J_0 by equation (5.17). Then the optimal boundary control is*

$$u_0 = \frac{1}{c_6}\tilde{F}^*\psi^*, \tag{5.19}$$

where ψ^* is uniquely obtained from equations

$$B(\psi, v) = \tfrac{1}{c_6}\tilde{F}(\tilde{F}^*\psi^*)(v),\ v \in H^3 \tag{5.20}$$

$$B(v, \psi^*) = c_1\langle v, \mathcal{D}^* e_{\mathbf{T}}(D_0 - \mathcal{D}\psi)\rangle_{L_2(G)^3},\ v \in H^3. \tag{5.21}$$

Proof. The cost function J_0 is now convex and condition (5.16) is necessary and sufficient for the optimal control. Denote

$$J_1(u) := \langle D_0 - \mathcal{D}\psi(u), D_0 - \mathcal{D}\psi(u)\rangle_{L_2(\mathbf{T})},$$
$$J_2(u) := \langle u, u\rangle_{L_2(\Gamma\times I\times S)}.$$

Then

$$J_0(u) = c_1 J_1(u) + c_6 J_2(u),$$

whose derivative respect to u is

$$J_0'(u)w = c_1 J_1'(u)w + c_6 J_2'(u)w,$$

where

$$\begin{aligned} J_1'(u)w &= -2\langle D_0 - \mathcal{D}\psi(u), \mathcal{D}\psi(w)\rangle_{L_2(\mathbf{T})} \\ &= -2\langle \mathcal{D}^* e_{\mathbf{T}}(D_0 - \mathcal{D}\psi(u)), \psi(w)\rangle_{L_2(G)^3} \end{aligned}$$

and

$$J_2'(u)w = 2\langle u, w\rangle_{L_2(\Gamma\times I\times S)}.$$

Hence, one finds that $J_0'(u)w = 0$, if and only if

$$-2c_1\langle \mathcal{D}^* e_{\mathbf{T}}(D_0 - \mathcal{D}\psi(u)), \psi(w)\rangle_{L_2(G)^3} + 2c_6\langle u, w\rangle_{L_2(\Gamma\times I\times S)} = 0,$$

which can be cast into the form

$$\langle c_1\mathcal{D}^* e_{\mathbf{T}}(D_0 - \mathcal{D}\psi(u)), \psi(w)\rangle_{L_2(G)^3} = \langle c_6 u, w\rangle_{L_2(\Gamma\times I\times S)}. \tag{5.22}$$

Suppose that $\psi^* = \psi^*(w)$ is the solution of the adjoint problem defined by equation (5.21). Then from the adjoint equation (5.21), one finds that

$$B(\psi(w), \psi^*) = \langle \psi(w), c_1\mathcal{D}^* e_{\mathbf{T}}(D_0 - \mathcal{D}\psi(u))\rangle_{L_2(G)^3}. \tag{5.23}$$

When using equation (5.22) to the previous equation (5.23), one obtains

$$B(\psi(w), \psi^*) = \langle c_6 u, w\rangle_{L_2(\Gamma\times I\times S)}. \tag{5.24}$$

On the other hand, from equation (5.12) one obtains

$$\begin{aligned} B(\psi(w),\psi^*) &= (\tilde{F}_j w)(\psi^*) \\ &= \langle \tilde{F}_j^* \psi^*, w\rangle_{L_2(\Gamma\times I\times S)}, \end{aligned} \tag{5.25}$$

where also equations (5.11) and (5.18) are used. Combining equations (5.24) and (5.25) leads to

$$\langle \tilde{F}_j^* \psi^*, w\rangle_{L_2(\Gamma\times I\times S)} = \langle c_6 u, w\rangle_{L_2(\Gamma\times I\times S)},$$

which can be cast into the form

$$\langle \tilde{F}_j^* \psi^* - c_6 u, w\rangle_{L_2(\Gamma\times I\times S)} = 0,$$

from which the optimal boundary control (5.19) is received. Equation (5.20) is obtained from equation (5.12) using boundary control equation (5.19). □

5.3.2 Optimal control applying parametrization

Here the optimal control is used for the coupled BTEs with the application of so called parametrization. The method is presented in [175]. Let $\mathcal{A} : L_2(G)^3 \to L_2(G)^3$ be an operator

$$\begin{aligned} D(\mathcal{A}) &= H^3 \\ \mathcal{A}\psi &= (\mathbf{\Omega}\cdot\nabla + K)\psi, \end{aligned}$$

where $D(\mathcal{A})$ is the domain of $\mathcal{A}$. With these definitions the coupled BTEs (4.3) with the stated incoming photon boundary condition (3.19) can be formulated as follows

$$\mathcal{A}\psi = 0 \tag{5.26}$$

$$\tilde{r}\psi_1 = u,\ \tilde{r}\psi_2 = \tilde{r}\psi_3 = 0, \tag{5.27}$$

where $\tilde{r} : H^3 \to L_2(\partial V \times I \times S)$ is the restriction operator $\tilde{r}\psi_j = \psi|_{\Gamma\times I\times S}$. The electron incident boundary condition (3.20) can be given by

$$\tilde{r}\psi_2 = u,\ \tilde{r}\psi_1 = \tilde{r}\psi_3 = 0. \tag{5.28}$$

Now the problem (5.26) with photon (5.27) or electron (5.28) boundary conditions can be given in a matrix form

$$\mathcal{A}_j \begin{pmatrix} \psi \\ u \end{pmatrix} = 0, \tag{5.29}$$

where $\psi = (\psi_1, \psi_2, \psi_3)^{\mathrm{T}}$. The boundary condition is indicated by a subindex $j = 1, 2$. Thus, the matrices $\mathcal{A}_1$ and $\mathcal{A}_2$ are

$$\mathcal{A}_1 = \begin{pmatrix} (\mathbf{\Omega}\cdot\nabla + K) & 0 \\ \tilde{r} & -1 \\ \tilde{r} & 0 \\ \tilde{r} & 0 \end{pmatrix}, \quad \mathcal{A}_2 = \begin{pmatrix} (\mathbf{\Omega}\cdot\nabla + K) & 0 \\ \tilde{r} & 0 \\ \tilde{r} & -1 \\ \tilde{r} & 0 \end{pmatrix}.$$

Now, one finds that $\mathcal{A}_j$ is a linear operator

$$\mathcal{A}_j : H^3 \times L_2(\Gamma \times I \times S) \to L_2(G)^3 \times L_2(\Gamma \times I \times S)^3. \tag{5.30}$$

The control system (5.29) is said to be parametrizable, if there exists a normed space X and a linear operator $\mathcal{S} : X \to H^3 \times L_2(\Gamma \times I \times S)$ such that

$$\mathcal{A}_j \begin{pmatrix} \psi \\ u \end{pmatrix} = 0 \Leftrightarrow \begin{pmatrix} \psi \\ u \end{pmatrix} = \mathcal{S}f, \ f \in X.$$

$\mathcal{S}$ is the compatibility operator of the given control system (5.29). The normed space X depends on the given control system. Parametrizability is a kind of structural (internal) property of the control system. It is related to the null space of the system.

Let p_1 and p_2 be the canonical projections $p_1 : H^3 \times L_2(\Gamma \times I \times S) \to H^3$ and $p_2 : H^3 \times L_2(\Gamma \times I \times S) \to L_2(\Gamma \times I \times S)$. Then

$$\psi = p_1(\mathcal{S}f) := S_1 f, \ f \in X$$

and

$$u = p_2(\mathcal{S}f) := S_2 f, \ f \in X.$$

Further, the optimal control u_0 of the problem (5.14) is $u_0 = S_2 f_0$, where $f_0 \in X$ is the global minimum (if it exists) of the unconstrained problem: *Find the minimum*

$$\min_{f \in X} \tilde{J}(f),$$

where

$$\begin{aligned} \tilde{J}(f) &= c_1 ||D_0 - \mathcal{D}S_1 f||^2_{L_2(\mathbf{T})} \\ &+ c_2 ||(D_{\mathbf{C}} - \mathcal{D}S_1 f)_-||^2_{L_2(\mathbf{C})} \\ &+ c_3 ||(D_{\mathbf{N}} - \mathcal{D}S_1 f)_-||^2_{L_2(\mathbf{N})} \\ &+ c_4 \left(\left(v_0 - \frac{1}{N_{\mathbf{C}}} \sum_{p=1}^{N_{\mathbf{C}}} H_{\mathrm{a}}((\mathcal{D}S_1 f)(\boldsymbol{x}_p) - d_{\mathbf{C}}) \right)_- \right)^2 \\ &+ c_5 ||(S_2 f)_-||^2_{L_2(\Gamma \times I \times S)} + c_6 ||S_2 f||^2_{L_2(\Gamma \times I \times S)}. \end{aligned} \tag{5.31}$$

Instead of exact seeking of the compatibility operator $\mathcal{S}$, the discretized control system is considered in the following.

5.4 Finite element discretization of the control systems

Let ψ^{h}, defined by equation (4.39), be the finite element approximation of the variational form (4.40) in a finite dimensional subspace $X_{\mathrm{h}} = [\Phi_1, ..., \Phi_{3N}]$ as in Section 4.7. Further, let Y_{h} be a finite dimensional subspace of $L_2(\Gamma \times I \times S)$. The linear hull $Y_{\mathrm{h}} = [(w_{1,1}, 0, ..., 0), ..., (w_{M_1,1}, 0, ..., 0), (0, w_{1,2}, 0, ..., 0), ...,$

$(0, w_{M_2,2}, 0, ..., 0), ..., (0, ..., 0, w_{1,L}), ..., (0, ..., 0, w_{M_L,L})] =: [Y_1, ..., Y_M]$. M_i is the number of nodal points in a field s_i and $M = M_1 + ... + M_L$. The basis functions are denoted $Y_l,\ (l = 1, ..., M)$ and the i^{th} component of the vector Y_l is denoted as $Y_{l,i},\ (i = 1, .., L)$. Define the finite element approximation u^{h} of the boundary flux to be

$$u^{\text{h}} = (\sum_{m=1}^{M_1} \beta_{(m,1)} w_{m,1}, ..., \sum_{m=1}^{M_L} \beta_{(m,L)} w_{m,L})^{\text{T}}, \tag{5.32}$$

where $w_{m,l} = w_{m,l}(\boldsymbol{x}, E, \boldsymbol{\Omega})$ and $\beta_{(m,i)}$ $(m = 1, ..., M_i)$ are the unknown parameters of the boundary fluxes u_i $(i = 1, ..., L)$. Then the finite element approximation of the variational problem (4.40) of the coupled BTEs is defined as (again $j = 1, 2$ indicate the incoming particle)

$$B(\psi^{\text{h}}, v) = (\tilde{F}_j u^{\text{h}})(v),\ \forall v \in X_{\text{h}}, \tag{5.33}$$

which leads to the matrix equation

$$\boldsymbol{A}\alpha = \boldsymbol{B}_j \beta, \tag{5.34}$$

where $\beta = (\beta_{(1,1)}..., \beta_{(M_1,1)}, ..., \beta_{(1,L)}..., \beta_{(M_L,L)})^{\text{T}}$ and $\boldsymbol{A}$ is the matrix needed for the forward problem ($\boldsymbol{A}\alpha = \boldsymbol{b}_j$) and can be defined for example by equation (4.43). The matrix $\boldsymbol{B}_j \in \mathcal{M}(3N \times M)$ is defined such that

$$\boldsymbol{B}_j(l, t) = \sum_{i=1}^{L} \int_S \int_I \int_{\Gamma_i} (\boldsymbol{\Omega} \cdot \boldsymbol{n})_- Y_{t,i} \Phi_{l,j} \mathrm{d}\boldsymbol{s}\mathrm{d}E\mathrm{d}\boldsymbol{\Omega}, \tag{5.35}$$

where $\Phi_{l,j}$ is the j^{th} component of the vector Φ_l $(l = 1, ..., 3N)$. The matrix equation (5.34) can be cast into the form

$$(\boldsymbol{A},\ -\boldsymbol{B}_j) \begin{pmatrix} \alpha \\ \beta \end{pmatrix} = 0, \tag{5.36}$$

which is the discrete form of the control system (5.29).

5.5 Discrete system parametrization with SVD

The discrete control system is said to be parametrizable if there exist $p \in \mathbb{N}$ and a matrix $\boldsymbol{S} \in \mathcal{M}(3N + M \times p)$ such that

$$(\boldsymbol{A},\ -\boldsymbol{B}_j) \begin{pmatrix} \alpha \\ \beta \end{pmatrix} = 0 \Leftrightarrow \begin{pmatrix} \alpha \\ \beta \end{pmatrix} = \boldsymbol{S}\gamma,\ \gamma \in \mathbb{R}^p. \tag{5.37}$$

Let p_1, p_2 be the canonical projections $p_1 : \mathbb{R}^{3N+M} \to \mathbb{R}^{3N}$ and $p_2 : \mathbb{R}^{3N+M} \to \mathbb{R}^M$. Denote $\boldsymbol{S}_1\gamma = p_1(\boldsymbol{S}\gamma)$ and $\boldsymbol{S}_2\gamma = p_2(\boldsymbol{S}\gamma)$, where $\boldsymbol{S}_1 \in \mathcal{M}(3N \times p)$ and $\boldsymbol{S}_2 \in \mathcal{M}(M \times p)$. Then $\alpha = \boldsymbol{S}_1\gamma$ and $\beta = \boldsymbol{S}_2\gamma$. Thus, the finite element approximations (4.39) and (5.32) are of the form

$$\psi^{\text{h}}(\boldsymbol{x}, E, \boldsymbol{\Omega}) = \sum_{k=1}^{N} ((\boldsymbol{S}_1\gamma)_k, (\boldsymbol{S}_1\gamma)_{N+k}, (\boldsymbol{S}_1\gamma)_{2N+k})^{\text{T}}\, \phi_k(\boldsymbol{x}, E, \boldsymbol{\Omega}) =: S_1\gamma \tag{5.38}$$

and

$$u^{\mathrm{h}} = (\sum_{m=1}^{M_1} (\boldsymbol{S}_2\gamma)_m w_{1,m}(\boldsymbol{x}, E, \boldsymbol{\Omega}), ..., \sum_{m=1}^{M_L} (\boldsymbol{S}_2\gamma)_{M-M_L+m} w_{L,m}(\boldsymbol{x}, E, \boldsymbol{\Omega}))^{\mathrm{T}} =: S_2\gamma, \tag{5.39}$$

where $\gamma \in \mathbb{R}^p$. The notation $(\cdot)_m$ is the m^{th} component of the vector. Then the discretized optimal control problem states: *The finite element approximation* u_0^{h} *for the optimal control* u_0 *of the problem (5.14) is*

$$u_0^{\mathrm{h}} = (\sum_{m=1}^{M_1} (\boldsymbol{S}_2\gamma_0)_m w_{1,m}(\boldsymbol{x}, E, \boldsymbol{\Omega}), ..., \sum_{m=1}^{M_L} (\boldsymbol{S}_2\gamma_0)_{M-M_L+m} w_{L,m}(\boldsymbol{x}, E, \boldsymbol{\Omega})),$$

where $\gamma_0 \in \mathbb{R}^p$ *is the global minimum of the unconstrained problem:*

$$\min_{\gamma\in\mathbb{R}^p} \hat{J}(\gamma), \tag{5.40}$$

where

$$\begin{aligned} \hat{J}(\gamma) &= c_1||D_0 - \mathcal{D}(S_1\gamma)||^2_{L_2(\mathbf{T})} \\ &+ c_2||(D_{\mathbf{C}} - \mathcal{D}(S_1\gamma))_-||^2_{L_2(\mathbf{C})} \\ &+ c_3||(D_{\mathbf{N}} - \mathcal{D}(S_1\gamma))_-||^2_{L_2(\mathbf{N})} \\ &+ c_4 \left(\left(v_0 - \frac{1}{N_{\mathbf{C}}} \sum_{p=1}^{N_{\mathbf{C}}} H_{\mathrm{a}}(\mathcal{D}(S_1\gamma)(\boldsymbol{x}_p) - d_{\mathbf{C}}) \right)_- \right)^2 \\ &+ c_5||(S_2\gamma)_-||^2_{L_2(\Gamma\times I\times S)} + c_6||S_2\gamma||^2_{L_2(\Gamma\times I\times S)}. \end{aligned} \tag{5.41}$$

An initial point for the global optimization can be achieved from the solution of the quadratic problem

$$\min_{\gamma\in\mathbb{R}^p} \hat{J}_0(\gamma), \tag{5.42}$$

where

$$\hat{J}_0(\gamma) = c_1||D_0 - \mathcal{D}(S_1\gamma)||^2_{L_2(\mathbf{T})} + c_6||S_2\gamma||^2_{L_2(\Gamma\times I\times S)}.$$

The elements of the matrices $\boldsymbol{S}_1$ and $\boldsymbol{S}_2$ are denoted by $\boldsymbol{S}_1(k,l)$ and $\boldsymbol{S}_2(m,l)$. Then one can construct following.

Theorem 6 *The minimum* γ *of the problem (5.42) satisfies the linear equations* $(l = 1, ..., p)$

$$\begin{aligned} &c_1 \textstyle\sum_{k=1}^{N} \langle \mathcal{D}^*(e_{\mathbf{T}}(\mathcal{D}S_1\gamma)), (\boldsymbol{S}_1(k,l), (\boldsymbol{S}_1(N+k,l), \boldsymbol{S}_1(2N+k,l))^{\mathrm{T}}\phi_k\rangle_{L_2(G)^3} \\ &+c_6\langle S_2\gamma, (\textstyle\sum_{m=1}^{M_1} \boldsymbol{S}_2(m,l)w_{1,m}, ..., \sum_{m=1}^{M_L} \boldsymbol{S}_2(M-M_L+m,l)w_{L,m})^{\mathrm{T}}\rangle_{L_2(\Gamma\times I\times S)} \\ &= c_1 \textstyle\sum_{k=1}^{N} \langle \mathcal{D}^*(e_{\mathbf{T}}(D_0)), (\boldsymbol{S}_1(k,l), (\boldsymbol{S}_1(N+k,l), \boldsymbol{S}_1(2N+k,l))^{\mathrm{T}}\phi_k\rangle_{L_2(G)^3} \end{aligned} \tag{5.43}$$

Proof. The minimum point satisfies $\hat{J}_0'(\gamma) = 0$. One receives

$$\begin{aligned}\hat{J}_0'(\gamma)y &= -2c_1\langle D_0 - \mathcal{D}S_1\gamma, \mathcal{D}S_1 y\rangle_{L_2(\mathbf{T})} + 2c_6\langle S_2\gamma, S_2 y\rangle_{L_2(\Gamma\times I\times S)} \\ &= -2c_1\langle \mathcal{D}^*(e_{\mathbf{T}}(D_0 - \mathcal{D}S_1\gamma)), S_1 y\rangle_{L_2(G)^3} \\ &\quad +2c_6\langle S_2\gamma, S_2 y\rangle_{L_2(\Gamma\times I\times S)}. \end{aligned} \tag{5.44}$$

For any $v \in L_2(G)^3$ it holds that

$$\begin{aligned}\langle v, S_1 y\rangle_{L_2(G)^3} &= \langle v, \sum_{k=1}^{N}((\boldsymbol{S}_1 y)_k, (\boldsymbol{S}_1 y)_{N+k}, (\boldsymbol{S}_1 y)_{2N+k})^{\mathrm{T}}\phi_k\rangle_{L_2(G)^3} \\ &= \sum_{k=1}^{N}\langle v, \sum_{l=1}^{p}(\boldsymbol{S}_1(k,l)y_l, \boldsymbol{S}_1(N+k,l)y_l, \boldsymbol{S}_1(2N+k,l)y_l)^{\mathrm{T}}\phi_k\rangle_{L_2(G)^3} \\ &= \sum_{l=1}^{p} y_l \sum_{k=1}^{N}\langle v, (\boldsymbol{S}_1(k,l), \boldsymbol{S}_1(N+k,l), \boldsymbol{S}_1(2N+k,l))^{\mathrm{T}}\phi_k\rangle_{L_2(G)^3}. \end{aligned}$$

Similarly, for any $w \in L_2(\Gamma \times I \times S)$ it holds that

$$\begin{aligned}&\langle w, S_2 y\rangle_{L_2(\Gamma\times I\times S)} = \langle w, (\sum_{m=1}^{M_1}(\boldsymbol{S}_2 y)_m w_{1,m}, ..., \sum_{m=1}^{M_L}(\boldsymbol{S}_2 y)_{M-M_L+m} w_{L,m})^{\mathrm{T}}\rangle_{L_2(\Gamma\times I\times S)} \\ &= \langle w, (\sum_{m=1}^{M_1}\sum_{l=1}^{p}\boldsymbol{S}_2(m,l)y_l w_{1,m}, ..., \sum_{m=1}^{M_L}\sum_{l=1}^{p}\boldsymbol{S}_2(M-M_L+m,l)y_l w_{L,m})^{\mathrm{T}}\rangle_{L_2(\Gamma\times I\times S)} \\ &= \sum_{l=1}^{p} y_l \langle w, (\sum_{m=1}^{M_1}\boldsymbol{S}_2(m,l)w_{1,m}, ..., \sum_{m=1}^{M_L}\boldsymbol{S}_2(M-M_L+m,l)w_{L,m})^{\mathrm{T}}\rangle_{L_2(\Gamma\times I\times S)}. \end{aligned}$$

Substituting these into equation (5.44) and assigning it to zero leads to the linear equations (5.43) when compared componentwise. □

Furthermore, γ can be solved easily from the linear equations (5.43), because

$$\begin{aligned}\mathcal{D}^*(e_{\mathbf{T}}(\mathcal{D}S_1\gamma)) &= \sum_{q=1}^{N}\mathcal{D}^*\left(e_{\mathbf{T}}\left(\mathcal{D}\left(((\boldsymbol{S}_1\gamma)_q, (\boldsymbol{S}_1\gamma)_{N+q}, (\boldsymbol{S}_1\gamma)_{2N+q})^{\mathrm{T}}\phi_q\right)\right)\right) \\ &= \sum_{r=1}^{p}\gamma_r\sum_{q=1}^{N}\mathcal{D}^*\left(e_{\mathbf{T}}\left(\mathcal{D}\left((\boldsymbol{S}_1(q,r), \boldsymbol{S}_1(N+q,r), \boldsymbol{S}_1(2N+q,r))^{\mathrm{T}}\phi_q\right)\right)\right) \end{aligned}$$

and

$$S_2\gamma = \sum_{r=1}^{p}\gamma_r(\sum_{m=1}^{M_1}\boldsymbol{S}_2(m,r)w_{1,m}, ..., \sum_{m=1}^{M_L}\boldsymbol{S}_2(M-M_L+m,r)w_{L,m})^{\mathrm{T}}.$$

SVD can be used in the parametrization of the discrete system (5.37). First, consider the parametrization of the general equation $FX = 0$, where $F \in \mathcal{M}(m \times n)$. Hence, consider the existence of a matrix $S \in \mathcal{M}(m \times p)$ such that

$$FX = 0 \Leftrightarrow X = SY. \tag{5.45}$$

The SVD is defined as follows [80].

Theorem 7 *If F is a real $(m \times n)$-matrix with rank r, then there exist orthogonal matrices*

$$U = [U_1, ..., U_m] \in \mathcal{M}(m \times m), \quad V = [V_1, ..., V_n] \in \mathcal{M}(n \times n)$$

such that

$$U^{\mathrm{T}} F V = \begin{pmatrix} D_r & \mathbf{0} \\ \mathbf{0} & \mathbf{0} \end{pmatrix} := D \in \mathcal{M}(m \times n), \tag{5.46}$$

where $D_r = \mathrm{diag}(\sigma_1, ..., \sigma_r)$ and $\sigma_1 \geq \sigma_2 \geq ... \geq \sigma_r > 0$.

In the previous Theorem 7, the singular values $\sigma_j = \sqrt{\mu_j}$, $(j = 1, ..., r)$, where μ_j are the nonzero eigenvalues of the matrix $F^{\mathrm{T}}F$. Furthermore, $V_1, ..., V_r$ are the orthonormal eigenvectors of $F^{\mathrm{T}}F$ corresponding to eigenvalues $\mu_1, ..., \mu_r$, respectively. $V_{r+1}, ..., V_m$ are the eigenvectors corresponding to zero eigenvalues i.e. $\mathrm{span}\{V_{r+1}, ..., V_m\}$ forms the null space of $F^{\mathrm{T}}F$. For orthogonal matrix V it holds that $V^{\mathrm{T}}V = I_n$, where I_n is the identity matrix of size $(n \times n)$. Because U and V are orthogonal, one receives from equation (5.46)

$$F = UDV^{\mathrm{T}}, \tag{5.47}$$

which is the SVD of F. Now it is possible to formulate the following.

Theorem 8 *For any $(m \times n)$-matrix F with rank r there exists an $m \times (n - r)$-matrix S such that equivalence (5.45) is valid. Moreover, $S = [V_{r+1}, ..., V_n]$.*

Proof. Let $F = UDV^{\mathrm{T}}$ be the SVD of F. Define $S = [V_{r+1}, ..., V_n]$ and let

$$P = \begin{pmatrix} \mathbf{0} \\ I_{n-r} \end{pmatrix} \in \mathcal{M}(n \times n - r), \quad Y \in \mathcal{M}(n - r \times 1).$$

Then for $X = SY = VPY$ and one obtains

$$FX = FVPY = UDV^{\mathrm{T}}VPY = UDPY = \mathbf{0},$$

because $DP = \mathbf{0}$ always.

Conversely, suppose that $FX = \mathbf{0}$. Then also $U^{\mathrm{T}}FX = \mathbf{0}$. Since V is nonsingular there exists $Z \in \mathcal{M}(n \times 1)$ such that $VZ = X$. Denote $Z = (Z', Z'')^{\mathrm{T}}$, where $Z' \in \mathcal{M}(r \times 1)$ and $Z'' \in \mathcal{M}(n - r \times 1)$. Then one finds that

$$\mathbf{0} = U^{\mathrm{T}}FX = (U^{\mathrm{T}}FV)Z = DZ = \begin{pmatrix} D_r Z' \\ \mathbf{0} \end{pmatrix}. \tag{5.48}$$

Relation (5.48) implies that $D_r Z' = \mathbf{0}$ and since D_r is nonsingular $Z' = 0$. This shows that

$$X = VZ = V \begin{pmatrix} \mathbf{0} \\ Z'' \end{pmatrix} = V \begin{pmatrix} \mathbf{0} \\ I_{n-r} \end{pmatrix} Z'' = VPZ'' = SZ''.$$

□

Now Theorem 8 can be used for the parametrization of the discrete control system (5.37) using $F = [\boldsymbol{A},\ -\boldsymbol{B}]$ and computing the vectors, which span the null space of $F^{\mathrm{T}}F$. It should be noted that in FEM with linear basis the matrices $\boldsymbol{A}$ and $\boldsymbol{B}$ have always full rank. Thus, the rank of matrix F is always $r = 3N$ and the size of γ is $p = M$.

5.6 Global optimization with Simulated Annealing

In finding the global minimum of the unconstrained problem (5.40), one needs to use some optimizer to find the minimum of the function (5.41). Function defined in equation (5.41) is non-convex i.e. it may contain multiple local extrema. One possibility is to use a Simulated Annealing algorithm, which is a global optimization algorithm, so, it does not easily stuck in a local minima [109, 56]. The values of the decision parameters are changed randomly and objective function values are calculated. If new objective function value F is better than the current best objective function value F_{best}, the new parameters are accepted. If new objective function value is worse, the new parameters are accepted with probability

$$P = \exp(-\frac{\Delta F}{T}), \tag{5.49}$$

where $\Delta F = F - F_{\mathrm{best}}$ and T is in the same magnitude as F and its value decreases as the iteration proceeds.

5.7 FEM simulations for the radiotherapy inverse problems

To simulate the theories given in Sections 5.3-5.5, the presented control problems were solved using FEM and only one BTE to describe the traveling of arbitrary particles in a 2D plane ($\boldsymbol{x} = (x_2, x_3)$). In fact, photon scattering data was used, but because only one BTE equation was used, the dose computation was done artificially from the photon flux using arbitrary stopping powers $\tau(\boldsymbol{x}, E)$. The particles were assumed to scatter in the spatial 2D plane. Thus, the angular variable was $\theta \in [0, 2\pi[$ and $\boldsymbol{\Omega}_{2\mathrm{D}} = (\sin\theta, \cos\theta)$, which meant that $\theta = 0$ was toward the x_3-axis. This caused small inaccuracy to the computations of the forward problem, because the scattering out of plane was neglected. However, it was thought to be unessential in the purpose of these simulations, which was to show that the given inverse and control theories work in theory. All these simulations were made using MATLAB® in a normal PC (2 GHz Pentium with 2 GB memory).

For one BTE the linear hull is $[\phi_1, ..., \phi_N]$ and the finite element approximation in 2D is

$$\psi^{\mathrm{h}}(\boldsymbol{x}, E, \theta) = \sum_{k=1}^{N} \alpha_k \phi_k(\boldsymbol{x}, E, \theta).$$

The linear system of one BTE is

$$A\alpha = b, \tag{5.50}$$

where $\alpha = (\alpha_1, ..., \alpha_N)$. A is as $A_{1\to 1}$ and is defined by equation (4.61). The right hand sides of the control problems are defined later. Separable basis functions are used as in Section 4.7.3. The basis functions of the boundary fluxes are defined in Section 5.4. The separable basis functions of the boundary fluxes are defined as $w_{t,i}(\boldsymbol{x}, E, \theta) = w^{\boldsymbol{x}}_{t_\mathrm{s},i}(\boldsymbol{x}) w^{E}_{t_\mathrm{e},i}(E) w^{\theta}_{t_\mathrm{o},i}(\theta)$, $(i = 1, ..., L,\ t = 1, ..., M_i,\ t_\mathrm{s} = 1, ..., M_i^\mathrm{s},\ t_\mathrm{e} = 1, ..., M_i^\mathrm{e},\ t_\mathrm{o} = 1, ..., M_i^\mathrm{o})$, where M_i is the number of nodes in a field i, M_i^s, M_i^e, M_i^o are the number of spatial, energy and angular nodes in a field i, respectively, and $M_i = M_i^\mathrm{s} M_i^\mathrm{e} M_i^\mathrm{o}$. $M = \sum_{i=1}^{L} M_i$ is the total number of nodes in all fields. The finite element approximation u^h of the boundary flux is defined by equation (5.32).

5.7.1 Initial point control problem simulation

Here the simulations for the control problem (5.19)-(5.21) are presented. The finite element approximation of the adjoint particle flux is

$$\psi^{*\mathrm{h}}(\boldsymbol{x}, E, \theta) = \sum_{k=1}^{N} \alpha_k^* \phi_k(\boldsymbol{x}, E, \theta).$$

The unknown parameters α_k and α_k^* in finite element approximations are found by demanding

$$B(\psi^\mathrm{h}, v) = \tfrac{1}{c_6} \tilde{F}(\tilde{F}^* \psi^{*\mathrm{h}})(v) \tag{5.51}$$

$$B(v, \psi^{*\mathrm{h}}) = c_1 \langle v, \mathcal{D}^* e_{\mathbf{T}} (D_0 - \mathcal{D}\psi^\mathrm{h}) \rangle_{L_2(G)^3} \tag{5.52}$$

for all $v \in [\phi_1, ..., \phi_N]$. The basis functions are used as test functions $v = \phi_t$, $(t = 1, ..., N)$.

If the problem (5.50) describes the forward problem of one BTE, then the control problem (5.51)-(5.52) can be written in the matrix form

$$\begin{pmatrix} A & -\frac{1}{c_6} M_\Gamma \\ c_1 M_{\mathbf{T}} & A^\mathrm{T} \end{pmatrix} \begin{pmatrix} \alpha \\ \alpha^* \end{pmatrix} = \begin{pmatrix} 0 \\ c_1 b_{\mathbf{T}} \end{pmatrix}, \tag{5.53}$$

where $\alpha^* = (\alpha_1^*, ..., \alpha_N^*)^\mathrm{T}$, the matrix A is defined as in equation (5.50),

$$\begin{aligned} M_\Gamma(l,k) &= \sum_{i=1}^{L} \int_0^{2\pi} \int_I \int_{\Gamma_i} ((\boldsymbol{\Omega}_{2\mathrm{D}} \cdot \boldsymbol{n})_-)^2 \phi_l \phi_k \mathrm{d}\boldsymbol{s} \mathrm{d}E \mathrm{d}\theta \\ &= \sum_{i=1}^{L} \sum_{r=1}^{N_{\Gamma_i}} \left(\int_{\Gamma_{i,r}} \phi^{\boldsymbol{x}}_{k_\mathrm{s}} \phi^{\boldsymbol{x}}_{l_\mathrm{s}} \mathrm{d}\boldsymbol{s} \int_0^{2\pi} ((\boldsymbol{\Omega}_{2\mathrm{D}} \cdot \boldsymbol{n}_r)_-)^2 - \phi^{\theta}_{k_\mathrm{o}} \phi^{\theta}_{l_\mathrm{o}} \mathrm{d}\theta \right) \int_I \phi^E_{k_\mathrm{e}} \phi^E_{l_\mathrm{e}} \mathrm{d}E, \end{aligned} \tag{5.54}$$

$$
\begin{aligned}
M_{\mathbf{T}}(l,k) &= \int_0^{2\pi}\int_I\int_{\mathbf{T}} \left(\tau(\boldsymbol{x},E)\phi_l \int_0^{2\pi}\int_I \tau(\boldsymbol{x},E')\phi_k \mathrm{d}E'\mathrm{d}\theta'\right)\mathrm{d}\boldsymbol{x}\mathrm{d}E\mathrm{d}\theta, \\
&= \sum_{d_\mathrm{s}=1}^{N_\mathrm{s}}\sum_{d_\mathrm{e}=1}^{N_\mathrm{e}} S_d \sum_{d'_\mathrm{s}=1}^{N_\mathrm{s}}\sum_{d'_\mathrm{e}=1}^{N_\mathrm{e}} \tau_{d'} \int_{\mathbf{T}} \phi^{\boldsymbol{x}}_{d_\mathrm{s}}\phi^{\boldsymbol{x}}_{d'_\mathrm{s}}\phi^{\boldsymbol{x}}_{k_\mathrm{s}}\phi^{\boldsymbol{x}}_{l_\mathrm{s}}\mathrm{d}\boldsymbol{x} \\
&\quad \cdot \int_0^{2\pi}\phi^{\theta}_{k_\mathrm{o}}\mathrm{d}\theta \int_0^{2\pi}\phi^{\theta}_{l_\mathrm{o}}\mathrm{d}\theta \int_I \phi^{E}_{d'_\mathrm{e}}\phi^{E}_{k_\mathrm{e}}\mathrm{d}E \int_I \phi^{E}_{d_\mathrm{e}}\phi^{E}_{l_\mathrm{e}}\mathrm{d}E \qquad (5.55)
\end{aligned}
$$

and

$$
\begin{aligned}
b_{\mathbf{T}}(l) &= \int_0^{2\pi}\int_I\int_{\mathbf{T}} D_0\tau(\boldsymbol{x},E)\phi_l \mathrm{d}\boldsymbol{x}\mathrm{d}E\mathrm{d}\theta \\
&= D_0 \sum_{d_\mathrm{s}=1}^{N_\mathrm{s}}\sum_{d_\mathrm{e}=1}^{N_\mathrm{e}} \tau_d \int_{\mathbf{T}} \phi^{\boldsymbol{x}}_{d_\mathrm{s}}\phi^{\boldsymbol{x}}_{l_\mathrm{s}}\mathrm{d}\boldsymbol{x} \int_I \phi^{E}_{d_\mathrm{e}}\phi^{E}_{l_\mathrm{e}}\mathrm{d}E \int_0^{2\pi}\phi^{\theta}_{l_\mathrm{o}}\mathrm{d}\theta. \qquad (5.56)
\end{aligned}
$$

In the previous, Γ_i is assumed to consist of N_{Γ_i} patches $\Gamma_{i,r}$, in which the normal vector $\boldsymbol{n}_r$ is constant, i.e. $\Gamma_i = \cup_{r=1}^{N_{\Gamma_i}}\Gamma_{i,r}$. From the solution $(\alpha,\alpha^*)^{\mathrm{T}}$ of the linear system (5.53), the optimal boundary control u_0 can be computed from equation (5.19).

INICONTROL1

The geometry and the source nodes of the fields for the first initial guess FEM simulation are shown in Figure 5.2 with the optimized dose distribution. The number of spatial nodes was $N_\mathrm{s} = 121$. The angular domain $\theta \in [0, 2\pi[$ was divided into 8 evenly distributed elements and the energy domain $E \in [0.1, 10]$ MeV was divided into 5 evenly distributed elements. Thus, $N_\mathrm{o} = 8$, $N_\mathrm{e} = 6$ and $N = 5808$. The source nodes were allowed to have all energies and directions, which were included in the optimization. Homogeneous dose $D_0 = 10$ (in arbitrary units) was assumed to locate at the target with $c_1 = 10^5$ and $c_6 = 0.1$. The initial solution was computed from the linear system (5.53). The computations took 2 hours. The boundary fluxes at different energies are presented in Figure 5.3.

INICONTROL2

In the second initial guess FEM simulation, three fields were assumed to locate at the boundaries. The geometry and the source nodes for the fields can be found in Figure 5.4. The number of spatial nodes was $N_\mathrm{s} = 121$. The angular domain was as in the previous INICONTROL1 simulation with $N_\mathrm{o} = 8$. The energy domain $E \in [0.1, 10]$ MeV was divided into 3 evenly distributed elements. Thus, $N_\mathrm{e} = 4$ and $N = 8192$. All energies and directions were included in the optimization, in which $D_0 = 10$ was desired to the target domain ($c_1 = 10^5$ and $c_6 = 0.1$). The computations took 3 hours. The dose distribution is presented in Figure 5.4 and the boundary fluxes at different energies are presented in Figure 5.5.

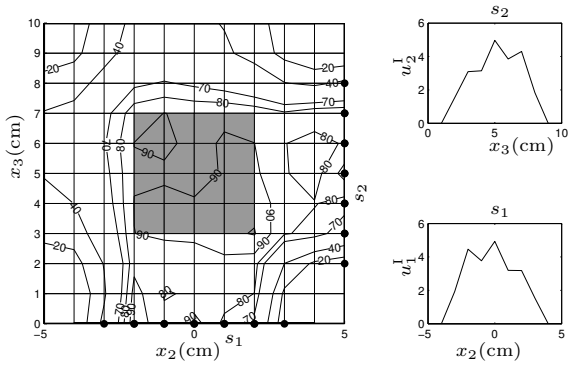

Figure 5.2: The INICONTROL1 simulation results. On the left there is the spatial grid drawn with straight lines. The spatial source nodes at the boundary are illustrated as black circles. The gray box inside the grid is the target. The optimized dose profile is presented with isodoses 20, 40, 70, 80, 90, 100, in which 100% describes D_0=10. On the rigth there are the angle and energy integrated boundary flux values $u_1^{\mathrm{I}}(\mathrm{cm}^{-2})$ and $u_2^{\mathrm{I}}(\mathrm{cm}^{-2})$ for fields s_1 and s_2, respectively.

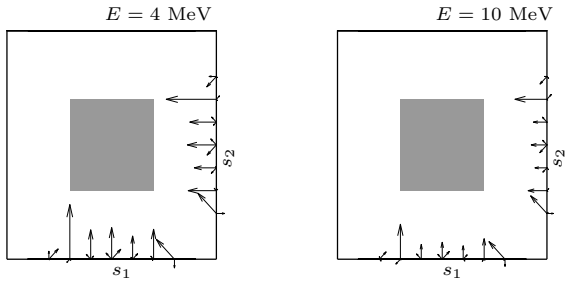

Figure 5.3: The INICONTROL1 simulation results. On the left there are the boundary fluxes $u_1(\mathrm{cm}^{-2}\mathrm{MeV}^{-1}\mathrm{sr}^{-1})$ and $u_2(\mathrm{cm}^{-2}\mathrm{MeV}^{-1}\mathrm{sr}^{-1})$ at the energy $E = 4$ MeV for the fields s_1 and s_2, respectively. On the right there are u_1 and u_2 at $E = 10$ MeV. Both boundary fluxes are in the same scale.

5.7.2 Control problem simulation using parametrization and SVD

In the control problem simulation with SVD parametrization, first the null space of matrix $F = [A,\ -B] \in \mathcal{M}(N \times N + M)$ was computed from the matrix $F^{\mathrm{T}}F$ using the SVD. The matrix A was defined by the forward problem (5.50) and the

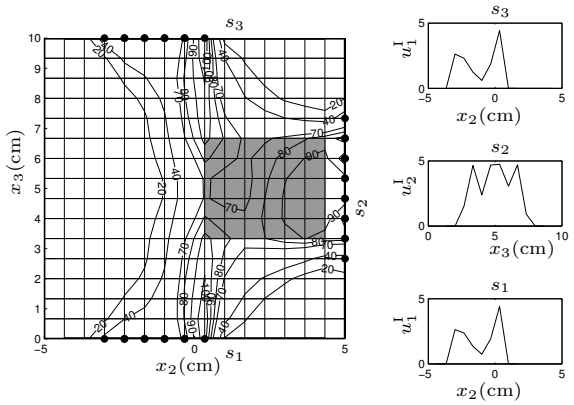

Figure 5.4: The INICONTROL2 simulation results. On the left there is the spatial grid drawn with straight lines. The spatial source nodes at the boundary are illustrated as black circles. The gray box inside the grid is the target. The optimized dose profile is presented with isodoses 20, 40, 70, 80, 90, 100, in which 100% describes D_0=10. On the rigth there are the angle and energy integrated boundary flux values $u_i^{\mathrm{I}}(\mathrm{cm}^{-2})$ for fields s_i $(i = 1, 2, 3)$, respectively.

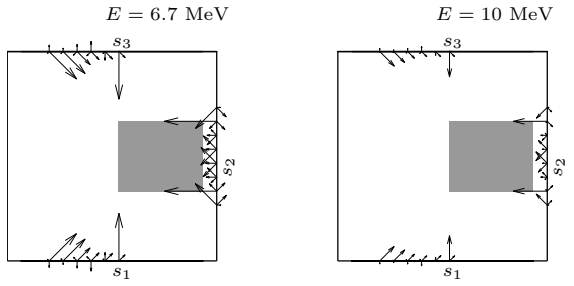

Figure 5.5: The INICONTROL2 simulation results. On the left there are the boundary fluxes $u_i(\mathrm{cm}^{-2}\mathrm{MeV}^{-1}\mathrm{sr}^{-1})$ $(i = 1, 2, 3)$ at the energy $E = 6.7$ MeV for the fields s_i. On the right there are u_i at $E = 10$ MeV. Both boundary fluxes are in the same scale.

matrix $B \in \mathcal{M}(N \times M)$ was of the form

$$B = \begin{pmatrix} B_1 & & \mathbf{0} \\ & \ddots & \\ \mathbf{0} & & B_L \end{pmatrix}, \tag{5.57}$$

where the elements of matrix B_i, $(i = 1, ..., L)$ were defined by

$$\begin{aligned} B_i(l,t) &= \int_S \int_I \int_{\Gamma_i} (\boldsymbol{\Omega}\cdot\boldsymbol{n})_- w_{t,i}\phi_l \mathrm{d}\boldsymbol{s}\mathrm{d}E\mathrm{d}\theta \\ &= \sum_{r=1}^{N_{\Gamma_i}} \left(\int_{\Gamma_{i,r}} \phi_{l_\mathrm{s}}^{\boldsymbol{x}} w_{t_\mathrm{s},i}^{\boldsymbol{x}} \mathrm{d}\boldsymbol{s} \int_0^{2\pi} (\boldsymbol{\Omega}_{\mathrm{2D}}\cdot\boldsymbol{n}_r)_- \phi_{l_\mathrm{o}}^{\theta} w_{t_\mathrm{o},i}^{\theta} \mathrm{d}\theta \right) \int_I \phi_{l_\mathrm{e}}^{E} w_{t_\mathrm{e},i}^{E} \mathrm{d}E, \end{aligned} \quad (5.58)$$

where the index t was calculated from the formula $t = t_\mathrm{o} + (t_\mathrm{e} - 1)M_i^\mathrm{o} + (t_\mathrm{s} - 1)M_i^\mathrm{e}M_i^\mathrm{o}$, which came from the Kronecker tensor product. The rank of matrix F was N. By Theorem 8, $S = [V_{N+1}, ..., V_{N+M}]$, which corresponds to the zero eigenvalue eigenvectors of the matrix $F^\mathrm{T}F$. $S = (S_1, S_2)^\mathrm{T}$, where $S_1 \in \mathcal{M}(N \times M)$ and $S_2 \in \mathcal{M}(M \times M)$ were the parametrization matrices for α and β, respectively. Thus, $\alpha = S_1\gamma$ and $\beta = S_2\gamma$.

An initial point for the global optimization was achieved by solving the linear equations (5.43), which resulted in a matrix system

$$\left(c_1 S_1^\mathrm{T} M_{\mathbf{T}} S_1 + c_6 S_2^\mathrm{T} M_{\Gamma,0} S_2\right)\gamma = c_1 S_1^\mathrm{T} b_{\mathbf{T}}, \quad (5.59)$$

where $M_{\mathbf{T}}$ and $b_{\mathbf{T}}$ are defined by equations (5.55) and (5.56). The elements of the matrix $M_{\Gamma,0} \in \mathcal{M}(M \times M)$ are of the form

$$\begin{aligned} M_{\Gamma,0}(t,s) &= \sum_{i=1}^{L} \int_0^{2\pi} \int_I \int_{\Gamma_i} w_{t,i} w_{s,i} \mathrm{d}\boldsymbol{s}\mathrm{d}E\mathrm{d}\theta, \\ &= \sum_{i=1}^{L} \int_{\Gamma_i} w_{t_\mathrm{s},i}^{\boldsymbol{x}} w_{s_x,i}^{\boldsymbol{x}} \mathrm{d}\boldsymbol{s} \int_0^{2\pi} w_{t_\mathrm{o},i}^{\theta} w_{s_\mathrm{o},i}^{\theta} \mathrm{d}\theta \int_I w_{t_\mathrm{e},i}^{E} w_{s_\mathrm{e},i}^{E} \mathrm{d}E. \end{aligned}$$

For the global optimization one needs to compute $\mathcal{D}(S_1\gamma)$. One obtains

$$\begin{aligned} \mathcal{D}(S_1\gamma) &= \int_0^{2\pi} \int_I \tau(\boldsymbol{x}, E) S_1\gamma \mathrm{d}E\mathrm{d}\theta \\ &= \sum_{k=1}^{N}\sum_{t=1}^{M} S_1(k,t)\gamma_t \int_0^{2\pi}\int_I \tau(\boldsymbol{x},E)\phi_k \mathrm{d}E\mathrm{d}\theta \\ &= S_1^\mathrm{T} D_\mathrm{d}\gamma, \end{aligned} \quad (5.60)$$

where $D_\mathrm{d} \in \mathcal{M}(N \times N_\mathrm{s})$ is of the form

$$D_\mathrm{d}(l_\mathrm{s}, k) = \sum_{d_\mathrm{s}=1}^{N_\mathrm{s}} \sum_{d_\mathrm{e}=1}^{N_\mathrm{e}} \tau_d \phi_{d_\mathrm{s}}^{\boldsymbol{x}} \phi_{l_\mathrm{s}}^{\boldsymbol{x}} \int_I \phi_{d_\mathrm{e}}^{E} \phi_{k_\mathrm{e}}^{E} \mathrm{d}E \int_0^{2\pi} \phi_{k_\mathrm{o}}^{\theta} \mathrm{d}\theta.$$

The FEM simulations using the SVD parametrization was done in a $[-5, 5] \times [0, 10]$ cm^2 domain, which consisted of water. The geometry and the source nodes for the fields are shown in Figure 5.7. In the same figure, also the spatial grid

and the optimized dose distribution are shown. The number of spatial nodes was $N_\mathrm{s} = 144$. The angular domain $\theta \in [0, 2\pi[$ was divided into 8 evenly distributed elements and the energy domain $E \in [0.1, 10]$ MeV was divided into 3 evenly distributed elements. Thus, $N_\mathrm{o} = 8$, $N_\mathrm{e} = 4$ and $N = 1608$. Only inward directions ($M_\mathrm{o} = 3$) and maximum energy $E = 10$ MeV ($M_\mathrm{e} = 1$) was allowed at the source nodes ($M_\mathrm{s} = 32,\ M = 96$). The computation of the matrix S took 3 hours. Because the spatial domain was homogeneous and the source nodes were the same, the matrix S was the same in both PARA1 and PARA2 simulations. Thus, only the objective function and the initial guess equation (5.59) were changed before the global optimization.

PARA1

In the first parametrization FEM simulation, the target and critical organ are shown in Figure 5.8 with the boundary flux results. $D_0 = 10$ was assumed to locate at the target. The initial solution was computed from the linear system (5.59), in which $c_1 = 3$ and $c_6 = 10^{-6}$. The initial computations took few seconds. The results for the initial solution are presented in Figure 5.6. The global optimization was done using Simulated Annealing algorithm (Section 5.6) and objective function was as in equation (5.41), in which $c_1 = 3,\ c_2 = 1.5,\ c_3 = 0.5,\ c_4 = 0,\ c_5 = 100,\ c_6 = 0$ and $D_0 = 10,\ D_\mathbf{N} = 5,\ D_\mathbf{C} = 2$. The global optimization took 20 minutes. The dose distribution is presented in Figure 5.7 and the boundary fluxes at energy $E = 10$ MeV are presented in Figure 5.8.

PARA2

In the second parametrization FEM simulation, the target and critical organ are shown in Figure 5.11 with the boundary flux results. The initial guess was computed similarly as in the previous parametrization simulation. The computation of the initial guess took a few seconds and the results are presented in Figure 5.9. The global optimization was done similarly with the same weights and dose limits as in the PARA1 simulation. The global optimization took 30 minutes. The dose distribution is presented in Figure 5.10 and the boundary fluxes at energy $E = 10$ MeV are presented in Figure 5.11.

5.8 Discussion for the inverse simulations

The given inverse planning theories were tested by simulations in Section 5.7. In the INICONTROL1 and INICONTROL2 simulations, the initial guess was computed by minimizing the quadratic cost function J_0 (5.17). It was found that the convergence rate in solving the obtained matrix system (5.53) was quite poor and the desired residual had to be quite small to achieve desirable results. This was probably because J_0 contained terms, in which the dose in the tumor was desired to be as close as possible to the desired dose and at the same time the incoming flux value was minimized. Thus, the goals were conflicting. From the solution of the matrix system one received ψ^h and $\psi^{*\mathrm{h}}$. By the theory, ψ^h should be those particle flux values, which are affected by the boundary control u_0, which

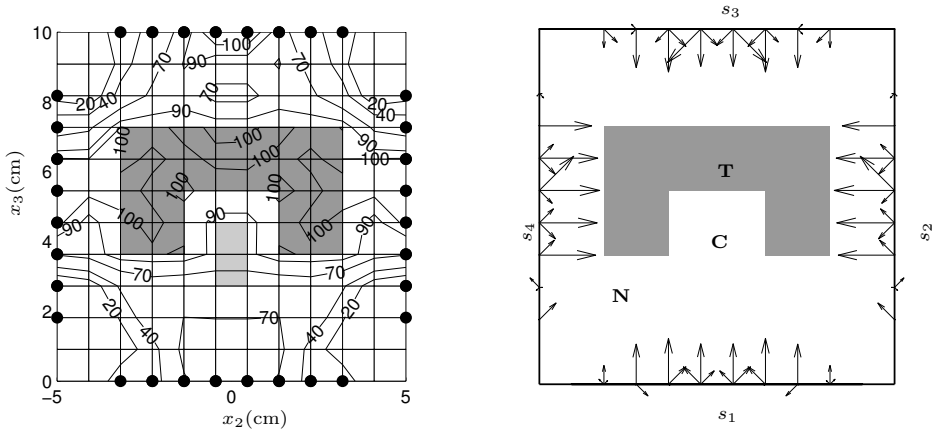

Figure 5.6: The initial results for the PARA1 simulation. On the left the spatial grid is shown with black circles as source nodes. The optimized dose profile is presented with isodoses 20, 40, 70, 90, 100, in which 100% describes D_0=10. On the right there are the resulted initial boundary fluxes $u_i(\mathrm{cm}^{-2}\mathrm{MeV}^{-1}\mathrm{sr}^{-1})$ in the fields s_i $(i = 1, ..., 4)$ at the energy $E = 10$ MeV. Also the target **T**, critical organ **C** and normal tissue **N** are shown.

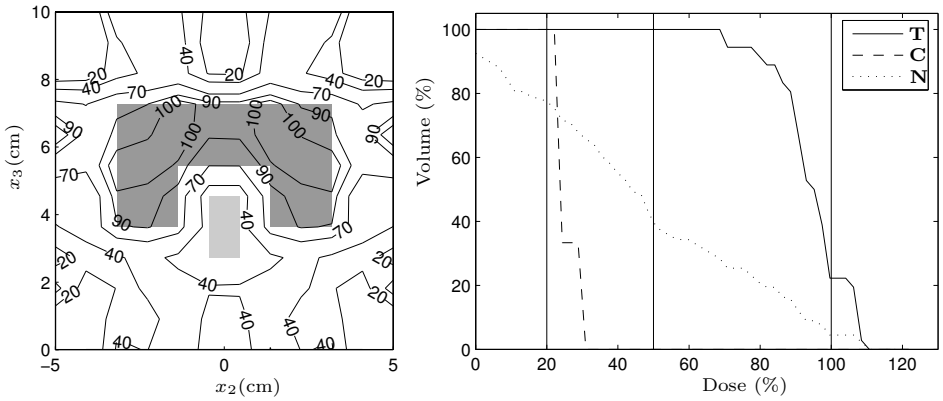

Figure 5.7: The PARA1 simulation results. On the left the optimized dose profile is presented with isodoses 20, 40, 70, 90, 100, in which 100% describes D_0=10. On the right there is the dose volume histogram for percentage doses at the target **T**, critical organ **C** and normal tissue **N**. The vertical lines illustrate the dose limits.

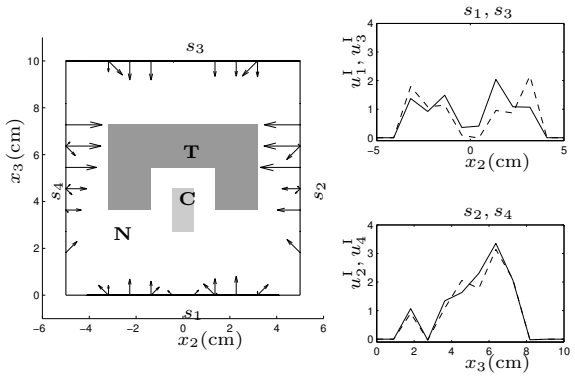

Figure 5.8: The PARA1 simulation results. On the left are the resulted boundary fluxes $u_i(\mathrm{cm}^{-2}\mathrm{MeV}^{-1}\mathrm{sr}^{-1})$ in the fields s_i $(i = 1, ..., 4)$ at the energy $E = 10$ MeV. Also the target **T**, critical organ **C** and normal tissue **N** are shown. On the right in upper figure there are the angle and energy integrated boundary flux values $u_1^{\mathrm{I}}(\mathrm{cm}^{-2})$ (line) and $u_3^{\mathrm{I}}(\mathrm{cm}^{-2})$ (dotted line) for the fields s_1 and s_3, respectively. On the right in lower figure there are the angle and energy integrated boundary flux values $u_2^{\mathrm{I}}(\mathrm{cm}^{-2})$ (line) and $u_4^{\mathrm{I}}(\mathrm{cm}^{-2})$ (dotted line) for the fields s_2 and s_4, respectively.

can be computed from $\psi^{*\mathrm{h}}$. However, probably because of the poor convergence rate, the dose computed from ψ^{h} was much closer to the desired dose than what was received by the forward computations using the boundary control u_0. In Figures 5.2 and 5.4, these afterward computed dose from the resulted boundary controls are shown. Although the dose distributions are not very close to the optimum, clearly the optimization had a right direction and the shapes of the initial boundary fluxes are those that one would expect them to be. For example in Figure 5.3, the integrated boundary fluxes u_1^{I} and u_2^{I} are slightly wedge like, i.e. u_1^{I} is mostly decreasing for increasing x_1 and u_2^{I} is mostly increasing for increasing x_2 just what one would expect them to be to get more dose at the upper left corner of the square target **T**.

The initial guess method for the control problem did not control the dose in normal tissue, but the minimization of the boundary flux did minimize the dose in the whole volume by the minimization of the boundary control. That is why the dose in the normal tissue was weakly considered in the optimization. Also, the positivity of the boundary fluxes were not controlled in INICONTROL1 and INICONTROL2 simulations. However, negative boundary flux values are only slightly present at the results. This is probably due to the minimization of the boundary flux value and because of the use of the adjoint operators.

The initial point control problem was considered here because it forms a linear system of equations. One could derive the equations for the whole radiotherapy

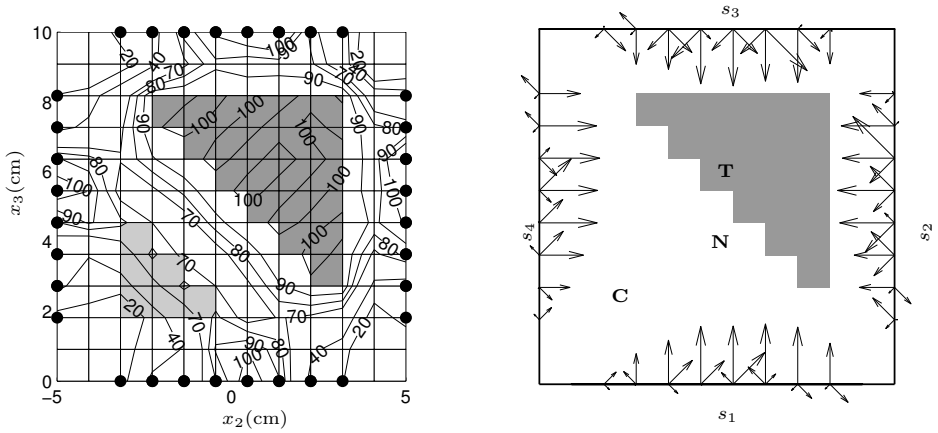

Figure 5.9: The initial results for the PARA2 simulation. On the left the spatial grid is shown with black circles as source nodes. The optimized dose profile is presented with isodoses 20, 40, 70, 90, 100, in which 100% describes D_0=10. On the right there are the resulted initial boundary fluxes $u_i(\text{cm}^{-2}\text{MeV}^{-1}\text{sr}^{-1})$ in the fields s_i $(i = 1, ..., 4)$ at the energy $E = 10$ MeV. Also the target **T**, critical organ **C** and normal tissue **N** are shown.

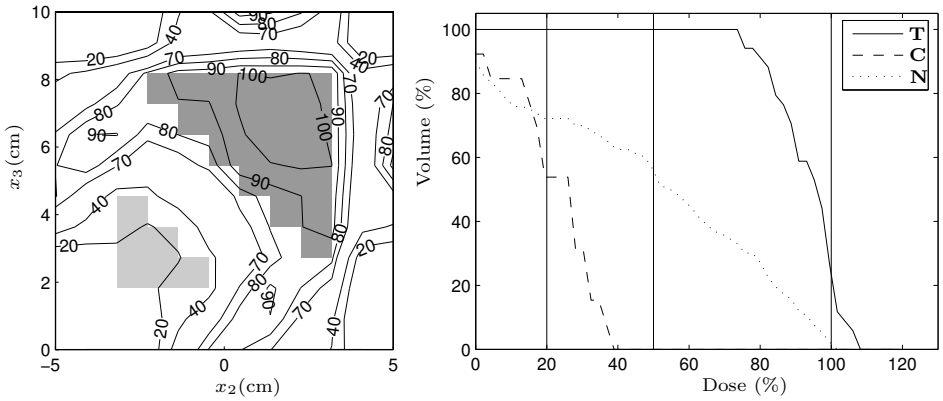

Figure 5.10: The PARA2 simulation results. On the left the optimized dose profile is presented with isodoses 20, 40, 70, 90, 100, in which 100% describes D_0=10. On the right there is the dose volume histogram for percentage doses at the target **T**, critical organ **C** and normal tissue **N**. The vertical lines illustrate the dose limits.

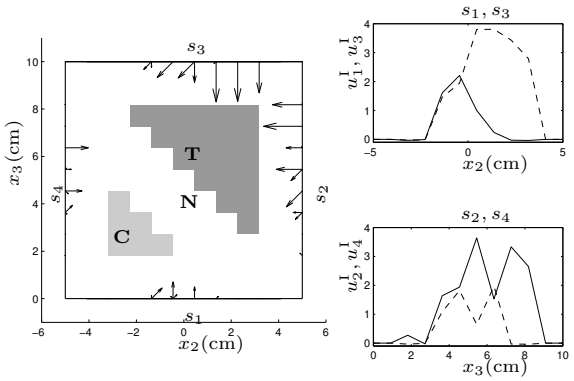

Figure 5.11: The PARA2 simulation results. On the left there are the resulted boundary fluxes u_i in the fields s_i $(i = 1, ..., 4)$ at the energy $E = 10$ MeV. Also the target **T**, critical organ **C** and normal tissue **N** are shown. On the right in upper figure there are the angle and energy integrated boundary flux values $u_1^{\mathrm{I}}(\mathrm{cm}^{-2})$ (line) and $u_3^{\mathrm{I}}(\mathrm{cm}^{-2})$ (dotted line) for the fields s_1 and s_3, respectively. On the right in lower figure there are the angle and energy integrated boundary flux values $u_2^{\mathrm{I}}(\mathrm{cm}^{-2})$ (line) and $u_4^{\mathrm{I}}(\mathrm{cm}^{-2})$ (dotted line) for the fields s_2 and s_4, respectively.

optimization problem and solve the resulted nonlinear equations using some nonlinear system solution algorithm. However, the resulted nonlinear equations are multi-extremal and a good initial point is necessity. Here one alternative for the initial guess is presented. It may not be good at all if the geometry is such that the critical organs are at the locations where high dose values are obtained from the solution of the initial problem. The critical organs could be considered in the solution of the linear system for example by demanding some small dose value at the critical organs. This is not considered here.

With parametrization the global optimization was easy to implement, because the parametrization reduced the number of unknowns from $N + M = 4704$ to $M = 96$. The boundary flux values in each field s_i $(i = 1, ..., 4)$ at maximum energy were solved to optimize the dose by taking into account the critical organ and normal tissue dose limits. The simulation was made to demonstrate the tomotherapy approach, in which the treatment consist of small subfields each having some direction and energy. Now the source angular spectrum at each source node illustrate these small fields, when only maximum energy was allowed. This means that the energy was not exactly optimized, but in each source node the particle flux was allowed to be zero. One could optimize the energy spectrum as well by allowing the energy nodes to change freely, here only the maximum energy node could be changed.

In Figures 5.7 and 5.10, the drawn isodose curves show that the dose in the

tumor is quite smooth and 90% curve nearly rounds the target. Also the critical organ receives a dose, which is quite low, although, it is slightly more than it was allowed to be. In the PARA1 simulation the critical organ is quite close to the target and it makes the dose distribution quite poor near the critical organ. In the PARA2 simulation, the optimal dose distribution is clearly not yet achieved, because in Figure 5.11 the boundary fluxes u_1 and u_4 have values at fields s_1 and s_4 near the critical organ, which increases the dose in it. When a weighted cost function is used, the effect of individual cost is disappeared and it is more difficult to control the dose in critical organ individually.

The used initial guess method in the parametrization simulations does not restrict negative boundary flux values. A big weight was given to restrict negative boundary fluxes in the global optimization. However, because initial guess contained negative flux values, the initial point may not be a good choice. The used Simulated Annealing global optimization algorithm is not a robust one and to better the parametrization simulation results some other more effective global optimizer should be used. In parametrization, the information of the boundary flux and dose values are lost in γ and it is very difficult to assigns some bounds for parameter γ in global optimization. In the simulations with Simulated Annealing the parameter γ was allowed change freely. This makes the computations long and impractical. The resulted dose distributions may not be optimal globally, because of the used global optimization algorithm. Maybe with better global optimizer or with better initial guess one could obtain slightly better results. However, clearly from the optimized dose distributions one can see that the optimization works in general, because it tend to minimize the dose in critical organs, and still the targets receive almost desired dose.

Chapter VI

Conclusion

In this work, the BTE based model in radiotherapy purposes was studied. The interaction cross sections were introduced in Chapter 2 with the definitions of the ionizing radiation. The model consisting of three coupled BTEs was derived in Chapter 3 with typical external radiotherapy boundary conditions. Also the formulas for the dose and the coupled system of B-CSDAEs were presented.

In Chapter 4, the variational form of the coupled BTEs and coupled B-CSDAEs were derived. Also the existence of the solution of these equations were studied. It was found that some restrictions are demanded on the cross sections to fulfill the coercivity criterion for the coupled BTEs. It was also found that these restrictions have physical foundations and are thus physically relevant. Similar restrictions were found for the restricted cross sections of the coupled B-CSDAEs to fulfill the coercivity condition with an additional restriction for the restricted stopping power. The conditions for the restricted cross sections are physically relevant, because the restricted total cross section is computed by integrating the restricted differential cross section. The additional condition for the restricted stopping power was found not to hold for any data and it was suggested that the cut-off energy of the restricted cross sections should be selected such that the restricted stopping power would fulfill the demanded condition.

The finite element discretization of the forward problem was derived in Chapter 4 for the coupled BTEs and for the coupled B-CSDAEs. Also the stream-line diffusion method and related discretizations of these equations were presented. The radiotherapy forward problem describing photon incident external radiotherapy was simulated using two coupled B-CSDAEs in 2D and in 3D spatial domain. The electron incident external radiotherapy simulation was done for one B-CSDAE in 3D spatial domain. The results were compared with the MC computations. 2D photon incident results were very close to the MC data. In 3D, the results had similarities with MC data and most errors were assumed to be based on the sparse finite element grids, which caused the angular spectrum of the photon source to be wider than in the MC simulation and thus the photon flux spread more at high depths. Also the differences between the cross sections used in FEM and MC simulations explained some of the differences in the results. In the photon incident simulations, the obtained electron flux had to be multiplied with some

value to be comparable with the MC data. If the FEM results were normalized according to the photon flux at some point, then the normalized electron flux was much smaller than the MC electron flux. It was thought that this is probably caused by the differential cross section normalization, in which the delta-function shaped cross sections are divided by the size of the elements neighbor to the related node to fulfill the coercivity criterion. With further study, this normalization can be accounted in the calculation of the dose. Also one could integrate the cross sections directly over the delta shaped angular domain and not present them with separable basis. Also the electron incident simulation results had similarities with the MC results, in which the FEM simulation results followed quite well the MC results with respect the depth at the central axis. The stream-line diffusion method was tested for electron incident simulations. It was found that the linear system became stable and convergence was faster, although, the algorithm that was used made the computational times much longer.

The simulations suggested that it is possible to use FEM to solve the radiotherapy forward problem. However, the long computational times and memory problems due to discretization suggest that special methods are required to shorten the calculations times. No preconditioning was used in the forward problem simulations. The use of preconditioning would decrease the computational times significantly [60]. Also one could use for example multigroup method for energy discretization [67]. The parallel domain decomposition methods [62, 171], the selection of the basis functions, the use of spherical wavelet basis in angular domain [45] and adaptivity [63, 68, 102, 157, 187] are also worth of further study. Although the simulations were made for simplicity in homogeneous domains with straight edges to demonstrate photon and electron scattering, the derived forward problems are not restricted to these domains. With the finite element discretization the patient heterogeneity and arbitrary body contours could be considered, but to be practical it would require more dense grids, which would increase the computation times significantly.

The radiotherapy inverse problem was presented in Chapter 5. There the control approach was used to find the optimal dose distribution within the patient. The model for the inverse problems was derived using the coupled BTEs. An initial point was obtained from the solution of the quadratic problem. The approach of parametrization made the transport model easier to handle with global optimization techniques. These methods were tested by simulations using one BTE in 2D spatial domain. The simulations suggested that the radiotherapy inverse problem can be solved with parametrization and initial point can be obtained by solving the quadratic problem.

The use of parametrization showed that the linear system could be reduced and the global optimization was possible. The simple simulations showed that the optimization process works in practice. The global optimization could be improved by using more effective global optimization algorithm instead of Simulated Annealing, using non-weighted methods such as multi criteria optimization [36] or using more precise cost functions such as is suggested in [49, 51]. One problem was also the computation of the parametrization, which is very costly. Special

methods such as Lanczos methods [80] and the use of only approximative forms of the vectors, which span the null space being still accurate enough for the dose computation, should be studied for the parametrization purposes. Also the use of other methods for the parametrization than those related directly to the null space is worth studying.

As a conclusion one could say that FEM can be used in solving the radiotherapy forward problem using transport equations. The coupled system of B-CSDAEs or some other approximation has to be used to implement charged particle traveling on sparse spatial grids. Further study has to be done in the modeling of the electron elastic scattering and preconditioning. Also the adaptivity is worth of further study. Also one could conclude that the radiotherapy inverse problem can be solved using parametrization and BTE based dose calculation model. Further study has to be done in the development of the parametrization, initial guess and global optimization.

[1] R.T. Ackroyd. Generalized least squares as a generator of variational principles and weighted residual methods for FEM transport methods. *Prog Nucl Energ*, 18(1/2):45–62, 1986.

[2] R.T. Ackroyd. *Finite Element Methods for Particle Transport.* John Wiley and Sons, Inc., 1997.

[3] M.L. Adams and W.R. Martin. Slab geometry transport spatial discretization schemes with infinite-order convergence. *Transport Theor Stat*, 15(5):651–671, 1986.

[4] A. Ahnesjö and M.M. Aspradakis. Dose calculations for external photon beams in radiotherapy. *Phys Med Biol*, 44:R99–R155, 1999.

[5] A. Ahnesjö, B. Hårdemark, U. Isacsson, and A. Montelius. The IMRT information process–mastering the degrees of freedom in external beam therapy. *Phys Med Biol*, 51:R381–R402, 2006.

[6] M. Alber and F. Nüsslin. Optimization of intensity modulated radiotherapy under constraints for static and dynamic MLC delivery. *Phys Med Biol*, 46:3229–3239, 2001.

[7] E.J. Allen. A finite element approach for treating the energy variable in the numerical solution of the neutron transport equation. *Transport Theor Stat*, 15(4):449–478, 1986.

[8] P. Andreo. Monte Carlo techniques in medical radiation physics. *Phys Med Biol*, 36(7):861–920, 1991.

[9] G. Arfken. *Mathematical methods for physicists.* Academic Press, Inc., 1985.

[10] S.R. Arridge, M. Schweiger, M. Hiraoka, and D.T. Delpy. A finite element approach for modeling photon transport in tissue. *Med Phys*, 20(2):299–309, 1993.

[11] M. Asadzadeh. The discrete ordinates method for the neutron transport equation in an infinite cylindrical domain. *SIAM J Numer Anal*, 35(4):1299–1314, 1998.

[12] M. Asadzadeh, P. Kumlin, and S. Larsson. The discrete ordinates method for the neutron transport equation in an infinite cylindrical domain. *Math Mod Meth Appl S*, 2:317–338, 1992.

[13] F.H. Attix. *Introduction to Radiological Physics and Radiation Dosimetry.* John Wiley and Sons, Inc., 1986.

[14] A. Badruzzaman. Finite-moments approaches to the time-dependent Boltzmann equation. *Prog Nucl Energ*, 25(2-3):127–157, 1991.

[15] W. Bär, M. Alber, and F. Nüsslin. A variable fluence step clustering and seg-

mentations algorithm for step and shoot IMRT. *Phys Med Biol*, 46:1997–2007, 2001.

[16] L.B. Barichello. Some comments concerning inverse problems in particle transport theory. In *4th International Conference on Inverse Problems in Engineering*, Rio de Janeiro, Brazil, 2002.

[17] D.E. Bartine, R.G. Alsmiller, Jr., F.R. Mynatt, W.W. Engle, Jr., and J. Barish. Low-energy electron transport by the method of discrete ordinates. *Nucl Sci Eng*, 48:159–178, 1972.

[18] G.I. Bell and S. Glasstone. *Nuclear Reactor Theory.* Van Nostrand Reinhold Company, 1970.

[19] M.J. Berger, J.H. Hubbell, S.M. Seltzer, J. Chang, J.S. Coursey, R. Sukumar, and D.S. Zucker. *XCOM: Photon Cross Section Database (version 1.3).* National Institute of Standards and Technology, Gaithersburg, MD., 2005. Online http://physics.nist.gov/xcom (January 24, 2007).

[20] J. Berntsen and T.O. Espelid. Algorithm 706: DCUTRI: An algorithm for adaptive cubature over a collection of triangles. *ACM Trans Math Softw*, 18(3):329–342, 1992.

[21] A.F. Bielajew. Plural and multiple small-angle scattering from a screened Rutherford cross section. *Nucl Instrum Meth B*, 86:257–269, 1994.

[22] A.F. Bielajew. A hybrid multiple-scattering theory for electron-transport Monte Carlo calculations. *Nucl Instrum Meth B*, 111:195–208, 1996.

[23] A.F. Bielajew, R. Wang, and S. Duane. Incorporation of single elastic scattering in the EGS4 Monte Carlo code system: Tests of Molière theory. *Nucl Instrum Meth B*, 82:503–512, 1993.

[24] A.V. Bobylev and G. Spiga. On a model transport equation with inelastic scattering. *SIAM J Appl Math*, 58(4):1128–1137, 1998.

[25] E. Boman, T. Lyyra-Laitinen, P. Kolmonen, K. Jaatinen, and J. Tervo. Simulations for inverse radiation therapy treatment planning using a dynamic MLC algorithm. *Phys Med Biol*, 48(7):925–942, 2003.

[26] E. Boman, J. Tervo, and M. Vauhkonen. Modelling the transport of ionizing radiation using the finite element method. *Phys Med Biol*, 50(7):265–280, 2005.

[27] E. Boman, M. Vauhkonen, and J. Tervo. Modeling radiation transport in a medium with Boltzmann transport equation using finite element method. In *ECCOMAS 2004*, Jyväskylä, Finland, July 2004.

[28] C. Börgers. A fast iterative method for computing particle beams penetrating matter. *J Comput Phys*, 133:323–339, 1997.

[29] C. Börgers. Complexity of Monte Carlo and deterministic dose-calculation methods. *Phys Med Biol*, 43:517–528, 1998.

[30] C. Börgers. Radiation therapy planning problem. In C. Börgers and F. Natterer, editors, *Computational Radiology and Imaging: Therapy and diagnostic*. Springer-Verlag, 1999.

[31] C. Börgers and E.W. Larsen. The transversely intergrated scalar flux of a narrowly focused particle beam. *SIAM J Appl Math*, 55(1):1–22, 1995.

[32] C. Börgers and E.W. Larsen. Asymptotic derivation of the Fermi pencil-beam approximation. *Nucl Sci Eng*, 123:343–357, 1996.

[33] C. Börgers and E.W. Larsen. On the accuracy of the Fokker-Planck and Fermi pencil beam equations for charged particle transport. *Med Phys*, 23(10):1749–1759, 1996.

[34] T. Bortfeld. Optimized planning using physical objectives and constraints. *Sem.*

Rad. Onc., 9(1):20–34, 1999.

[35] T. Bortfeld. IMRT: a review and preview. *Phys Med Biol*, 51:R363–R379, 2006.

[36] T. Bortfeld, K.-H. Küfer, M. Monz, A. Scherrer, C. Thieke, and H. Trinkaus. *Intensity-Modulated Radiotherapy: A Large Scale Multi-Criteria Programming Problem*. 43. Fraunhofer-Institut für Techno- und Wirtschaftsmathematik ITWM, 2003. Online http://www.itwm.fraunhofer.de (January 24, 2007).

[37] A. Brahme, editor. *Special issue: Optimization of the three-dimensional dose delivery and tomotherapy*, volume 6. Int J Imag Syst Tech, 1995.

[38] A. Brahme. Treatment optimization: Using physical and radiological objective functions. In A.R. Smith, editor, *Radiation Therapy Physics*, pages 209–246. Springer, 1995.

[39] A. Brahme. Optimized radiation therapy based on radiobiological objectives. *Sem Rad Onc*, 9(1):35–47, 1999.

[40] A. Brahme. Development of radiation therapy optimization. *Acta Onc*, 39(5):579–595, 2000.

[41] L.L. Briggs, W.F. Miller, Jr., and E.E. Lewis. Ray-effet mitigation in discrete ordinate-like angular finite element approximation in neutron transport. *Nucl Sci Eng*, 57:205–217, 1975.

[42] I.A.D. Bruinvis, W.A.F. Mathol, and P. Andreo. Inclusion of electron range straggling in the Fermi-Eyges multiple-scattering theory. *Phys Med Biol*, 34(4):491–507, 1989.

[43] T.A. Brunner. Forms of approximate radiation transport. Technical report SAND2002-1778, Sandia National Laboratories, Albuquerque, New Mexico 87185 and Livermore, California 94550, July 2002.

[44] D. Brusa, G. Stutz, J.A. Riveros, J.M. Fernández-Varea, and F. Salvat. Fast sampling algorithm for the simulation of photon Compton scattering. *Nucl Instrum Meth A*, 379:167–175, 1996.

[45] A.G. Buchan, C.C. Pain, M.D. Eaton, R.P. Smedley-Stevenson, and A.J.H. Goddard. Linear and quadratic octahedral wavelets on the sphere for angular discretisations of the boltzmann transport equation. *Ann Nucl Energy*, 32:1224–1273, 2005.

[46] M. Caro and J. Ligou. Treatment of scattering anisotropy of neutrons through the Boltzmann-Fokker-Planck equation. *Nucl Sci Eng*, 83:242–252, 1983.

[47] K.M. Case and P.F. Zweifel. *Linear Transport Theory*. Addison-Wesley, 1967.

[48] Y. Censor. Mathematical aspects of radiation therapy treatment planning: Continuous inversion versus full discretization and optimization versus feasibility. In C. Börgers and F. Natterer, editors, *Computational Radiology and Imaging: Therapy and Diagnosis*, volume 110, pages 101–112. Springer-Verlag, New York, NY, 1999.

[49] Y. Censor, T. Bortfeld, B. Martin, and A. Trofimov. A unified approach for inversion problems in intensity-modulated radiation therapy. *Phys Med Biol*, 51:2353–2365, 2006.

[50] C. Cercignani. *The Boltzmann equation and its applications*. Springer, 1988.

[51] Y. Chen, D. Michalski, C. Houser, and J.M. Galvin. A deterministic iterative least-squares algorithm for beam weight optimization in conformal radiotherapy. *Phys Med Biol*, 47:1647–1658, 2002.

[52] C.-S. Chui, T. LoSasso, and S. Spirou. Dose calculation for photon beams with intensity modulation generated by dynamic jaw or multileaf collimations. *Med Phys*, 21(8):1237–1244, 1994.

[53] P.G. Ciarlet. *The finite element method for elliptic problems*. North-Holland Publishing company, 1978.

[54] G.G.M. Coppa, G. Lapenta, and P. Ravetto. Angular finite element techniques in neutron transport. *Ann Nucl Energy*, 17(7):363–378, 1990.

[55] G.G.M. Coppa and R. Ravetto. Quasi-singular angular finite element methods in neutron transport problems. *Transport Theor Stat*, 24(1-3):155–172, 1995.

[56] A. Corana, M. Marchesi, C. Martini, and S. Ridella. Minimizing multimodal functions of continuous variables with the "simulated annealing" algorithm. *ACM Trans Math Softw*, 13(3):262–280, 1987.

[57] S.M. Crooks and L. Xing. Linear algebraic methods applied to intensity modulated radiation therapy. *Phys Med Biol*, 46:2587–2606, 2001.

[58] C. Cuvelier, A. Segal, and A.A. van Steenhoven. *Finite element methods and Navier-Stokes equations*. D. Reidel Publishing company, 1986.

[59] R. Dautray and J.-L. Lions. *Mathematical Analysis and Numerical Methods for Science and Technology*. Springer-Verlag, 1993.

[60] E.F. D'azevedo, B. Messer, A. Mezzacappa, and M. Liebendörfer. An ADI-like preconditioner for Boltzmann transport. *SIAM J. Sci. Comput.*, 26(3):810–820, 2005.

[61] M. de Gersem, F. Claus, C. de Wagter, B. van Duyse, and W. de Neve. Leaf position optimization for step-and-shoot IMRT. *Int J Rad Onc Biol Phys*, 51(5):1371–1388, 2001.

[62] C.R.E. de Oliveira, C.C. Pain, and J.H. Goddard. Parallel domain decomposition methods for large-scale finite element transport modelling. In *ANS M&C International Topical Conference, Mathematics and Computations, Reactor Physics, and Environmental Analyses*, pages 490–498, Portland, Oregon, April 30 - May 4 1995.

[63] A. Dedner and P. Vollmöller. An adaptive higher order method for solving the radiation transport equation on unstructured grids. *J Comput Phys*, 178:263–289, 2002.

[64] C.R. Drumm. Multidimensional electron-photon transport with standard discrete ordinates codes. *Nucl Sci Eng*, 127:1–27, 1997.

[65] C.R. Drumm. Parallel finite element electron-photon transport analysis on 2-D unstructured mesh. Technical report SAND99-0098, Sandia National Laboratories, Albuquerque, New Mexico 87185 and Livermore, California 94550, January 1999.

[66] C.R. Drumm and J. Lorenz. Parallel FE approximation of the even/odd-parity form of the linear Boltzmann equation. *Math Comput Model*, 31:55–71, 2000.

[67] J.J. Duderstadt and W.R. Martin. *Transport Theory*. John Wiley and Sons, Inc., 1979.

[68] P.E. Dyshlovenko. Adaptive numerical method for Poisson-Boltzmann equation and its application. *Comput Phys Commun*, 147:335–338, 2002.

[69] S. Balay et. al. *PETSc Users Manual*. Mathematical and computer science division, 2003. Online http://www.mcs.anl.gov/petsc (January 24, 2007).

[70] J.A. Favorite. Using the Schwinger variational functional for the solution of the inverse transport problem. *Nucl Sci Eng*, 146:51–70, 2004.

[71] J.A. Favorite and R. Sanchez. An inverse method for radiation transport. *Radiat Prot Dosim*, 116(1-4):482–485, 2005.

[72] J.E. Fernández. Polarisation effects in multiple scattering photon calculation using the Boltzmann vector equation. *Radiat Phys Chem*, 56:27–59, 1999.

[73] J.E. Fernández, V.G. Molinari, and F. Teodori. Mathematical modelling of 3D electron-photon transport in microbeam analysis. *Mikrochim Acta*, 132:219–224,

2000.

[74] M. Fippel, M. Alber, M. Birkner, W. Laub, F. Nüsslin, and I. Kawrakow. *Advanced Monte Carlo for radiation physics, particle transport simulation and applications: Proceedings of the Monte Carlo 2000 conference*, chapter Inverse treatment planning for radiation therapy based on fast Monte Carlo dose calculation. Springer, 2001.

[75] T.-P. Fries and H.G. Matthies. *A Review of Petrov-Galerking Stabilization Approaches and an Extension to Meshfree Methods.* 2004-01. Institut für Wissenschaftliches Rechnen, 2004. Online http://opus.tu-bs.de/opus/volltexte/2004/549/ (January 24, 2007).

[76] J.M. Galvin, Y. Xiao, Y. Chen, G. Bednarz, D. Michalski, Y. Censor, C. Houser, M. Hossain, and M.S. Huq. The optimization of inverse planning and IMRT. In *44th AAPM (American Association of Physicists in Medicine) Annual Meeting*, Montreal, Canada, July 14-18 2002.

[77] R. García-Pelayo. Multiple scattering. *Physica A*, 258:365–382, 1998.

[78] K.A. Gifford, J.L. Horton, Jr, T.A. Wareing, G. Failla, and F. Mourtada. Comparison of a finite-element multigroup discrete-ordinates code with Monte Carlo for radiotherapy calculations. *Phys Med Biol*, 51:2253–2265, 2006.

[79] H. Goldstein. *Fundamental aspects of reactor shielding.* Addison-Wesley Publishing Company, 1959.

[80] G.H. Golub and C.F. van Loan. *Matrix Computations.* The Johns Hopkins University Press, 1989.

[81] A. Gustafson, B.K. Lind, and A. Brahme. A generalized pencil beam algorithm for optimization of radiation therapy. *Med Phys*, 21:343–356, 1994.

[82] J. Haataja, J. Heikonen, Y. Leino, J. Rahola, J. Ruokolainen, and V. Savolainen. *Numeeriset menetelmät käytännössä.* CSC–Tieteellinen laskenta, 2002. Online http://www.csc.fi/oppaat/num.kayt/ (January 24, 2007).

[83] H. Hensel, R. Iza-Teran, and N. Siedow. Deterministic model for dose calculation in photon radiotherapy. *Phys Med Biol*, 51:675–693, 2006.

[84] K.R. Hogstrom and P.R. Almond. Review of electron beam therapy physics. *Phys Med Biol*, 51:R455–R489, 2006.

[85] K.R. Hogstrom, M.D. Mills, and P.R. Almond. Electron beam dose calculations. *Phys Med Biol*, 26(3):445–459, 1981.

[86] H. Huizenga and P.R.M. Storchi. Numerical calculation of energy deposition by broad high-energy elecron beams. *Phys Med Biol*, 34(10):1371–1396, 1989.

[87] ICRU. Stopping powers for electrons and positrons, ICRU report 37. International Commission on Radiation Units and measurements (ICRU), Washington D.C., 1984.

[88] ICRU. Fundamental Quantities and Units for Ionising Radiation, ICRU report 60. International Commission on Radiation Units and measurements (ICRU), Washington D.C., 1998.

[89] A. Ishimaru. *Wave Propagation and Scattering in Random Media*, volume 1: Single Scattering and Transport Theory. Academic Press, Inc., 1978.

[90] A. Jablonski, F. Salvat, and C.J. Powell. NIST electron elastic scattering cross-section database - version 3.0. Technical report, National Institute of Standards and Technology, Gaithersburg, MD, 2002.

[91] J.J. Janssen, D.E.J. Riedeman, M. Morawska-Kaczyńska, P.R.M. Storchi, and H. Huizenga. Numerical calculation of energy deposition by high-energy electron beams: III. Three-dimensional heterogeneous media. *Phys Med Biol*, 39:1351–1366,

1994.

[92] R. Jeraj and P.J. Keall. Monte Carlo-based inverse treatment planning. *Phys Med Biol*, 44:1885–1896, 1999.

[93] D. Jette. Electron dose calculation using multiple-scattering theory. A. Gaussian multiple-scattering theory. *Med Phys*, 15(2):123–137, 1988.

[94] D. Jette. Electron dose calculation using multiple-scattering theory: Localized inhomogeneities–A new theory. *Med Phys*, 18(2):123–132, 1991.

[95] D. Jette. Electron Beam Dose Calculations. In A.R. Smith, editor, *Medical Radiology, Radiation Therapy Physics*. Springer-Verlag, Berlin, 1995.

[96] D. Jette. Electron dose calculation using multiple-scattering theory: A new theory of multiple scattering. *Med Phys*, 23(4):459–477, 1996.

[97] D. Jette and A. Bielajew. Electron dose calculation using multiple-scattering theory: Second-order multiple-scattering theory. *Med Phys*, 16(5):698–711, 1989.

[98] D. Jette, L.H. Lanzl, A. Pagnamenta, M. Rozenfeld, D. Bernard, M. Kao, and A.M. Sabbas. Electron dose calculation using multiple-scattering theory: Thin planar inhomogeneities. *Med Phys*, 16(5):712–725, 1989.

[99] D. Jette and S. Walker. Electron dose calculation using multiple-scattering theory: Evaluation of a new model for inhomogeneities. *Med Phys*, 19(5):1241–1254, 1992.

[100] D. Jette and S. Walker. Electron dose calculation using multiple-scattering theory: Energy distribution due to multiple scattering. *Med Phys*, 24(3):383–400, 1997.

[101] C. Johnson. *Numerical solution of partial differential equations by the finite element method*. Claes Johnson and Studentlitteratur, 1987.

[102] G. Kanschat. *Parallel and adaptive galerkin methods for radiative transfer problems*. PhD thesis, Univ. of Heidelberg, 1996. Online http://www.math.tamu.edu/~kanschat/ (January 24, 2007).

[103] G. Kanschat. A robust finite element discretization for radiative transfer problems with scattering. *East-West J Numer Math*, 6(4):265–272, 1998.

[104] I. Kawrakow and D.W.O. Rogers. The EGSnrc code system: Monte Carlo simulation of electron and photon transport. Technical Report PIRS-701, National Research Council of Canada, 2002. Online http://www.irs.inms.nrc.ca/inms/irs/EGSnrc/EGSnrc.html (January 24, 2007).

[105] P.J. Keall, J.V. Siebers, M. Arnfield J.O. Kim, and R. Mohan. Monte Carlo dose calculations for dynamic IMRT treatments. *Phys Med Biol*, 46:929–941, 2001.

[106] F.M. Khan. *The Physics of Radiation Therapy, 3rd ed.* Lippincott Williams&Wilkins, 2003.

[107] L. Kissel. RTAB: the rayleigh scattering database. *Radiation Physics and Chemistry*, 59:185–200, 2000. Online http://www-phys.llnl.gov/Research/scattering/RTAB.html (January 24, 2007).

[108] H.W. Koch and J. W. Motz. Bremsstrahlung cross-section formulas and related data. *Rev Mod Phys*, 31(4):920–955, 1959.

[109] P. Kolmonen. *The Direct Control of the Multi-Leaf Collimator in the Inverse Problem of Radiotherapy Treatment Planning*. PhD thesis, University of Kuopio, Kuopio, Finland, 2004.

[110] P. Kolmonen, J. Tervo, and T. Lahtinen. Use of the Cimmino algorithm and continuous approximation for the dose deposition kernel in the inverse problem of radiation treatment planning. *Phys Med Biol*, 43(9):2539–2554, 1998.

[111] M. Landesman and J.E. Morel. Angular Fokker-Planck decomposition and representation techniques. *Nucl Sci Eng*, 103:1–11, 1989.

[112] E.W. Larsen. Diffusion-synthetic acceleration methods for discrete-ordinates prob-

lems. *Transport Theor Stat*, 13(1-2):107–126, 1984.

[113] E.W. Larsen. The amplitude and radius of a radiation beam. *Transport Theor Stat*, 26(4-5):533–554, 1997.

[114] E.W. Larsen. The nature of transport calculations used in radiation oncology. *Transport Theor Stat*, 26:739, 1997.

[115] E.W. Larsen, M.M. Miften, B.A. Fraas, and I.A.D. Bruinvis. Electron dose calculations using the Method of Moments. *Med Phys*, 24(1):111–125, 1997.

[116] M.S. Lazo and J.E. Morel. A linear discontinuous galerkin approximation for the continuous slowing down operator. *Nucl Sci Eng*, 92:98–109, 1986.

[117] C.L. Leakeas and E.W. Larsen. Asymptotic correction to Fermi-Eyges theory for electron transport problems. In *Joint Internation Conference on Mathematical Methods and Supercomputing for Nuclear Applications*, volume 2, pages 1319–1328, Saratoga Springs, New York, October 5-9 1997.

[118] P. Lesaint and P.A. Raviant. On a finite element method for solving the neutron transport equation. In C. de Boor, editor, *Mathematical Aspects of Finite Elements in Partial Differential Equations*, pages 89–123. Academic Press, New York, 1974.

[119] E.E. Lewis and W.F. Miller, Jr. *Computational Methods of Neutron Transport*. John Wiley and Sons., 1984.

[120] J.L. Lions. *Optimal Control of Systems Governed by Partial Differential Equations*. Springer-Verlag, 1971.

[121] J. Liscum-Powell. Finite element numerical solution of a self-adjoint transport equation for coupled electron-photon problems. Technical report SAND2000-2017, Sandia National Laboratories, Albuquerque, New Mexico 87185 and Livermore, California 94550, 2000.

[122] J.L. Liscum-Powell, A.K. Prinja, J.E. Morel, and L.J. Lorence, Jr. Finite element numerical solution of a self-adjoint transport equation for coupled electron-photon problems. *Nucl Sci Eng*, 142:270–291, 2002.

[123] L.J. Lorence, Jr. and D.E. Beutler. Radiation transport phenomena and modeling. Part A: Codes. Technical report SAND97-2135, Sandia National Laboratories, Albuquerque, New Mexico 87185 and Livermore, California 94550, 1997.

[124] L.J. Lorence, Jr., J.E. Morel, and G.D. Valdez. Physics guide to CEPXS: A multigroup coupled electron-photon cross section generating code. Technical report SAND89-1685, Sandia National Laboratories, Albuquerque, New Mexico 87185 and Livermore, California 94550, 1989.

[125] L.J. Lorence, Jr., W.E. Nelson, and J.E. Morel. Coupled electron-photon transport calculations using the method of discrete ordinates. *IEEE T Nucl Sci*, NS-32(6):4416–4420, 1985.

[126] T.R. Mackie. History of tomotherapy. *Phys Med Biol*, 51:R427–R453, 2006.

[127] A. Majorana and S.A. Marano. Space homogeneous solutions to the cauchy problem for semiconductor Boltzmann equations. *SIAM J Math Anal*, 28(6):1294–1308, 1997.

[128] T.A. Manteuffel, K.J. Ressel, and G. Starke. A boundary functional for the least-squares finite-element solution of neutron transport problems. *SIAM J Numer Anal*, 37(2):556–586, 2000.

[129] C. Martens, W. de Gersem, W. de Neve, and C. de Wagter. Combining the advantages of step-and-shoot and dynamic delivery of intensity-modulated radiotherapy by interrupted dynamic sequences. *Int J Rad Onc Biol Phys*, 50(2):541–550, 2001.

[130] W.R. Martin and J.J. Duderstadt. Finite element solutions of the neutron transport equation with applications to strong heterogeneities. *Nucl Sci Eng*, 62:371–

390, 1977.

[131] W.R. Martin, C.E. Yehnert, L. Lorence, and J.J. Duderstadt. Phase-space finite element methods applied to the first-order form of the transport equation. *Ann Nucl Energy*, 8:633–646, 1981.

[132] J. McLellan, L. Papiez, G.A. Sandison, W. Huda, and P. Therrien. A numerical method for electron transport calculations. *Phys Med Biol*, 37(5):1109–1125, 1992.

[133] T.A. Mehlhorn and J.J. Duderstadt. A discrete ordinates solution of the Fokker-Planck equation characterizing charged particle transport. *J Comput Phys*, 38:86–106, 1980.

[134] Y. Mejaddem, Dž. Belkić, A. Brahme, and S. Hyödynmaa. Development of the electron transport theory and absorbed dose computation in matter. *Nucl Instrum Meth A*, 187:499–524, 2002.

[135] V.G. Molinari, S. Manservisi, F. Rocchi, and F. Teodori. Modelling of radiation transport. *Nucl Instrum Meth B*, 213:75–81, 2004.

[136] M. Morawska-Kaczyńska and H. Huizenga. Numerical calculation of energy deposition by broad high-energy electron beams: II. Multi-layered geometry. *Phys Med Biol*, 37(11):2103–2116, 1992.

[137] M. Mordant. Linear discontinuous finite elements for phase-space multidimensional transport calculations. *Nucl Sci Eng*, 92:218–227, 1986.

[138] J.E. Morel. Fokker-Planck calculations using standard discrete ordinates transport codes. *Nucl Sci Eng*, 79:340–356, 1981.

[139] J.E. Morel. A hybrid collocation-Galerkin-S_n method for solving the Boltzmann transport equation. *Nucl Sci Eng*, 101:72–87, 1989.

[140] J.E. Morel and J.M. McGhee. A self-adjoint angular flux equation. *Nucl Sci Eng*, 132:312–325, 1999.

[141] J.E. Morel, T.A. Wareing, R.B. Lowrie, and D.K. Parsons. Analysis of ray-effect mitigation techniques. *Nucl Sci Eng*, 144:1–22, 2003.

[142] R.L. Morin. *Monte Carlo simulation in the radiological science*. CRC Press, Inc., 1988.

[143] I.E. Mozolevski. Modeling of high energy ion implantation based on splitting of the Boltzmann transport equation. *Comput Mater Sci*, 25:435–446, 2002.

[144] A.E. Nahum, editor. *The computation of dose distribution in electron beam radiotherapy*. Ume University, 1985.

[145] S.J. Norton. A general nonlinear inverse transport algorithm using forward and adjoint flux computations. *IEEE T Nucl Sci*, 44(2):153–162, 1997.

[146] J.R. Palta and T.R. Mackie, editors. *Intensity-Modulated Radiation Therapy, The State Of The Art*. Number 29 in Medical Physics Monograph. American Association of Physicists in Medicine, 2003. Summer School Proceedings, Colorado.

[147] C.V. Pao. A nonlinear Boltzmann equation in transport theory. *T Am Math Soc*, 194:167–175, 1974.

[148] G.C. Pomraning. *The equations of Radiation Hydrodynamics*. Pergamon press, Inc., 1973.

[149] G.C. Pomraning. Flux-limited diffusion and Fokker-Planck equations. *Nucl Sci Eng*, 85:116–126, 1983.

[150] G.C. Pomraning. The Fokker-Planck operator as an asymptotic limit. *Math Mod Meth Appl S*, 2(1):21–36, 1992.

[151] G.C. Pomraning and A.K. Prinja. Higher-order multiple scattering theories for charged particle transport. *Med Phys*, 23(10):1761–1774, 1996.

[152] L.M. Popescu. A computer code package for Monte Carlo photon-electron trans-

port simulation: Comparisons with experimental benchmarks. *Nucl Instrum Meth B*, 161-163:318–322, 2000.

[153] W.V. Prestwich and F. Kus. Radial dose profiles for pencil electron beams. *Radiat Phys Chem*, 50(6):535–543, 1997.

[154] R.A. Price, Jr., G.E. Hanks, S.W. McNeeley, E.M. Horwithz, and W.H. Pinover. Advantages of using noncoplanar vs. axial beam arrangements when treating prostate cancer with intensity-modulated radiation therapy and the step-and-shoot delivery method. *Int J Rad Onc Biol Phys*, 53(1):236–243, 2002.

[155] K. Przybylski and J. Ligou. Numerical analysis of the Boltzmann equation including Fokker-Planck terms. *Nucl Sci Eng*, 81:92–109, 1982.

[156] W.H. Reed and T.R. Hill. Triangular mesh methods for the neutron transport equation. Technical report, Los Alamos Scientific Laboratory report LA-UR-73-479, 1973.

[157] S. Richling, E. Meinköhn, N. Kryzhevoi, and G. Kanschat. Radiative transfer with finite elements I. Basic method and tests. *Astron Astrophys*, 380:776–788, 2001.

[158] D.W.O. Rogers. Fifty years of Monte Carlo simulations for medical physics. *Phys Med Biol*, 51:R287–R301, 2006.

[159] H. Ruotsalainen, E. Boman, K. Miettinen, and J. Hämäläinen. Interactive multiobjective optimization for imrt. Technical report, Helsinki School of Economics, Helsinki, 2006. Online http://hsepubl.lib.hse.fi/pdf/wp/w409.pdf (January 24, 2007).

[160] E. Schreibmann, M. Lahanas, L. Zing, and D. Baltas. Multiobjective evolutionary optimization of the number of beams, their orientations and weights for intensity-modulated radiation therapy. *Phys Med Biol*, 49:747–770, 2004.

[161] J. Selman. *The Basic Physics of Radiation Therapy*. C.C. Thomas, second edition, 1976.

[162] S.M. Seltzer and M.J. Berger. Bremsstrahlung energy spectra from electrons with kinetic energy 1 keV-10 GeV incident on screened nuclei and orbital electrons of neutral atoms with Z=1-100. *Atom Data Nucl Data*, 35:345–418, 1986.

[163] J. Sempau, S.J. Wilderman, and A.F. Bielajew. DPM, a fast, accurate Monte Carlo code optimized for photon and electron radiotherapy treatment planning dose calculations. *Phys Med Biol*, 45:2263–2291, 2000.

[164] A.R. Smith, editor. *Radiation Therapy Physics*. Springer, 1995.

[165] A.R. Smith. Proton therapy. *Phys Med Biol*, 51:R491–R504, 2006.

[166] G. Strang and G.J. Fix. *An analysis of the finite element method*. Prentice-Hall, Inc., 1973.

[167] P.R.M. Strochi, L.J. van Battum, and E. Woudstra. Calculation of a pencil beam kernel from measured photon beam data. *Phys Med Biol*, 44:2917–2928, 1999.

[168] H. Tagziria, editor. *Review of Monte Carlo and Deterministic Codes in Radiation Protection and Dosimetry*. NPL Report, Teddington, 2000.

[169] J. Tervo and P. Kolmonen. A model for the control of multileaf collimator and related inverse planning algorithm. *Inv Probl*, 16:1875–1895, 2000.

[170] J. Tervo and P. Kolmonen. Inverse radiotherapy treatment planning model applying Boltzmann-transport equation. *Math Mod Meth Appl S*, 12(1):109–141, 2002.

[171] J. Tervo, P. Kolmonen, E. Boman, and K. Jaatinen. Domain decomposition method for Boltzmann transport equation related to radiation treatment dose calculation. Technical Report Report 2/2005, Department of Mathematics and Statistics, University of Kuopio, Kuopio, Finland, 2005.

[172] J. Tervo, P. Kolmonen, E. Boman, and K. Jaatinen. On finite element and collo-

cation methods for Boltzmann transport equation related to radiation treatment dose calculation. Technical Report Report 1/2005, Department of Mathematics and Statistics, University of Kuopio, Kuopio, Finland, 2005.

[173] J. Tervo, P. Kolmonen, M. Vauhkonen, L.M. Heikkinen, and J.P. Kaipio. A finite-element model of electron transport in radiation therapy and a related inverse problem. *Inverse Probl*, 15:1345–1361, 1999.

[174] J. Tervo, T. Lyyra-Laitinen, P. Kolmonen, and E. Boman. An inverse treatment planning model for intensity modulated radiation therapy with dynamic MLC. *Appl Math Comput*, 135:227–250, 2003.

[175] J. Tervo, M. Vauhkonen, and E. Boman. Optimal control of particle transfer applying Boltzmann transport equation and parametrization. *submitted to Special Issue of the Journal Linear Algebra and Its Applications (LAA)*, 2007.

[176] J. Tervo, M. Vauhkonen, E. Boman, P. Kokkonen, and M. Nihtilä. Optimal control model for inverse radiation therapy treatment planning. In *44th IEEE Conference on Decision and Control and European Control Conference 2005*, Sevilla, Spain, Dec 12-15 2005.

[177] D.I. Thwaites and J.B. Tuohy. Back to the future: the history and development of the clinical linear accelerator. *Phys Med Biol*, 51:R343–R362, 2006.

[178] F. Treves. *Basic Linear Partial Differential Equations.* Academic Press, Inc., 1975.

[179] S. Ukai. Solution of multi-dimensional neutron transport equation by finite element method. *J Nucl Sci Technol*, 9(6):366–373, 1972.

[180] W. Ulmer and D. Harder. Applications of a triple Gaussian pencil beam model for photon beam treatment planning. *Z Med. Phys*, 6:68–74, 1996.

[181] H.A. van der Vorst. *Iterative Krylov methods for large linear systems.* Cambridge University Press New York, 2003.

[182] P.J. Vauhkonen. *Image Reconstruction in Three-Dimensional Electrical Impedance Tomography.* PhD thesis, University of Kuopio, Kuopio, Finland, 2004.

[183] W.F. Walters and J.E. Morel. Investigation of linear-discontinuous angular differencing for the 1-D spherical-geometry S_N equations. In *ANS M&C International Topical Meeting on Advances in Mathematics, Computation, and Reactor Physics*, pages 13.2 3– (1–8), Greentree Marriot, Pittsburgh, PA, April 28 - May 2 1995.

[184] T.A. Wareing, J.M. McGhee, J.E. Morel, and S.D. Pautz. Discontinuous finite element S_N methods on three-dimensional unstructured grids. *Nucl Sci Eng*, 138:256–268, 2001.

[185] J.S. Warsa. Analytical S_N solutions in heterogeneous slabs using symbolic algebra computer programs. *Ann Nucl Energy*, 29(7):851–874, 2002.

[186] J.S. Warsa and A.K. Prinja. Bilinear-discontinuous numerical solution of the time dependent transport equation in slab geometry. *Ann Nucl Energy*, 26(3):195–215, 1999.

[187] J.S. Warsa and A.K. Prinja. p-adaptive numerical methods for particle transport. *Transport Theor Stat*, 28:229, 1999.

[188] S. Webb, editor. *The Physics of Three-Dimensional Radiation Therapy: Conformal Radiotherapy, Radiosurgery and Treatment Planning.* IOP, 1993.

[189] S. Webb, editor. *The Physics of Conformal Radiotherapy: Advances in Techonology.* IOP, 1997.

[190] S. Webb. Concepts for shuttling multileaf collimators for intensity-modulated radiation therapy. *Phys Med Biol*, 46:637–651, 2001.

[191] S. Webb. Motion effects in (intensity modulated) radiation therapy: a review. *Phys Med Biol*, 51:R403–R425, 2006.

[192] B.L. Werner, P.S. Cho, and J. Pfund. The FE-lspd model for electron beam dosimetry. *Phys Med Biol*, 43:291–311, 1998.
[193] L.E. Williams, editor. *Nuclear Medical Physics*, volume I. CRC Press, Inc., 1987.
[194] M.L. Williams, D. Ilas, E. Sajo, D.B. Jones, and K.E. Watkins. Deterministic photon transport calculations in general geometry for external beam radiation therapy. *Med Phys*, 30(12):3183–3195, 2003.
[195] M.L. Williams and E. Sajo. Deterministic calculations of photon spectra for clinical accelerator targets. *Med Phys*, 29(6):1019–1028, 2002.
[196] M.M.R. Williams, editor. *Mathematical Methods in Particle Transport Theory*. Butterworth & Co Ltd, 1971.
[197] M.M.R. Williams. The role of the Boltzmann transport equation in radiation damage calculations. *Prog Nucl Energ*, 3(1):1–65, 1975.
[198] J.F. Williamson. Brachytherapy technology and physics practice since 1950: a half-century of progress. *Phys Med Biol*, 51:R303–R325, 2006.
[199] C.D. Zerby and F.L. Keller. Electron transport theory, calculations, and experiments. *Nucl Sci Eng*, 27:190–218, 1967.
[200] L. Zheng-Ming and A. Brahme. High-energy electron transport. *Phys Rev B*, 46(24):15 739–15 752, 1992.
[201] L. Zheng-Ming and A. Brahme. An overwiew of the transport theory of charged particles. *Radiat Phys Chem*, 41(4/5):673–703, 1993.